frontiers | Research Topics

Science and technology in deep underground laboratories

Edited by
Aldo Ianni, Sean M. Paling, Carlos Peña Garay and Jeter Hall

Published in
Frontiers in Physics

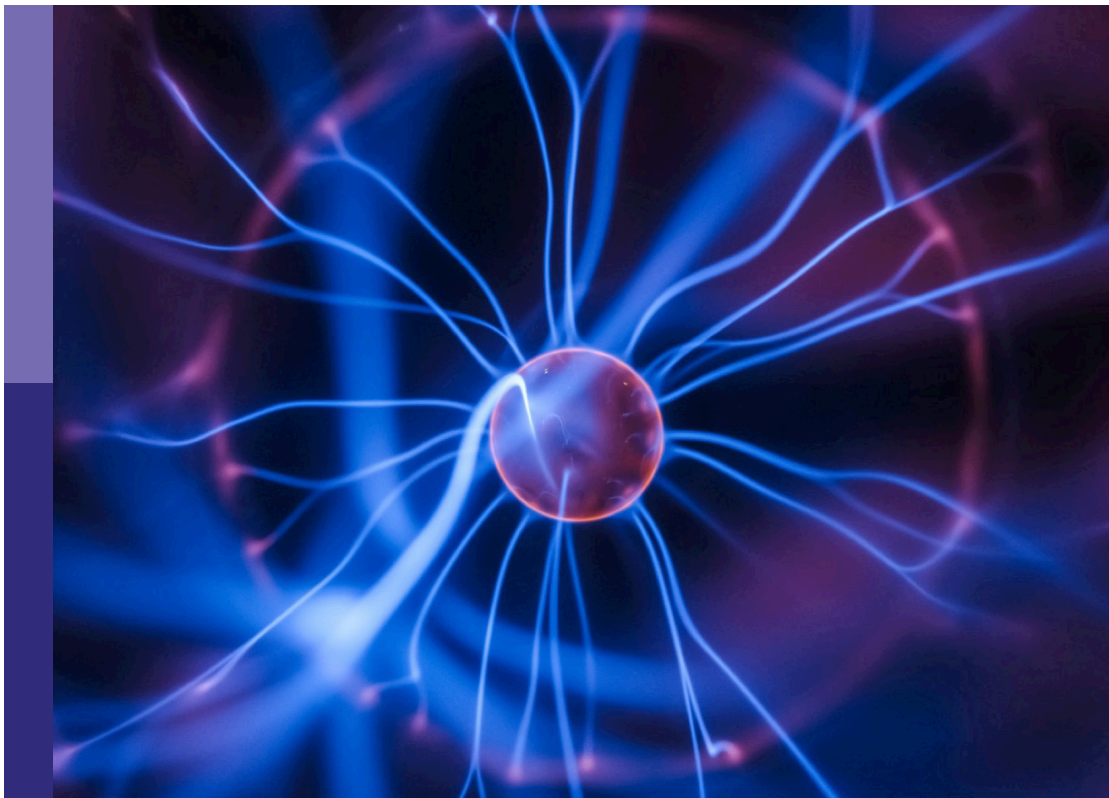

ISSN 1664-8714
ISBN 978-2-8325-5708-2
DOI 10.3389/978-2-8325-5708-2

About Frontiers

Frontiers is more than just an open access publisher of scholarly articles: it is a pioneering approach to the world of academia, radically improving the way scholarly research is managed. The grand vision of Frontiers is a world where all people have an equal opportunity to seek, share and generate knowledge. Frontiers provides immediate and permanent online open access to all its publications, but this alone is not enough to realize our grand goals.

Frontiers journal series

The Frontiers journal series is a multi-tier and interdisciplinary set of open-access, online journals, promising a paradigm shift from the current review, selection and dissemination processes in academic publishing. All Frontiers journals are driven by researchers for researchers; therefore, they constitute a service to the scholarly community. At the same time, the *Frontiers journal series* operates on a revolutionary invention, the tiered publishing system, initially addressing specific communities of scholars, and gradually climbing up to broader public understanding, thus serving the interests of the lay society, too.

Dedication to quality

Each Frontiers article is a landmark of the highest quality, thanks to genuinely collaborative interactions between authors and review editors, who include some of the world's best academicians. Research must be certified by peers before entering a stream of knowledge that may eventually reach the public - and shape society; therefore, Frontiers only applies the most rigorous and unbiased reviews. Frontiers revolutionizes research publishing by freely delivering the most outstanding research, evaluated with no bias from both the academic and social point of view. By applying the most advanced information technologies, Frontiers is catapulting scholarly publishing into a new generation.

What are Frontiers Research Topics?

Frontiers Research Topics are very popular trademarks of the *Frontiers journals series*: they are collections of at least ten articles, all centered on a particular subject. With their unique mix of varied contributions from Original Research to Review Articles, Frontiers Research Topics unify the most influential researchers, the latest key findings and historical advances in a hot research area.

Find out more on how to host your own Frontiers Research Topic or contribute to one as an author by contacting the Frontiers editorial office: frontiersin.org/about/contact

Science and technology in deep underground laboratories

Topic editors

Aldo Ianni — Gran Sasso National Laboratory (INFN), Italy

Sean M. Paling — Science & Technologies Facilities Council, United Kingdom Research and Innovation, United Kingdom

Carlos Peña Garay — Laboratorio Subterráneo de Canfranc, Spain

Jeter Hall — SNOLAB, Canada

Citation

Ianni, A., Paling, S. M., Garay, C. P., Hall, J., eds. (2025). *Science and technology in deep underground laboratories*. Lausanne: Frontiers Media SA.

doi: 10.3389/978-2-8325-5708-2

Table of contents

06 Editorial: Science and technology in deep underground laboratories
Aldo Ianni, Carlos Peña Garay, Jeter Hall and Sean M. Paling

09 Battery Earth: using the subsurface at Boulby underground laboratory to investigate energy storage technologies
Katherine A. Daniels, Jon F. Harrington, Andrew C. Wiseall, Edward Shoemark-Banks, Edward Hough, Humphrey C. Wallis and Sean M. Paling

16 The deep underground Bellotti Ion Beam Facility—status and perspectives
Matthias Junker, Gianluca Imbriani, Andreas Best, Axel Boeltzig, Alessandro Compagnucci, Antonino Di Leva, Federico Ferraro, David Rapagnani and Valentino Rigato

22 Overview of DISCOVER22 experiment in the framework of INFN-LNGS Cosmic Silence activity: challenges and improvements in underground radiobiology
Patrizia Morciano, Valentina Dini, Francesco Berardinelli, Giorgio Baiocco, Valeria Conte, Ion Udroiu, Federica Barbato, Jessica Marinaccio, Pasqualino Anello, Antonio Antoccia, Maria Antonella Tabocchini, Anna Selva, Stefania Canella, Anna Bianchi, Isabella Guardamagna, Leonardo Lonati, Emanuele Scifoni, Matthias Laubenstein, Marco Balata, Francesco Ferella, Daniela Grifoni, Angelo Galante, Mauro Maccarrone, Valentina Tirelli, Felicia Grasso, Massimo Sanchez and Antonella Sgura

29 Sub-background radiation exposure at the LNGS underground laboratory: dosimetric characterization of the external and underground facilities
Marco Ampollini, Pasqualino Anello, Marco Balata, Emanuela Bortolin, Federico Chiarelli, Daniele Chiti, Maurizio Chiti, Cinzia De Angelis, Giulia D'Imperio, Raffaella Donghia, Giuseppe Esposito, Francesco Ferella, Angelo Galante, Matthias Laubenstein, Patrizia Morciano, Stefano Nisi, Cristina Nuccetelli, Maria Cristina Quattrini, Maria Antonella Tabocchini and Claudia Tomei

44 Radioassay facilities at the STFC Boulby Underground Laboratory
Paul R. Scovell, Matthew Thiesse, Sid Ahmed Maouloud, Chamkaur Ghag and James Dobson

50 Sanford Underground Research Facility's approach to school education, community activities, and public outreach
Markus Horn and Erin Lorraine Woodward

58 Challenges for dark matter direct search with SiPMs
Alessandro Razeto and Nicola Rossi

69 CUTE: A Cryogenic Underground TEst facility at SNOLAB
Philippe Camus, Jonathan Corbett, Sean Crawford, Koby Dering, Eleanor Fascione, Gilles Gerbier, Richard Germond, Muad Ghaith, Jeter Hall, Ziqing Hong, Andrew Kubik, Adam Mayer, Serge Nagorny, Payam Pakarha, Wolfgang Rau, Silvia Scorza and Ryan Underwood

86 Enhancing equity, diversity, and inclusion in physics: perspectives from North American underground laboratories
Erica Caden, Samantha Kuula and Rochelle Zens

92 Callio lab: an underground and above ground, laboratory—overview and prospects for high energy and applied physics
Jari Joutsenvaara, Julia Puputti, Marko Holma and Ossi Kotavaara

103 An adaptive evacuation system for the Gran Sasso underground laboratory
Paolo Cavalcante and Gabriele Bucciarelli

109 Hyper-Kamiokande construction status and prospects
Ko Abe and Hide-Kazu Tanaka on behalf of the Hyper-Kamiokande collaboration

114 Construction of Yemilab
K. S. Park, Y. D. Kim, K. M. Bang, H. K. Park, M. H. Lee, J. So, S. H. Kim, J. H. Jang, J. H. Kim and S. B. Kim

121 Canfranc biology platform: exploring life in cosmic silence
Rebecca Hernández-Antolín, Laura Cid-Barrio and Carlos Peña-Garay

128 Indirect search of heavy neutral leptons using the DUNE near detector
S. Carbajal and A. M. Gago

140 Radioassay of the materials for AMoRE-II experiment
A. Agrawal, V. V. Alenkov, P. Aryal, H. Bae, J. Beyer, B. Bhandari, R. S. Boiko, K. Boonin, O. Buzanov, C. R. Byeon, N. Chanthima, M. K. Cheoun, J. S. Choe, S. Choi, S. Choudhury, J. S. Chung, F. A. Danevich, M. Djamal, D. Drung, C. Enss, A. Fleischmann, A. M. Gangapshev, L. Gastaldo, Y. M. Gavrilyuk, A. M. Gezhaev, O. Gileva, V. D. Grigorieva, V. I. Gurentsov, C. Ha, D. H. Ha, E. J. Ha, D. H. Hwang, E. J. Jeon, J. A. Jeon, H. S. Jo, J. Kaewkhao, C. S. Kang, W. G. Kang, V. V. Kazalov, S. Kempf, A. Khan, S. Khan, D. Y. Kim, G. W. Kim, H. B. Kim, H. J. Kim, H. J. Kim, H. L. Kim, H. S. Kim, M. B. Kim, S. C. Kim, S. K. Kim, S. R. Kim, W. T. Kim, Y. D. Kim, Y. H. Kim, K. Kirdsiri, Y. J. Ko, V. V. Kobychev, V. Kornoukhov, V. V. Kuzminov, D. H. Kwon, C. H. Lee, D. Y. Lee, E. K. Lee, H. J. Lee, H. S. Lee, J. Lee, J. Y. Lee, K. B. Lee, M. H. Lee, M. K. Lee, S. W. Lee, Y. C. Lee, D. S. Leonard, H. S. Lim, B. Mailyan, E. P. Makarov, P. Nyanda, Y. Oh, S. L. Olsen, S. I. Panasenko, H. K. Park, H. S. Park, K. S. Park, S. Y. Park, O. G. Polischuk, H. Prihtiadi, S. Ra, S. S. Ratkevich, G. Rooh, M. B. Sari, J. Seo, K. M. Seo, B. Sharma, K. A. Shin, V. N. Shlegel, K. Siyeon, J. So, N. V. Sokur, J. K. Son, J. W. Song, N. Srisittipokakun, V. I. Tretyak, R. Wirawan, K. R. Woo, H. J. Yeon, Y. S. Yoon and Q. Yue

155 NUOVA OFFICINA ASSERGI: a novel infrastructure for the production of cryogenic and radiopure Si-based photodetectors
L. Consiglio, A. Flammini, A. Ianni, A. Marasciulli, G. Panella, L. Pietrofaccia, D. Sablone and R. Tartaglia

161 The underground argon project: procurement and purification of argon for dark matter searches and beyond
P. Agnes, H. O. Back, W. Bonivento, M. G. Boulay, N. Canci, M. Caravati, S. Cebrian, V. Cocco, D. Diaz Mairena, D. Franco, F. Gabriele, D. Gahan, C. Galbiati, P. Garcia Abia, A. Gendotti, T. Hessel, S. Horikawa, R. Lopez Manzano, L. Luzzi, M. Martinez, V. Pesudo, M. Razeti, A. L. Renshaw, L. Romero, A. Rubbia, R. Santorelli, M. Simeone, R. Stefanizzi, A. Steri and S. Sulis on behalf of the Global Argon Dark Matter Collaboration (GADMC)

frontiers | Frontiers in Physics

TYPE Editorial
PUBLISHED 07 November 2024
DOI 10.3389/fphy.2024.1516502

OPEN ACCESS

EDITED AND REVIEWED BY
Alex Hansen,
Norwegian University of Science and Technology, Norway

*CORRESPONDENCE
Aldo Ianni,
aldo.ianni@lngs.infn.it

RECEIVED 24 October 2024
ACCEPTED 29 October 2024
PUBLISHED 07 November 2024

CITATION
Ianni A, Garay CP, Hall J and Paling SM (2024) Editorial: Science and technology in deep underground laboratories.
Front. Phys. 12:1516502.
doi: 10.3389/fphy.2024.1516502

Editorial: Science and technology in deep underground laboratories

Aldo Ianni[1]*, Carlos Peña Garay[2], Jeter Hall[3] and Sean M. Paling[4]

[1]Gran Sasso National Laboratory (INFN), L'Aquila, Italy, [2]Laboratorio Subterráneo de Canfranc, Canfranc, Spain, [3]SNOLAB, Sudbury, ON, Canada, [4]Science and Technology Facilities Council/Boulby, Boulby, United Kingdom

KEYWORDS

underground laboratories, biology in cosmic Silence, equity, diversity, inclusion, radioassay, safety, astroparticle and particle physics

Editorial on the Research Topic
Science and technology in deep underground laboratories

Deep Underground Laboratories (DULs) are **multidisciplinary research infrastructures** with a rock overburden that goes from a few hundred metres to a few kilometres. There are 13 laboratories in operation on three continents (North America, Europe, Asia, Australia) giving a global excavation volume of over a million cubic metres. The science enabled by DULs is growing in both depth and breadth. New laboratories are being constructed/proposed including a new one in South Africa.

This Research Topic collects contributions on the construction, exploitation and safety aspects of four DULs. It includes the excavation of one of the world's largest underground caverns to accommodate the Hyper-Kamiokande detector Abe et al., a world-leading international neutrino and nucleon decay experiment comprising the next-generation underground water Cherenkov detector (about 250 kton) and utilising the upgraded Japan Proton Accelerator Research Complex (J-PARC) neutrino beam. The scientific program of the next-generation neutrino experiments is very broad. In particular, near detectors offer opportunities to further test our understanding of particle physics. An example is presented with the search for heavy neutral leptons in the DUNE near detector Carbajal and Gago. The Research Topic also includes the new underground laboratory, Yemilab Park et al., which was completed in Jeongseon, Gangwon Province, with a depth of 1 km and an exclusive experimental area spanning 3,000 m^3, where the Yangyang Underground Laboratory facilities will be relocated. Additionally, Yemilab includes a cylindrical pit with a volume of approximately 6,300 m^3, designed as a multipurpose laboratory for next-generation experiments involving neutrinos, dark matter, and related research. A third underground laboratory is discussed, Callio Lab Joutsenvaara et al., which is a versatile multidisciplinary research platform, project-based, pay-by-service approach to organising and economically running the research activities, a mandatory approach for a platform operating without governmental funding. Improving safety underground is one of the necessary actions in DULs. The Gran Sasso National Laboratory (LNGS) is, at present, the largest deep underground laboratory in operation for astroparticle physics and rare event research. Cavalcante and Bucciarelli shows the study of an adaptive

evacuation system for LNGS to improve the evacuation performance in underground laboratories, which is composed of a combination of passive, dynamic, and adaptive signage that can adapt itself to lead the laboratory occupants to the safe location for evacuation.

The main reason to develop an underground infrastructure is to operate in a very low radioactive environment where muons from cosmic rays are strongly suppressed. This singular environment opens the possibility to search for very rare events such as low energy neutrino interactions, dark matter direct detection, and neutrinoless double beta decay, crucial to enhance our understanding of the Universe. Different naturally occurring radioactive products which lead to decay products and decay emissions on a wide spectrum of energies may adversely impact the sensitivity of a running particle physics detector. This Research Topic collects contributions on various efforts to monitor background levels in experiments. The Boulby UnderGround Screening (BUGS) Facility Scovell et al. comprises an array of germanium detectors, two XIA UltraLow-1800 surface-alpha counters, two radon emanation detectors and an Agilent ICP-MS system. Agrawal et al. presents the design and the construction materials used to build the AMoRE-II detector, an experiment to search for the double beta decay of ^{100}Mo nuclei using molybdate crystal scintillators, operating at milli-Kelvin (mK) temperatures and shielding system, including active and passive shielding, the cryostat, and the detector holders and instrumentation. The Global Argon Dark Matter Collaboration (GADMC) contribution Agnes et al. shows their efforts to reduce and monitor the ^{39}Ar activity in atmospheric argon, which is mainly produced and maintained by cosmic ray induced nuclear reactions and limits the ultimate size of argon-based detectors and restricts their ability to probe very low energy events. The discovery of argon from a deep underground well with significantly lower activation than atmospheric argon and a dedicated experiment to monitor the radioactive level are important steps in the development of direct dark matter detection experiments using argon as the active target. Devices based on superconductivity and superfluidity, low-temperature phase transitions or the low heat capacity of non-metals in the milli-Kelvin range are often sensitive to small energy depositions as can be caused by environmental radiation. Camus et al. shows the main design features and operating parameters of The Cryogenic Underground TEst facility [CUTE (Agnes et al.)] at SNOLAB, a platform for testing and operating cryogenic devices in an environment with low levels of background.

Several challenges faced by DUL science are dealt with using new technological infrastructures and technological applications. This Research Topic collects contributions such as the presentation of the Nuova Officina Assergi (NOA) Consiglio et al., a new facility for the production and integration of large-area silicon photodetectors operating at cryogenic temperatures. Silicon photomultipliers are proving to be a promising technology for next-generation experiments searching for rare events in underground laboratories. To overcome the issues in terms of the extreme radio-purity, costs, and technological feasibility of the future dark matter experiments, the novel silicon photomultiplier (SiPM)-based photodetector modules Razeto et al. seem to be promising candidates, capable of replacing the present light detection technology. However, the intrinsic features of SiPMs may limit the present expectations. It also collects the presentation of the **Bellotti Ion Beam Facility** (IBF) Junker et al. at LNGS which stands out as the worldwide only ion beam user facility deep underground. As this, it aims to provide the scientific community with access to intense proton, ^{4}He and ^{12}C ion beams in a low radiation environment achievable only in a deep underground site. The intense carbon beam and, more in general, the excellent long-term stability of the beams produced by the 3.5 MV Singletron™ accelerator are unique features of the Bellotti IBF. As an example of a technological application, Daniels et al. shows the potential of the DULs as a battery to store compressed air, using off-peak surplus energy. Natural accumulations of salt (halite deposits) in the UK represent a large and untapped natural storage reservoir for compressed air with the ability to provide instantaneous green energy to meet peak demand. To realise the potential of this emerging technology, a detailed knowledge of the relationship between mechanics, chemistry and geological properties is required to optimise cavern design, storage potential and economic feasibility.

In addition, the special environments in which DULs are located provide opportunities to carry out many and varied studies on geology, geophysics, biology and planetary exploration of significant interest and impact in both pure and applied science. Several investigations have evaluated the effects of low background radiation environments on living organisms. With this purpose, the Canfranc Underground Laboratory (LSC) launched the **Biology Platform** in 2021 Hernández-Antolín et al., joining efforts with other DUL by providing laboratory space for biology experiments. Two identical laboratories have been built (underground and on surface) to replicate biology experiments under the same conditions, with the main difference being the cosmic radiation background. A number of diverse biology experiments are ongoing in LSC, LNGS, SNOLAB, WIPP, and other DULs. DISCOVER22 (DNA Damage and Immune System Cooperation in VEry low Radiation environment 2022) Morciano1 et al. aims at investigating how the low radiation background modulates the Immune System (IS) response *in vitro* and *in vivo* models, linking physical microdosimetric measurements and the corresponding biological radiation responses by using radiation biophysical models. In determining the response of biological systems, the external and underground laboratories must be characterised and equipped to perform radiobiological studies Ampollini et al. aimed at understanding the involvement of the different low linear energy transfer components.

An emphasis on outreach and education is addressed in underground labs to inspire learning across generations. To achieve this mission, SURF Horn and Woodward operates an open-to-the-public visitor centre, hosts multiple public outreach events per month and an annual city-wide science festival, trains science educators, develops school curriculum units, and provides classroom materials, based on science researched at the laboratory. The strategic approach, specific methods, and successful outcomes of these programs may serve as examples for effective science education, public outreach, and community engagement. Underground laboratories are working on many different fronts to improve **Equity, Diversity, and Inclusion** (EDI) in their host countries and within particle physics collaborations. Laboratories can institute in their teams and also encourage the scientific collaborations they host to have policies and plans for increasing

EDI. North American underground laboratories Caden et al., SNOLAB and SURF, are each supporting their employees and user-bases in targeted outreach, consultation with experimental collaborations on their own policies, EDI training, and Indigenous cultural recognition.

Author contributions

AI: Writing–original draft. CG: Writing–original draft. JH: Writing–original draft. SP: Writing–original draft.

Funding

The author(s) declare that no financial support was received for the research, authorship, and/or publication of this article.

Conflict of interest

The authors declare that the research was conducted in the absence of any commercial or financial relationships that could be construed as a potential conflict of interest.

The author(s) declared that they were an editorial board member of Frontiers, at the time of submission. This had no impact on the peer review process and the final decision.

Publisher's note

frontiers | Frontiers in Physics

TYPE Perspective
PUBLISHED 17 October 2023
DOI 10.3389/fphy.2023.1249458

OPEN ACCESS

EDITED BY
Lorenzo Ferrari,
University of Pisa, Italy

REVIEWED BY
Zhenyuan Yin,
Tsinghua University, China

*CORRESPONDENCE
Katherine A. Daniels,
danielsk4@cardiff.ac.uk

†PRESENT ADDRESS
Katherine A. Daniels,
School of Earth and Environmental Sciences, Cardiff University, Cardiff, United Kingdom

RECEIVED 28 June 2023
ACCEPTED 19 September 2023
PUBLISHED 17 October 2023

CITATION
Daniels KA, Harrington JF, Wiseall AC, Shoemark-Banks E, Hough E, Wallis HC and Paling SM (2023), Battery Earth: using the subsurface at Boulby underground laboratory to investigate energy storage technologies.
Front. Phys. 11:1249458.
doi: 10.3389/fphy.2023.1249458

Battery Earth: using the subsurface at Boulby underground laboratory to investigate energy storage technologies

Katherine A. Daniels[1*†], Jon F. Harrington[1], Andrew C. Wiseall[1], Edward Shoemark-Banks[2], Edward Hough[1], Humphrey C. Wallis[1] and Sean M. Paling[2]

[1]Fluid Processes Research Laboratories, British Geological Survey, Nottingham, United Kingdom, [2]Boulby Underground Laboratory, Science and Technology Facilities Council, Saltburn-by-the-Sea, United Kingdom

Renewable energy provides a low-carbon alternative to power generation in the UK. However, the resultant supply varies on daily, weekly and seasonal cycles, such that for green energies to be fully exploited new grid-scale energy storage systems must be implemented. Two pilot facilities in Germany and the United States have demonstrated the potential of the Earth as a battery to store compressed air, using off-peak surplus energy. Natural accumulations of salt (halite deposits) in the UK represent a large and untapped natural storage reservoir for compressed air with the ability to provide instantaneous green energy to meet peak demand. To realise the potential of this emerging technology, a detailed knowledge of the relationship between mechanics, chemistry and geological properties is required to optimise cavern design, storage potential and economic feasibility. The variable stresses imposed on the rock matrix by gas storage, combined with the cyclic nature of cavern pressurisation are barriers to deployment that need to be addressed to enable large-scale adoption of schemes. Well-designed field experiments are a lynchpin for advancing research in this area, especially when supported by state-of-the-art characterisation and modelling techniques. The research facility at STFC's Boulby Underground Laboratory presents the ideal location to tackle these fundamental issues to optimise "Battery Earth".

KEYWORDS

energy storage, compressed air, hydrogen and gas storage, *in-situ* testing, rock salt, cyclic pressurisation, creep, wall rock failure, operational limits

1 Introduction

Security of energy supply, coupled with a transition towards greater production and use of renewable energy in the United Kingdom and globally, will necessitate an increase in both energy and grid-scale storage. Renewable energy generation (e.g., wind and solar) is susceptible to fluctuations in weather conditions, leading to irregular energy production and uneven supply. Compressed Air Energy Storage (CAES) and Compressed Hydrogen Gas Storage (CHGS) are viable energy technologies that are capable of assisting renewable energy production to be less time- and condition-dependent [1]. CAES systems generate electricity

similarly to conventional gas turbines but with the compression (storage) and expansion (generation) operations occurring independently [2]. Conventional diabatic CAES uses a compressor train to compress air (with coolers to reduce air temperature, increase efficiency and reduce thermal stress on the storage cavern), which is injected into the storage cavern. The pressurised air is mixed with natural gas during expansion and operation, and this mixture combusted, before being released and fed through an expander or generator train to generate electricity. The additional fuel is required both to achieve the desired air flow rate through the turbine and ensure there is no low temperature icing risk [2]. In simple terms, CAES systems store compressed air in pore space or voids using excess energy generated (for example, wind energy during periods of low demand such as at night). This and this compressed air is then released as required to drive turbines, producing electricity [3]. Potential storage sites for compressed air include energy bags that are anchored to the sea bed [4] and geological formations; these can be solution-mined salt caverns [1, 5, 6], depleted oil and gas reservoirs [7], aquifers [8] and lined [9, 10] and un-lined [11] rock caverns [12–16]. CHGS follows the same process as CAES, but with the possibility of also using the hydrogen for energy production. For CHGS, hydrogen would be pumped into a storage cavern and could be withdrawn over long periods (e.g., to support static or low-cyclic feedstock applications; these are already commercially operated), or for fast cycling (e.g., to support energy supply; these applications are currently not commercially operated) [17]. Two pilot CAES facilities (Huntorf: E. N. Kraftwerke, Germany; McIntosh: Alabama Electric Corporation, Alabama, United States) have demonstrated this technology's potential in combination with solution-mined salt caverns [18]; there is a limited amount of commercial-scale hydrogen storage in solution mined caverns [19], but the available salt resource is significantly underutilised for these purposes.

Halite formations are ideally suited to CAES and CHGS facility development because halite is a low permeability, self-healing (visco-plastic) material that can be solution-mined to produce custom-engineered storage caverns. Natural gas storage in the United Kingdom already occurs in salt caverns [20], but the mode of cavern usage will differ dramatically if used for CAES/CHGS. The halite formations in the United Kingdom are both onshore and offshore and were deposited in the Permian and Triassic [13, 16]. Solution-mining of halite to create caverns for CAES/CHGS raises a number of uncertainties including: irregularities in cavern morphology due to differential dissolution rates related to the evaporite's composition and structure, the impact of stress on cavern geometry and integrity, the presence of insoluble impurities that can affect dissolution and the "growth" of the cavern and build-up at the base of the cavern, and brine disposal produced as a by-product of solution-mining the halite [15]. Additionally, halite can deform plastically at high temperatures and pressures (so-called "creep") leading to mechanical instability and the collapse of the storage cavern, should the minimum operation pressure not be maintained. Equally, operating the cavern at high gas pressures could result in failure of the rock and leakage of gas. As well as these considerations, the usage of the cavern for CAES/CHGS will necessitate much faster pressure cycling of the cavern than seasonal natural gas storage does, leading to additional uncertainties surrounding creep rates, wall-rock damage and failure. Obtaining an improved understanding of the processes governing formation and operation of storage caverns in halite is therefore of great importance to both the emerging CAES and CHGS technologies and will have notable value on a global level, where extensive salt deposits exist.

2 UK salt deposits

United Kingdom geology provides the resource of two halite groups in the stratigraphic sequence: the Permian (298.9 Ma–251.9 Ma) halites, which are predominantly found in NE England, and the Triassic (251.9 Ma–201.4 Ma) halites, which are predominantly located in the Cheshire region (Figure 1). The Triassic halites are utilised for underground storage of methane gas in Cheshire, and have potential for hosting storage schemes in west Lancashire, Dorset, the East Irish Sea and possibly Somerset. In Cheshire, the Triassic halites are part of the Triassic Mercia Mudstone Group (MMG) and comprise an up to 1,200 m thick deposit of interbedded mudstone with subordinate halite and siltstone units that are part of the Cheshire Basin [13, 21–23]. The Northwich halite is up to 283 m thick, is one of the MMG's halite members in the Cheshire Basin, and has been studied to understand the control of petrology on dissolution for salt cavern formation [15, 24].

The Permian evaporite succession is deeper than the Triassic halites and lies under much of the North Sea; the Zechstein Group sequence containing the Permian halites extends eastwards between the United Kingdom, the Netherlands and Germany [13]. In contrast to Triassic halites, the Zechstein includes beds of higher solubility evaporites including sylvite and carnalite, and also complex polyhalite. This basin's edge is found at depth under the North Yorkshire coast [13]. These have been mined for potash for fertiliser, and rock salt for road de-icing since the 1960's [25], and currently mines polyhalite. The Boulby halite is mainly a massive, undeformed halite with an isotropic fabric and crystal grains up to 3 cm in diameter; it is 50 m ± 15 m thick and starts at a depth of 1,100 m [26]. In places it has a gneissose fabric with grains with 3:1 axis ratios, developed in response to structural deformation. In the north of the mine a dark argillaceous halite forms a horizon 5–6 m below the top of the halite [26]. Dolomite, mudstone and anhydrite are interbedded with the Permian salt deposits [13].

3 The Boulby Underground Laboratory

The Science and Technology Facilities Council's (STFC) Boulby Underground Laboratory (BUL) sits at approximately 1,070–1,100 m below ground surface [27, 28] within Boulby mine, a potash and polyhalite mine operated by Israel Chemicals Limited, in North Yorkshire. BUL, begun in 1988, was motivated by the search for dark matter [27] and hosts experiments requiring low background radiation conditions [28–32]. The background activity from radionuclide contamination (gamma radiation) is particularly low (approximately 0.1 ppm of uranium and thorium and 1,130 ppm of potassium) [27]. Additional mine excavation to increase the laboratory space occurred in 1995, 1998, 2003 [27] and most recently in 2017, when an entirely new laboratory was created. This growth has been advantageous both for the dark matter

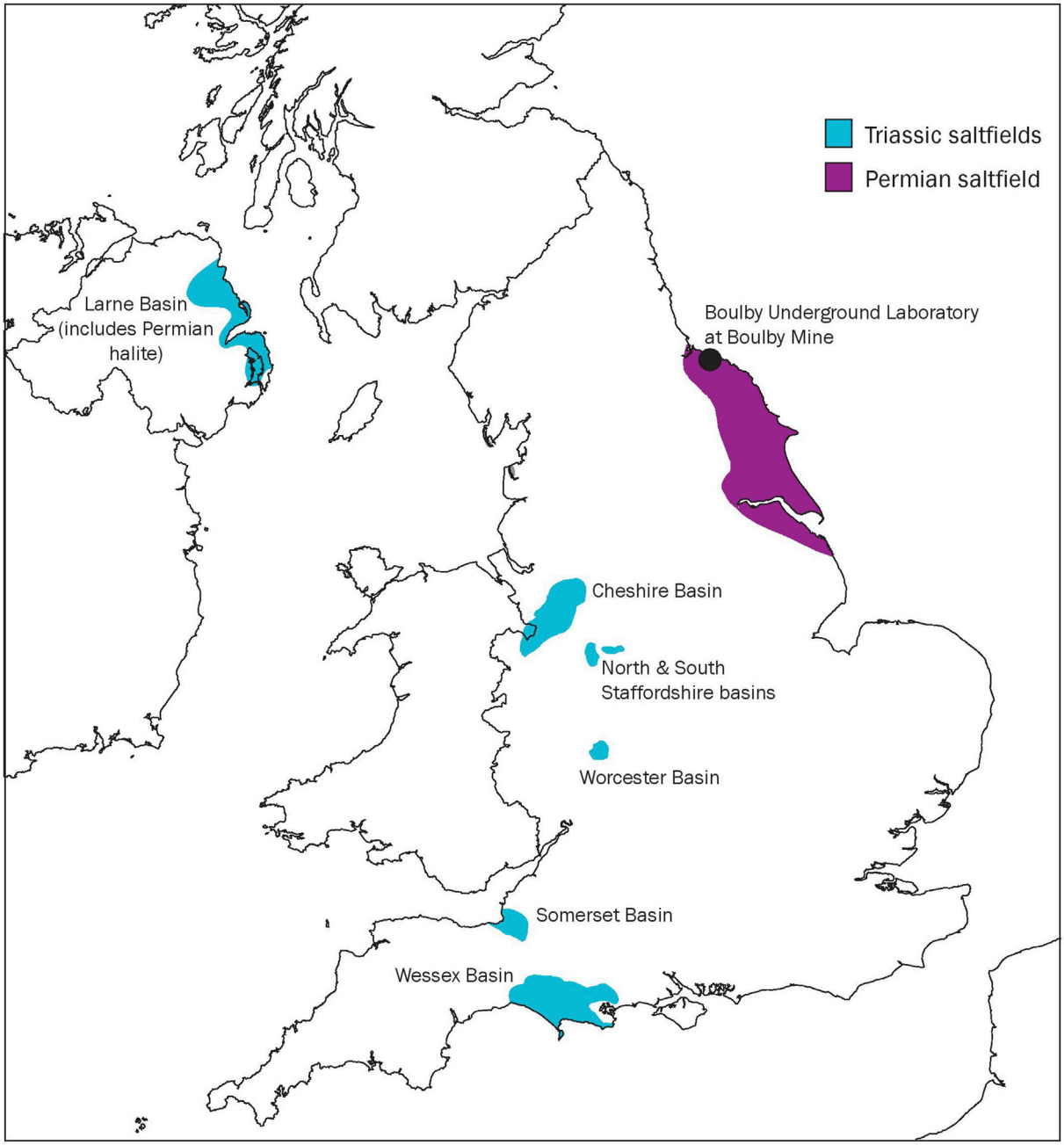

FIGURE 1
The UK's Permian and Triassic Saltfields showing the location of BUL within Boulby Mine (adapted from Evans and Holloway [49], Figure 1 © The Geological Society of London 2009.

physics community, but also for scientists wishing to diversify the research undertaken at BUL. As well as housing the United Kingdom Dark Matter Collaboration [30, 33], BUL has a broad appeal as a safe and supported facility for hosting multidisciplinary science. The surface facilities offer visitor office space, computer facilities, a conference suite and storage space for research equipment [27]. The ambient conditions underground are hot and dry; the air temperature is 28°C but rises to 35°C where it is unaffected by mine circulation [34]. The mine roadways are situated in the Boulby Halite and the proximal stratigraphy includes other Permian evaporites. The lithostatic pressure at BUL is 28 MPa and there is no obvious deviatoric stress within the rock mass, other than the decompressed region around the gallery openings.

3.1 Geo-energy research at Boulby Underground Laboratory

BUL offers an unparalleled environment in which to conduct research on geo-energy problems that use our subsurface geology.

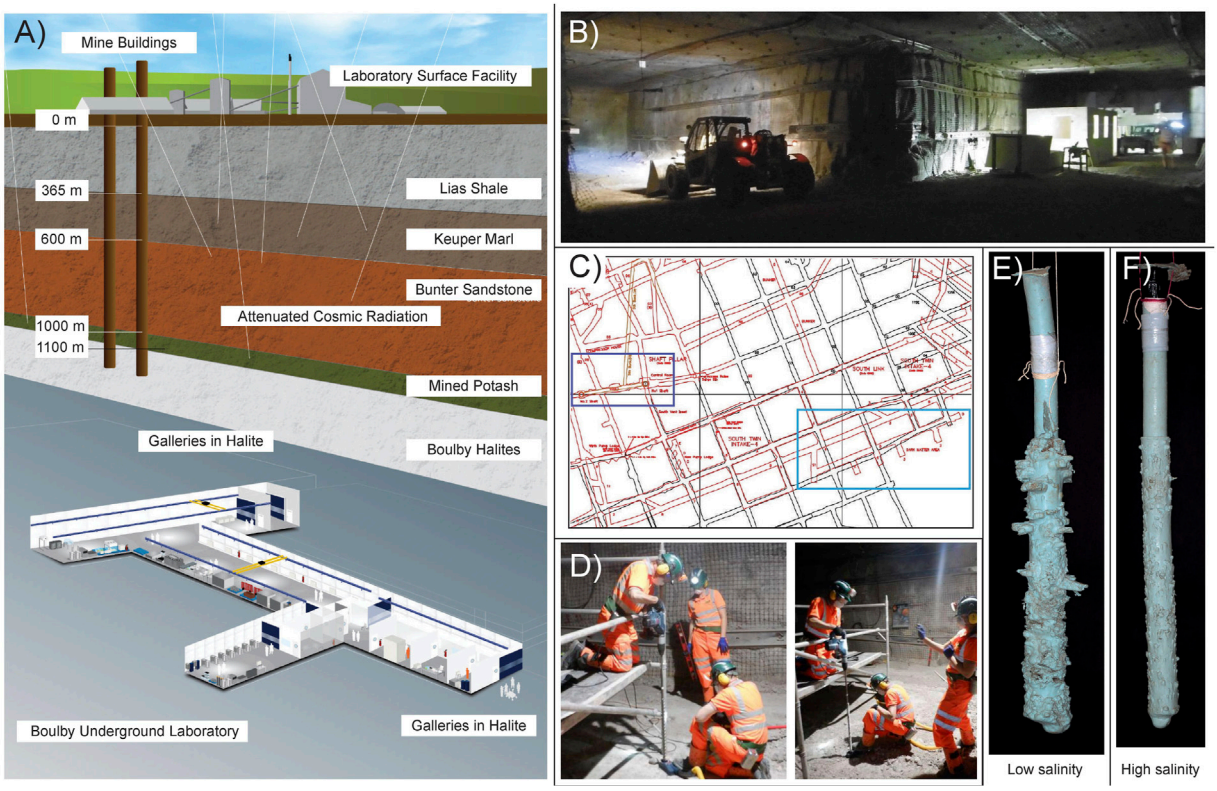

FIGURE 2
The tunnels and galeries around BUL can be used to investigate the dissolution of salt and creation of gas storage caverns. **(A)** The location of the Boulby Underground Laboratory below ground surface within the stratigrapic succession (modified from the original with permission from STFC, covered under a CC BY-NC-SA 4.0 license). **(B)** The gallery outside BUL provided the test location. **(C)** A plan of the galleries near to the shafts (dark blue rectangle), showing the location of the Boulby Underground Laboratory (Dark Matter Area) (light blue rectangle). **(D)** Scientists from BUL and BGS drill holes into the gallery floor and use both **(E)** low salinity and **(F)** high salinity fluids to dissolve elongate caverns during preliminary scoping works, which are then cast and dug out of the ground. The low salinity cast **(E)** has a length of 77 cm and a volume of 1750 cm^3 (measured by laser scanning), whilst the high salinity cast **(F)** has a length of 76.2 cm and a volume of 906 cm^3. The extracted casts have been photographed **(E, F)** and the surface can subsequently be analysed to provide information on the dissolution process.

BUL facilitates the use of representative rocks at depths and temperatures similar to those where some of the deeper gas storage is currently operated, and where new schemes for hydrogen and compressed air could be located to support the UKs net-zero ambitions. At these depths, there can be significant uncertainty in the character of the halite, and this will impact the efficiency of gas storage caverns that could be developed. The infrastructure available in the galleries surrounding the current STFC underground research facility can provide lighting, power, internet, water and waste services, specialist drilling equipment and dedicated science technician support (Figures 2A–C); the value of these services cannot be over-emphasised in what is otherwise a harsh operating mine environment.

With the facilities, expertise and equipment available at the mine, BUL has immense potential to simulate industrial salt-cavern formation through dissolution and the physical processes studied on an intermediate scale (i.e., between single rock sample/laboratory experiment and operational cavern) that is not possible in a standard laboratory (Figures 2B–D). With unique access to a bedded evaporite succession (that includes halite and higher solubility salts carnalite and sylvite, along with non-soluble anhydrite and mudstone), cylindrical caverns with lengths and diameters on the order of 1–3 m could be created at a variety of depths beneath the gallery floor or into the gallery walls (Figures 2B–F). This access would offer the possibility to visualise and quantify halite heterogeneity in three-dimensions in near *in-situ* conditions for many relevant parameters including lithology, temperature, halite morphology and stress state. A cavity laser scanner, sonic and ground penetrating radar (GPR) would be able provide direct monitoring and measurement during void formation and operation, enabling the study of convergence and creep behaviour related to host rock composition, as well as alterations in the material due to changes in the stress state (associated with opening the cavern volume as well as operating it through pressure cycling). To achieve this, caverns could be sealed with packers, and pressure-cycled over an extended time period, to investigate cyclic loading effects on cavern stability.

A principal area of potential research would be to produce voids at realistic temperatures, depths and lithostatic pressures, using fluids with variable NaCl concentrations and faster flow rates than are possible in the laboratory. If the ground conditions allowed, simulated caverns could be excavated and logged to enable a better understanding of the extent and distribution of heterogeneities and insoluble material in the halite unit, the dependence of cavern shape and volume on mineralogical composition and the consequent impact

on aspect ratio. Geophysical data acquisition from the cavern interior (e.g., laser scanning) could be used to create 3D prints for improved visualisation and for use as a public engagement tool. Together, these measurements would lead to an improved understanding of the longevity of gas and CAES storage caverns and the impact of different operational controls on cavern stability and integrity. Experiments would also raise public and stakeholder understanding of cavern storage benefits.

BUL also provides the opportunity to investigate mine heat as a low-carbon energy source. Boulby mine discharges approximately 5 million litres of water daily into the sea. The continued advancement of geothermal technologies means that this presents a considerable potential renewable heat resource that could be exploited. BUL would serve as a research site to optimise either direct air thermal transfer, or heat transfer for mine waters, joining with other subsurface observatories as part of a network investigating the value of mines in supporting net-zero ambitions. To optimise the geological asset that BUL represents, a structured research plan would be required to ensure early research activities do not preclude later activities, avoiding sterilisation of available bedrock through a poorly planned research program. Moreover, as the Boulby halite is within a depth range of 0.75–1.1 km, the stratigraphy is aligned with the anticipated depth of interest for many other renewable, geo-energy and waste disposal problems, including deep geothermal and geological CO_2 storage. This ensures BUL's wide appeal for addressing geo-energy related research problems.

4 Discussion

Increasing the amount of renewable energy used will require large-scale energy storage adoption, as intermittent supply, high initial capital outlay and low power output of conventional renewables also limit their grid-scale deployment. Whilst the United Kingdom is committed to decarbonisation through agreements such as the 2016 Paris accord [20], fossil fuels still comprise a significant proportion of the energy supplied (currently about 78% of all United Kingdom energy in 2022 [35]) and are acknowledged to remain a significant part of the energy mix for decades to come [36]. Whilst coal dependency has declined over the past decade [37], natural gas dependency has risen. The United Kingdom is increasingly dependent on natural gas imports, but has relatively little gas storage capacity compared with many EU member states, rendering it susceptible to the risk of gas supply shortfalls [20].

To achieve the emissions targets set out by the 2019 Net Zero amendment to the Climate Change Act (2008), and to optimise use of hydrogen as a route to achieving these, nascent CAES and CHGS technologies are required to allow transitioning from hydrocarbons to sustainable, clean power generation. Significant attention is now turning towards these technologies with the proposed establishment of two United Kingdom clusters (H21 Leeds City Gate Project [38] and HyNet North West Project [39]), and the Industrial Decarbonisation Research and Innovation Centre (IDRIC) [40]. Rock salt has been successfully used for the storage of natural gas since 1961 [20], but existing facilities offer limited storage capacity compared to the grid-scale requirements for industrial power generation. The United Kingdom has suitable salt formations for geological energy storage in abundance; a substantial and underutilised resource [41]. However, geological energy storage presents many technical and environmental challenges.

The greater Permian evaporite depths mean that although the rocks may provide large capacities for gas storage, the stress conditions for cavern formation are different to those experienced when solution mining in the shallower Triassic deposits, and plastic deformation will be a relevant consideration in some locations. Understanding the role of stress on the dissolution and subsequent cavern shape formed is of fundamental importance to the successful creation and operation of caverns in the Permian halite. Using the currently available compressor technology, the optimal depth for CAES is 300–1,500 m [3]. Compressor technology is continuing to improve; with better compressors, deeper cavern depths can be achieved. Pairing compression and storage facilities with renewable energy sources will enable excess energy to be used to electrically power a turbocompressor to compress air or hydrogen, and this compressed gas can then be stored in close proximity, reducing the need for transport infrastructure and associated costs, and increasing the system efficiency. The North Sea is a favourable location for wind-farms and therefore the Permian evaporite succession is an ideal host rock for salt cavern formation for CAES and CHGS [42], as the improved compressor technology allows deeper formations to be accessed; offshore hydrogen production via sea water hydrolysis is a distinct possibility. In addition, offshore salt cavern formation would reduce both the environmental and societal impact [42].

In contrast to natural gas storage, CHGS and CAES experience rapid withdrawal and refilling cycles with corresponding rapid pressure changes. These result in large cavern wall temperature changes [43, 44], which can substantially reduce the tangential (or vertical) stress, leading to cracking if the material enters the failure regime; this is especially important for bedded salts where the cavern aspect ratios lead to large diameters with respect to cavern height [45]. To maintain cavern integrity, the tangential stresses at the wall must remain compressive during operation. Pressure, temperature and stress therefore emerge as key criteria in the consideration of short- and long-term cavern performance. These issues are strongly influenced by their orientation to the *in-situ* stress field, and must therefore be given attention when modelling cavern behaviour. Visco-plastic behaviour during pressure cycling often results in substantial reduction in cavern capacity (e.g., Eminence Salt Cavern, Mississippi) [46]. Understanding this behaviour is essential for accurate long-term volume loss predictions and consequently the economic potential through time. A solution to the problem of time-dependent deformation, temperature change, and the resultant stress response, is required to parameterise appropriate experimental scenarios (e.g., isobaric or isochoric storage), and to assess widespread geological energy storage viability. How these are impacted by differing lithologies, as well as lateral and vertical variability, will also need to be understood. These considerations directly control the permissible inter-cavern spacing, affecting infrastructure costs and optimising subsurface halite deposit use. As the storage facility "footprint" increases, it may also span multiple planning regions, complicating the permitting process. As cavern number and size increases, the population affected by CHGS/CAES is likely to increase. For these reasons, there are clear economic, engineering and public acceptance advantages in minimising industry footprint.

The intergenerational climate change challenge is one of the most significant threats facing society, and the United Kingdom government's pledge to reach net-zero by 2050 will contribute towards meeting it [47]. A shift towards renewable energy for electricity generation, heat and industrial processes will be necessary, requiring long-duration energy storage to ensure supply security [47]. The Carbon Trust [48] estimates that effective United Kingdom energy storage could save as much as £2.4 billion/year by 2030, leading to a significant reduction in the average household energy bill. CAES and CHGS could play an important role in realising this potential through UK-based storage sites, some of which are already planned. The BUL offers a unique environment to enable testing to answer the remaining questions surrounding using Earth as a battery; bringing this to the forefront of discussions is clearly extremely important.

4.1 Permission to reuse and copyright

Figures, tables, and images will be published under a Creative Commons CC-BY licence and permission must be obtained for use of copyrighted material from other sources (including re-published/adapted/modified/partial figures and images from the internet). It is the responsibility of the authors to acquire the licenses, to follow any citation instructions requested by third-party rights holders, and cover any supplementary charges.

Data availability statement

The raw data supporting the conclusion of this article will be made available by the authors, without undue reservation.

Author contributions

KD and JH contributed to conception and design of the study. KD, JH, AW, ES-B, HW, and SP organised preliminary fieldwork campaigns at Boulby Underground Laboratory. KD, JH, and AW analysed an initial dataset. KD wrote the first draft of the manuscript. JH and EH wrote sections of the manuscript. All authors contributed to the article and approved the submitted version.

Funding

Funding for this work was provided by the British Geological Survey and the Science and Technology Facilities Council.

Acknowledgments

The authors thank Dr. Lorraine Field of the British Geological Survey for her helpful review of an earlier version of the manuscript, and Dr. David Evans is thanked for his insightful discussion. Simon Holyoake provided assistance with the instrumentation and experimental apparatus during preliminary field testing and data acquisition, for which the authors are grateful. Wayne Leman is also thanked for his help in the manufacture of field equipment. This paper is published with the permission of the Director of the British Geological Survey, part of United Kingdom Research and Innovation (UKRI).

Conflict of interest

The authors declare that the research was conducted in the absence of any commercial or financial relationships that could be construed as a potential conflict of interest.

Publisher's note

References

1. Crotogino F, Donadei S. Grid scale energy storage in salt caverns. In: Proceedings of the 8th Int. Workshop on Large-Scale Integration of Wind Power into Power Systems; October 2009; Bremen, Germany (2009).

2. Succar S. *Chapter 5: Compressed air energy storage*. Boca Raton: CRC Press (2011). p. 111–52.

3. Luo X, Wang J. Overview of current development on compressed air energy storage. *Tech Rep* Coventry, United Kingdom: School of Engineering, University of Warwick (2013).

4. Pimm A, Garvey S, De Jong M. Design and testing of Energy Bags for underwater compressed air energy storage. *Energy* (2014) 66:496–508. doi:10.1016/j.energy.2013.12.010

5. Martinez JD. Role of salt domes in energy productions. In: Coogan AH, editor. *Fourth sym - posium on salt*. Cleveland: UT NEWS (1974). p. 259–66.

6. Allen RD, Doherty TJ, Thomas RL. Geotechnical factors and guidelines for storage of compressed air in solution mined salt cavities. *Tech Rep* (1982). doi:10.2172/5234728

7. Donadei S, Schneider GS. Chapter 6: Compressed air energy storage in underground formations. In: *Storing energy*. Amsterdam, Netherlands: Elsevier (2016). doi:10.1016/B978-0-12-803440-8.00006-3

8. Li Y, Li Y, Liu Y, Cao X. Compressed air energy storage in aquifers: Basic principles, considerable factors, and improvement approaches. *Rev Chem Eng* (2021) 37:561–84. doi:10.1515/revce-2019-0015

9. Kim HM, Rutqvist J, Ryu DW, Choi BH, Sunwoo C, Song WK. Exploring the concept of compressed air energy storage (CAES) in lined rock caverns at shallow depth: A modeling study of air tightness and energy balance. *Appl Energ* (2012) 92:653–67. doi:10.1016/j.apenergy.2011.07.013

10. Rutqvist J, Kim HM, Ryu DW, Synn JH, Song WK. Modeling of coupled thermodynamic and geomechanical performance of underground compressed air energy storage in lined rock caverns. *Int J Rock Mech Mining Sci* (2012) 52:71–81. doi:10.1016/j.ijrmms.2012.02.010

11. Zhou Y, Xia C, Zhao H, Mei S, Zhou S. An iterative method for evaluating air leakage from unlined compressed air energy storage. *CAES caverns* (2018) 120:434–45. doi:10.1016/j.renene.2017.12.091

12. Allen K. Caes: The underground portion. *IEEE Trans Power Apparatus Syst* (1985) 104:809–12. doi:10.1109/tpas.1985.319078

13. Cooper AH. Halite karst geohazards (natural and man-made) in the United Kingdom. *Environ Geology* (2002) 42:505–12. doi:10.1007/s00254-001-0512-9

14. Evans DJ, Chadwick RA. *Underground gas storage: An introduction and UK perspective*. London: Special Publication The Geological Society of London (2009). p. 1–11. doi:10.1144/SP313.1

15. Field LP, Milodowski AE, Parkes D, Evans DJ. Petrological and textural factors that may influence the dissolution of halite during the construction of salt caverns for the storage of natural gas and compressed air. *Tech Rep*. British Geological Survey (2013).

16. Evans DJ. Operational ranges of current and proposed underground natural gas storage and CAES facilities. *Tech Rep*. British Geological Survey (2013) 291pp.

17. Hydrogen TCP. *IEA Hydrogen TCP task 042: Underground hydrogen storage* (2023).

18. Dooner M, Wang J. Chapter 14: Compressed air energy storage. In: *Future energy*. Netherlands: Sciencedirect (2020).

19. Edlmann K, Dopffel N, Hough E, Xie Q, Groenenberg R, Yallup C, et al. *IEA Hydrogen TCP task 042: Underground hydrogen storage* (2023).

20. Evans D. An appraisal of Underground Gas Storage technologies and incidents, for the development of risk assessment methodology. *Tech Rep*. British Geological Survey, Open Report OR/07/023 (2007).

21. Brooks TG, O'Riordan NJ, Bird JF, Stirling R, Billington D. *Stabilisation of abandoned salt mines in north west England*. London: Geological Society of London (2006).

22. Maddox SJ, Blow R, Hardman M. *Hydrocarbon prospectivity of the central Irish sea basin with reference to block 42/12, offshore Ireland*. London: Special Publication The Geological Society of London (1995). p. 57–77.

23. Maingarm S, Izatt C, Whittington RJ, Fitches WR. Tectonic evolution of the southern-central Irish sea basin. *J Pet Geology* (1999) 22:287–304. doi:10.1111/j.1747-5457.1999.tb00988.x

24. Field LP, Milodowski AE, Evans DJ, Palumbo-Roe B, Hall MR, Marriott AL, et al. Determining constraints imposed by salt fabrics on the morphology of solution-mined energy storage cavities, through dissolution experiments using brine and seawater in halite. *Q J Eng Geology Hydrogeology* (2019) 52:240–54. doi:10.1144/qjegh2018-072

25. Kemp SJ, Smith FW, Wagner D, Mounteney I, Bell CP, Milne CJ, et al. An improved approach to characterize potash-bearing evaporite deposits, evidenced in North Yorkshire, United Kingdom. *Econ Geology* (2016) 111:719–42. doi:10.2113/econgeo.111.3.719

26. Talbot CJ, Tully CP, Woods PJE. The structural geology of Boulby (potash) mine, Cleveland, United Kingdom. *Tectonophysics* (1982) 85:167–204. doi:10.1016/0040-1951(82)90102-0

27. Miramonti L. European underground laboratories: An overview. *AIP Conf Proc* (2005) 785. doi:10.1063/1.2060447

28. De Angelis SH. Earth science at the UK's deepest laboratory. *Géotechnique* (2017) 33:132–7. doi:10.1111/gto.12190

29. Bettini A. Underground laboratories. *Nucl Instr Methods Phys Res Section A: Acc Spectrometers, Detectors Associated Equipment* (2011) 626-627:S64–8. doi:10.1016/j.nima.2010.05.017

30. Murphy A, Paling S. The Boulby mine underground science facility: The search for dark matter, and beyond. *Nucl Phys News* (2012) 22:19–24. doi:10.1080/10619127.2011.629920

31. Smith NJT. The development of deep underground science facilities. *Nucl Phys B* (2012) 229-232:333–41. doi:10.1016/j.nuclphysbps.2012.09.052

32. Cockell CS, Biller B, Bryce C, Cousins C, Direito S, Forgan D, et al. The UK Centre for astrobiology: A virtual astrobiology Centre. Accomplishments and lessons learned. *Astrobiology* (2018) 18:224–43. doi:10.1089/ast.2017.1713

33. Klinger J, Clark SJ, Coleman M, Gluyas JG, Kudryavtsev VA, Lincoln DL, et al. Simulation of muon radiography for monitoring CO2 stored in a geological reservoir. *Int J Greenhouse Gas Control* (2015) 42:644–54. doi:10.1016/j.ijggc.2015.09.010

34. Ianni A. Considerations on underground laboratories. *XV Int Conf Top Astroparticle Underground Phys* (2020) 1342:012003. doi:10.1088/1742-6596/1342/1/012003

35. UK Parliament. *Accelerating the transition from fossil fuels and securing energy supplies* (2023).

36. Petroleum. BP energy outlook 2019 edition (2019). Available at: https://www.bp.com/en/global/corporate/news-and-insights/press-releases/bp-energy-outlook-2019.html (Accessed January 31, 2023).

37. Department for Business Energy Industrial, Strategy. Digest of UK energy statistics annual data for UK (2021). Available at: https://assets.publishing.service.gov.uk/government/uploads/system/uploads/attachment_data/file/1130501/DUKES_2022.pdf (Accessed January 31, 2023).

38. H21 Programme. H21 Leeds city gate project Full Report (2016). https://h21.green/projects/h21-leeds-city-gate/ (Accessed January 31, 2023).

39. Cadent your gas Network. HyNet North West: From vision to reality, project report (2018). Available at: https://hynet.co.uk/app/uploads/2018/05/14368_CADENT_PROJECT_REPORT_AMENDED_v22105.pdf (Accessed January 31, 2023).

40. IDRIC. Industrial decarbonisation research and innovation Centre (2023). Available at: https://idric.org/ (Accessed January 31, 2023).

41. Williams JDO, Williamson JP, Parkes D, Evans DJ, Kirk KL, Nixon S, et al. Is there sufficient storage capacity to support a hydrogen economy? Estimating the salt cavern storage potential of bedded halites in the United Kingdom. *J Energ Storage* (2022) 53:105109. doi:10.1016/j.est.2022.105109

42. Kepplinger J, Donadei S. Large scale energy storage in geological formations. In: Proceedings of the 6th Dubrovnik Conference on Sustainable Development of Energy, Water and Environment Systems; January 2011; Croatia (2011).

43. Nieland J. Feasibility of off-loading chilled natural gas in salt caverns: Geomechanical assessment. In: Proceedings of the SMRI Spring Conference; October 2004; San Antonio, Texas (2004).

44. Nieland J. Salt cavern thermodynamics - comparison between hydrogen, natural gas and air storage. In: Proceedings of the SMRI Fall Conference; April 2008; Marble Falls, Texas, USA (2008).

45. Diessl J, Wang W, Bruno MS. *Investigation of pressure and temperature cycling influence on the stability of bedded salt caverns*. Berlin, Germany: Solution Mining Research Institute Fall Conference (2019).

46. Serata S, Cundey T. Design variables in solution cavities for storage of solids, liquids and gases. In: Proceedings of the 5th symposium on salt; October 1979; Adelaide, Australia (1979).

47. The Department for Business E, Strategy I. *The energy white paper: Powering our net zero future* (2020).

48. Lehmann N, Lever A, Sanders D, Ravishankar M, Ashcroft M. Can storage help reduce the cost of a future UK electricity system? *The Carbon Trust* (2016). Available at: https://www.carbontrust.com/our-work-and-impact/guides-reports-and-tools/energy-storage-report-can-storage-help-reduce-the-cost.html (Accessed April 19, 2023).

49. Evans DJ, Holloway S. *A review of onshore UK salt deposits and their potential for underground gas storage*. London: Geological Society, London, Special Publications (2009). p. 39–80. doi:10.1144/SP313.5

frontiers | Frontiers in Physics

TYPE Perspective
PUBLISHED 09 November 2023
DOI 10.3389/fphy.2023.1291113

OPEN ACCESS

EDITED BY
Jeter Hall,
SNOLAB, Canada

REVIEWED BY
Maurizio Maria Busso,
University of Perugia, Italy

*CORRESPONDENCE
Matthias Junker,
junker@lngs.infn.it

RECEIVED 08 September 2023
ACCEPTED 10 October 2023
PUBLISHED 09 November 2023

CITATION
Junker M, Imbriani G, Best A, Boeltzig A, Compagnucci A, Di Leva A, Ferraro F, Rapagnani D and Rigato V (2023), The deep underground Bellotti Ion Beam Facility—status and perspectives. *Front. Phys.* 11:1291113. doi: 10.3389/fphy.2023.1291113

The deep underground Bellotti Ion Beam Facility—status and perspectives

Matthias Junker[1]*, Gianluca Imbriani[2], Andreas Best[2], Axel Boeltzig[3], Alessandro Compagnucci[1,4], Antonino Di Leva[2], Federico Ferraro[1], David Rapagnani[2] and Valentino Rigato[5]

[1]INFN Laboratori Nazionali del Gran Sasso (LNGS), Assergi, Italy, [2]Dipartimento di Fisica "E. Pancini", Università degli Studi di Napoli "Federico II" Naples and INFN, Naples, Italy, [3]Institute of Radiation Physics, Helmholtz-Zentrum Dresden-Rossendorf, Dresden, Germany, [4]Gran Sasso Science Institute, L'Aquila, Italy, [5]INFN Laboratori Nazionali di Legnaro (LNL), Legnaro, Italy

For more than three decades, accelerators are in use in the underground laboratories of the Laboratori Nazionali del Gran Sasso (LNGS), located in central Italy. The LUNA Collaboration has exploited the potential of the site's low cosmic ray background to achieve important and often groundbreaking results in the field of nuclear astrophysics. This long success story stimulated the installation of accelerators in deep underground laboratories also in other countries, including the USA and China. Recently, LNGS took a major step forward with the activation of the Bellotti Ion Beam Facility, which will provide ion beams to the scientific community for research not only in nuclear astrophysics, but in all fields that can benefit from the low cosmic ray background conditions of the underground site.

KEYWORDS

ion beam accelerator, underground laboratory, nuclear astrophysics, applied sciences, ion beam analysis

1 Introduction: why going underground?

The flux of cosmic radiation that is present at ground level on the Earth's surface interacts with experimental setups for nuclear and particle physics studies, potentially creating a background or other disturbances to sensitive measurements. This particularly applies to rare event searches, such as those studying neutrinos or direct searches for dark matter, which do require effective shielding from cosmic radiation to achieve the necessary sensitivity. Laboratories located underground utilize a natural overburden of rock, corresponding to hundreds or even thousands of meters of water equivalent (m.w.e.) shielding—far greater than any man-made construction.

Compared to surface laboratories, an underground location poses additional logistical challenges, such as access to the underground location, space constraints, and provision of the necessary infrastructure and technical support for the experiments. Environmental radioactivity of the surrounding rock can still be a significant source of background radiation (in some cases even at higher levels than on surface). However, the attenuation of cosmic rays allows for massive custom experimental setups to shield the sensitive part, which on surface would be limited by secondary radiation created by cosmic rays. Low-background techniques have been developed and continue to achieve lower and lower background rates for increased sensitivity of large experiments. With their advantage of cosmic

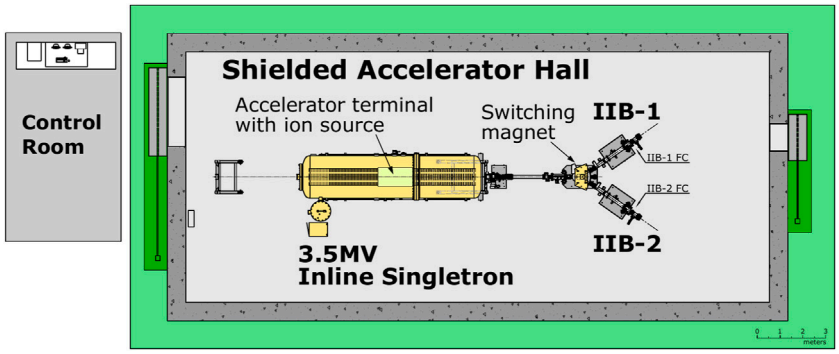

FIGURE 1
Schematic layout of the Bellotti Ion Beam Facility at the LNGS underground site.

background suppression, underground laboratories offer unique environments for scientific research.

The use of ion beam accelerators in underground laboratories was pioneered in the deep-underground laboratories of the Gran Sasso National Laboratory (LNGS), where the first accelerator used for nuclear astrophysics research was installed in 1992, to benefit from a reduction of the cosmic background by six orders of magnitude, thanks to the 1400 m of rock shielding of the laboratories (3,800 m water equivalent).

The first experiments, carried out by the LUNA collaboration, employed an accelerator constructed at University of Bochum (Germany). This machine was capable to produce Proton and ^{3,4}He beams with a beam energy of up to 50 keV. Most notably the machine was used to study the cross section of the fusion reaction ^{3}He+^{3}He at solar energies. Given the extremely low reaction rate, this measurement had not been possible in above-ground laboratories previously as events caused by cosmic rays obscured the signal [1]. The cross section at the lowest energy measured as low as 0.02(2) pb. This corresponded to an event rate of about 2 events/month, which is rather low even for the "silent" experiments of underground physics [2]. The experiment provided the first cross section measurement of a key reaction of the proton-proton chain at the thermal energy of the Sun, demonstrating the potential of an underground location and low-background physics techniques for measurements of nuclear cross sections down to the energy of the nucleosynthesis inside of stars [2].

Given the success of these experiments, the LUNA collaboration proposed the installation of LUNA-400, a commercial 400 kV Singletron® accelerator. LUNA-400 has been put to service in the year 2000 [3] and allowed to study key hydrogen burning reactions relevant to big bang nucleosynthesis, the p–p chain, the CNO cycle, and the NeNa and MgAl cycles. These studies have led to an improved understanding of energy generation and nucleosynthesis in various astrophysical sites, including the Sun, red giant and asymptotic giant branch stars, and classical novae [4].

Recently, a cross-section determination of the reaction D(p, γ)H, the most important reaction affecting the primordial abundance of deuterium during Big Bang Nucleosynthesis (BBN), settled the previously most uncertain nuclear physics input to BBN calculations. The reduced uncertainty of this result obtained at LUNA-400 affects the precision of BBN deuterium predictions and contributes to constrain the baryon density [5].

TABLE 1 Maximum beam intensity on target at different terminal voltages [6].

Ion species	Maximum beam intensity (eμA)	
	TV range 0.3 MV–0.5 MV	TV range 0.5 MV–3.5 MV
$^{1}H^{+}$	500	1000
$^{4}He^{+}$	300	500
$^{12,13}C^{+}$	100	150
$^{12,13}C^{2+}$	60	100

2 Characteristics of the Bellotti Ion Beam Facility

Building on the experience with accelerator experiments in a low cosmic ray background environment gained through the LUNA collaboration, INFN was able to obtain funding from the Italian Ministry for Research to purchase a 3.5 MV accelerator for installation in the LNGS underground laboratory. In 2022, the installation of the new 3.5 MV Singletron® accelerator, constructed by High Voltage Engineering Europa, has been completed in the underground laboratories. Figure 1 shows a layout of the facility.

The machine can provide intense proton, $^{4}He^{+}$, $^{12,13}C^{+}$ and $^{12,13}C^{2+}$ with the specifications listed in Table 1. It features a terminal voltage stability of 10 ppm and a terminal voltage drift in the order of 10^{-5} [6]. To exclude any interference of the accelerator operation with close-by rare event search experiments, the machine is located inside a building made of 80 cm thick concrete walls, which serves to shield the neutrons generated during operation of the accelerator. Outside the shielded accelerator room, these measures prevent any change in the natural neutron flux, which in the underground site is reduced by three orders of magnitude with respect to the earth surface [7, 8]. This has been assessed by GEANT4 and FLUKA simulations reviewed by the LNGS Scientific Committee.

The 3.5 MV Singletron® is part of the Bellotti Ion Beam Facility (Bellotti IBF) run as a scientific user facility. The ion beams of the Bellotti IBF are available to the scientific community through yearly calls published on the web-site of the facility https://l.infn.it/bellotti. Proposals are evaluated by a dedicated Program Advisory Committee (PAC) which is part of the Scientific Committee of LNGS. The Accelerator Service of LNGS is in charge to support research groups interested in conducting their projects in order to ensure the full success of the proposed research activities. It also takes care of operating the accelerators and the related plants of the Bellotti IBF.

As a next development step, the LUNA-400 Singletron® will be overhauled, moved to the immediate vicinity of 3.5 MV Singletron® and integrated into the Bellotti IBF. Once concluded, this effort will make proton and alpha beams in the energy range between 30 keV and 3.5 MeV available to the scientific community.

3 Scientific perspectives

Due to its deep underground location and the characteristics of the accelerators, the Bellotti IBF offers excellent opportunities not only in the field of nuclear astrophysics, as shown by the work of the LUNA Collaboration, but also in the applied sciences.

3.1 H burning—^{14}N(p, γ)^{15}O

The CNO cycle is the dominant mechanism for energy production in massive main-sequence stars during the hydrogen burning phase.

The ^{14}N(p, γ)^{15}O reaction is the slowest reaction of the CNO cycle and controls the rate of energy generation of this process. As a consequence, it directly determines the lifetime of massive stars. In our Sun ~1% of energy is produced through CNO, contributing also to 1.6% of the solar neutrino flux. As recently assessed by the Borexino collaboration [9], the ^{14}N(p, γ)^{15}O remains the second largest contribution to the uncertainty budget in the estimation of the C and N abundances in the Sun after the CNO neutrino flux itself.

This reaction has been extensively studied by the LUNA collaboration [10–13] and other groups [14, 15] down to a center of mass energy of 70 keV. In fact, thanks to one of the first results obtained at the LUNA-400 accelerator, its rate was found to be a factor of two slower than expected [12]. This result had several implications, such as increasing the age of globular clusters by about 1 Gy [10] and reducing the expected CNO solar neutrino rates by a factor of two [11]. Recently, a new underground measurement was performed by Frentz et al. [16] at the CASPAR accelerator (SURF).

Nonetheless experimental data still lies far from the solar Gamow window at E = 27 keV. Low-energy reaction rate data therefore relies on extrapolations done with R-matrix analysis [17]. Up to the current days, the R-matrix analysis of the reaction failed to provide a consistent view of both the low and high energy data for the reaction. The presence of consistent gaps in the data sets and the fact that several weaker transitions have not been measured since Schröder et al. [18] therefore reinforce the need for a precision measurement of the ^{14}N(p, γ)^{15}O over a wide energy range with an angular distribution experiment. The high-current 3.5 MV Singletron® of the Bellotti IBF represents the perfect framework where such an experiment can be conducted given the relatively weak population of some of the transitions and the reduction of the background in the γ-ray spectra given by the deep-underground location of the facility.

In this context, an improvement in the reaction rate, alongside the recently improved CNO flux measurement and further improvements from future such measurements, could provide important elements to solve the tension between solar models obtained using different metallicity levels [19].

3.2 He burning and n sources

Helium burning, and more generally, processes involving α-capture reactions, contribute greatly to the isotopic abundances observed in the Universe. After the bridging of the A = 5 and A = 8 mass gaps through the triple-α reaction [20, 21], helium burning begins at at $T \approx 0.2$ GK and proceeds through the reactions ^{12}C(α, γ)^{16}O and ^{16}O(α, γ)^{20}Ne. The latter reaction is sufficiently slow to provide only for a partial conversion of carbon into oxygen, leading to the currently observed ^{12}C/^{16}O abundance ratio of ca. 0.4 [22].

The cross section of ^{12}C(α, γ)^{16}O needs to be known at $E_{\mathrm{c.m.}}$ = 300 keV as an input for stellar models. At these energies, direct measurements are highly challenging due to the extremely low experimental count rates [53]. One approach to direct cross section measurements that has proven quite successful in the past is based on recoil separators [23–25]; γ-ray measurements in the deep underground will provide high-quality complementary cross section data.

Other α-capture induced reactions of great importance are (α, n) reactions on ^{13}C and ^{22}Ne during thermal pulses in AGB stars and, in the case of ^{22}Ne(α, n)^{25}Mg, core He and shell C burning in massive stars [26–28]. They constitute the neutron sources for the main and weak s processes, responsible for the production of about half of all heavy (A > 56) elements in the Universe [29].

Also the measurements of the neutron sources suffer from very low cross sections that have prevented progress towards direct measurements at low energies in surface laboratories [30–34]. The ^{13}C(α, n)^{16}O reaction has recently been measured at previously unreachable energies deep underground by the LUNA and the JUNA collaborations [35, 36]. The Bellotti IBF will allow to connect the low-energy data from LUNA-400 to the high-energy region, providing an insight into normalization issues seen between the many high-energy data sets. In addition, the availability of ^{13}C as a beam could allow measurements in inverse kinematics, penetrating deeper into the Gamow peak with a more advanced setup.

^{22}Ne(α, n)^{25}Mg has not been directly measured in over 20 years, and the ultra-low neutron background at the Bellotti IBF combined with the high-intensity α beam and an innovative setup constructed in the framework of the SHADES ERC project aims at providing for the first time data in the astrophysical energy range.

3.3 C burning

Carbon burning is a key stage of stellar evolution determining the final destiny of massive stars and of low mass stars in close binary

systems, whose understanding is of paramount importance for the comprehension of SuperNova (SN) outcomes. SNe play a pivotal role in astrophysics, providing a major contribution to the chemical and physical evolution of galaxies, and generating the most compact objects in nature, such as neutron stars and black holes (type II, core collapse SNe). SNe are also used to determine distances on cosmological scale, to probe the history of the Universe (type Ia, carbon explosive burning) [37]. The efficiency of carbon burning in massive stars also determines the compactness of the stellar core at the onset of the final core collapse. The compactness of the core is a critical parameter that determines the final fate of these stars, whether they end their life as a supernova or directly collapse into a black hole [38, 39]. Moreover, carbon burning can trigger superburst events, which are long, energetic, and rare thermonuclear flashes on accreting neutron stars in low-mass X-ray binaries. These bursts are considered to be triggered by the unstable $^{12}C+^{12}C$ burning in the ash left over from the rp-process on the surface of a neutron star [40].

The large uncertainty affecting the low energy cross section of the $^{12}C+^{12}C$ reaction hampers the knowledge of the final the fate of stellar structures and, in turn, our understanding of SN phenomena. The $^{12}C+^{12}C$ fusion in stars proceeds primarily through the $^{12}C(^{12}C, \alpha)^{20}Ne$ and the $^{12}C(^{12}C, p)^{23}Na$ reactions, at higher energy the neutron channel $^{12}C(^{12}C, n)^{23}Mg$ can be open. The cross sections of these processes are extremely low, in the sub-femto-barn range. Successful modelling of supernovae requires the cross sections to be known down to E around 1.5 MeV. Due to the extremely small cross sections, direct experiments are challenging already at energies above 2.2 MeV [41–46]. To overcome the experimental limitations, an indirect measurement was performed using the THM [47], covering the entire astrophysical region of interest from E = 2.7 MeV down to 0.8 MeV and revealing well resolved resonance structures. Further theory calculations [48] resulted in large corrections to the initially reported S-factors. Therefore, a direct measurement aiming to reach the astrophysical relevant energy is of crucial importance to reduce the present uncertainty. Measurements may be done detecting the γ-rays generated by the decay of the ^{23}Na and ^{20}Ne excited states, or by searching for the charged particles, p and α, emitted in the two reactions.

A prior experiment [43] used a HPGe detector equipped with 15 cm thick lead shield and an active muon veto in a surface laboratory to study the $^{12}C(^{12}C, p)^{23}Na$ and the $^{12}C(^{12}C, \alpha)^{20}Ne$ reactions. The reaction yield has been measured observing the transitions from the first excited state to the ground state of the daughter nuclei, involving the emission of photons with energies of 440 and 1634 keV, respectively. This study demonstrates the potential of this technique and supports future experiments in an underground location to take advantage of a lower background and extend the measurements to lower energy. The LUNA collaboration already showed that the combination of the 3800 m.w.e. rock shield provided by the Gran Sasso massif, a 25 cm thick lead shield, a copper liner and nitrogen flushing is highly effective in reducing the gamma background in HPGe detectors. The reduction factor ranges between 10^3 and 10^4 both for the energy region above natural radioactivity and below it [49] (see Section 1). In particular, based on preliminary background measurements at LNGS, in the regions of the spectrum close to 440 keV and 1634 keV the Bellotti IBF will allow to achieve a gamma background about two orders of magnitude lower with respect to [43], enabling the measurement of the cross section in the energy range relevant to astrophysics.

3.4 Applications

Unlike other MeV ion beam facilities that operate in standard laboratories located at the surface, the severe limitation of prompt radiation production, especially neutrons, imposes a compelling severe limitation to the beam intensities and energies and to the materials that may be subject to irradiation in the underground laboratory. Despite the limitations, Ion Beam Analysis (IBA) niche applications (in particular depth profiling using narrow resonant (p, γ) and (α, γ) reactions for sub ppm sensitivity analysis and nm depth resolution) may be considered potential high value and cutting edge applications of the 3.5 MV underground accelerator. IBA is generally accomplished with 100 pnA to few pμA proton or helium currents that can be too small for the present configuration of the accelerator, but could be part of a future development if extensive programs of key material micro-analyses will be proposed. The Nuclear Resonance Reaction Analysis (NRRA) technique is far the most interesting niche application at IBF. While Elastic Backscattering (EBS) and Particle Induced X-ray Emission (PIXE) are sensitive to medium to heavy elements, Particle Induced Gamma-ray Emission (PIGE) is best suited for light elements and isotopes analysis and an intense program of material characterization involving the study of light impurities at (sub)ppm level may be specific of the underground laboratory taking the full advantage of the high sensitivity gamma spectrometers and the extremely low gamma background coupled to the unprecedented ion beam energy stability and low energy spread of the 3.5 MV Singletron® accelerator of the Bellotti Facility. In parallel, a scientific plan aiming at the accurate measurement of unexplored (p, γ) and (α, γ) reactions suitable for IBA provides another field of investigation which will fully profit of the characteristics of the underground facility. In addition, it must be mentioned that in quantum technology the possibility to accurately implant $^{12,13}C$ ions in a fairly wide energy range (0.3–7 MeV) coupled to the possibility to use the proton and He beams for in-situ pre(post) irradiation and analysis might offer a valuable possibility to create new color centers in semiconductors for the development of single photon sources in advanced quantum photonics applications.

4 Discussion

In recent year a number of deep underground accelerators like JUNA in China [50] and CASPAR in the US [51] have taken up science operation lately, focusing on nuclear astrophysics research and enabling a rich scientific program of underground research.

The Bellotti IBF at LNGS stands out being the worldwide only ion beam user facility deep underground. As this, it aims to provide the scientific community with access to intense proton, ^4He and $^{12,13}C$ ion beams in a low radiation environment achievable only in a deep underground site. The intense carbon beam and, more in general, the excellent long term stability of the beams produced by the 3.5 MV Singletron® accelerator are unique features of the Bellotti IBF.

As outline above, the very low radiation environment implies advantages and disadvantages for industrial applications of the, ^{1}H, ^{4}He, ^{12,13}C beams produced at the Bellotti IBF. On the other hand, the extremely low radiation background provides for an excellent signal to background ratio which in turn results in a high detection sensitivity. The related, groundbreaking possibilities have been explored in the context of Nuclear Astrophysics by the LUNA collaboration in the course of the last 25 years. At the same time, these activities opened insights to the potential related to sample characterizations [52]. In spite of the restrictions, the Bellotti IBF thus opens new frontiers not only in the fields of nuclear astrophysics and nuclear physics but also to applied sciences.

The experience gained during the first year of operation of the 3.5 MV Singletron® will be used to optimize its usability for applications like IBA as well as for nuclear astrophysics. This includes the production of stable ion beams with intensities significantly lower than 1 μA as needed for applications, and measures to increase the beam intensity at high energies still maintaining the imposed limit for the neutron production.

Data availability statement

The original contributions presented in the study are included in the article/Supplementary Material, further inquiries can be directed to the corresponding author.

Author contributions

MJ: Writing–original draft, Writing–review and editing. GI: Writing–original draft, Writing–review and editing. AnB: Writing–original draft, Writing–review and editing. AxB: Writing–original draft, Writing–review and editing. AC: Writing–original draft, Writing–review and editing. AL: Writing–original draft, Writing–review and editing. FF: Writing–original draft, Writing–review and editing. DR: Writing–original draft, Writing–review and editing. VR: Writing–original draft, Writing–review and editing.

Funding

The authors declare financial support was received for the research, authorship, and/or publication of this article. The Bellotti IBF received funding from the Italian Ministry for Research (Progetti Premiali "LUNA-MV" 2011 and 2012) and by the National Scientific Committee 3 (CSN3) of INFN. SHADES is funded by the European Union (ERC #852016).

Acknowledgments

The authors acknowledge the continuous support the management of INFN and LNGS for establishing the facility as well as the support of the Technical Division of LNGS as well as the LNGS Services for Safety, Environment and Technical Coordination during design and construction of the required infrastructures. The authors are greatly indebted to Donatello Ciccotti for his continuous, competent and enthusiastic contributions and generous availability during the infrastructure installation, accelerator commissioning and operation.

Conflict of interest

The authors declare that the research was conducted in the absence of any commercial or financial relationships that could be construed as a potential conflict of interest.

Publisher's note

References

1. Krauss A, Becker H, Trautvetter H, Rolfs C. Astrophysical $S(E)$ factor of ^{3}He(^{3}He, $2p$)^{4}He at solar energies. *Nuc Phys A* (1987) 467:273–90. doi:10.1016/0375-9474(87)90530-6

2. Bonetti R, Broggini C, Campajola L, Corvisiero P, D'Alessandro A, Dessalvi M, et al. First measurement of the ^{3}He(^{3}He, $2p$)^{4}He cross section down to the lower edge of the solar Gamow peak. *Phys Rev Lett* (1999) 82:5205–8. doi:10.1103/PhysRevLett.82.5205

3. Formicola A, Imbriani G, Junker M, Bemmerer D, Bonetti R, Broggini C, et al. The LUNA II accelerator. *Nucl Instrum Methods Phys Res A* (2003) 507:609–16. doi:10.1016/S0168-9002(03)01435-9

4. Aliotta M, Boeltzig A, Depalo R, Gyürky G. Exploring stars in underground laboratories: challenges and solutions. *Annu Rev Nucl Part Sci* (2022) 72:177–204. doi:10.1146/annurev-nucl-110221-103625

5. Mossa V, Stöckel K, Cavanna F, Ferraro F, Aliotta M, Barile F, et al. The baryon density of the Universe from an improved rate of deuterium burning. *Nature* (2020) 587:210–3. doi:10.1038/s41586-020-2878-4

6. Sen A, Domínguez-Cañizares G, Podaru N, Mous D, Junker M, Imbriani G, et al. A high intensity, high stability 3.5 MV Singletron™ accelerator. *Nucl Instrum Methods Phys Res B* (2019) 450:390–5. doi:10.1016/j.nimb.2018.09.016

7. Best A, Görres J, Junker M, Kratz KL, Laubenstein M, Long A, et al. Low energy neutron background in deep underground laboratories. *Nucl Instr Methods Phys Res Section A: Acc Spectrometers, Detectors Associated Equipment* (2016) 812:1–6. doi:10.1016/j.nima.2015.12.034

8. Bruno G, Fulgione W. Flux measurement of fast neutrons in the Gran Sasso underground laboratory. *The Eur Phys J C* (2019) 79:747. doi:10.1140/epjc/s10052-019-7247-9

9. Appel S, Bagdasarian Z, Basilico D, Bellini G, Benziger J, Biondi R, et al. Improved measurement of solar neutrinos from the carbon-nitrogen-oxygen cycle by Borexino and its implications for the standard solar model. *Phys Rev Lett* (2022) 129:252701. doi:10.1103/PhysRevLett.129.252701

10. Imbriani G, Costantini H, Formicola A, Bemmerer D, Bonetti R, Broggini C, et al. The bottleneck of CNO burning and the age of Globular Clusters. *Astron Astrophys* (2004) 420:625–9. doi:10.1051/0004-6361:20040981

11. Formicola A, Imbriani G, Costantini H, Angulo C, Bemmerer D, Bonetti R, et al. Astrophysical S-factor of ^{14}N(p, γ)^{15}O. *Phys Lett B* (2004) 591:61–8. doi:10.1016/j.physletb.2004.03.092

12. Bemmerer D, Confortola F, Lemut A, Bonetti R, Broggini C, Corvisiero P, et al. Low energy measurement of the ^{14}N(p, γ)^{15}O total cross section at the LUNA

underground facility. *Nuc Phys A* (2006) 779:297–317. doi:10.1016/j.nuclphysa.2006.09.001

13. Marta M, Formicola A, Gyürky G, Bemmerer D, Broggini C, Caciolli A, et al. Precision study of ground state capture in the ^{14}N(p,γ)^{15}O reaction. *Phys Rev C* (2008) 78:022802. doi:10.1103/PhysRevC.78.022802

14. Li Q, Görres J, deBoer RJ, Imbriani G, Best A, Kontos A, et al. Cross section measurement of ^{14}N(p,γ)^{15}O in the CNO cycle. *Phys Rev C* (2016) 93:055806. doi:10.1103/PhysRevC.93.055806

15. Wagner L, Akhmadaliev S, Anders M, Bemmerer D, Caciolli A, Gohl S, et al. Astrophysical *S* factor of the ^{14}N(p, γ)^{15}O reaction at 0.4-1.3 MeV. *Phys Rev C* (2018) 97:015801. doi:10.1103/PhysRevC.97.015801

16. Frentz B, Aprahamian A, Boeltzig A, Borgwardt T, Clark AM, deBoer RJ, et al. Investigation of the ^{14}N(p,γ)^{15}O reaction and its impact on the CNO cycle. *Phys Rev C* (2022) 106:065803. doi:10.1103/PhysRevC.106.065803

17. Azuma RE, Uberseder E, Simpson EC, Brune CR, Costantini H, de Boer RJ, et al. AZURE: an R-matrix code for nuclear astrophysics. *Phys Rev C* (2010) 81:045805. doi:10.1103/PhysRevC.81.045805

18. Schröder U, Becker H, Bogaert G, Görres J, Rolfs C, Trautvetter H, et al. Stellar reaction rate of ^{14}N(p, γ)^{15}O and hydrogen burning in massive stars. *Nuc Phys A* (1987) 467:240–60. doi:10.1016/0375-9474(87)90528-8

19. Villante FL, Serenelli A. The relevance of nuclear reactions for Standard Solar Models construction. *Front Astron Space Sci* (2021) 7:112. doi:10.3389/fspas.2020.618356

20. Hoyle F. On nuclear reactions occuring in very hot stars. I. The synthesis of elements from carbon to nickel. *Astrophys J Suppl* (1954) 1:121. doi:10.1086/190005

21. Cook CW, Fowler WA, Lauritsen CC, Lauritsen T. B^{12}, C^{12}, and the red giants. *Phys Rev* (1957) 107:508–15. doi:10.1103/PhysRev.107.508

22. deBoer RJ, Görres J, Wiescher M, Azuma RE, Best A, Brune CR, et al. The ^{12}C(α,γ)^{16}O reaction and its implications for stellar helium burning. *Rev Mod Phys* (2017) 89:035007. doi:10.1103/RevModPhys.89.035007

23. Kremer RM, Barnes CA, Chang KH, Evans HC, Filippone BW, Hahn KH, et al. Coincidence measurement of the ^{12}C(α,γ)^{16}O cross section at low energies. *Phys Rev Lett* (1988) 60:1475–8. doi:10.1103/PhysRevLett.60.1475

24. Schürmann D, Di Leva A, Gialanella L, Rogalla D, Strieder F, De Cesare N, et al. First direct measurement of the total cross-section of ^{12}C(α, γ)^{16}O. *Eur Phys J A* (2005) 26:301–5. doi:10.1140/epja/i2005-10175-2

25. Schürmann D, Di Leva A, Gialanella L, Kunz R, Strieder F, De Cesare N, et al. Study of the 6.05 MeV cascade transition in ^{12}C(α, γ)^{16}O. *Phys Lett B* (2011) 703:557–61. doi:10.1016/j.physletb.2011.08.061

26. Straniero O, Gallino R, Cristallo S. s process in low-mass asymptotic giant branch stars. *Nuc Phys A* (2006) 777:311–39. doi:10.1016/j.nuclphysa.2005.01.011

27. Cristallo S, La Cognata M, Massimi C, Best A, Palmerini S, Straniero O, et al. The importance of the ^{13}C(α,n)^{16}O reaction in asymptotic giant branch stars. *Astrophys J* (2018) 859:105. doi:10.3847/1538-4357/aac177

28. Adsley P, Battino U, Best A, Caciolli A, Guglielmetti A, Imbriani G, et al. Reevaluation of the ^{22}Ne(α,γ)^{26}Mg and ^{22}Ne(α,n)^{25}Mg reaction rates. *Phys Rev C* (2021) 103:015805. doi:10.1103/PhysRevC.103.015805

29. Käppeler F, Gallino R, Bisterzo S, Aoki W. The *s* process: nuclear physics, stellar models, and observations. *Rev Mod Phys* (2011) 83:157–93. doi:10.1103/RevModPhys.83.157

30. Wolke K, Harms V, Becker HW, Hammer JW, Kratz KL, Rolfs C, et al. Helium burning of ^{22}Ne. *Z Phys A* (1989) 334:491–510. doi:10.1007/bf01294757

31. Harms V, Kratz KL, Wiescher M. Properties of ^{22}Ne(α,n)^{25}Mg resonances. *Phys Rev C* (1991) 43:2849–61. doi:10.1103/PhysRevC.43.2849

32. Drotleff HW, Denker A, Knee H, Soine M, Wolf G, Hammer JW, et al. Reaction rates of the s-process neutron sources Ne-^{22}Ne(α, n)^{25}Mg and ^{13}C(α,n)^{16}O. *Astrophys J* (1993) 414:735. doi:10.1086/173119

33. Jaeger M, Kunz R, Mayer A, Hammer JW, Staudt G, Kratz KL, et al. ^{22}Ne(α,n)^{25}Mg: the key neutron source in massive stars. *Phys Rev Lett* (2001) 87:202501. doi:10.1103/PhysRevLett.87.202501

34. Heil M, Detwiler R, Azuma RE, Couture A, Daly J, Görres J, et al. The ^{13}C(α, n) reaction and its role as a neutron source for the s process. *Phys Rev C* (2008) 78:025803. doi:10.1103/PhysRevC.78.025803

35. Ciani GF, Csedreki L, Rapagnani D, Aliotta M, Balibrea-Correa J, Barile F, et al. Direct measurement of the ^{13}C(α,n)^{16}O cross section into the *s*-process Gamow peak. *Phys Rev Lett* (2021) 127:152701. doi:10.1103/PhysRevLett.127.152701

36. Gao B, Jiao TY, Li YT, Chen H, Lin WP, An Z, et al. Deep underground laboratory measurement of ^{13}C(α,n)^{16}O in the Gamow windows of the *s* and *i* processes. *Phys Rev Lett* (2022) 129:132701. doi:10.1103/PhysRevLett.129.132701

37. Aliotta M, Buompane R, Couder M, Couture A, deBoer RJ, Formicola A, et al. The status and future of direct nuclear reaction measurements for stellar burning. *J Phys G* (2022) 49:010501. doi:10.1088/1361-6471/ac2b0f

38. Chieffi A, Roberti L, Limongi M, La Cognata M, Lamia L, Palmerini S, et al. Impact of the new measurement of the ^{12}C + ^{12}C fusion cross section on the final compactness of massive stars. *Astrophys J* (2021) 916:79. doi:10.3847/1538-4357/ac06ca

39. Imbriani G, Limongi M, Gialanella L, Terrasi F, Straniero O, Chieffi A. The ^{12}C(α, γ)^{16}O reaction rate and the evolution of stars in the mass range $0.8 \leq M/M_{\odot} \leq 25$. *Astrophys J* (2001) 558:903–15. doi:10.1086/322288

40. Lewin W, van der Klis M, editors. *Compact stellar X-ray sources*. Cambridge Astrophysics: Cambridge University Press (2006). doi:10.1017/CBO9780511536281

41. Fruet G, Courtin S, Heine M, Jenkins D, Adsley P, Brown A, et al. Advances in the direct study of carbon burning in massive stars. *Phys Rev Lett* (2020) 124:192701. doi:10.1103/PhysRevLett.124.192701

42. Tan WP, Boeltzig A, Dulal C, deBoer RJ, Frentz B, Henderson S, et al. New measurement of ^{12}C +^{12}C fusion reaction at astrophysical energies. *Phys Rev Lett* (2020) 124:192702. doi:10.1103/PhysRevLett.124.192702

43. Spillane T, Raiola F, Rolfs C, Schürmann D, Strieder F, Zeng S, et al. ^{12}C + ^{12}C fusion reactions near the Gamow peak. *Phys Rev Lett* (2007) 98:122501. doi:10.1103/PhysRevLett.98.122501

44. Becker HW, Kettner KU, Rolfs C, Trautvetter HP. The ^{12}C + ^{12}C reaction at subcoulomb energies. *Z Phys A* (1981) 303:305–12. doi:10.1007/BF01421528

45. Zickefoose J, Di Leva A, Strieder F, Gialanella L, Imbriani G, De Cesare N, et al. Measurement of the ^{12}C(^{12}C, p)^{23}Na cross section near the Gamow energy. *Phys Rev C* (2018) 97:065806. doi:10.1103/PhysRevC.97.065806

46. Bucher B, Tang XD, Fang X, Heger A, Almaraz-Calderon S, Alongi A, et al. First direct measurement of ^{12}C(^{12}C, n)^{23}Mg at stellar energies. *Phys Rev Lett* (2015) 114:251102. doi:10.1103/PhysRevLett.114.251102

47. Tumino A, Spitaleri C, Cognata ML, Cherubini S, Guardo GL, Gulino M, et al. An increase in the ^{12}C + ^{12}C fusion rate from resonances at astrophysical energies. *Nature* (2018) 557:687–90. doi:10.1038/s41586-018-0149-4

48. Mukhamedzhanov AM, Kadyrov AS, Pang DY. Trojan horse method as an indirect approach to study resonant reactions in nuclear astrophysics. *Eur Phys J A* (2020) 56:233. doi:10.1140/epja/s10050-020-00214-9

49. Caciolli A, Agostino L, Bemmerer D, Bonetti R, Broggini C, Confortola F, et al. Ultra-sensitive in-beam γ-ray spectroscopy for nuclear astrophysics at LUNA. *Eur Phys J A* (2009) 39:179–86. doi:10.1140/epja/i2008-10706-3

50. Liu WP, Cui BC, Gao BS, Guo B, He JJ, Jiang YC, et al. Progress of underground nuclear astrophysics experiment JUNA in China. *Nucl Phys News* (2023) 33:10–3. doi:10.1080/10619127.2023.2168102

51. Robertson D, Couder M, Greife U, Strieder F, Wiescher M. Underground nuclear astrophysics studies with CASPAR. *EPJ Web of Conferences* (2016) 109:09002. doi:10.1051/epjconf/201610909002

52. Ciani GF, Csedreki L, Balibrea-Correa J, Best A, Aliotta M, Barile F, et al. A new approach to monitor ^{13}C-targets degradation *in situ* for ^{13}C(α, n)^{16}O cross-section measurements at LUNA. *Eur Phys J A* (2020) 56:75. doi:10.1140/epja/s10050-020-00077-0

53. Bonasera A, Natowitz JB. Calculation of the ^{12}C + ^{12}C sub-barrier fusion cross section in an imaginary-time-dependent mean field theory. *Phys Rev C* (2020) 102:061602. (R). doi:10.1103/PhysRevC.102.061602

frontiers | Frontiers in Physics

TYPE Perspective
PUBLISHED 10 November 2023
DOI 10.3389/fphy.2023.1263338

OPEN ACCESS

EDITED BY
Carlos Peña Garay,
Laboratorio Subterráneo de Canfranc, Spain

REVIEWED BY
Giulia Festa,
Museo Storico della Fisica e Centro Studi e Ricerche Enrico Fermi, Italy

*CORRESPONDENCE
Patrizia Morciano,
patrizia.morciano@lngs.infn.it

†These authors share first authorship

RECEIVED 19 July 2023
ACCEPTED 30 October 2023
PUBLISHED 10 November 2023

CITATION
Morciano P, Dini V, Berardinelli F, Baiocco G, Conte V, Udroiu I, Barbato F, Marinaccio J, Anello P, Antoccia A, Tabocchini MA, Selva A, Canella S, Bianchi A, Guardamagna I, Lonati L, Scifoni E, Laubenstein M, Balata M, Ferella F, Grifoni D, Galante A, Maccarrone M, Tirelli V, Grasso F, Sanchez M and Sgura A (2023), Overview of DISCOVER22 experiment in the framework of INFN-LNGS Cosmic Silence activity: challenges and improvements in underground radiobiology. *Front. Phys.* 11:1263338. doi: 10.3389/fphy.2023.1263338

Overview of DISCOVER22 experiment in the framework of INFN-LNGS Cosmic Silence activity: challenges and improvements in underground radiobiology

Patrizia Morciano[1,2*†], Valentina Dini[3,4†], Francesco Berardinelli[5,6], Giorgio Baiocco[7,8], Valeria Conte[9], Ion Udroiu[4,5], Federica Barbato[5,6], Jessica Marinaccio[5,6], Pasqualino Anello[3,4], Antonio Antoccia[5,6], Maria Antonella Tabocchini[4], Anna Selva[9], Stefania Canella[9], Anna Bianchi[9], Isabella Guardamagna[7,8], Leonardo Lonati[7,8], Emanuele Scifoni[10], Matthias Laubenstein[1], Marco Balata[1], Francesco Ferella[1], Daniela Grifoni[2], Angelo Galante[11,12], Mauro Maccarrone[11,13], Valentina Tirelli[4,14], Felicia Grasso[15], Massimo Sanchez[4,15] and Antonella Sgura[5,6]

[1]INFN—Laboratori Nazionali del Gran Sasso, Assergi L'Aquila, Italy, [2]Dipartimento di Medicina clinica, sanità pubblica, scienze della vita e dell'ambiente, Università degli Studi dell'Aquila, L'Aquila, Italy, [3]Centro Nazionale di Tecnologie Innovative in Sanità Pubblica, Istituto Superiore di Sanità, Rome, Italy, [4]INFN, Sezione di Roma1, Rome, Italy, [5]Dipartimento di Scienze, Università degli Studi Roma Tre, Rome, Italy, [6]INFN, Sezione di Roma3, Rome, Italy, [7]Dipartimento di Fisica, Università degli Studi di Pavia, Pavia, Italy, [8]INFN Pavia, Pavia, Italy, [9]INFN—Laboratori Nazionali di Legnaro, Padova, Italy, [10]INFN-Trento Institute for Fundamental Physics and Applications (TIFPA), Trento, Italy, [11]Dipartimento di Scienze Cliniche Applicate e Biotecnologiche, Università degli Studi dell'Aquila, L'Aquila, Italy, [12]CNR-SPIN, c/o Università degli Studi dell'Aquila, L'Aquila, Italy, [13]European Center for Brain Research/IRCCS Santa Lucia Foundation, Rome, Italy, [14]Servizio Tecnico Scientifico Grandi Strumentazioni e Core Facilities, Istituto Superiore di Sanità, Rome, Italy, [15]Dipartimento Malattie Infettive, Istituto Superiore di Sanità, Rome, Italy

One of the most intriguing and still pending questions in radiobiology is to understand whether and how natural environmental background radiation has shaped Life over millions of years of evolution on Earth. Deep Underground Laboratories (DULs) represent the ideal below-background exposure facilities where to address such a question. Among the few worldwide DULs, INFN-Laboratorio Nazionale del Gran Sasso (LNGS) is one of the largest in terms of size and infrastructure. Designed and built to host neutrino and dark matter experiments, since the 1990 s the LNGS has been one of the first DULs to systematically host radiobiology experiments. Here we present the DISCOVER22 (DNA Damage and Immune System Cooperation in VEry low Radiation environment 2022) experiment recently started at LNGS. DISCOVER22 aims at investigating how the low radiation background modulates the Immune System (IS) response in *in vitro* and *in vivo* models. Underground radiobiology experiments are particularly complex and tricky to design and perform. In these studies, the accurate characterization of exposure scenarios is mandatory, but a challenging aspect is to understand how the very few ionizing tracks in the ultra-Low Radiation Environment (LRE) interact with the

living matter in space and time in order to trigger different biological responses. In this Perspective, we describe these challenges and how we address them through a microdosimetric and a radiobiological approaches. We aim at linking physical microdosimetric measurements and the corresponding biological radiation responses by using radiation biophysical models that could shed light on many as yet unresolved questions.

KEYWORDS

underground radiobiology, deep underground laboratories, environmental radiation, immune response, low radiation, microdosimetry, biophysical model

Introduction

Natural Background Radiation (NBR), which is the sum of space radiations, reaching the Earth, and terrestrial radiation, from radionuclids present in rocks, is an inescapable abiotic factor to which all living organisms are exposed. NBR, which surrounds us and has always been present, has accompanied the evolution of Life on Earth. Important and fascinating questions remain open about its role in the metabolism of living beings and on their evolution. The first experiment conceived to answer these questions date back to the 1980. Planel *et al.* grew the protozoan *Paramecium tetraurelia* and the cyanobacterium *Synechococcus lividus* either in a shielded condition and in an underground laboratory located under 200 m of rock in the Pyrenees, demonstrating that "*radiation can stimulate the proliferation of these two single-celled organisms*" [1]. This study provided first evidences questioning the Linear No-threshold (LNT) model for Below-Background Radiation (BBR), suggesting a role for NBR in maintaining biological functions for microorganisms. Since then, further studies have been conducted on different living systems giving rise to a new and exciting area of research, the Underground Radiobiology (URb). So far, our and other groups have demonstrated that living organisms, from bacteria to multicellular organisms, sense and respond to BBR in different ways, highlighting a role of NBR in maintaining efficient defense responses [2]. Deep Underground Laboratories (DULs) represent the ideal location where to perform these investigations since the space radiation contribution is largely reduced. An overall view on the research activities in DULs around the world shows a growing interest for underground biology in the recent years, testified by many proposals, investment of dedicated spaces, funding and long-term biology programs. However, URb experiments are particularly complex. In addition to the logistical and technical issues that have to be addressed and that have been widely discussed in [2–4], an important aspect is the need for strict environmental control in both underground and reference laboratories in which the parallel cultures are maintained for biological tests. This tight control allows the observed biological differences to be attributed with reasonable certainty to the reduction of NBR in the underground environment.

The interdisciplinary Cosmic Silence Collaboration (CSC), as well as other groups conducting URb investigations, have been working hard in this direction, minimising environmental variables as much as possible and further reducing environmental radiation exposure through radon mitigation/abatement systems in the underground laboratory [5–7] and modulating the contribution of low-LET gamma rays with shielding and natural sources [2]. A precise and complete dosimetric characterisation of the radiation field is mandatory for optimising experiments and interpreting biological results correctly and in detail. DISCOVER22 (DNA Damage and Immune System Cooperation in VEry low Radiation environment 2022) is a three-year INFN-Interdisciplinary Scientific Commission 5 funded experiment, in the framework of CSC activities at INFN- Gran Sasso National Laboratory (LNGS). The experiment, started in the beginning of 2023, aims at investigating how BBR modulates the immune response *in vitro* and *in vivo* models. Here we present the DISCOVER22 experiment by describing the biological, microdosimetric, and modeling approaches used. We believe that applying the strategy of linking direct microdosimetric measurements with biological analysis through modelling will allow us to answer several open questions about the nature of interactions between ultra-low doses and living matter. To our knowledge, it is the first time that a direct microdosimetric measurement is applied to URb experiments, this aspect having been addressed so far only through the use of simulations [8].

DISCOVER 22-the biological question

To date, the study of biological responses below the NBR suggested that environmental radiation exposure is an essential stimulus to efficiently activate the stress-response capability in many living organisms (from protozoan to human cells) [9–18]. Most of these studies come from URb experiments conducted for more than 3 decades at LNGS facilities. However, to our knowledge, no data are available on the modulation of immunological responses in such conditions and further studies are needed.

The basic cellular and molecular mechanisms underlying the radiation-induced immune response are still largely unknown and research on this area is becoming a hot topic. Indeed, investigation of the Immune System (IS) response to Low Dose Radiation (LDR)/dose rates has been also identified as a priority in the Strategic Research Agenda (SRA) of Multidisciplinary European Low Dose Initiative (MELODI) [19].

LDR has been shown to modulate a variety of immune response processes [20–22]. At low doses, the IS may be affected, leading to accelerated immune aging and increased risk of various health issues, such as age-related degenerative disorders and cancer. On the other hand, LDR therapy has been found to have positive effects on chronic inflammatory and degenerative diseases, including anti-inflammatory and pain-relieving properties [23]. Several studies have confirmed that the effect of LDR on innate and adaptive

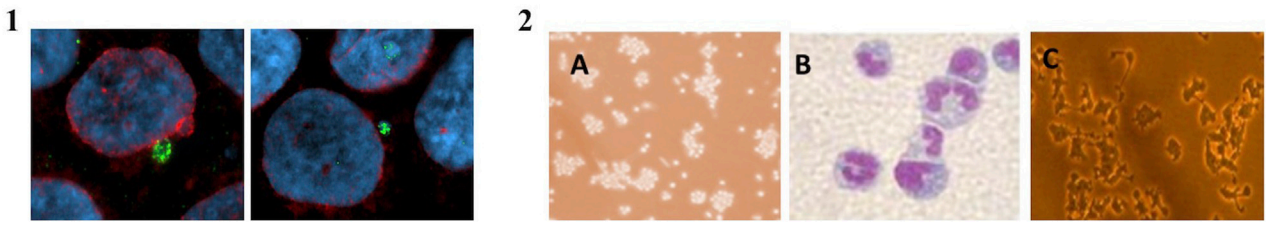

FIGURE 1
Panel 1—Representative image of human keratinocytes stained with MN cGAS positive. The green color represents cGAS protein, in blue DNA and red the nuclear envelope. Panel 2—Image of AP HL60 **(A)**, Np **(B)**, and Mp **(C)**. HL60 cells grow in suspension whereas Np and Mp grow in monolayer.

immunity depends on many factors, including status of immune cells, microenvironment, and immune cell-cell interaction, suggesting that it is a well-orchestrated phenomenon with clinical potential [24–26]. Moreover, radiobiological data suggest that cytokines modulating immunological responses are differentially up- or downregulated with doses around 0.5 Gy [27, 28]. Furthermore, the anti-inflammatory *versus* pro-inflammatory responses at doses as low as 10 and 50 mGy are not clear-cut but rather the result of a balance between the two types of effect [29].

In DISCOVER22, experiments in BBR (LNGS underground laboratory) and in NBR (LNGS aboveground laboratory), will be carried out in parallel to investigate whether BBR:

1. Influences the activation of the cGAS/STING pathway following radiation-induced DNA damage in human keratinocytes (Figure 1. Panel 1);
2. Influences the ability of immature immune cells both to differentiate into macrophages (Mp) and neutrophils (Np) and to maintain their biological functions (Figure 1. Panel 2);
3. Modulates immuno-related gene expression in *Drosophila melanogaster*.

Regarding the first objective, the project will investigate whether human cells maintained in BBR for 2–4 weeks differently respond to a challenging ionizing radiation (IR) exposure in terms of Innate Immune Response (IRR) activation.

We hypothesize that permanence of cells in BBR could influence the activation of the innate IS induced by DNA damage. One potential outcome is that cells cultured in BBR may downregulate IS activation caused by DNA damage, resulting in reduced immune responsiveness to high doses of acute IR. Recent studies have provided mechanistic information on how DNA damage induces interferon (IFN) type I and other immuno-regulatory cytokines [30]. Among the different pathways, we decided to focus on the cGAS-STING that is activated by a protein called cycling-GMP-AMP synthase (cGAS) able to detect cytosolic DNA (*e.g.*, viral DNA but also endogenous fragmented DNA originating from DNA damage) and synthesize cGAMP [31]. The second cGAMP messenger binds to a specific region of the STING protein resulting in a conformational change [32]. STING multimerizes and moves from endoplasmic reticulum to Golgi, where it binds and is phosphorylated by the dimer TANK-binding kinase 1 (TBK1), a serin-threonine kinase, or by the complex IKK (IκB kinase). Activation of STING-TBK1/IKK leads to phosphorylation of the transcription factor IRF3 (Interferon Regulatory Factor 3) resulting in dimerization [33] and activation of NF-kB, which enters the nucleus and binds to the promoter of the IFN beta, a type I-IFN, activating its transcription [34]. This pathway provides a direct link between IR-induced DNA damage and innate immunity activation and to our knowledge, no data are present in the literature on the modulation of the cGAS/STING pathway in BBR conditions.

Regarding the second objective, the influence of the BBR in modulating the differentiation capability will be evaluated using human promyeloblast leukemia (HL60) cells, a well-characterized cellular model of the IS. Although literature data are scarce in this field, some suggestion came from the study of Chun *et al.* showing that bone marrow cells from low-dose irradiated mice can differentiate into dendritic cells [34]. The HL60 cells [35] proliferate in suspension and can be induced to differentiate *in vitro* [36], using dimethyl sulphoxide [37] and 12-O-tetradecanoylphorbol-13-acetate (TPA) [38], into Np and Mp, respectively, similar in morphological and functional characteristics to those *in vivo*. HL60 cells will be induced to differentiate, after being grown in BBR and NBR. To study the differentiation, the expression of specific membrane antigens (CDs) and ROS level, will be analyzed by flow cytometry (FC) [39]. Any shift in CD expression, ROS level profiles, in BBR and NBR will be indicative of immune modulation. Finally, the capability of Np and Mp to maintain their phagocytic functions, that play a crucial role in host defenses against pathogens, will also be investigated. These functions will be studied through a quantitative colorimetric nitroblue tetrazolium assay [40], in Mp, and through an immunological mechanism called NETosis, in Np. Neutrophil Extracellular Traps (NETs) are web-like structures, consisting of a DNA core to which histones, proteins and enzymes are attached, through which neutrophils eliminate pathogens [41, 42]. In *D. melanogaster*, the response to an immune challenge mainly relies on two distinct pathways (Toll and Imd signaling pathways) where each of them comprises molecules that have a counterpart in mammalian signaling pathways activated during innate immune defenses. Like in human beings, in fruit flies the homeostasis of the IS is maintained through tissue communication making them a remarkable model for deciphering the IS at the organismal scale [43, 44]. Fruit flies have previously been successfully used as model organism in underground biology experiments [13, 15, 45]. Starting

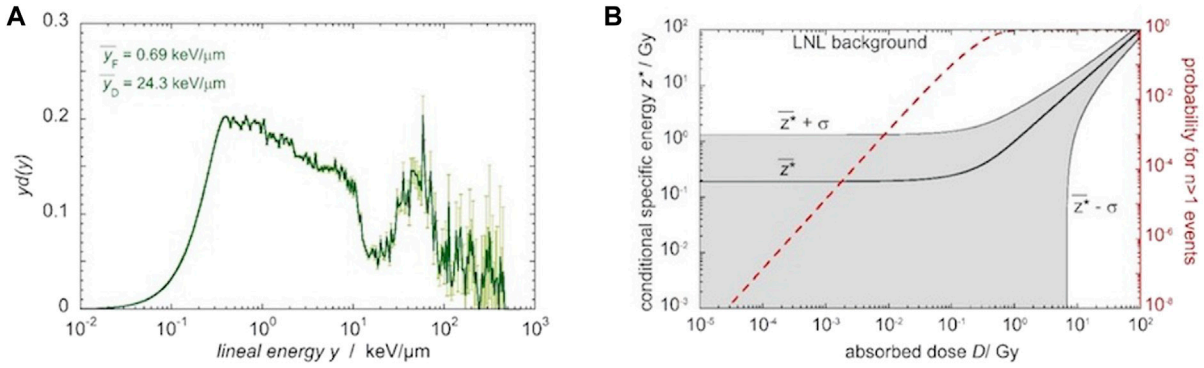

FIGURE 2
(A) The microdosimetric spectrum measured in a 1 µm sensitive site in the background environmental radiation field at INFN-LNL. Equal visual areas correspond to equal contributions to the total absorbed dose. The thick line shows the sampled data, the thin light-lines represent statistical uncertainties as 2 standard deviations. **(B)** The specific energy for critical sites, z^*, as a function of the macroscopic absorbed dose D. Results correspond to the radiation field shown in Figure 2. The dashed red line depicts the probability of a 1 µm site being affected by more than one energy deposition event. The thick black line represents the mean value of the conditional specific energy, while the shadow area indicates the fluctuations of z^* considering one standard deviation. The dashed red line depicts the probability of a 1 µm site being affected by more than one energy deposition event. Calculation was performed following the method described in [52].

from a comparative transcriptomic experiments already performed (still unpublished) in the framework of LNGS-RENOIR experiment [2], the modulation of IRR will also be analyzed focusing on the pathways and factors analog to those found *in vitro* in the human counterpart [46]. New experiments will be carried out and a comprehensive real-time PCR analysis will be carried out on target genes. This approach will confirm and/or add new information at the whole organism scale.

DISCOVER 22-the microdosimetric approach

Traditional dosimetry primarily focuses on measuring the absorbed dose, which represents the total energy deposited in a given mass of tissue and is a macroscopic quantity. However, the biological effects of radiation are not solely determined by the absorbed dose. The spatial distribution and nature of energy deposition within cells and their microenvironments also play a crucial role. LDR exposures often involve stochastic effects, where the probability of biological damage occurring increases with dose but individual events are random and unpredictable. It is crucial to consider that even with the same absorbed dose, the microscopic patterns of energy deposition can vary. In general, an inhomogeneous pattern resulting from densely IR is more effective in terms of biological impact than a homogeneous pattern caused by sparsely IR. This highlights the importance of understanding the spatial distribution and nature of energy deposition at the microscopic level in order to fully comprehend the biological effects of irradiation [4, 8, 47, 48]. In the context of the dose rate of 27 nSv/h at the underground LNGS ["*Sub-background radiation exposure at the LNGS underground laboratory: dosimetric characterization of the external and underground facilities*" in Research Topic: Science and Technology In Deep Underground Laboratories. *Frontiers in Physics* currently under revision process], microdosimetry emerges as a valuable approach for gaining insights into the radiation field [49]. Figure 2A shows a typical microdosimetric spectrum measured in the NBR field at Legnaro National Laboratories of INFN (INFN-LNL), utilizing a tissue equivalent proportional counter (TEPC) that simulates a 1 µm site. Measurements were performed inside the office building at INFN-LNL and the spectrum was calibrated on the electron-edge [50]. The lineal energy variable, y, is defined as the energy imparted to the target site divided by the mean chord length of the site. The probability density function, $d(y)$, signifies the likelihood that the absorbed dose results from events with a lineal energy ranging between y and $y + dy$. In Figure 2A's layout, which is commonly employed to illustrate microdosimetric spectra, equal visual areas correspond to equal contributions to the total absorbed dose. Figure 2B presents the corresponding stochastic distribution of the conditional specific energy, z^*, which represents the microdosimetric equivalent of absorbed dose, conditioned on the occurrence of at least one energy deposition event (sites that have at least one energy deposition event are called critical sites). At the extremely low dose levels relevant to this project (less than 10 µGy in 10 days), it is important to note that the likelihood of a critical subcellular structure being affected by an energy deposition event is extremely low, and the probability of more than one event is negligible. This makes microdosimetry a valuable approach for characterizing the radiation quality. From an experimental perspective, detecting events within a 1 µm diameter sphere poses a significant challenge due to the low dose rate, resulting in an expected count rate of only 5×10^{-7}/h. However, this challenge can be overcome by replacing the 1 µm of biological tissue with a larger volume of low-density tissue-equivalent gas, which substantially increases the counting rate. This technique is commonly employed in ionization chambers and TEPCs, and it greatly enhances the sensitivity of radiation detection. To enable continuous monitoring of fluctuations in the radiation field, encompassing both dose and microdosimetric quantities, we propose the construction and use of

a TEPC with a large sensitive volume. A diameter of 10 cm enables detection with an estimated count rate of 5,000 events per hour, resulting in 1.2×10^5 events detected in a single day. Thus, employing a 10 cm diameter TEPC allows for daily monitoring of both the dose and the microdosimetric spectrum with statistically significant data. The design and construction of the TEPC will be carried out leveraging the expertise and infrastructure available at INFN-LNL. Meanwhile, preliminary microdosimetric measurements will be carried out using a spherical TEPC with a segmented cathode, which has been previously developed at INFN-LNL [51]. The detector and data acquisition system will have local and remote-control capabilities, allowing real-time monitoring of the radiation field. Upon completion, the newly designed device will be installed in the underground laboratory of LNGS, enabling continuous monitoring of both dose and microdosimetric quantities in the radiation field.

DISCOVER 22-the biophysical model

Cell-cycle models are a valid tool to identify and quantify differences—if any—in the progression through the replicative cycle and, more in general, in the radiation response of cells grown in different background-radiation conditions [53, 54]. To this aim, we will reproduce with a deterministic compartmental model the cell-cycle progression of human keratinocytes, both for the BBR and NBR conditions. Experimental model inputs are cell-cycle time; FC data on cell percentages in G1, S, and G2/M phases. Model parameters represent transition rates between phases [55, 56]. The correlations between model parameters and microdosimetric quantities characterizing the radiation environment will be explored. The model will then be adapted to describe the cell-cycle perturbation for cells grown in BBR and NBR and exposed to the challenging 2 Gy X-ray dose, using FC data at different post-irradiation times (e.g., 6, 24, and 48 h). In the irradiated condition, the expected induction of DNA breaks per unit dose and the probability of their spatial proximity will be considered. Given the transition rate through mitosis of cells harboring lesions that can lead to incorrect segregation of the genomic material, the model will be developed to define the probabilities of: survival with Micronuclei (MN) formation; MN rupture activating the IRR via the cGAS-STING pathway. In such a way, it will be tuned to reproduce the experimental yield of radiation-induced MN, the expected fraction of micronucleated cells, and the observed fraction of cGAS-positive MN. Again, differences in the behaviour of BBR vs. NBR-grown cells, if any, will be quantified and interpreted based on model parameter values. One of the risk of URb studies is that changes in any cell behaviour, which can undoubtedly be attributed to the different background-radiation conditions, might be subtle, masked by biological variability or variation in the radiation environment, and therefore difficult to identify. To this aim, a good strategy is represented by the integration of datasets on different endpoints, resorting to data analysis techniques based on machine learning algorithms. In the project, all different data obtained with the *in vitro* HL60 cell model grown in BBR and NBR conditions (CD markers, ROS level, and cell-cycle data, etc.,) will be integrated and analysed through techniques based on data dimensionality reduction, such as PCA (*Principal Component Analysis*) or t-SNE (*t-distributed Stochastic Neighbor Embedding*) will be used (see, e.g., [57] for a more classical application to–omics dataset; [58] for PCA applied to identify changes in *in vitro* immune response to radiation). The new parametrizations of the dataset, obtained as linear/non-linear transformations of physical and biological parameters, would possibly be better suited to highlight changes between the two conditions.

Discussion and conclusion

Radiobiological experiments performed in DULs have been important to challenge the LNT model used in radiation protection, showing that the permanence below the environmental radiation increases the radiation response. To date, modulation of immunological responses to LDR represents an unexplored aspect in URb. The objective of the DISCOVER22 project is to dissect this topic by analyzing it at both cellular and organismal levels, gaining insights into radiation exposure-dependent immune response modulation. Specifically, we aim at providing *in vitro* data on the effect of the permanence of human cells in LRE in terms of the activation of the innate IS in response to radiation induced DNA damage, as well as the differentiation of immature into specialized immune cells. Furthermore, comparative gene expression analysis in flies grown in LRE and RRE will significantly contribute to a better understanding of the role of NRB in the modulation of IRR *in vivo*. A big challenge in LDR exposure is to perform direct microdosimetric measurements. The proposed TEPC, with its large site diameter, will enable daily assessment of both dose and microdosimetric spectrum with statistically significant data, enabling better characterisation of environmental radiation. By quantifying microdosimetric quantities, microdosimetry provides insights into the probability and nature of radiation interactions at the cellular and subcellular levels. This information is valuable for understanding the entity and the underlying mechanism (s) leading biological effects induced by LDR. Finally, the application of modelling will link physical and biological parameters, and allow to extract quantitative indicators to describe and interpret the response of the biological system, and the application of analysis techniques based on machine learning algorithms and data integration will help identify changes in such response that can be attributed to the different background radiation levels. We believe that the approach of the DISCOVER22 experiment represents a further step in URb to define both the priority aspect of microdosimetric characterisation of the radiation field in BBR environment and the understanding of the interactions between radiation and living matter at such ultra LDR in modulation of DNA damage and immune response.

Impact and possible implications of this study are mainfold: 1) providing information useful for the understanding of the relationship between radiation exposure and immune response also in view of possible implications in LDR therapy. 2) clarifying the influence of cosmic radiation on the IS, that may be also relevant for deep space exploration, pointing to possible immunosuppressive effects of shielding, such as in the case of habitation modules built in caves as proposed for Mars

colonization 3) obtaining clues to more fundamental topics, such as the adaptation of Life during the evolution of living organisms.

Data availability statement

The original contributions presented in the study are included in the article/Supplementary material, further inquiries can be directed to the corresponding author.

Author contributions

PM: Conceptualization, Methodology, Supervision, Visualization, Writing–original draft, Writing–review and editing. VD: Conceptualization, Methodology, Writing–original draft, Writing–review and editing, Visualization. FrB: Writing–review and editing. GB: Methodology, Writing–original draft, Writing–review and editing. VC: Methodology, Writing–original draft, Writing–review and editing, Visualization. IU: Writing–review and editing. FeB: Writing–review and editing. JM: Writing–review and editing. PA: Writing–review and editing. AA: Writing–review and editing. MT: Writing–review and editing. ASe: Writing–review and editing. SC: Writing–review and editing. AB: Writing–review and editing. IG: Writing–review and editing. LL: Writing–review and editing. ES: Writing–review and editing. ML: Writing–review and editing. MB: Writing–review and editing. FF: Writing–review and editing. DG: Writing–review and editing. AG: Writing–review and editing. MM: Writing–review and editing. VT: Writing–review and editing. FG: Writing–review and editing. MS: Writing–review and editing. ASg: Conceptualization, Funding acquisition, Methodology, Writing–original draft, Writing–review and editing, Visualization.

Funding

The author(s) declare financial support was received for the research, authorship, and/or publication of this article. This work is supported by INFN-CSN5 (DISCOVER22 Experiment 2023-2025) and by a grant from INFN- Laboratori Nazionali del Gran Sasso (C.A. 04.03.01.05.03.)

Acknowledgments

The Cosmic Silence Collaboration would like to thank LNGS and all technical Services for their skilled assistance and support for the experiment.

Conflict of interest

The authors declare that the research was conducted in the absence of any commercial or financial relationships that could be construed as a potential conflict of interest.

The author(s) declared that they were an editorial board member of Frontiers, at the time of submission. This had no impact on the peer review process and the final decision.

Publisher's note

References

1. Planel H, Soleilhavoup JP, Tizador R, Richoilley G, Conter A, Croute F, et al. Influence on cell proliferation of background radiation or exposure to very low, chronic γ radiation. *Health Phys* (1987) 52(5):571–8. doi:10.1097/00004032-198705000-00007

2. Esposito G, Anello P, Ampollini M, Bortolin E, De Angelis C, D'Imperio G, et al. Underground radiobiology: a perspective at gran Sasso national laboratory. *Front Public Health* (2020) 8:611146. doi:10.3389/fpubh.2020.611146

3. Liu J, Ma T, Liu Y, Zou J, Gao M, Zhang R, et al. History, advancements, and perspective of biological research in deep-underground laboratories: a brief review. *Environ Int* (2018) 120:207–14. doi:10.1016/j.envint.2018.07.031

4. Lampe N, Breton V, Sarramia D, Sime-Ngando T, Biron D. Understanding low radiation background biology through controlled evolution experiments. *Evol Appl* (2017) 10:658–66. doi:10.1111/eva.12491

5. Kennedy KJ, LeBlanc A, Pirkkanen J, Thome C, Tai TC, LeClair R, et al. Dosimetric characterisation of a sub-natural background radiation environment for radiobiology investigations. *Radiat Prot Dosimetry* (2021) 195(2):114–23. doi:10.1093/rpd/ncab120

6. Wadsworth J, Cockell CS, Murphy AS, Nilima A, Paling S, Meehan E, et al. There's plenty of room at the bottom: low radiation as a biological extreme. *Front Astron Sp Sci* (2020) 7. doi:10.3389/fspas.2020.00050

7. Pérez-Pérez J, Amare JC, Bandac IC, Bayo A, Borjabad-Sanchez S, Calvo-Mozota JM, et al. Radon mitigation applications at the Laboratorio Subterráneo de Canfranc (LSC). *Universe* (2022) 8:112. doi:10.3390/universe8020112

8. Lampe N, Biron DG, Brown JMC, Incerti S, Marin P, Maigne L, et al. Simulating the impact of the natural radiation background on bacterial systems: implications for very low radiation biological experiments. *PLoS ONE* (2016) 11(11):e0166364. doi:10.1371/journal.pone.0166364

9. Van Voorhies WA, Castillo HA, Smith GB. Thawng CN and Smith GB *The phenotypic and transcriptomic responseof the caenorhabditis elegans nematode to background and below-background radiation levels*. *Front Public Health* (2020) 8:1–12. doi:10.3389/fpubh.2020.581796

10. Satta L, Antonelli F, Belli M, Sapora O, Simone G, Sorrentino E, et al. Influence of a low background radiation environment on biochemical and biological responses in V79 cells. *Radiat Environ Biophys* (2002) 41:217–24. doi:10.1007/s00411-002-0159-2

11. Carbone MC, Pinto M, Antonelli F, Amicarelli F, Balata M, Belli M, et al. The Cosmic Silence experiment: on the putative adaptive role of environmental ionizing radiation. *Radiat Environ Biophys* (2009) 48:189–96. doi:10.1007/s00411-008-0208-6

12. Fratini E, Carbone C, Capece D, Esposito G, Simone G, Tabocchini MA, et al. Low-radiation environment affects the development of protection mechanisms in V79 cells. *Radiat Environ Biophys* (2015) 54:183–94. doi:10.1007/s00411-015-0587-4

13. Morciano P, Iorio R, Iovino D, Cipressa F, Esposito G, Porrazzo A, et al. Effects of reduced natural background radiation on *Drosophila melanogaster* growth and development as revealed by the FLYINGLOW program. *J Cel Physiol.* (2018) 233:23–9. doi:10.1002/jcp.25889

14. Fischietti M, Fratini E, Verzella D, Vecchiotti D, Capece D, Di Francesco B, et al. *Low radiation environment Switches the overgrowth-induced cell apoptosis toward autophagy*. *Front Public Health* (2021) 8:594789. doi:10.3389/fpubh.2020.594789

15. Zarubin M, Gangapshev A, Gavriljuk Y, Kazalov V, Kravchenko E. First transcriptome profiling of *D. melanogaster* after development in a deep underground low radiation background laboratory. *PLoS ONE* (2021) 16:e0255066. doi:10.1371/journal.pone.0255066

16. Castillo H, Smith GB. Below-background ionizing radiation as an environmental cue for bacteria. *Front.Microbiol.* (2017) 8:1–7. doi:10.3389/fmicb.2017.00177

17. Pirkkanen J, Lalonde C, Lapointe M, Laframboise T, Mendonca MS, Boreham DR, et al. The REPAIR project, a deep-underground radiobiology experiment investigating

the biological effects of natural background radiation: the first 6 years. *Radiat Res* (2023) 199(3):290–3. doi:10.1667/RADE-22-00193.1

18. Morciano P, Cipressa F, Porrazzo A, Esposito G, Tabocchini MA, Cenci G. Fruit flies provide new insights in low radiation background biology at the INFN underground Gran Sasso National Laboratory (LNGS). *Radiat Res* (2018) 190: 217–25. doi:10.1667/RR15083.1

19. Kreuzer M, Auvinen A, Cardis E, Durante M, Harms-Ringdahl M, Jourdain JR, et al. Multidisciplinary European Low Dose Initiative (MELODI): strategic research agenda for low dose radiation risk research. *Radiat Environ Biophys* (2018) 57:5–15. doi:10.1007/s00411-017-0726-1

20. Feinendegen LE, Pollycove M, Neumann RD. Hormesis by low dose radiation effects: low-dose cancer risk modeling must recognize up-regulation of protection. In: Baum RP, editor. *Therapeutic nuclear medicine*. Berlin: Springer (2013). p. 789–805.

21. Scott BR. Radiation-hormesis phenotypes, the related mechanisms and implications for disease prevention and therapy. *J Cel Commun Signal* (2014) 8: 341–52. doi:10.1007/s12079-014-0250-x

22. Bauer G. Low dose radiation and intercellular induction of apoptosis: potential implications for the control of oncogenesis. *Int J Radiat Biol* (2007) 83:873–88. doi:10.1080/09553000701727523

23. Lumniczky K, Impens N, Armengol G, Candéias S, Georgakilas AG, Hornhardt S, et al. Low dose ionizing radiation effects on the immune system. *Environ Int* (2021) 149: 106212. doi:10.1016/j.envint.2020.106212

24. Anderson RE, Lefkovits I. *In vitro* evaluation of radiation-induced augmentation of the immune response. *Am J Pathol* (1979) 97:456–72.

25. Kojima S, Nakayama K, Ishida H. Low-dose γ-rays activate immune functions via induction of glutathione and delay tumor growth. *J Radiat Res* (2004) 45:33–9. doi:10.1269/jrr.45.33

26. Liu S, Jin S, Liu X, Sun Y. Role of CD28/B7 costimulation and IL-12/IL-10 interaction in the radiation-induced immune changes. *BMC Immunol* (2001) 2:8. doi:10.1186/1471-2172-2-8

27. Little MP, Tawn EJ, Tzoulaki I, Wakeford R, Hildebrandt G, Paris F, et al. A systematic review of epidemiological associations between low and moderate doses of ionizing radiation and late cardiovascular effects, and their possible mechanisms. *Radiat Res* (2008) 169:99–109. doi:10.1667/RR1070.1

28. Averbeck D, Salomaa S, Bouffler S, Ottolenghi A, Smyth V, Sabatier L. Progress in low dose health risk research: novel effects and new concepts in low dose radiobiology. *Mutat Res* (2018) 776:46–69. doi:10.1016/j.mrrev.2018.04.001

29. Schröder S, Juerß D, Kriesen S, Manda K, Hildebrandt G. Immunomodulatory properties of low-dose ionizing radiation on human endothelial cells. *Int J Radiat Biol* (2019) 95:23–32. doi:10.1080/09553002.2018.1486515

30. Erdal E, Haider S, Rehwinkel J, Harris AL, McHugh PJ. A prosurvival DNA damage-induced cytoplasmic interferon response is mediated by end resection factors and is limited by Trex1. *Genes Dev* (2017) 31(4):353–69. doi:10.1101/gad.289769.116

31. Sun L, Wu J, Du F, Chen X, Chen ZJ. Cyclic GMP-AMP synthase is a cytosolic DNA sensor that activates the type I interferon pathway. *Science* (2013) 339(6121): 786–91. doi:10.1126/science.1232458

32. Ishikawa H, Barber GN. STING is an endoplasmic reticulum adaptor that facilitates innate immune signalling. *Nature* (2008) 455(7213):674–8. doi:10.1038/nature07317

33. Tanaka Y, Chen ZJ. STING specifies IRF3 phosphorylation by TBK1 in the cytosolic DNA signaling pathway. *Sci Signal* (2012) 5(214):ra20. doi:10.1126/scisignal.2002521

34. Chun SH, Park G, Han YK, Kim SD, Kim JS, Lee CG, et al. Effect of low dose radiation on differentiation of bone marrow cells into dendritic cells. *Dose Response* (2012) 11:374–84. doi:10.2203/dose-response.12-041.Lee

35. Collins SJ, Gallo RC, Gallagher RE. Continuous growth and differentiation of human myeloid leukaemic cells in suspension culture. *Nature* (1977) 270:347–9. doi:10.1038/270347a0

36. Collins SJ. The HL-60 promyelocytic leukemia cell line: proliferation, differentiation, and cellular oncogene expression. *Blood* (1987) 70:1233–44.

37. Collins SJ, Ruscetti FW, Gallagher RE, Gallo RC. Terminal differentiation of human promyelocytic leukemia cells induced by dimethyl sulfoxide and other polar compounds. *Proc Natl Acad Sci USA* (1978) 75:2458–62. doi:10.1073/pnas.75.5.2458

38. Rovera G, Santoli D, Damsky C. Human promyelocytic leukemia cells in culture differentiate into macrophage-like cells when treated with a phorbol diester. *Proc Natl Acad Sci USA* (1979) 76:2779–83. doi:10.1073/pnas.76.6.2779

39. Barber N, Gez S, Belov L, Mulligan SP, Woolfson A, Christopherson RI. Profiling CD antigens on leukaemias with an antibody microarray. *FEBS Lett* (2009) 583: 1785–91. doi:10.1016/j.febslet.2009.03.018

40. Choi HS, Kim JW, Cha YN, Kim C. A quantitative nitroblue tetrazolium assay for determining intracellular superoxide anion production in phagocytic cells. *J Immunoassay Immunochem* (2006) 27(1):31–44. doi:10.1080/15321810500403722

41. Kolaczkowska E, Kubes P. Neutrophil recruitment and function in health and inflammation. *Nat Rev Immunol* (2013) 13:159–75. doi:10.1038/nri3399

42. Guo Y, Gao F, Wang Q, Wang K, Pan S, Pan Z, et al. Differentiation of HL-60 cells in serum-free hematopoietic cell media enhances the production of neutrophil extracellular traps. *Exp Ther Med* (2021) 21:353. doi:10.3892/etm.2021.9784

43. Dhankhar J, Agrawal N, Shrivastava A. An interplay between immune response and neurodegenerative disease progression: an assessment using Drosophila as a model. *J Neuroimmunol* (2020) 346:577302. doi:10.1016/j.jneuroim.2020.577302

44. Yu S, Luo F, Xu Y, Zhang Y, Jin LH. Drosophila innate immunity involves multiple signaling pathways and coordinated communication between different tissues. *Front Immunol* (2022) 13:905370. doi:10.3389/fimmu.2022.905370

45. Porrazzo A, Esposito G, Grifoni D, Cenci G, Morciano P, Tabocchini MA. Reduced environmental dose rates are responsible for the increased susceptibility to radiation-induced DNA damage in larval neuroblasts of Drosophila grown inside the LNGS underground laboratory. *Int J Mol Sci* (2022) 23:5472. doi:10.3390/ijms23105472

46. Cai H, Meignin C, Imler JL. cGAS-like receptor-mediated immunity: the insect perspective. *Curr Opin Immunol* (2022) 74:183–9. doi:10.1016/j.coi.2022.01.005

47. Baiocco G, Bartzsch S, Conte V, Friedrich T, Jakob B, Tartas A, et al. A matter of space: how the spatial heterogeneity in energy deposition determines the biological outcome of radiation exposure. *Radiat Environ Biophys* (2022) 61:545–59. doi:10.1007/s00411-022-00989-z

48. Jonathan IK. Comment on Castillo et al. (2015). *Int J Radiat Biol* (2015) 92(3): 169–70. doi:10.3109/09553002.2016.1135265

49. ICRU Microdosimetry. *International commission on radiation units and measurements*. Bethesda, MD: ICRU Report (1983).

50. Moro D, Chiriotti S, Conte V, Colautti P, Grosswendt B. Lineal energy calibration of a spherical TEPC. *Radiat Prot Dosim* (2015) 166(1-4):233–7. doi:10.1093/rpd/ncv153

51. Moro D, Chiriotti S. EuTEPC: measurements in gamma and neutron fields. *Radiat Prot Dosimetry* (2015) 166(1-4):266–70. doi:10.1093/rpd/ncv154

52. Booz J. Mapping of fast neutron radiation quality. In: Burger G, Ebert HG, editors. *Proceedings of the third symposium on neutron dosimetry in biology and medicine, report No. EUR 5848*. Luxembourg: Commission of the European Communities (1978).

53. Tyson JJ, Novák B. Models in biology: lessons from modeling regulation of the eukaryotic cell cycle. *BMC Biol* (2015) 13:46. doi:10.1186/s12915-015-0158-9

54. Seaton DD, Krishnan J. Model-based analysis of cell cycle responses to dynamically changing environments. *Plos Comput Biol* (2016) 12(1):e1004604. doi:10.1371/journal.pcbi.1004604

55. Basse B, Baguley BC, Marshall ES, Joseph WR, van Brunt B, Wake G, et al. A mathematical model for analysis of the cell cycle in cell lines derived from human tumors. *J Math Biol* (2003) 47(4):295–312. doi:10.1007/s00285-003-0203-0

56. Lonati L, Barbieri S, Guardamagna I, Ottolenghi A, Baiocco G. Radiation-induced cell cycle pertURbations: a computational tool validated with flow-cytometry data. *Sci Rep* (2021) 11(1):925. doi:10.1038/s41598-020-79934-3

57. Yao F, Coquery J, Lê Cao KA. Independent Principal Component Analysis for biologically meaningful dimension reduction of large biological data sets. *BMC Bioinformatics* (2012) 13:24. doi:10.1186/1471-2105-13-24

58. Borsci G, Barbieri S, Guardamagna I, Lonati L, Ottolenghi A, Ivaldi GB, et al. Immunophenotyping reveals No significant perturbation to PBMC subsets when Co-cultured with colorectal adenocarcinoma caco-2 cells exposed to X-rays. *Front Immunol* (2020) 11:1077. doi:10.3389/fimmu.2020.01077

frontiers | Frontiers in Physics

TYPE Original Research
PUBLISHED 28 November 2023
DOI 10.3389/fphy.2023.1274110

OPEN ACCESS

EDITED BY
Sean M. Paling,
Science and Technologies Facilities Council, United Kingdom

REVIEWED BY
Stanislav Pospíšil,
Czech Technical University in Prague, Czechia
Canel Eke,
Akdeniz University, Türkiye

*CORRESPONDENCE
Giuseppe Esposito,
giuseppe.esposito@iss.it

RECEIVED 07 August 2023
ACCEPTED 10 November 2023
PUBLISHED 28 November 2023

CITATION
Ampollini M, Anello P, Balata M, Bortolin E, Chiarelli F, Chiti D, Chiti M, De Angelis C, D'Imperio G, Donghia R, Esposito G, Ferella F, Galante A, Laubenstein M, Morciano P, Nisi S, Nuccetelli C, Quattrini MC, Tabocchini MA and Tomei C (2023), Sub-background radiation exposure at the LNGS underground laboratory: dosimetric characterization of the external and underground facilities. *Front. Phys.* 11:1274110. doi: 10.3389/fphy.2023.1274110

Sub-background radiation exposure at the LNGS underground laboratory: dosimetric characterization of the external and underground facilities

Marco Ampollini[1], Pasqualino Anello[1,2], Marco Balata[3], Emanuela Bortolin[1], Federico Chiarelli[4], Daniele Chiti[4], Maurizio Chiti[4], Cinzia De Angelis[1], Giulia D'Imperio[2], Raffaella Donghia[4], Giuseppe Esposito[1,2]*, Francesco Ferella[3], Angelo Galante[3,5,6], Matthias Laubenstein[3], Patrizia Morciano[3,5], Stefano Nisi[3], Cristina Nuccetelli[1], Maria Cristina Quattrini[1], Maria Antonella Tabocchini[2] and Claudia Tomei[2]

[1]Istituto Superiore di Sanità (ISS), Rome, Italy, [2]Istituto Nazionale di Fisica Nucleare (INFN) Sezione Roma 1, Rome, Italy, [3]Laboratori Nazionali del Gran Sasso (INFN), L'Aquila, Italy, [4]Laboratori Nazionali di Frascati (INFN), Frascati, Italy, [5]Dipartimento di Medicina Clinica, Sanità Pubblica, Scienze della Vita e Dell'Ambiente, Università Dell'Aquila, L'Aquila, Italy, [6]Consiglio Nazionale delle Ricerche—SuPerconducting and other INnovative materials and devices institute, Università Dell'Aquila, L'Aquila, Italy

Radiobiological studies conducted in Deep Underground Laboratories allow to improve the knowledge of the biological effects induced by ionizing radiation at low doses/dose rates. At the Gran Sasso National Laboratory of the Italian Institute of Nuclear Physics we can study the possible differences in behavior between parallel biological systems, one maintained in a Reference-Radiation Environment (RRE, external) and the other maintained in an extremely Low-Radiation Environment (LRE, underground), in the absence of pressure changes, the RRE and LRE laboratories being at the same altitude. For these investigations, it is mandatory to evaluate the dose rate values at RRE and LRE. The aim of our work is to provide a comprehensive dosimetric analysis for external and underground laboratories. Measurements of the different low Linear Energy Transfer (LET) components at RRE and LRE were performed using different detectors. Gamma dose rates were 31 nSv/h at RRE and 27 nSv/h at LRE respectively. The muon dose rate was 47 nSv/h at RRE and negligible at LRE (less than pGy/h). Dosimetric measurements were also carried out to characterize the devices used to modulate the gamma dose rate, namely, a gamma source irradiator (to increase the dose rate by about 90 nSv/h) and shields (of iron at LRE and lead at RRE). Using the iron shield at LRE a dose reduction factor of about 20, compared to the RRE, was obtained for the low LET components; inside the lead shield at RRE the gamma component was negligible compared to the muonic component. Radon activity concentrations were approximately of 20 Bq/m^3 at both LRE and RRE. The intrinsic contribution of radioactivity in the experimental set up was of 0.25 nGy/h, as evaluated with a GEANT4-simulation, using as input the measured activity

concentrations. GEANT4 simulations were also performed to calculate the neutron dose rate at RRE, yielding a value of 1.4 nGy/h, much larger than that at LRE (which is less than pGy/h). In conclusion, RRE and LRE are currently characterized and equipped to perform radiobiological studies aimed at understanding the involvement of the different low LET components in determining the response of biological systems.

KEYWORDS

low radiation environment, RENOIR, dosimetric characterization, LNGS underground laboratory, Monte Carlo simulation

1 Introduction

Radiobiological studies conducted in Deep Underground Laboratories (DULs) are very useful to answer questions about radiation protection, as they can improve substantially the knowledge of the biological effects induced by ionizing radiation at low doses/dose rates and contribute to better estimate the radiation risk for human health in that range of doses/dose rates, providing useful data for testing radiation health risk models [1]. The experimental approach in these studies is the following: maintain, for a certain amount of time, biological systems in parallel in a low radiation background and in the natural radiation background and then observe any differences in their behavior.

One of the first such studies conducted by Planel et al. in a cave in the Pyrenees, showed that growth of protozoa and cyanobacteria was reduced in the underground location [2]. Similarly, Satta et al. observed inhibition of yeast cell growth and increased mutation frequency, in experiments performed at the Gran Sasso National Laboratory (LNGS) [3]. The result on cell growth was confirmed by subsequent investigations carried out more recently at the Waste Isolation Pilot Plant (WIPP) [4, 5]. Presently, several studies, performed using *in vitro* cell systems and *in vivo* organisms, report different biological responses in the biological systems growing in Low-Radiation Environment (LRE) like an impaired stress response [6–8], reduced cellular defenses against spontaneous mutations [9], higher sensitivity to a challenging irradiation [10–12]. The results of these experiments suggest that the natural radiation background plays a "positive" role for biological systems, acting as a conditioning factor that maintains the efficiency of cellular responses. Surprisingly, this effect was observed even after a short time of permanence underground of the biological system [13].

In the "Radiation ENvirOnment triggers bIological Responses in flies" (RENOIR) experiment funded by the Italian Institute of Nuclear Physics (INFN), under the frame of the Cosmic Silence Collaboration, we aimed to obtain information about the involvement of the low Linear Energy Transfer (LET) components of the environmental radiation field on the biological response of the fruit fly *Drosophila melanogaster* [14].

Our Collaboration spent significant efforts trying to minimize all confounding factors that may affect qualitatively and quantitatively the experimental results. The underground LNGS facility, where the LRE laboratory is located, has a horizontal entrance so that there is no difference in terms of atmospheric pressure with respect to the aboveground RRE laboratory; since the RRE and RRE laboratories are very close to each other, the same operator is able to perform the experimental activities, minimizing differences in sample handling. Moreover, the incubators in which organisms are maintained are identical, to remove any other physical interference such as light and relative humidity. Finally, the culture media used in the experiments come from the same batch and are prepared in the same way [14].

A detailed characterization of the background radiation dose rates values at the RRE and LRE of LNGS is essential to elucidate the role of the different components of the environmental radiation field on the observed biological responses. The components of the radiation field at RRE and LRE laboratory are both low-LET components: gamma rays and cosmic rays (mainly muons), and high-LET components: neutrons and alpha particles from radon. The relative contribution of the same component is different at RRE with respect to LRE. In this paper, we focused on a dosimetric characterization of the low-LET components in both RRE and LRE laboratories and of the devices used for modulating of the gamma component. However, a characterization was also obtained for the neutron component, in terms of flux, and for the radon component in terms of gas concentration. Monte Carlo simulations, using GEANT4 code, were carried out to estimate the dose rate values from environmental neutrons, and from intrinsic radioactivity of the setup materials.

2 Materials and methods

2.1 Radiobiological experimental laboratories

Two different radiation environments are usually considered when performing radiobiological experiments, where the biological system can be maintained at controlled parameters of temperature, relative humidity, and 12 h light-dark alternation:

RRE–external laboratory of LNGS, located at Assergi (Italy) (about 1,000 m altitude), located on the ground floor of a concrete building; LRE–underground laboratory of LNGS, located under the Gran Sasso mountain (Italy) with 1,400 m of overhanging dolomitic rocks poor in uranium and thorium. LNGS offers an effective shielding from environmental radiation, reducing the flux of cosmic rays and neutrons by a factor of 10^6 and 10^3 with respect to that in the external environment, respectively [15, 16]. Due to this, the muon and neutron dose rate value at LRE is small compared to that of the other components of the radiation field and can be considered negligible for our purposes.

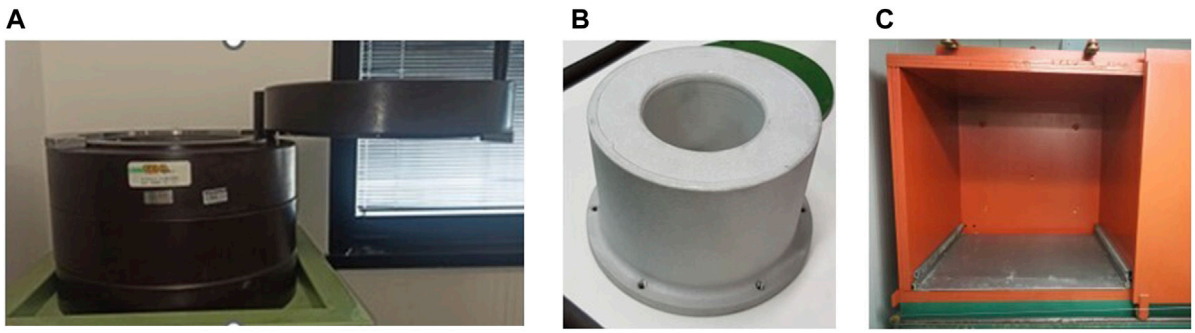

FIGURE 1
(A) Image of the lead shield in which the biological system can be housed. **(B)** Image of the aluminum Marinelli beaker. **(C)** Image of the 5-cm-thick iron shielding.

2.2 Devices for the radiation field modulation

In order to study the specific influence of the gamma component on the biological response, the gamma exposure can be modulated with shields or natural radioactive sources. A shield consisting of a 10 cm thick lead (Pb) hollow cylinder can be used at RRE to strongly reduce the gamma component (Figure 1A). The shield has been optimized for *Drosophila* growth and maintenance with a ventilation system and with a light source to ensure the day/night cycle. The room temperature, in which the lead shield is located, is maintained at the desired temperature level with an air conditioner and continuously monitored.

Moreover, the gamma component can be increased at LRE using a customized aluminum Marinelli beaker filled with natural gamma emitter building material (tuff) [14] and sealed to avoid any radon exposure (Figure 1B). The size of the Marinelli allows it to be kept inside the cooled *Drosophila* incubator.

Finally, the gamma component can be also reduced at LRE using a 5-cm-thick iron shielding, 970 mm high, 970 mm wide and 970 mm deep (Figure 1C).

2.3 Dosimetric characterization of low-LET components at RRE and LRE laboratories

Systematic measurements of radiation field inside both the laboratories were carried out using a 3" (7.62 cm × 7.62 cm, diameter x height) NaI(Tl) scintillator (crystal and Photomultiplier Tube (PMT) from Ortec, United States; Gammastream Multi Channel Analyzer (MCA) base from CAEN, Italy) in order to identify the most suitable location in which to keep the biological system. This detector, properly calibrated, gives a measure of the energy spectrum of the gamma (up to 3 MeV using a photomultiplier voltage of 800 V) interacting with the detector. The energy calibration was performed at the beginning of each measurement day using well detected peaks from a ^{232}Th rich source and the energy-channel curve was fitted with a quadratic function. The dose rate of gamma rays in the NaI(Tl) crystal was determined by calculating the total energy released into the NaI(Tl) crystal from the integral of the full detected spectrum, and by dividing this total energy by the mass of the crystal and by the active acquisition time.

Once identified the appropriate position, environmental dosimetric measurements were carried out using the following detectors.

2.3.1 TLD-700H

The thermoluminescent dosimeters, TLD-700H, (3.2 × 3.2 mm^2 surface and 0.89 mm thickness, Thermo Fisher Scientific, United States) were characterized by a high gamma sensitivity and signal stability [17, 18]. They were calibrated at National Laboratory of Frascati (LNF) of the INFN with a ^{137}Cs source (dose rate: 1,455.22 μGy/h) in terms of air-kerma in the range (5–350) μGy. For each dose point five TLD were simultaneously irradiated. An individual sensitivity factor was calculated for each dosimeter as the ratio of the batch average value and the individual value of the TL response. The TLD signal was corrected for individual factors, background of the TLD reader and the signal cumulated in the trip for their positioning and return in the ISS laboratory for their measurement. The air-kerma value was converted into ambient dose equivalent, H*(10), using the coefficient, H*(10)/ka, of 1.21 [19]. Sets of 5 TLDs were housed in vials similar to those used to keep *Drosophila*; the dosimeters were put at about 2 cm from the bottom corresponding to the surface of the feed layer. Measurements were done keeping the TLDs *in situ* for periods of about 4 weeks and of about 3.5 months (the latter is a proper time period in which no fading effects are expected). TLD-700H show a relative response to ^{137}Cs better than 0.98 in the range (0.016–1) MeV.

2.3.2 NaI(Tl) Canberra InSpector 1000™

This is a portable 2″ spectrometer (Mirion Technologies Inc., United States) that is capable of measuring dose-rate with an internal Geiger-Mueller (GM) detector (for high dose/count rate measurements) as well as calculating dose-rate, performing nuclide identification and activity measurements with an external NaI(Tl) gamma scintillation detector probe for gamma up to 3 MeV (dimension of 5.08 cm × 5.08 cm). The InSpector 1000 uses the count rate data from the internal GM tube to determine whether the GM data or the NaI probe data will be used for data display. For each NaI probe, two threshold points are used to implement switching

hysteresis. Hysteresys stabilizes the dose reading by preventing erratic swithching from one detector to the other. When a falling count rate passes the "Low threshold", the InSpector 1000 begins displaying the NaI probe's count rate data. When a rising count rate passes the High Threshold, the InSpector 1000 begins displaying the GM tube's count rate data. Considering our experiment conditions with dose rates below the level of μSv/h, the "high threshold" for passing from NaI to GM has not been overcome and the InSpector 1000 has been used to provide measurements of the gamma ambient dose equivalent, H*(10), from NaI data.

2.3.3 Automess-Scintillator Probe 6150 AD-b

This detector consists of a calibratable Scintillator Probe (Automess - Automation und Messtechnik GmbH, GER) which, in conjunction with a GM dose rate meter, can be used to measure photon radiation (gamma and X-rays) in the operational quantity ambient dose equivalent H*(10). A cylindrical 7.62 cm × 7.62 cm organic scintillator serves as the radiation detector. The energy range of the instrument with (without) its protective cover is 38 keV–7 MeV (20 keV–7 MeV).

The detectors described in sections 2.3.2 and 2.3.3 were used as independent detection systems with a standard methodology of measured data evaluation supplied by the manufacturers.

2.3.4 Reuter Stokes- RSS-112

This detector consists of a 7.9-L high pressurized ionizing Chamber (Reuter Stokes, United States) that contains approximately 25 atm of ultrahigh purity argon and provides measurement of the ambient dose equivalent H*(10). It has a nearly flat energy response from 70 keV to 10 MeV (±5% accuracy at background) and an omni directional response.

The response of Automess and Reuter Stokes detectors was calibrated at the beginning of the measurement campaigns at secondary standard certified laboratory with Am-241 (60 keV), Cs-137 (662 keV) and Co-60 (1,250 keV) sources. The calibration of the InSpector 1000 was provided by the manufacturer and the response goodness of this detector has then been compared with respect to that of Automess and Reuter Stokes detectors.

2.4 Neutron flux and radon measurements

Neutrons are produced in the interaction of cosmic rays with our atmosphere and for this reason they are present in above-ground experimental locations, with a flux that extends from thermal energies (meV - eV) to GeV, and an intensity that varies with altitude, geomagnetic field, and solar magnetic activity [20]. In underground sites such as LNGS, low energy neutrons (below 10 MeV) are produced by spontaneous fission and (α, n) reactions, while fast neutrons are produced by nuclear reactions induced by residual cosmic ray muons in the rock.

To perform measurement of neutron flux in the energy range 0–20 MeV, a portable detection system, called "Direction-aware Isotropic and Active neutron MONitor" DIAMON spectrometer (RAYLAB, ITA), was used. It allows a real-time measurement of the neutron flux from thermal energies to 20 MeV and with a sensitivity of the order of 10^{-3} n/cm^2/s, which is well suited for our purposes concerning the above ground laboratory. The principle of operation of the DIAMON spectrometer is similar to the one of the Bonner Sphere, that is a device that measures the energy of a neutron via a neutron detector embedded in a layer of moderating material. DIAMON contains a matrix of semiconductor-based thermal neutron sensors which are positioned at different depths inside the moderator body (made of high-density polyethylene). In this way, each detector sees a different layer of moderating material and is sensitive to a different neutron energy. The detailed internal design of the DIAMON spectrometer is protected by a patent. The counts registered by the neutron sensors are then processed by an unfolding software, that reconstructs the neutron flux in energy and direction [21].

A contribution to the environmental dose/dose rate also comes from the radon (^{222}Rn) and its daughters' decay products. This contribution depends on the radon concentration, which should be reduced inside the underground laboratory. A ventilation system provides air change inside the underground facilities keeping the overpressure of the laboratory as regards the motorway tunnel. This system collects air from the underground environment and expels it outdoors (at a rate of 35,000 m^3 of air per hour) to prevent the accumulation of ^{222}Rn activity indoors. Air is supplied to the underground laboratories by two ventilation stations: Teramo Station: duct characteristics length: 4.3 km, material: steel, diameter: 1.5 m. L'Aquila Station: duct characteristics length: 6.5 km, material: stainless steel, diameter: 1.5 m. The two stations can operate combined or separately in case of failure of one of them. Moreover, at LRE laboratory, an additional local ventilation system increases the exchange air flow rate in underground in order to keep radon concentrations as constant as possible. Radon concentration in the air at LRE and RRE laboratories, along with temperature, pressure and relative humidity was continuously monitored, using a radon meter (AlphaGUARD P30, Saphymo Instruments GmbH, Montigny-le-Bretonneux, France). Since the access door to the RRE and LRE incubators is routinely opened, it was assumed that the radon concentrations within the incubators matched the laboratory air concentration.

2.5 Intrinsic radioactivity in experimental setup

The evaluation of the intrinsic ionizing radiation contribution from the experimental setup, namely, polypropylene vials, acetate cellulose plugs, fly culture medium (food) and *Drosophilae*, was carried out using the two techniques: Inductively Coupled Plasma Mass Spectrometry (ICP-MS) and gamma-ray spectrometry using high purity germanium detector (HPGe).

2.5.1 ICP-MS analysis

2.5.1.1 Instruments

Chemicals used in samples preparation were HNO_3 ultra-pure grade (VWR Chemicals, Canada), obtained through sub-boiling system (DuoPur, Milestone, Italy), and H_2O ultra-pure (resistivity 18.2 MΩ/cm at 25°C) obtained from a Milli-Q apparatus (Millipore Corporation, Billerica, MA, United States). A closed-vessel microwave system (Ethos UP, Milestone, Sorisole, Italy) equipped with fiber-optic temperature sensor was used for performing

digestions, instrument was equipped with a rotor with 6 politetrafluoroetilene (PTFE) vials with volume of 100 mL. All measurements were performed by mean Sector Field High Resolution Inductively Plasma Mass Spectrometer (Element II, Thermo Fisher Scientific, United States) with an ASX520 autosampler from Cetac (Omaha, NE, United States).

2.5.1.2 Experimental procedures

Microwave assisted digestion was carried out to perform analysis of fly food. This choice was made as it proved to be very effective for complete mineralization of samples; an amount of 500 mg was used to process digestion, specific method has been fine-tuned to this procedure. Ramp start for 15 min at 1,800 W to reach 200°C, which have been kept constant for other 15 min, then they gradually decrease to perform cooling down. Procedure made use of HNO_3 UP and H_2O_2 30% in ratio 4/1 up to 25 mL with an amount of sample about 500 mg. Regarding mineralization of vials and caps, 3 g and 1.5 g respectively were incinerated in muffle at 650°C for 4 h, crucibles used were previously rinsed with 10 mL of 10% UP HNO_3 and they have been measured before each treatment. One portion of each sample was used to estimated K, Th, U, recovery efficiency adding a known amount (100 ppt Th U and 1,000 ppb K) of reference solution. Flies were treated in hotplate to obtain complete solubilization, during first cycle 1 mL of HNO_3 UP and 100 µl of H_2O_2 30% were used at 120°C for 1 h, then 8 mL of H_2O UP was added to dissolve total amount of sample; subsequently 1 mL of HNO_3 UP and 4 mL of H_2O UP were used in two different moments to washing vials and to recover sample's trace still inside vials.

2.5.2 HPGe spectrometry

Empty polypropylene vials (20 pieces, total mass 130.5 g), cellulose acetate plugs (27 pieces, total mass 40.9 g) and food (total mass 218.09 g) were first measured separately and then all together in vials prepared to host the flies (n. 12 vials, total mass 180.6 g). No special sample treatment was required, as we wanted to assess the background coming from these parts as they are used in the real experiment. The measurements were carried out in the low background counting laboratory "SubTErranean Low Level Assay" STELLA of LNGS [22]. Different detectors were used to assess the samples, all of them being p-type, semi-coaxial HPGe detectors, built in ultra-low background (ULB) configuration, i.e., with especially selected radio-pure materials, surrounded by a large lead/copper shielding, designed to reduce the ambient gamma-ray background by several orders of magnitude. The lead used in these shielding set-ups was selected with respect to its low intrinsic content of ^{210}Pb minimizing its contribution through Bremsstrahlung to the intrinsic background of the detector. Therefore, the innermost part of the set-up is also made of high purity copper. Moreover, the set-ups are enclosed in thick, airtight plastic boxes, continuously flushed with highly pure nitrogen gas to avoid any influence from radon gas present in the environment. The nitrogen gas is produced through boil-off from liquid nitrogen. The quality of the liquid nitrogen is 5.0 (i.e. 99.999% purity). Measurements performed on this boil-off nitrogen confirmed that it contains less than 50 µBq/m^3 of radon. Data analysis was carried out searching for the relevant peaks in the spectra for the radionuclides of interest (natural radioactivity from ^{238}U, ^{235}U, ^{232}Th and ^{40}K, as well as possible presence of man-made radioactivity, i.e., mainly ^{137}Cs, and cosmogenic activity, i.e., mainly ^{7}Be). The efficiencies for the full energy peaks were determined through Monte Carlo simulations using well-tested computer codes. This is a commonly used method in case of complex geometries as were vials and plugs.

2.6 GEANT4 simulations

To simulate the dose rate absorbed by the biological system from neutrons, a GEANT4-based Monte Carlo simulation code was developed. The same code was also used to evaluate the dose rate in water inside the vial for *Drosophila*, due to the radioactive contamination of the different components of the experimental setup (plug, vial, medium), taking as input the measured activities. The simulation code implements the dimensions and materials of the experimental setup, namely, the standard vials that contain the *Drosophilae*, the lead shielding and the Marinelli beaker described above. The dimensions of the standard vials are as follows: height = 95 mm, external diameter = 23 mm, internal diameter = 22 mm, bottom thickness = 1 mm. The vials are filled with water up to 20 mm and with air for the remaining volume. Particles were generated according to their respective energy spectra and propagated inside the simulated setup. The energy deposits were registered in a water cube placed at the center of the vial, with a volume of 1 cm^3 (scoring volume), that was used for the calculation of the dose. To study in more detail the distribution of the dose within the scoring volume, the volume of the water cube was divided into voxels of x = 10 mm, y = 2 mm and z = 2 mm. For each voxel, the corresponding energy deposits were added and divided by 5 to calculate the energy released in an isotropic 2 × 2 × 2 mm^3 voxel. Then the total energy deposited was transformed into dose rate dividing by the mass of the voxel and by the time corresponding to the measurement (calculated from the number of simulated events).

3 Results

3.1 Measurements

In the RENOIR experiment, measurements of the dose rate due to gamma rays and muons were performed at RRE laboratory, while at LRE laboratory only measurements of the dose rate due to the gamma component were carried out, since in this laboratory the muon dose rate values are so small (below pSv/h, as evaluated by muon flux measurements already known in the literature) to be considered negligible for our purposes [15].

Regarding the high-LET components, only radon concentration measurements at LRE and RRE and neutron flux measurements at RRE were carried out. At LRE, the neutron component is so small (below pGy/h as evaluated by neutron flux measurements already known in the literature) to be considered negligible for our purposes [15]. Dose rate values inside the special devices (lead shield, Marinelli beaker) for the modulation of the gamma component were also measured. Finally, the specific activity (mBq/kg) of the setup materials of the experimental apparatus was measured.

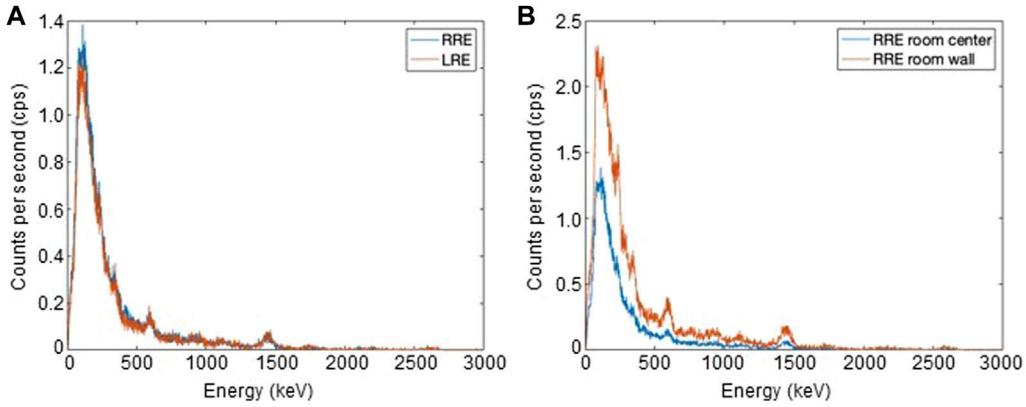

FIGURE 2
(A) Energy spectra measured at the center of RRE **(A)** and LRE **(B)** laboratories with acquisition times of 364 s and 304 s respectively. **(B)** Energy spectra measured at the center and near to the wall of RRE laboratory.

TABLE 1 Dose rate values expressed as absorbed dose rate by the NaI(Tl) crystal using the 7.62 cm × 7.62 cm NaI(Tl) scintillator for energy of gamma rays in the range (0–3) MeV. The errors represent the statistical and systematic uncertainties.

Measurement location	RRE laboratory (nGy/h)	LRE laboratory (nGy/h)
One-meter-high desk at the center of the laboratory	25.2 ± 2.5	23.6 ± 2.4
Inside the incubator at the center of the laboratory	25.3 ± 2.5	26.9 ± 2.7
One-meter-high desk near the walls of the laboratory	57.3 ± 5.7	
Floor at the center of the laboratory	33.5 ± 3.4	

TABLE 2 Ambient dose equivalent rate values at LRE and LRE laboratories obtained using different type of detectors. TLDs have been kept *in situ* for periods of about 3.5 months. The errors represent the statistical and systematic uncertainties.

	NaI(Tl) InSpector 1000 (nSv/h)	Automess (nSv/h)	TLD (nSv/h)	Reuter Stokes (nSv/h)
RRE laboratory	31.6 ± 2.5	55.0 ± 4.7	67.0 ± 1.8	78.3 ± 4.5
LRE laboratory	24.7 ± 2.2	26.8 ± 2.0	28.1 ± 2.2	28.0 ± 2.1

3.1.1 Dosimetric characterization of RRE and LRE laboratories

The spectra, measured at the center of the two laboratories RRE and LRE, placing the 3″ NaI(Tl) scintillator on a 1-m-high desk, are reported as an example in Figure 2A. The total number of counts was always such as to make the statistical error less than 1%. The dose rate values, expressed as absorbed dose rate by the NaI(Tl) crystal, obtained for the various measurement points are shown in Table 1. The dose values outside and inside the incubator were similar. Therefore, the incubator did not significantly perturb the radiation field in the two laboratories.

Regarding the RRE laboratory, the dose rate value measured near the walls was much higher than in the center of the laboratory. This was evidenced by comparing the spectra normalized for the acquisition time measured in the two positions of the RRE laboratory (Figure 2B). The spectrum acquired near the wall roughly showed a double events rate respect to the center of the laboratory and the value on the floor was approximately 50% higher than that on the 1-m-high desk. This is probably due to the presence of gamma emitters in cladding tiles of the walls and floor. Indeed, such ceramic tiles easily contain radioactive elements of the thorium or uranium family. Based on these measurements, the detectors used for the H*(10) rate measurements were placed on the 1-m-high desk at the center of the RRE laboratory to minimize the spatial dependence of dose on the distance from the tiles. These detectors were also placed on the 1-m-high desk at the center of the LRE laboratory. Table 2 shows the H*(10) rate values measured using all detectors available for RRE and LRE laboratories. The RRE laboratory is characterized by the presence of both gamma rays and muons. Each of these detectors measures the total dose rate due to both gamma rays and muons $[H^*(10)/t]_{mis} = [H^*(10)/t]_\gamma + [H^*(10)/t]_\mu$. Reuter Stokes accurately measures both $[H^*(10)/t]_\gamma$ and $[H^*(10)/t]_\mu$, while Automess and TLD-700H accurately measures $[H^*(10)/t]_\gamma$ but may underestimate $[H^*(10)/t]_\mu$ [23]. Moreover NaI(Tl) Canberra InSpector 1000 accurately measures $[H^*(10)/t]_\gamma$ but has a negligible muon detection efficiency, i. e., $[H^*(10)/t]_{mis} \approx (H^*(10)/t)_\gamma$ for this detector. A value of $[H^*(10)/t]_{mis} = [H^*(10)/t]_\gamma + [H^*(10)/t]_\mu$ = 78.3 ± 4.5 nSv/h was measured using the high

TABLE 3 Ambient dose equivalent rate values for gamma rays and muons obtained at LRE and LRE.

Source	RRE (nSv/h)	LRE (nSv/h)
Gamma-rays	31	27
Muons	47	<< 1
Total dose rate	**78**	**27**

The bold values indicate total dose rates.

pressurized ion chamber, Reuter Stokes, while values of $[H^*(10)/t]_{mis}$ equal to 55.0 ± 4.7 nSv/h and 67.0 ± 1.8 nSv/h were obtained using Automess and TLD-700H respectively. Finally, a value of $[H^*(10)/t]_{mis} \approx (H^*(10)/t)_\gamma = 31.6 \pm 2.5$ nSv/h was obtained using the NaI(Tl) Canberra InSpector 1000 (corresponding to the ambient dose equivalent rate value of the gamma rays component at RRE), The H*(10) rate values corresponding to the muon component can be obtained for Reuter Stokes, Automess and TLD detectors, by subtracting from their measured values, the value provided by the NaI(Tl) Canberra InSpector 1000 detector. The values obtained were 46.7 ± 5.1 nSv/h (for Reuter Stokes detector), 23.4 ± 5.3 nSv/h (for Automess detector) and 35.4 ± 3.1 nSv/h (for TLD-700H). The underestimation of the muon dose rate of Automess detector and TLD-700H with respect to Reuter Stokes detector, evaluated as percentage variation coefficient, was of 50% for Automess and of 24% for TLD. These results agree with the literature data mentioned by other authors [23, 24].

An additional measurement campaign was carried out using the Reuter Stokes detector exposed in a boat at Civitavecchia harbor, at a distance greater than 200 m from the pier/land and with a depth greater than 12 m to obtain an independent determination of the H*(10) rate value corresponding to the muon component. The result was 47 nSv/h, that is the muon dose rate value at sea level. This value must be corrected for the factor 1.28 due to the altitude of the LNGS RRE and, also, for the attenuation factor of the building where the RRE laboratory is located, equal to 0.8 (according to the UNSCEAR 2000 report Vol. I: Sources) [25]. Therefore, an H*(10) rate value corresponding to the muon component at RRE of 48.1 ± 5.6 nSv/h was obtained, in agreement with the 46.7 ± 5.1 nSv/h value mentioned above. The H*(10) rate value corresponding to the gamma rays component was determined by subtracting this value 48.1 nSv/h from the value 78.3 nSv/h measured using the Reuter Stokes at the RRE laboratory (gamma + muons); it was equal to 30.2 nSv/h, which is compatible with 31.6 nSv/h measured with the NaI(Tl) Canberra InSpector 1000 detector. An average of the values, determined with these two methods, was considered thus obtaining about 47 nSv/h for muons and about 31 nSv/h for gamma rays at RRE laboratory.

The situation is different at LRE laboratory where, since the muon flux value is reduced by a factor of 10^6, the muon dose rate value was assumed to be negligible respect to the external value and the only low-LET component of the radiation field is given by gamma rays. H*(10) rate values in the range 25–28 nSv/h were measured at LRE using all available detectors. The lowest value of about 25 nSv/h was obtained using the NaI(Tl) InSpector 1000 detector and the highest value of about 28 nSV/h was obtained using TLDs and Reuter Stokes detector. These values

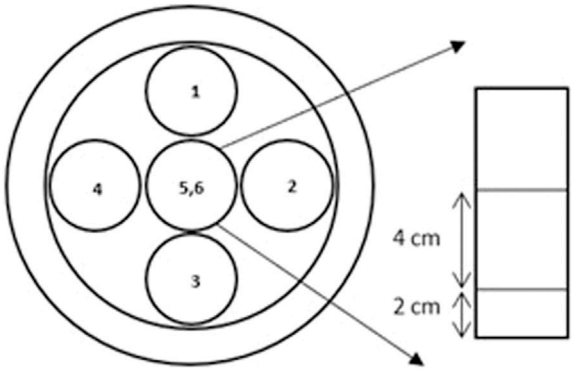

FIGURE 3
Arrangement of the vials containing TLDs inside the Marinelli beaker.

agree within the experimental uncertainty, as we expected, since the muon component is not present in this underground site. An average of these values was considered thus obtaining a value of about 27 nSv/h for gamma rays at LRE laboratory. The H*(10) rate mean values for gamma and muon components obtained at RRE and LRE laboratory, are summarized in Table 3. Therefore, a dose rate reduction of the low LET components (photons + muons) of about 3 can be obtained at LRE laboratory compared to RRE.

3.1.2 Dosimetric characterization of the devices for the radiation field modulation useable in radiobiological studies

The dosimetric characterization was also performed inside the devices used to modulate the low LET dose rate component, i.e., in the Marinelli beaker containing tuff, and inside the shielding consisting of a 10 cm thick lead hollow cylinder placed at RRE laboratory and a 5 cm thick iron parallelepiped placed at LRE laboratory. The dosimetric characterization of the lead shielding at RRE laboratory was performed using both the 7.62 cm × 7.62 cm NaI(Tl) scintillator and TLDs. The NaI(Tl) scintillator allows to measure the gamma dose rate reduction factor since this detector has a muon detection efficiency equal to zero. This factor was equal to about 16. In addition, sets of TLDs were placed inside the lead shielding for about 3.5 months to measure the total dose rate reduction factor of gamma and muons components together. This factor was equal to about 2, much lower than that measured with the NaI(Tl) scintillator since the muons are only slightly stopped by the Pb shielding. The dosimetric characterization of the iron shielding at LRE laboratory was performed using both the 7.62 cm × 7.62 cm NaI(Tl) scintillator and TLDs. The gamma dose rate reduction factor for the iron shielding was equal to about 6. Moreover, a dose rate reduction of the low LET components (photons + muons) of about 17 can be obtained inside the iron shield at LRE laboratory compared to the value at RRE laboratory.

The dosimetric characterization of the Marinelli beaker, was performed using TLDs at both RRE and LRE laboratories. The Marinelli beaker, containing about 2,800 g of tuff, was placed inside the lead shielding at RRE laboratory, to eliminate the ambient gamma component, and on the 1-m-high desk located at the

TABLE 4 Ambient dose equivalent rate values inside the Marinelli Beaker at LRE and LRE laboratories using TLDs. Dosimeters were kept *in situ* for periods of about 4 weeks. The errors represent the statistical and systematic uncertainties.

	Marinelli location	TLD location	(nSv/h)
RRE laboratory	Inside the lead shielding	Centre h = 2 cm	119.6 ± 6.0
		Centre h = 6 cm	120.9 ± 6.0
		Edge h = 2 cm	138.8 ± 6.9
LRE laboratory	On 1-m-high desk	Centre h = 2 cm	115.5 ± 5.8
		Centre h = 6 cm	120.0 ± 6.0
		Edge h = 2 cm	137.7 ± 6.9

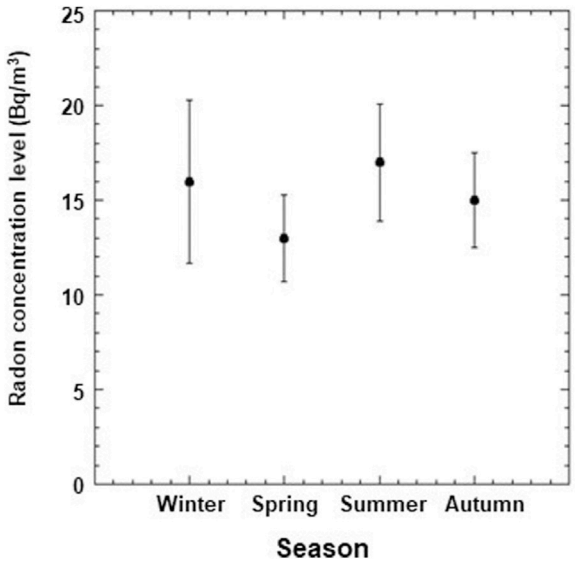

FIGURE 4
Seasonal variations of radon concentration levels at RRE Laboratory for the year 2020 only. Data points and error bars represent the mean values and the standard deviations from the means.

center of LRE laboratory. Sets of 5 TLDs were housed in five vials similar to those used for *Drosophila*. Figure 3 shows a sketch of the vials inside the Marinelli beaker (open circles in Figure 3). The dosimeters were put at about 2 cm from the bottom corresponding to the surface of the feed layer. To evaluate the dose rate distribution of the radiation field inside the Marinelli beaker, TLDs were placed at the same height from the base in five vials, four of them around and one in the center. Moreover, the vial placed at the centre of the Marinelli beaker was selected to house the TLDs at two different heights (5,6 in Figure 3) (2 cm and 6 cm respectively). Measurements were performed keeping TLDs *in situ* for periods of about 4 weeks. The results of these measurements are reported in Table 4. A small variation of the dose rate was evidenced at the center of the cylindrical hole of the Marinelli beaker for different heights. A mean value equal to about 120 nSv/h and 118 nSv/h was obtained at RRE and LRE laboratories respectively. Moreover, a higher dose rate value was found at the perimeter of the Marinelli internal hole (for the minimum height). The mean value of the

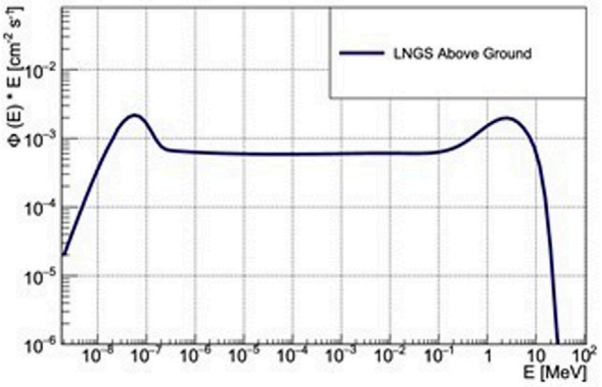

FIGURE 5
Neutron energy spectrum measured above-ground at the INFN-LNGS, inside the RENOIR RRE.

H*(10) rate into the cylindrical hole of the Marinelli beaker at the minimum height was about 129 nSv/h and 127 nSv/h at RRE and LRE laboratories respectively. The uniformity was such that the variations in the irradiated area are less than 16% (acceptable for most radiobiological experiments).

The dose rate value due only to the tuff was 89 nSv/h at RRE, calculated by subtracting the value obtained in the lead shielding without the Marinelli, 31 nSv/h, from the mean value at the center, 120 nSv/h. The estimate of dose rate due to the tuff alone at the LRE laboratory can also be derived by subtracting the value obtained using TLDs on the 1-m-high desk located at the center of the laboratory, 28 nSv/h, from the mean value at the center of the cylindrical hole of the Marinelli beaker, 118 nSv/h. In this case, a dose rate of 90 nSv/h was obtained, confirming the value found at RRE laboratory.

3.1.3 Radon

The average values of radon activity concentration in the air for LRE and RRE laboratories measured from March 2019 to July 2021 were 22 Bq/m^3 and 15 Bq/m^3 with standard deviations of 11 Bq/m^3 and 3 Bq/m^3 respectively. For the RRE laboratory, seasonal variations of radon concentration levels, measured during 2020 are shown in Figure 4. There were no seasonal variations of radon concentration observed in the LRE laboratory.

3.1.4 Neutron

The neutron flux was measured placing the DIAMON spectrometer on the 1-m-high desk located at the center of the RRE laboratory for about 40 h. A measured value of 0.018 neutrons/cm^{2}s^{-1} was obtained, with an average experimental data uncertainty of about 7%. The energy spectrum of neutrons at LRE can be seen in Figure 5.

3.1.5 Intrinsic radioactivity of the setup materials

To further characterize the radioactive background of our experiments, the intrinsic contribution of radioactivity in experimental set up (caps, vials and culture medium, see

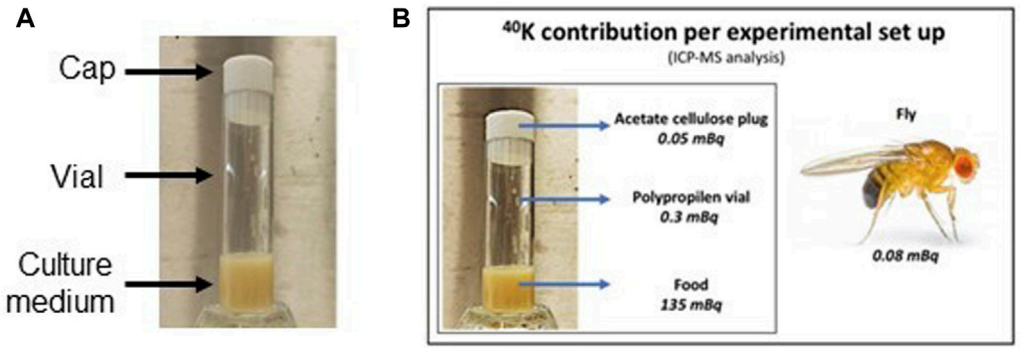

FIGURE 6
(A) Elements of the experimental set up. **(B)** ^{40}K contribution calculated for single element of the experimental set up by ICP-MS analysis.

TABLE 5 Results from Inductively Coupled Plasma Mass Spectrometry (ICP-MS) and HpGe spectroscopy analyses.

Specific activity (mBq/kg)								
		ICP-MS				HpGe		
		Vial	Plug	Food	Fly	Vial	Plug	Food
^{232}Th		0.2	1.1	2.8	0.8			
	^{228}Ra					<5.8	<9.5	<23.0
	^{228}Th					<5.4	<15.0	<15.0
^{238}U		0.9	2.4	6.2	2.5			
	^{226}Ra					5.0	<5.8	<8.6
	^{234}Th					<340	<57	<210
	^{234m}Pa					<220	<250	<560
^{40}K		42	32	19*10^3	93*10^3	<45	<120	17.8*10^3
	^{235}U					<4.7	<8.0	<19.0
	^{137}Cs					<1.5	<5.9	<7.0
	^{7}Be					30		

Figure 6A) was carried out by gamma ray spectrometry with high pure germanium (HPGe) detectors and Inductively Coupled Plasma Mass Spectrometry (ICP-MS) (Element II, Thermo Scientific, United States). The analysis was carried out by these two different techniques taking advantage of the LNGS expertise for the measurement of ultra-low-level radioactivity applied to the study of rare fundamental physics phenomena, such as double-beta decay, nuclear decays and dark matter, [26, 27]. It is worth remembering that these techniques are very different in terms of detectable nuclides (precursors vs. daughters), sensitivity and time of measurement. Furthermore, ICP-MS is considered a destructive technique that requires elaborate sample processing prior the analysis. On the other hand, HPGe spectroscopy allows for very easy sample handling although it requires long time of measurement and a large amount of sample. Usually, the choice of one over the other technique depends on the physical properties of the sample, the amount of available sample and time [26]. Concerning the natural decay chains of uranium and thorium, HPGe spectrometry and ICP-MS address different nuclides. They also have different sensitivity and times of measurement, ICP-MS being usually much faster and more sensitive to uranium and thorium themselves, whereas gamma-ray spectrometry is more sensitive to the gamma-active shorter-lived progenies within their decay chains, but with longer measurements times. A combination of both can usually give a complete picture on the status of the decay chain and identify possible ruptures of the secular equilibrium within it. It is important to point out that ICP-MS analysis directly quantifies the concentration of ^{39}K and the concentration/specific activity of ^{40}K is derived based on its natural isotope abundance (0.012%).

Each experimental set consists of a polypropylene vial weighing about 6.6 g, a cellulose acetate cap weighing about 1.5 g and Nutrifly medium weighing about 7 g. As expected, the major contribution in terms of specific activity comes from ^{40}K. The results from the two analyses are in good agreement with each other, especially for the ^{40}K activity (Table 5). The analysis on fly was carried out only by ICP-MS. Figure 6B reports the values from the ICP-MS analysis, with the contribution of ^{40}K calculated for the single element of the experimental set up taking into account the weight of the elements (i.e. 1.5 g plug; 6.6 g vial; 7 g food and 0.9 × 10^{-3} g fly).

3.2 Simulations

Simulations were performed to evaluate the dose rate values in water inside the standard vial due to the neutron component in the RRE laboratory only, since, as above mentioned, in the LRE laboratory the neutron flux is so small to be considered negligible for our purposes. Moreover, Monte Carlo simulations were performed also to evaluate the intrinsic contribution of radioactivity in the experimental set up.

3.2.1 Neutrons

The neutron flux measured with the DIAMON spectrometer at RRE was used as input for the Monte Carlo simulation, to evaluate the neutron dose rate at RRE. In the simulation the neutrons were uniformly generated from the surface of a 10 cm sphere around the experimental setup. The angular distribution

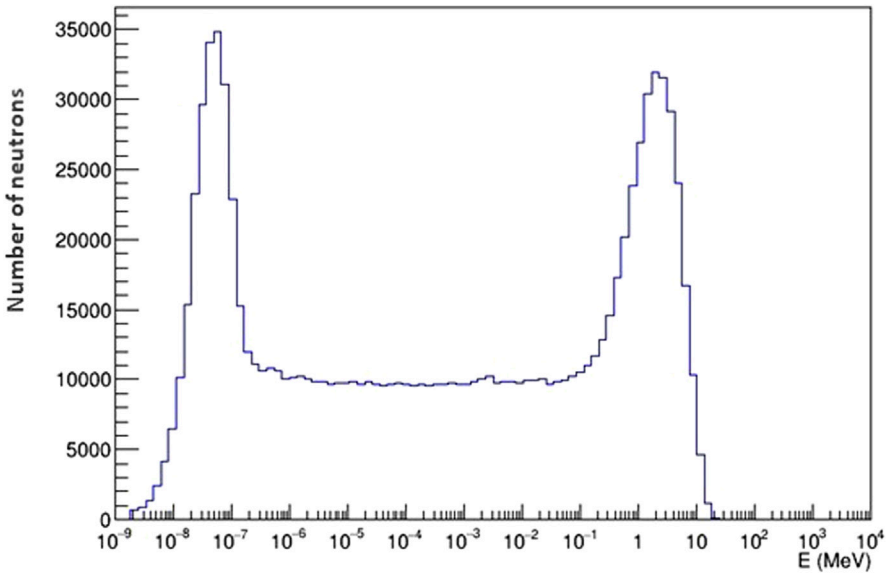

FIGURE 7
Energy distribution of simulated neutrons.

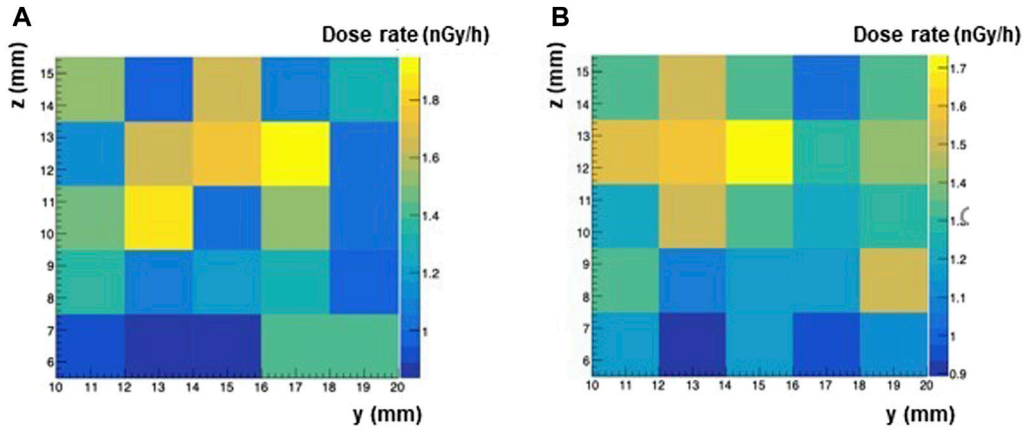

FIGURE 8
Map of neutron dose rates calculated with Monte Carlo simulations for two different values of the sphere radius and of simulated events. **(A)** 1M events and sphere radius = 10 cm. **(B)** 10M events and sphere radius = 20 cm.

of neutrons was isotropic, while the energy distribution reproduced the spectrum of Figure 5 from thermal energies to about 20 MeV (see Figure 7). Two simulations were performed varying the sphere radius from 10 cm to 20 cm and considering 10^7 and 10^8 simulated events, which resulted in excellent agreement. The 2D map of neutron dose rates calculated in the 1 cm^3 water scoring volume are shown in Figure 8, for the simulation with the sphere radius of 10 cm and 20 cm. Each pixel gives the dose rate value calculated for the corresponding voxel. To extract from the maps an average value of the physical dose rate due to neutrons, we did not consider the external layer of pixels to minimize possible border effects. By averaging over the central pixels from the simulation with 10^8 neutrons, a dose rate of 1.4 nGy/h was obtained with a standard deviation of 0.2 nGy/h.

3.2.2 Dose rate from intrinsic radioactivity of the setup materials

Simulations were performed to evaluate the dose rate in water inside the vial for *Drosophila* due to the radioactive contamination of the different components (plug, vial, medium) starting from their measured activities. We focused on the ^{40}K contained in the medium that gives the prevailing contribution to the dose rate (as from Table 5). In the simulation, the vial geometry has been implemented as in Figure 9A with ^{40}K decays uniformly distributed in the medium. The dose has been estimated in a cube of water with

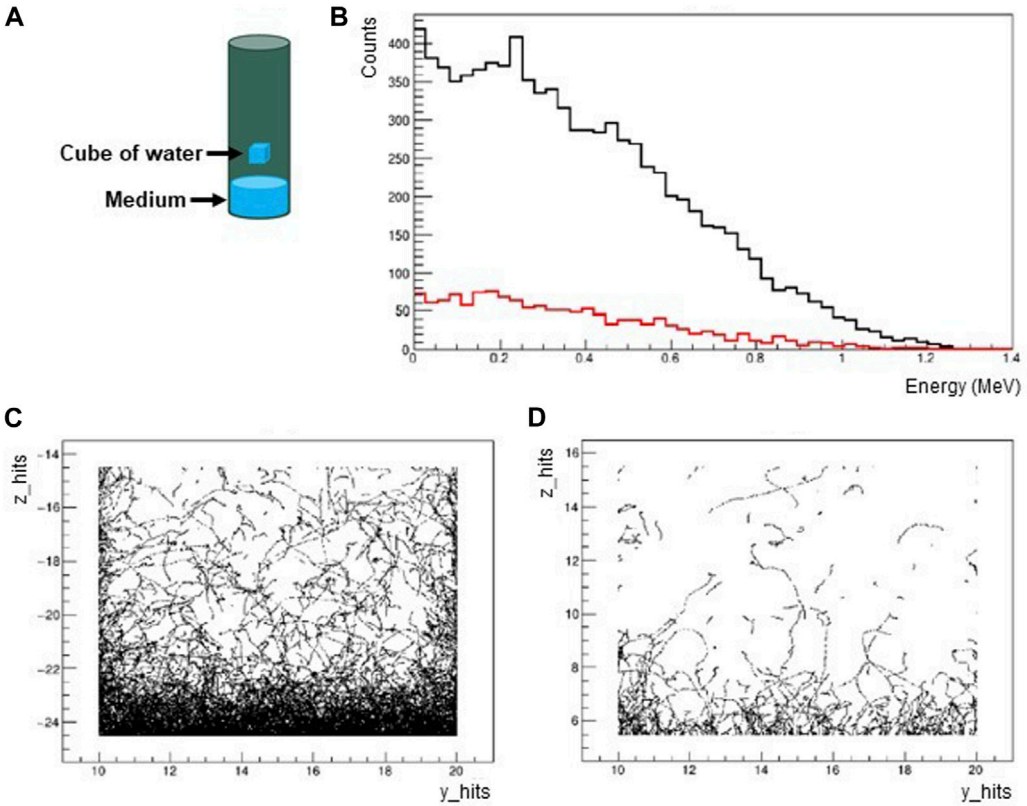

FIGURE 9
(A) The simulated vial is a plastic cylinder with 23 mm diameter, 95 mm height and 1 mm thickness. The vial is filled with the medium up to 20 mm and with air for the remaining part. The dose rate is estimated in a cube of water with volume equal to 1 cm^3 placed at different heights with respect to the medium. **(B)** Spectrum of gamma energy deposits in the water cube for the distances of the cube with respect to the medium of 2 mm (black) and 30 mm (red). **(C)** Spatial distribution of energy deposits for the distance of the cube with respect to the medium of 2 mm. **(D)** Spatial distribution of energy deposits for the distance of the cube with respect to the medium of 30 mm.

volume equal to 1 cm^3 placed at different heights with respect to the medium. The spectrum of gamma energy deposits in the water cube is shown in Figure 9B. The spatial distributions of energy deposit evaluated for distances of the cube with respect to the medium of 2 mm and 30 mm respectively are shown in Figures 9C, D.

In the situation where the water cube is placed at the center of the vial (30 mm distance from the medium), a gamma dose rate in the range 0.025–0.25 nGy/h was calculated. Since the medium has been located at the bottom of the vial, there is a variability of dose rates (lower dose rates with higher distances from the medium). The estimated intrinsic gamma dose rate can be considered low and negligible compared to the environmental contribution.

4 Discussion

For several decades many studies have been carried out, in various underground laboratories and with different biological systems (cells and organisms), which have highlighted a different behavior of the biological systems maintained in low radiation background conditions with respect to those maintained in reference environmental background conditions [28]. A common opinion is that environmental radiation plays a role in these phenomena. Direct evidences of the involvement of the environmental radiation field in such effects were obtained, performing specific experiments [5, 12]. In these types of experiments, knowledge of the radiation field in the external reference laboratory and the underground laboratory must be deepened [29–32]. To this purpose we quantified the background radiation dose rate within the two laboratories, RRE and LRE, and performed measurements within the available devices designed to increase (Marinelli beaker with tuff) or reduce (Pb and Fe shields in the RRE and LRE respectively) such background.

4.1 Low-LET radiation components

The ambient equivalent dose H*(10) was chosen as a reference quantity for the experimental dosimetric characterization of the low-LET components of the radiation field at RRE and LRE laboratories as well as within the devices used for the modulation of the gamma component. It is a measurable equivalent of the effective dose, which quantifies the risk to human health associated to radiation exposure. For its exact definition see ICRU Report 51 [33]. The H*(10) rate values (nSv/h) measured at LNGS RRE and LRE laboratories were compared with absorbed dose rate in water (nGy/h) obtained in other underground laboratories [29, 30, 32, 34]. For the comparison,

TABLE 6 Dose rate values relevant to radiobiological experiments at the LNGS, SNOLAB, Modane lab and WIPP facilities.

	Source	RRE (nSv/h)	LRE (nSv/h)
LNGS	Gamma-rays	31*	27*
	Muons	47*	<< 1
	Total dose rate	**78**	**27**
SNOLAB	Gamma -rays	6**	8**
	Muons	55**	<< 1
	Total dose rate	**61**	**8**
Modane lab	Gamma -rays	150*	20*
	Muons	45**	<< 1
	Total dose rate	**195**	**20**
WIPP	Gamma -rays	35*	8*
	Muons	-	<< 1
	Total dose rate	-	**8**

*measured values; ** simulated values using Monte Carlo simulation. The bold values indicate total dose rates.

the latter values, in nGy/h, were converted to equivalent dose rate, in nSv/h, using a radiation weighting factor for low-LET radiation equal to 1 [35], see Table 6.

4.1.1 External laboratories

Terrestrial gamma dose rate values in the external laboratories are similar for LNGS and WIPP, while SNOLAB and Modane report a lower and higher value respectively. The elevated gamma dose rate value at Modane laboratory is caused by naturally high radiation levels due to the soil composition [29]. The dose rate values of muon component in the external environment, measured at LNGS and simulated with Monte Carlo Code at SNOLAB and Modane laboratories, are very similar. To our knowledge, WIPP group did not measure or simulate the dose rate corresponding to the muon component. However, for several radiobiological experiments, WIPP group did not consider the external environment as a reference but they used a source consisting of KCl salt (containing ^{40}K, a beta-particle, and gamma-ray emitter) within their underground facility to simulate the external reference environment with a dose rate of about 70 nSv/h, a level matching typical average surface background radiation levels [7].

Of course, a single source of radiation does not represent the multitude of natural sources; in particular, the difference is given by the muons that are in above-ground environment but not in underground environment. However, since muons and gamma rays are both low-LET radiation, some biological systems may not be affected by this difference, at least for some endpoints [12].

4.1.2 Underground laboratories

Muon dose rate values are negligible for all underground laboratories. Higher values of gamma dose rate were obtained at LNGS and Modane laboratories, while a value of only 8 nSv/h was obtained at SNOLAB and WIPP. Overall, the dose rate values of the low LET component are reduced, compared to those obtained in the external laboratories, by a factor of approximately 3 and 8 for LNGS and SNOLAB respectively, 10 for Modane and WIPP. A 'lead castle' constructed with 10-cm-thick lead bricks was used in underground environment of SNOLAB, obtaining a strong reduction of gamma dose rate [32]. Shields were also used in the other underground laboratories. At LNGS a 5-cm-thick iron shield was used to reduce the gamma dose rate; a stronger reduction, like that evaluated by SNOLAB, can be obtained by moving the lead shield from LNGS RRE laboratory to LRE laboratory. A gamma dose rate value < 1nSv/h was obtained at Modane underground laboratory using a lead shield consisting of an interior layer of 5 cm of copper, surrounded by 10 cm of lead [30]. Finally, a 15 cm-thick vault made from pre-World War II, low-activity steel was used at WIPP to reduce gamma dose rate up to 0.16 nGy/h [5]. However, a different behavior of the biological system, maintained in parallel in low radiation background conditions with respect to those maintained in normal environmental background conditions, was observed even without using shields [12, 15].

4.2 High-LET radiation components at RRE and LRE laboratories

Both RRE and LRE laboratories are characterized by the presence of alpha particles from radon decay products; the alpha particle dose rate contribution depends on the radon concentration. Typically, the radon concentration values in the air (and consequently the alpha particle dose rate values) in underground laboratories would be much higher than those in external laboratories in the absence of ventilation systems or other air purification systems [32]. The underground LNGS laboratories are equipped with a powerful and efficient air ventilation system. When this system is working, the radon activity concentration values at LRE laboratory decrease from more than 100 Bq/m^3 to about 20 Bq/m^3, close to the value measured in the RRE laboratory. Currently, this reduction was acceptable for our purposes, since we wanted to keep the radon activity concentration values equal at RRE and LRE. Seasonal variations of radon concentration levels at RRE with respect to the annual average were of a few percent value and they were considered insignificant. The dose rate value of alpha particles from radon gas, which depends not only on the radon concentration but also on the biological system (cultured cells or organisms having different respiratory systems) was not evaluated. However, this value is expected to be the same at both LRE and RRE laboratories since the radon activity concentration is similar in the two environments (about 20 Bq/m^3). This allowed to carry out studies on the biological effects due to the reduction of muon and neutron components at LRE having the same dose of alpha particles at LRE and RRE. Moreover, we are evaluating to further strengthen the ventilation system in order to reduce the radon concentration up to 4–5 Bq/m^3. In this case, alpha dose rate estimates have been reported in the literature only for cell cultures [9, 32]. The possibility to install a radon abatement system or to use radon-free facilities at LRE, following the approaches of Modane and SNOLAB laboratories [36, 37], was also taken into consideration for carrying out experiments with very low radiation background. This will allow to evaluate how the

absence of the alpha component affects the behavior of the biological system.

Another high LET component of the radiation field is the neutron component. A value of the neutron flux in the energy range 0–20 MeV equal to 0.018 neutrons/cm^{2}s^{-1} at RRE laboratory was measured. This value is in good agreement with the neutron fluxes measured outside the LNGS in different energy ranges [38, 39]. The absorbed dose rate value by the fruit fly *D. melanogaster* due to neutrons was estimated at RRE laboratory using a Monte Carlo simulation and it was equal to 1.4 nGy/h. The neutron dose rate values, evaluated at SNOLAB and Modane external environment using Monte Carlo simulation were 4.52 nGy/h and 4.4 nGy/h respectively [30, 32].

4.3 Devices for the radiation field modulation useable in radiobiological studies

An accurate measure of the dose rate inside the lead and iron shields and Marinelli beaker, used to vary the gamma dose rate, was done using the 3″ NaI(Tl) scintillator and TLD-700H. No other detectors were used because they were too big to fit inside these devices.

4.3.1 Lead and iron shields

The lead shield at RRE laboratory allowed for a strong gamma dose rate reduction as measured with the NaI(Tl) scintillator detector. Therefore, within the lead shield at the RRE laboratory the biological system is basically exposed only to the muon component. The muon dose rate value obtained inside the lead shield by TLD measurements was 30.8 ± 4.2 nSv/h. We would like to point out that the lead shield at RRE allows for a complementary situation to the one at the LRE where the biological system is exposed only to the photonic component. Studies on the single components of low LET can be made to understand how each of them can affect the response of the biological system. To exploit this possibility radiobiological experiments are planned considering the fruit fly *D. melanogaster* as biological systems maintained in parallel inside and outside the lead shield at the RRE laboratory and also at the LRE laboratory. Moreover, the iron shield at LRE allows to further reduce the gamma dose rate. Overall, thanks to the use of iron shield the total dose rate (gammas + muons) at LRE is 17 times lower than that at RRE, making the LRE laboratory a suitable location to carry out radiobiological studies with a strong reduced dose rate.

4.3.2 Marinelli beaker

The gamma dose rate can be increased at LRE using the especially designed Marinelli beaker filled with tuff, a natural gamma-emitting building material. The energy spectrum of the tuff was already reported in a previous paper [14]. When this is filled with about 2,800 g of tuff, an H*(10) rate value increase of about 90 nSv/h can be obtained. This value is higher than the low LET environmental dose rate value at both RRE and LRE laboratories. However, it is possible to reduce the intensity of the "Marinelli beaker" source by decreasing the amount of tuff within it. Starting from the measured value of about 27 nGy/h, the approach of modulating the amount of tuff inside the Marinelli beaker allows for a gradual increase in the gamma dose rate at the LRE laboratory in order to understand wheather there is a threshold value of the H*(10) rate that induces a response switch of the biological system, causing it to change from one state to another.

4.4 Dose rate contribution by experimental setup

In our experiment, an additional source of background radiation comes from isotopes present in polypropylene vials, acetate cellulose plugs, fly culture medium (food) and *Drosophila* themselves. The contribution of ^{40}K in terms of specific activity is clearly higher than that of the other radioisotopes; moreover, the vials and plugs contribution is small compared to that of food and *Drosophilae*. In our experimental setup, since the food mass (7 g) is much larger than the *Drosophila* mass (0.9×10^{-3} g for each fly), the ^{40}K activity for food (135 mBq) is much higher than that for one *Drosophila* (0.08 mBq) (number of flies per vial in the range 20–40). Therefore, only the former contribution to the dose rate was estimated. The maximum dose rate value obtained by the Monte Carlo simulation was 0.25 nGy/h (at minimum distance from the medium). We can conclude that even for the higher intrinsic contamination measured in the experimental setup, the dose rate is two orders of magnitude below that of the gamma environmental radiation field and therefore it can be considered not relevant. The dose rate contribution from ^{40}K in a cell culture media was calculated by the SNOLAB group obtaining a value of about 2.4 nGy/h. The WIPP group also examined ^{40}K in the cell growth media, obtaining a dose rate value of 0.75 nGy/h, a value closer to that obtained in our work. Finally, the Modane lab found a much higher ^{40}K dose rate contribution of 26 nGy/h. These quite different values are due to the fact that different underground laboratories use different biological models with different amounts of potassium in the culture media.

5 Conclusion

It is legitimate to ask whether the biological response obtained in radiobiological experiments can be related to the mean value of the absorbed dose rate, independently of the weight of each radiation type, or if it depends on the contribution of specific components. In our RENOIR experiment [14], information was obtained about the involvement of the low LET components of the environmental radiation field (in particular of the gamma component) on the biological response of the fruit fly *D. melanogaster* [12]. Here we focused on a dosimetric characterization [in terms of H*(10)] of the low-LET components of the radiation field both at RRE and LRE laboratories and of the devices used for the modulation of the gamma component. Moreover, information on the high-LET components of the radiation field was also obtained. Monte Carlo simulation, using GEANT4 code, allowed us to quantify the absorbed dose rates by the fruit fly *D. melanogaster*, housed in the appropriate vials with the culture medium (food), due to neutrons. GEANT4 code was also used to determine the absorbed dose rates by the fruit fly due to ^{40}k radionuclides contained in the food, that are not directly measurable by our instrumentations.

A rigorous approach to proceed in underground radiobiology experiments should be to identify a location for the biological system in which there is a stable value of the dose rate. Moreover, the dose rate values may be different depending on the position inside the laboratory [30]. A campaign of dosimetric measurements was conducted at LNGS, using a 3″ NaI(Tl) scintillator, identifying the best location for the biological system. To minimize the spatial dependence of the dose on the distance from the walls and the floor, the biological system was placed on a 1-m-high desk located at the center of the RRE and LRE laboratories. Moreover, devices to decrease or increase the gamma dose rate have been designed and implemented at LNGS. These devices are important in the radiobiological experiments involving parallel testing in an underground laboratory and in an above ground laboratory, where the modulation of gamma dose rate is considered. The main results obtained are the following.

1. The reduction in the dose rate of the low LET components at the LRE laboratory compared to the LRE laboratory is small (only by a factor of 3). However by using the iron shield placed at LRE a much larger reduction factor of 17 was obtained (comparable to that of other underground laboratories), allowing radiobiological studies to be carried out with very low radiation background
2. The lead shield strongly reduces the gamma component at the RRE laboratory, allowing to carried out radiobiological studies with only the muon component, complementary to those in the LRE laboratory where, the biological system is exposed to gamma component only.
3. The Marinelli beaker filled with tuff is an apparatus suitable for use as a source of gamma radiation at the LRE laboratory, allowing the exposure of the biological system to a gradually increasing dose rate. Important information on biological mechanisms can be obtained in this type of study.

In conclusion, the LNGS external and underground facilities are currently equipped to carry out radiobiological experiments aimed at understanding the role of different low LET components of the environmental radiation field in determining the response of biological systems.

Data availability statement

The raw data supporting the conclusion of this article will be made available by the authors, without undue reservation.

Author contributions

MA: Writing–original draft. PA: Writing–original draft. MB: Writing–original draft. EB: Methodology, Writing–original draft. FC: Methodology, Writing–original draft. DC: Methodology, Writing–original draft. MC: Methodology, Writing–original draft. CA: Methodology, Writing–original draft, Writing–review and editing. GD'I: Methodology, Writing–original draft. RD: Methodology, Writing–original draft. GE: Conceptualization, Project administration, Supervision, Writing–original draft, Writing–review and editing, Methodology. FF: Methodology, Writing–original draft. AG: Methodology, Writing–original draft, Writing–review and editing. ML: Methodology, Writing–original draft. PM: Methodology, Writing–original draft, Writing–review and editing. SN: Methodology, Writing–original draft. CN: Methodology, Writing–original draft, Writing–review and editing. MQ: Methodology, Writing–original draft. MT: Methodology, Writing–original draft, Writing–review and editing. CT: Methodology, Writing–original draft, Writing–review and editing.

Funding

The author(s) declare financial support was received for the research, authorship, and/or publication of this article. This work has been supported by the "Operative Collaboration for R&D Activities in the Field of on Radiobiology" (Assegno di ricerca n. 20573/2018 to PM) in the framework of the General INFN-ISS Agreement, and by 2020–2022 INFN-CSN5 RENOIR experiment.

Acknowledgments

The authors are indebted with the LNGS and all technical services for their skilled assistance and support for the experiments.

In memoriam

The authors dedicate this work to the memory of Maurizio Chiti, who passed away suddenly during the writing of the article. Maurizio Chiti made a valuable contribution to underground radiobiology experiments and to science as a whole for many years.

Conflict of interest

The authors declare that the research was conducted in the absence of any commercial or financial relationships that could be construed as a potential conflict of interest.

Publisher's note

References

1. Lampe N, Breton V, Sarramia D, Sime-Ngando T, Biron DG. Understanding low radiation background biology through controlled evolution experiments. *Evol Appl* (2017) 10:658–66. doi:10.1111/eva.12491

2. Planel H, Soleilhavoup JP, Tixador R, Richoilley G, Conter A, Croute F, et al. Influence on cell proliferation of background radiation or exposure to very low, chronic gamma radiation. *Health Phys* (1987) 52(5):571–8. doi:10.1097/00004032-198705000-00007

3. Satta L, Augusti-Tocco G, Ceccarelli R, Esposito A, Fiore M, Paggi P, et al. Low environmental radiation background impairs biological defence of the yeast *Saccharomyces cerevisiae* to chemical radiomimetic agents. *Mutat Res* (1995) 347(3-4):129–33. doi:10.1016/0165-7992(95)00031-3

4. Smith GB, Grof Y, Navarrette A, Guilmette RA. Exploring biological effects of low level radiation from the other side of background. *Health Phys* (2011) 100(3):263–5. doi:10.1097/hp.0b013e318208cd44

5. Castillo H, Schoderbek D, Dulal S, Escobar G, Wood J, Nelson R, et al. Stress induction in the bacteria Shewanella oneidensis and Deinococcus radiodurans in response to below-background ionizing radiation. *Int J Radiat Biol* (2015) 91(9):749–56. doi:10.3109/09553002.2015.1062571

6. Castillo H, Li X, Schilkey F, Smith GB. Transcriptome analysis reveals a stress response of Shewanella oneidensis deprived of background levels of ionizing radiation. *PLoS One* (2018) 13(5):e0196472. doi:10.1371/journal.pone.0196472

7. Van Voorhies WA, Castillo HA, Thawng CN, Smith GB. The phenotypic and transcriptomic response of the *Caenorhabditis elegans* nematode to background and below-background radiation levels. *Front Public Health* (2020) 8:581796. doi:10.3389/fpubh.2020.581796

8. Zarubin M, Gangapshev A, Gavriljuk Y, Kazalov V, Kravchenko E. First transcriptome profiling of *D. melanogaster* after development in a deep underground low radiation background laboratory. *PLoS One* (2021) 16(8):e0255066. doi:10.1371/journal.pone.0255066

9. Fratini E, Carbone C, Capece D, Esposito G, Simone G, Tabocchini MA, et al. Low-radiation environment affects the development of protection mechanisms in V79 cells. *Radiat Environ Biophys* (2015) 54(2):183–94. doi:10.1007/s00411-015-0587-4

10. Satta L, Antonelli F, Belli M, Sapora O, Simone G, Sorrentino E, et al. Influence of a low background radiation environment on biochemical and biological responses in V79 cells. *Radiat Environ Biophys* (2002) 41(3):217–24. doi:10.1007/s00411-002-0159-2

11. Carbone MC, Pinto M, Antonelli F, Amicarelli F, Balata M, Belli M, et al. The Cosmic Silence experiment: on the putative adaptive role of environmental ionizing radiation. *Radiat Environ Biophys* (2009) 48(2):189–96. doi:10.1007/s00411-008-0208-6

12. Porrazzo A, Esposito G, Grifoni D, Cenci G, Morciano P, Tabocchini MA. Reduced environmental dose rates are responsible for the increased susceptibility to radiation-induced DNA damage in larval neuroblasts of Drosophila grown inside the LNGS underground laboratory. *Int J Mol Sci* (2022) 23(10):5472. doi:10.3390/ijms23105472

13. Fischietti M, Fratini E, Verzella D, Vecchiotti D, Capece D, Di Francesco B, et al. Low radiation environment switches the overgrowth-induced cell apoptosis toward autophagy. *Front Public Health* (2021) 8:594789. doi:10.3389/fpubh.2020.594789

14. Esposito G, Anello P, Ampollini M, Bortolin E, De Angelis C, D'Imperio G, et al. Underground radiobiology: a perspective at gran Sasso national laboratory. *Front Public Health* (2020) 8:611146. doi:10.3389/fpubh.2020.611146

15. Morciano P, Cipressa F, Porrazzo A, Esposito G, Tabocchini MA, Cenci G. Fruit flies provide new insights in low-radiation background biology at the INFN underground gran Sasso national laboratory (LNGS). *Radiat Res* (2018) 190(3):217–25. doi:10.1667/RR15083.1

16. Wulandari H, Jochum J, Rau W, von Feilitzsch F. Neutron flux at the Gran Sasso underground laboratory revisited. *Astropart Phys* (2004) 22(3-4):313–22. doi:10.1016/j.astropartphys.2004.07.005

17. Romanyukha A, Grypp MD, Trompier F, Thompson AK, Minniti R, Debroas J, et al. Performance evolution of TLD-700H/600H dosimetry system at extended issue periods. *Radiat Meas* (2018) 108:45–51. doi:10.1016/j.radmeas.2017.12.003

18. McKeever SWS, Moscovitch M, Townsend PD. *Thermoluminescence dosimetry materials: properties and uses*. Ashford, UK: Nuclear Technology Publishing (1995).

19. Dombrowski H. On the conversion coefficient from air kerma to ambient dose equivalent valid for a Cs-137 photon field—a critical review. *Rad Prot Dos* (2018) 182(4):562–6. doi:10.1093/rpd/ncy100

20. Gordon MS, Goldhagen P, Rodbell KP, Zabel TH, Tang HHK, Clem JM, et al. Measurement of the flux and energy spectrum of cosmic-ray induced neutrons on the ground. *IEEE Trans Nucl Sci* (2004) 51(6):3427–34. doi:10.1109/TNS.2004.839134

21. Pola A, Rastelli D, Treccani M, Pasquato S, Bortot D. DIAMON: a portable, real-time and direction aware neutron spectrometer for field characterization and dosimetry. *Nucl Instr Methods Phys Res Sect A* (2020) 969:164078. doi:10.1016/j.nima.2020.164078

22. Laubenstein M. Screening of materials with high purity germanium detectors at the Laboratori Nazionali del Gran Sasso. *Int J Mod Phys A* (2017) 32(30):1743002. doi:10.1142/S0217751X17430023

23. Bøtter-Jensen L, Thompson IMG. An international intercomparison of passive dosemeters, electronic dosemeters and dose rate meters used for environmental radiation measurements. *Rad Prot Dos* (1995) 60(3):201–11. doi:10.1093/oxfordjournals.rpd.a082718

24. Budzanowski M, Burgkhardt B, Olko P, Pessara W, Waligórski MPR. Long-term investigation on self-irradiation and sensitivity to cosmic rays of TL detector types TLD-200, TLD-700, MCP-N and new phosphate glass dosemeter. *Rad Prot Dos* (1996) 66(1-4):135–8. doi:10.1093/oxfordjournals.rpd.a031701

25. United Nations Scientific Commitee on the Effects of Atomic Radation. *Sources and effects of ionizing radiation, UNSCEAR 2000 report to the general assembly, annex A and B:. Vol I: sources*. New York, NY: United Nations (2000).

26. Nisi S, Di Vacri A, Di Vacri ML, Stramenga A, Laubenstein M. Comparison of inductively coupled mass spectrometry and ultra low-level gamma-ray spectroscopy for ultra low background material selection. *Appl Radiat Isot* (2009) 67:828–32. doi:10.1016/j.apradiso.2009.01.021

27. Laubenstein M, Lawson I. Low background radiation detection techniques and mitigation of radioactive backgrounds. *Front Phys* (2020) 8:577734. doi:10.3389/fphy.2020.577734

28. Liu J, Ma T, Liu Y, Zou J, Gao M, Zhang R, et al. History, advancements, and perspective of biological research in deep-underground laboratories: a brief review. *Environ Int* (2018) 120:207–14. doi:10.1016/j.envint.2018.07.031

29. Lampe N, Biron DG, Brown JMC, Incerti S, Marin P, Maigne L, et al. Simulating the impact of the natural radiation background on bacterial systems: implications for very low radiation biological experiments. *PLoS One* (2016) 11(11):e0166364. doi:10.1371/journal.pone.0166364

30. Lampe N, Marin P, Castor J, Warot G, Incerti S, Maigne L, et al. Background study of absorbed dose in biological experiments at the Modane Underground Laboratory. *EPJ Web of Conferences* (2016) 124:00006. doi:10.1051/epjconf/201612400006

31. Szkliniarz K. Characteristics of the natural radioactivity of the underground laboratories in the Baltic Sea Region participating in the BSUIN and EUL projects. *Adv Geosci* (2022) 57:9–19. doi:10.5194/adgeo-57-9-2022

32. Kennedy KJ, LeBlanc A, Pirkkanen J, Thome C, Tai TC, LeClair R, et al. Dosimetric characterisation of a sub-natural background radiation environment for radiobiology investigations. *Rad Prot Dos* (2021) 195(2):114–23. doi:10.1093/rpd/ncab120

33. ICRU. *Quantities and units in radiation protection dosimetry* (1993). Report 51.

34. Chiou HC, Hayes R. Creating a baseline radiological standard for the waste isolation pilot plant underground. *Isotopes Environ Health Stud* (2004) 40(3):213–20. doi:10.1080/10256010410001678053

35. Pelliccioni M. Radiation weighting factors and high energy radiation. *Rad Prot Dos* (1998) 80(4):371–8. doi:10.1093/oxfordjournals.rpd.a032556

36. Štekl I, Hůlka J, Mamedov F, Fojtík P, Čermáková E, Jílek K, et al. Low radon cleanroom for underground laboratories. *Front Public Health* (2021) 8:589891. doi:10.3389/fpubh.2020.589891

37. Pirkkanen J, Laframboise T, Liimatainen P, Sonley T, Stankiewicz S, Hood M, et al. A novel specialized tissue culture incubator designed and engineered for radiobiology experiments in a sub-natural background radiation research environment. *J Environ Radioactivity* (2021) 228:106512. doi:10.1016/j.jenvrad.2020.106512

38. Rindi A, Celani F, Lindozzi M, Miozzi S. Underground neutron flux measurement. *Nucl Instr Methods Phys Res Sect A* (1988) 272:871–4. doi:10.1016/0168-9002(88)90772-3

39. Bonardi A, Aglietta M, Bruno G, Fulgione W, Bergamini Machado AA. Direct measurement of the atmospheric neutron flux in the energy range 10–500 MeV. *Astropart Phys* (2010) 34(4):225–9. doi:10.1016/j.astropartphys.2010.07.004

frontiers | Frontiers in Physics

TYPE Review
PUBLISHED 14 December 2023
DOI 10.3389/fphy.2023.1310146

OPEN ACCESS

EDITED BY
Aldo Ianni,
Gran Sasso National Laboratory (INFN), Italy

REVIEWED BY
Luciano Pandola,
Universities and Research, Italy
Grzegorz Zuzel,
Jagiellonian University, Poland
Guillaume Warot,
UMR5821 Laboratoire De Physique Subatomique Et Cosmologie (LPSC), France

*CORRESPONDENCE
Paul R. Scovell,
paul.scovell@stfc.ac.uk

RECEIVED 09 October 2023
ACCEPTED 28 November 2023
PUBLISHED 14 December 2023

CITATION
Scovell PR, Thiesse M, Ahmed Maouloud S, Ghag C and Dobson J (2023), Radioassay facilities at the STFC Boulby Underground Laboratory. *Front. Phys.* 11:1310146. doi: 10.3389/fphy.2023.1310146

Radioassay facilities at the STFC Boulby Underground Laboratory

Paul R. Scovell[1]*, Matthew Thiesse[2], Sid Ahmed Maouloud[1,3], Chamkaur Ghag[4] and James Dobson[5]

[1]STFC Boulby Underground Laboratory, Boulby Mine, Redcar & Cleveland, United Kingdom, [2]Department of Physics and Astronomy, University of Sheffield, Sheffield, United Kingdom, [3]School of Physics and Astronomy, University of Edinburgh, Edinburgh, United Kingdom, [4]Department of Physics and Astronomy, University College London (UCL), London, United Kingdom, [5]Department of Physics, King's College London, London, United Kingdom

For future low-background particle physics experiments, it will be essential to assay candidate detector materials using an array of assay techniques. To minimise the risk of sample contamination whilst moving between assay techniques, it is also sensible to minimise the distance between assay stations, particularly for non-destructive techniques where the sample may end up being installed into an experiment. The Boulby UnderGround Screening (BUGS) Facility comprises an array of germanium detectors, two XIA UltraLo-1800 surface-alpha counters, two radon emanation detectors and an Agilent ICP-MS system. This article describes each of these systems.

KEYWORDS

gamma spectrometry, surface alpha counting, radon emanation, mass spectrometry, radioassay

1 Introduction

The STFC (Science and Technology Facilities Council) Boulby Underground Laboratory is located in the north-east of England at Boulby Mine. The laboratory is at a depth of 1100 m (2840 m water equivalent). The Boulby UnderGround Screening (BUGS) Facility has been operational since 2015 and has been involved in the assay programmes of several leading low-background particle physics experiments [1,2] and a number of environmental studies [3–5]. BUGS is one of several underground low-background material assay facilities worldwide including at SNOLAB [6], the Laboratori Nazionali del Gran Sasso (LNGS) [7,8], the Sandford Underground Research Facility (SURF) [9], the Laboratoire Souterrain de Modane (LSM) [10], the Laboratorio Subterraneo de Canfranc (LSC) [11] and the Kamioka Observatory [12].

To provide a comprehensive understanding of the radioactivity profile of a candidate material or component for a low background particle physics experiment, it is important that the entire decay chain of the Naturally Occurring Radioactive Material (NORM) isotopes is studied. In general, the naturally occurring radioisotopes of interest for such studies are ^{238}U, ^{235}U, ^{232}Th, ^{4} K, ^{137}Cs and, for some materials, ^{60}Co. There are other material dependent radioisotopes that occur due to cosmogenic activation [13], which are also studied. For the isotopes of uranium and thorium, these begin long decay chains within which breaks from secular equilibrium are possible. Different decay products and decay emissions on a wide spectrum of energies may adversely impact the sensitivity of a running particle physics detector. Thus it is important to use techniques that probe the whole decay chain.

Radioactive assay techniques can be split into two categories. Destructive techniques are those whereby the materials assayed are dissolved or digested for assay, and as such, cannot

TABLE 1 Characteristics of the Boulby HPGe detectors [1]. *Extrapolated from the ^{60}Co 1332 keV full-energy peak.

Detector	Type	S-ULB	Volume (cm^3)	Relative efficiency (%)	Front face area (cm^2)	Resolution @1408 keV (keV)
Belmont	p-type	✓	600	160	-	2.0
Merrybent	p-type	✓	375	100	-	2.0
Lunehead	p-type	-	375	100	-	1.9*
Roseberry	BEGe	✓	195	-	65	1.7
Chaloner	BEGe	-	150	-	50	1.7
Lumpsey	SAGe well	✓	263	-	-	1.8

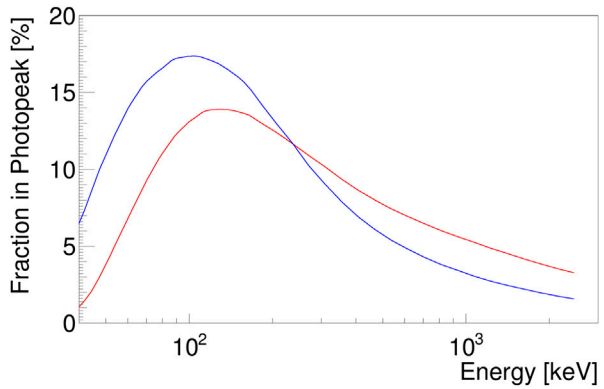

FIGURE 1
Geometrical efficiencies for a 100 g powder sample with a density of 1.22 g/cm^2 on the Belmont coaxial (red) and Roseberry BEGe (blue) detectors.

themselves be used to construct low background experiments. This includes, for example, Inductively Coupled Plasma Mass Spectrometry (ICP-MS). These techniques are used to directly measure the concentrations of long-lived uranium and thorium in a material but generally cannot tell us what is happening lower in the chain where decay half-lives are much shorter. Non-destructive techniques take a candidate material and component, determine their radioactivity profile, then return them to an experiment for manufacture or installation. This includes techniques such gamma-ray spectrometry using High Purity Germanium (HPGe) detectors, radon emanation studies, and surface-alpha counting. These techniques are not sensitive to measuring uranium and thorium directly, rather they look at isotopes lower in the decay chain where gamma and alpha particle emission is measurable given the technique. This allows us to determine any breaks in equilibrium that cannot be determined using mass spectrometry alone.

The BUGS facility currently comprises six HPGe detectors, two XIA UltraLo-1800 surface alpha counters, a dual-detector radon emanation system and an Agilent-8900 triple quadrupole ICP-MS.

2 Gamma spectrometry

The BUGS facility operates six HPGe detectors with a variety of configurations. Belmont and Merrybent are Mirion (Canberra) specialty ultra-low background (S-ULB) p-type coaxial detectors and Lunehead is an Ortec p-type coaxial detector mounted in a low background cryostat. Roseberry and Chaloner are Mirion (Canberra) S-ULB and standard Broad Energy Germanium (BEGe) detectors, respectively. Finally, Lumpsey is a Mirion (Canberra) S-ULB SAGe-well detector. The BEGe type detectors are optimised for the detection of low energy (below 200 keV) gamma-rays, maximising sensitivity to the 46.5 keV gamma-ray from the decay of ^{210}Pb. Detector mass is maximised in the p-type detectors which optimises sensitivity to gamma-rays of 200 keV and above. The SAGe well detector is optimised for small samples placed in the well where there is almost 4π germanium crystal coverage.

Table 1 details the characteristics of each detector. Figure 1 compares the geometric efficiency of the Belmont and Roseberry detectors (the largest coaxial and BEGe type detectors, respectively) with a 100 g powder sample. The geometric efficiency is determined using a GEANT4 [14] simulation of the respective HPGe detectors. Additionally, where necessary, coincidence summing effects are considered as described in [15]. It is clear that, despite the larger mass of the Belmont coaxial detector, the efficiency below approximately 250 keV is greater using the Roseberry BEGe detector. The inferred minimum detectable activities (MDAs) for the BUGS detectors are discussed in detail in [16].

Table 2 shows the integral and peak rates for the BUGS HPGe detectors, also compared in Figure 2 for the S-ULB detectors. The Belmont detector reaches 0.4 (2) counts/kg/day for the 609 keV full energy peak associated with ^{214}Bi. By means of comparison, the GeMPI detector reaches $\leq$0.07 counts/kg/day for the same full energy peak [7].

In Figure 2, the spectrum of Lumpsey shows two full energy peaks that are not due to decay of NORM isotopes at 811 keV and 835 keV. These are due to the cosmogenically produced ^{58}Co and ^{54}Mn, respectively. This background was taken soon after the detector was installed underground.

3 Surface alpha counting

The BUGS facility operates two XIA UltraLo-1800 surface alpha detectors. The UltraLo-1800 is an alpha particle detector that employs a dual-channel pulse shape analysis to distinguish between alpha particles emitted from the sample and those emitted by the walls of the detector. The dual channel method uses readouts from both the anode (above the sample tray) and the

TABLE 2 Count rates for the Boulby HPGe detectors. These runs were all performed in early 2021.[16].

Detector	Count rate (/kg/day)						
	Integral 100–2700 keV	351 keV ^{214}Pb	609 keV ^{214}Bi	238 keV ^{212}Pb	1461 keV ^{40}K	2615 keV ^{208}Tl	46.5 keV ^{210}Pb
Belmont	90 (9)	0.2 (1)	0.4 (2)	0.13 (8)	1.0 (2)	0.3 (1)	-
Merrybent	145 (12)	2.5 (3)	1.8 (3)	0.3 (1)	1.9 (3)	0.8 (2)	-
Lunehead	540 (25)	5.6 (5)	4.7 (4)	8.3 (5)	9.1 (6)	2.0 (3)	-
Roseberry	130 (11)	0.15 (7)	0.15 (7)	0.8 (3)	0.8 (2)	0.2 (1)	0.4 (6)
Chaloner	1045 (30)	5 (1)	4 (1)	7 (1)	8.4 (14)	2.1 (5)	1.8 (11)
Lumpsey	515 (25)	1.1 (7)	1.3 (3)	1.1 (7)	1.7 (7)	0.2 (2)	1.7 (6)

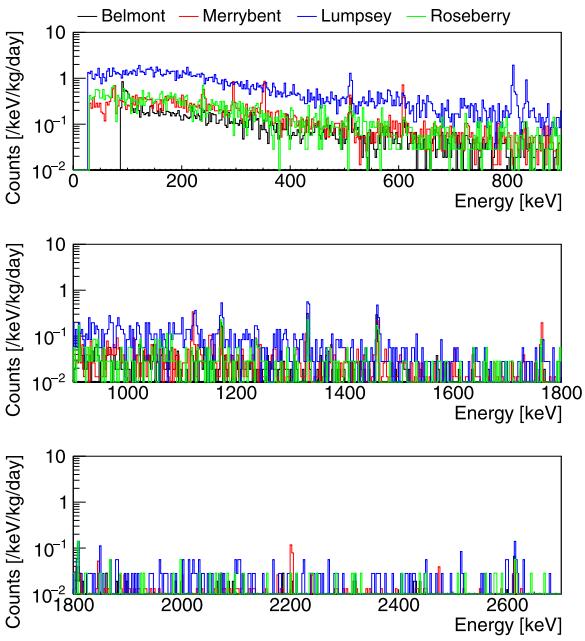

FIGURE 2
Comparison of background rates for the four S-ULB detectors operated in the BUGS facility.

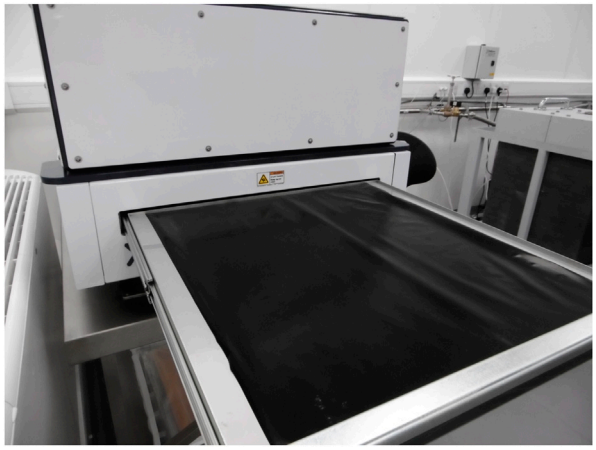

FIGURE 3
One of the BUGS XIA UltraLo-1800 detectors with a PTFE liner installed. The results for this sample are shown in Table 3.

guard rail (positioned on the side). In the UltraLo-1800, the sample, or the tray upon which a sample would be loaded, acts as the cathode. A comparison between signals from these two readout planes can be used to veto any signals not originating from the sample. The UltraLo-1800 has been used in a number of assay programmes [17–19].

The first UltraLo-1800 detector was installed in the BUGS facility in 2018 with a second added in 2021. The detectors use boil off argon gas from two 240 L dewars. When not in use, the detectors are purged using a dry source of nitrogen in order to maintain low levels of humidity in the detector without the cost of liquid argon.

Table 3 shows the results of a background characterisation programme which looked at the emissivity with a number of different setups. Firstly, the detector was run using the bare stainless steel tray. Following this, the process was repeated using a sheet of PTFE and some electroformed copper from Pacific Northwestern National Laboratory (PNNL). The characterisation and spectral response of the XIA UltraLo-1800 is detailed in [20]. Figure 3 shows the PTFE liner on one of the XIA UltraLo-1800 detectors. This study clearly shows the importance of material selection even for the tray upon which samples will sit. In addition, this table shows assays of two samples of titanium, one cleaned with isopropyl alcohol and the other etched using Citranox - a commercial product containing citric acid which has been used for cleaning copper in other low-background particle physics experiments [21]. This shows the main aim of the XIA assay programme–to develop cleaning methods for various materials that will be used in future low background particle physics experiments. Additionally, the XIA UltraLo-1800 can also be used to measure bulk radioactivity as described in [22].

4 Radon emanation

BUGS operates a dual-detector radon emanation system which uses two 80 L electrostatic alpha detectors designed and constructed

TABLE 3 Background measurements performed with the UltraLo-1800 detector. The best measurement achieved with the BUGS system was using a sample of electroformed copper on loan from Pacific Northwestern National Laboratory.

Sample	Duration (hrs)	Alphas	Surface area cm^2	Emissivity α/khr/cm^2	Activity mBq/m^2
Background (SS Tray)	168	342	1800	1.24 (7)	6.9 (4)
Background (PTFE Liner)	168	103	1800	0.38 (4)	2.1 (2)
PNNL Copper	168	13	707	0.13 (4)	0.7 (2)
Titanium (IPA)	168	4779	707	46.7 (7)	259 (3)
Titanium (Citranox)	168	2302	707	22.1 (5)	123 (3)

by Cosmotec [23–25]. The design of the system builds on knowledge gained from a similar facility at the Mullard Space Science Laboratory (MSSL) [26] and the Cryogenic Radon Emanation Facility (CREF) [27]. The system will also incorporate a radon concentration line which will allow us to enhance its sensitivity. Figure 4 shows images from the commissioning of one of the detectors.

Samples measured are initially sealed inside an electropolished vacuum chamber to allow the emanating radon to come to equilibrium with the decaying radon. After some time, the radon-filled gas is transported to the electrostatic detector where an electric field causes positively-charged radon daughters to collect on the PIN diode. Alphas emitted from the ^{222}Rn decay chain—6002 keV from ^{218}Po and 7687 keV from ^{214}Po—are detected with efficiencies 25.92% ± 0.10% and 37.73% ± 0.15%, respectively, allowing a measure of the rate of ^{222}Rn emanation from the sample. Alphas emitted from the ^{220}Rn decay chain—8785 keV from ^{212}Po—are also detected in the background and from some samples, but the efficiency of measurement is not calibrated and thus these alphas are not useable for ^{220}Rn emanation analysis at this time.

The radon backgrounds of the emanation chambers, pipework, gas handling system, and electrostatic detectors are minimised by electropolishing and by choosing materials known to have very low intrinsic radon emanation. The background count rate of the detector is 0.53 ± 0.07 counts per day for ^{214}Po and 2.12 ± 0.14 counts per day for ^{218}Po. The background contribution from the emanation chambers is less than that of the detector itself, and thus is below the detection limit of the system. The radon detectors have been commissioned and calibrated using a Pylon RN-1025 ^{222}Rn source. The minimum detectable activity (MDA), as defined in [28], of the detector system is 56.2 μBq, 40.0 μBq, and 11.0 μBq for 95%, 90% and 68% confidence levels (C.L.), respectively. These MDA are shown in Figure 5 with their respective measurement times. At 68% C.L., the MDA is achieved in only 3.76 days of detector measurement time.

Previous experience [28] suggests that the Rn emanation MDA of the electrostatic detector could be improved by two orders of magnitude after implementing the radon concentration line. Further improvements are planned to mitigate the efficiency loss due to electronegative impurity outgassing from sample materials.

5 Mass spectrometry

ICP-MS has been used routinely in material characterisation for low-background particle physics. In 2022, the UCL ICP-MS facility [29], including an Agilent 8900 triple-quadrupole ICP-MS

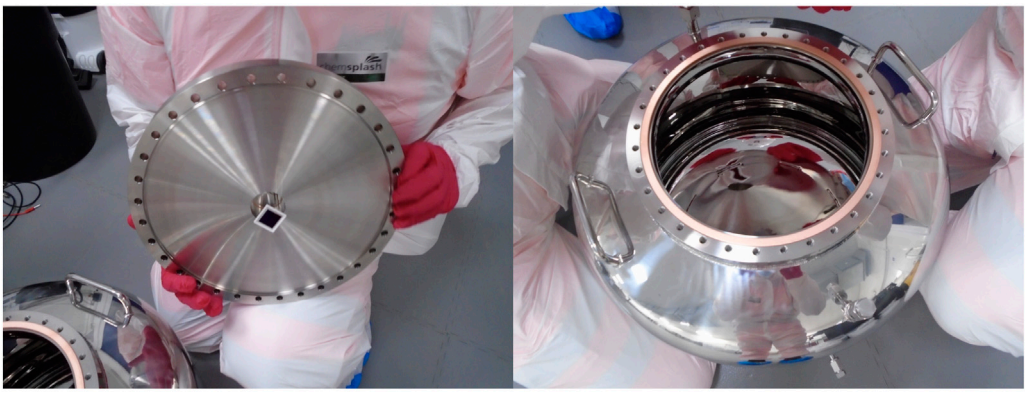

FIGURE 4
Images from the commissioning of the radon emanation detctors. Shown are the PIN diode on the underside of the upper detector plate (left) and an internal view the electropolished detector chamber (right).

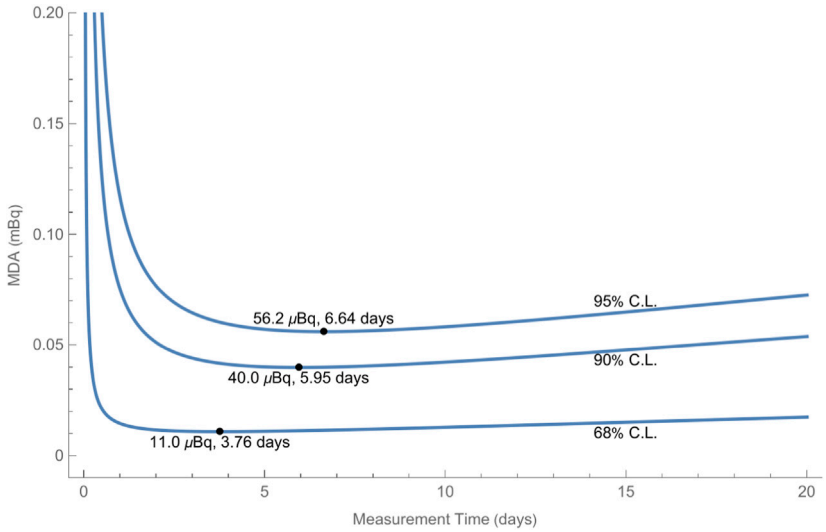

FIGURE 5
MDA for ^{214}Po in the BUGS radon detectors. The three lines are different confidence levels (68%, 90% and 95%) and the points are local minima with x and y values annotated.

FIGURE 6
The UCL Agilent 8900 Triple Quadrupole ICP-MS (ICP-QQQ) system installed in the ISO-6 certified cleanroom at the Boulby Surface Laboratory.

(ICP-QQQ), was relocated to the Boulby Underground Laboratory to be operated in a new ISO-6-certified clean room in the above-ground laboratory.

In addition to the ICP-QQQ, a number of sample preparation systems have also been relocated to Boulby. These include an ETHOS-UP closed vessel microwave digestion system with SK-15 high-pressure rotor, a Pyro–260 microwave ashing system (for samples that are HF resistant, such as PTFE), a sub-boiling point acid distillation (subClean) system, a reflux cleaning (traceClean) system, and a Veolia PURELAB FLEX 3 type 1 water system.

With a combination of precise sample preparation and detector sensitivity, the Agilent 8900 ICP-QQQ is capable of reaching sensitivities $< 10^{-15}$ g/g (< 1 part-per quadrillion (ppq) g/g). Figure 6 shows the ICP-QQQ in the cleanroom.

The Agilent 8900 ICP-QQQ offers unparalleled sensitivity and specificity, making it a cornerstone for low-background radioassay measurements at the BUGS facility. Its design features superior interference removal, enabling accurate analysis of elements present at trace levels. The system is equipped with high-efficiency ion optics and a unique collision/reaction cell that eliminates polyatomic interferences.

Our primary goal with the ICP-QQQ at the Boulby Underground Laboratory is to push the boundaries of low-background radioassay measurements. With its advanced features, we aim to achieve unparalleled precision, particularly profiling backgrounds with a comprehensive understanding of the complete U/Th-chains. To ensure the accuracy of our measurements, our methodology incorporates an internal standard approach for real-time correction of matrix effects and instrumental drift. We will further enhance the reliability of our data by periodically analyzing quality control samples.

Efforts are underway to refine the system's capabilities further and improve the precision of assays, aiming to define component-specific requirements on activity and precision.

Author contributions

PS: Writing–original draft. MT: Writing–original draft. SA: Writing–original draft. CG: Writing–Review & Editing. JD: Writing–Review & Editing.

Funding

The author(s) declare financial support was received for the research, authorship, and/or publication of this article. This work was supported in by the UKRI's Science & Technology Facilities Council and in part through specific award numbers ST/R003181/1, ST/V006185/1, and ST/X002438/1.

Acknowledgments

The authors wish to acknowledge ICL-Boulby for their support in hosting the STFC Boulby Underground Laboratory and therein BUGS. The University of Edinburgh is a charitable body, registered in Scotland, with the registration number SC005336.

Conflict of interest

The authors declare that the research was conducted in the absence of any commercial or financial relationships that could be construed as a potential conflict of interest.

Publisher's note

References

1. Akerib DS, Akerlof CW, Akimov DY, Alquahtani A, Alsum SK, Anderson TJ, et al. The LUX-ZEPLIN (LZ) radioactivity and cleanliness control programs. *Eur Phys J C* (2020) 80:1044. doi:10.1140/epjc/s10052-020-8420-x

2. Hosokawa K, Ikeda M, Okada T, Sekiya H, Fernández P, Labarga L, et al. Development of ultra-pure gadolinium sulfate for the Super-Kamiokande gadolinium project. *Prog Theor Exp Phys* (2022) 2023:013H01. doi:10.1093/ptep/ptac170

3. Aguilar-Arevalo A, Alvarado-Mijangos S, Bertou X, Canet C, Cruz-Pérez M, Deisting A, et al. Characterization of germanium detectors for the first underground laboratory in Mexico. *J Instrum* (2020) 15:11014. doi:10.1088/1748-0221/15/11/P11014

4. Aguilar-Arevalo A, Bertou X, Canet C, Cruz-Pérez MA, Deisting A, Dias A, et al. Dosimetry and calorimetry performance of a scientific CMOS camera for environmental monitoring. *Sensors* (2020) 20:5746. doi:10.3390/s20205746

5. Wadsworth J, Cockell CS, Murphy AS, Nilima A, Paling S, Meehan E, et al. There's plenty of room at the bottom: low radiation as a biological extreme. *Front Astron Space Sci* (2020) 7:50. doi:10.3389/fspas.2020.00050

6. Lawson I. Low background measurement capabilities at SNOLAB. *J Phys Conf Ser* (2020) 1342:012086. doi:10.1088/1742-6596/1342/1/012086

7. Heusser G, Laubenstein M, Neder H. Low-level germanium gamma-ray spectrometry at the μBq/kg level and future developments towards higher sensitivity. *Radioactivity Environ* (2006) 8:495–510. doi:10.1016/S1569-4860(05)08039-3

8. Baudis L, Ferella AD, Askin A, Angle J, Aprile E, Bruch T, et al. Gator: a low-background counting facility at the gran Sasso underground laboratory. *J Instrum* (2011) 6:P08010. doi:10.1088/1748-0221/6/08/P08010

9. Mount BJ, Thomas KJ, Oliver-Mallory KC, Lesko KT, Schnee RW, Henning R, et al. Black hills state university underground campus. *Appl Radiat Isot* (2017) 126:130–3. doi:10.1016/j.apradiso.2017.02.025

10. Loaiza P, Brudanin V, Piquemal F, Rukhadze E, Rukhadze N, Stekl I, et al. Obelix, a new low-background HPGe at Modane underground laboratory. *AIP Conf Proc* (2015) 1672:130002. doi:10.1063/1.4928012

11. Bandac I, Borjabad S, Ianni A, Nuñez-Lagos R, Pérez C, Rodríguez S, et al. Ultra-low background and environmental measurements at Laboratorio Subterráneo de Canfranc (LSC). *Appl Radiat Isot* (2017) 126:127–9. doi:10.1016/j.apradiso.2017.02.046

12. Ichimura K, Ikeda H, Kishimoto Y, Kurasawa M, Suzuki AA, Gando Y, et al. *Development of a low-background HPGe detector at Kamioka observatory* (2023). arXiv:2308.05302.

13. Cebrián S, Gómez H, Luzón G, Morales J, Tomás A, Villar J. Cosmogenic activation in germanium and copper for rare event searches. *Astropart Phys* (2010) 33:316–29. doi:10.1016/j.astropartphys.2010.03.002

14. Agostinelli S, Allison J, Amako K, Apostolakis J, Araujo H, Arce P, et al. Geant4 - a simulation toolkit. *Nucl Instrum Meth A* (2003) 506:250–303. doi:10.1016/S0168-9002(03)01368-8

15. Scovell P, Meehan E, Araújo H, Dobson J, Ghag C, Kraus H, et al. Low-background gamma spectroscopy at the Boulby underground laboratory. *Astropart Phys* (2018) 97:160–73. doi:10.1016/j.astropartphys.2017.11.006

16. Scovell PR, Meehan E, Paling SM, Thiesse M, Liu X, Ghag C, et al. *Ultra-low background germanium assay at the Boulby underground laboratory* (2023). arXiv:2308.03444.

17. Nakib MZ, Cooley J, Guiseppe VE, Kara B, Qiu H, Rielage K, et al. Screening materials with the XIA UltraLo alpha particle counter at southern methodist university. *AIP Conf Proc* (2013) 1549:78–81. doi:10.1063/1.4818080

18. McNally BD, Coleman S, Warburton WK, Autran JL, Clark BM, Cooley J, et al. Sources of variability in alpha emissivity measurements at LA and ULA levels, a multicenter study. *Nucl Instrum Meth A* (2014) 750:96–102. doi:10.1016/j.nima.2014.02.052

19. Abe K, Hiraide K, Ichimura K, Kishimoto Y, Kobayashi K, Kobayashi M, et al. Identification of ^{210}Pb and ^{210}Po in the bulk of copper samples with a low-background alpha particle counter. *Nucl Instrum Meth A* (2018) 884:157–61. doi:10.1016/j.nima.2017.12.015

20. Bunker R, Aramaki T, Arnquist I, Calkins R, Cooley J, Hoppe E, et al. Evaluation and mitigation of trace ^{210}Pb contamination on copper surfaces. *Nucl Instrum Meth A* (2020) 967:163870. doi:10.1016/j.nima.2020.163870

21. Park BJ, Choi JJ, Choe JS, Gileva O, Ha C, Iltis A, et al. Development of ultra-pure NaI(Tl) detectors for the COSINE-200 experiment. *Eur Phys J C* (2020) 80:814. doi:10.1140/epjc/s10052-020-8386-8

22. Zuzel G, Pelczar K, Wójcik M. Studies of surface and bulk ^{210}Po in metals using an ultra-low background large surface alpha spectrometer. *Appl Radiat Isot* (2017) 126:165–7. doi:10.1016/j.apradiso.2017.01.030

23. Hosokawa K, Murata A, Nakano Y, Onishi Y, Sekiya H, Takeuchi Y, et al. Development of a high-sensitivity 80 L radon detector for purified gases. *Prog Theor Exp Phys* (2015) 2015:033H01. doi:10.1093/ptep/ptv018

24. Pronost G, Ikeda M, Nakamura T, Sekiya H, Tasaka S. Development of new radon monitoring systems in the Kamioka mine. *Prog Theor Exp Phys* (2018) 2018:093H01. doi:10.1093/ptep/pty091

25. Okamoto K, Nakano Y, Pronost G, Sekiya H, Tasaka S, Takeuchi Y, et al. *Improvement of radon detector performance by using a large-sized PIN-photodiode* (2021). arXiv.2112.06614.

26. Liu XR. Radon mitigation strategy and results for the SuperNEMO experiment. *J Phys Conf Ser* (2017) 888:012085. doi:10.1088/1742-6596/888/1/012085

27. Perry E. The cold radon emanation facility. *AIP Conf Proc* (2023) 2908:080005. doi:10.1063/5.0167505

28. Liu XR. Low background techniques for the SuperNEMO experiment. United Kingdom: University College London (2017). Ph.D. thesis.

29. Dobson J, Ghag C, Manenti L. Ultra-low background mass spectrometry for rare-event searches. *Nucl Instrum Meth A* (2018) 879:25–30. doi:10.1016/j.nima.2017.10.014

frontiers | Frontiers in Physics

TYPE Original Research
PUBLISHED 15 December 2023
DOI 10.3389/fphy.2023.1310451

OPEN ACCESS

EDITED BY
Aldo Ianni,
Gran Sasso National Laboratory (INFN), Italy

REVIEWED BY
Minfang Yeh,
Brookhaven National Laboratory (DOE), United States
Jenni Kotila,
University of Jyväskylä, Finland

*CORRESPONDENCE
Markus Horn,
mhorn@sanfordlab.org

RECEIVED 09 October 2023
ACCEPTED 27 November 2023
PUBLISHED 15 December 2023

CITATION
Horn M and Woodward EL (2023), Sanford Underground Research Facility's approach to school education, community activities, and public outreach.
Front. Phys. 11:1310451.
doi: 10.3389/fphy.2023.1310451

Sanford Underground Research Facility's approach to school education, community activities, and public outreach

Markus Horn* and Erin Lorraine Woodward

Sanford Underground Research Facility, Lead, SD, United States

The Sanford Underground Research Facility (SURF) is the deepest underground science facility in the United States. SURF hosts world-leading experiments in neutrino, astroparticle and nuclear physics, as well as projects in biology, geology, and engineering, and is home to a major excavation project making space for Fermi National Accelerator Laboratory's Long-Baseline Neutrino Facility (LBNF), which will power the Deep Underground Neutrino Experiment (DUNE). An emphasis on outreach and education is embedded in SURF's mission statement: "to advance world-class science and inspire learning across generations." To achieve this mission, SURF goes beyond established science communication methods, including operating an open-to-the-public visitor center, hosting multiple public outreach events per month, and an annual city-wide science festival. Furthermore, SURF is training K-12 science educators, developing school curriculum units, and providing classroom materials, based on science researched at the laboratory. The strategic approach, specific methods, and successful outcomes of these programs, which are based on SURF's science, location, and community, may serve as examples for effective science education, public outreach, and community engagement.

KEYWORDS

astroparticle physics, underground laboratories, multidisciplinary science, education, public outreach

1 SURF overview

1.1 History, legacy and context of the underground facility

The Black Hills, a mountain range rising from the Great Plains of North America, is located in the western region of South Dakota. Called Paha Sapa, "The Heart of Everything That Is", in Lakota language, the Black Hills are considered sacred to many Native American tribes, primarily of the Lakota and Dakota nations, and the core of their spiritual inheritance. The region's complex geology and discovery of gold eroded from hard-rock deposits, lead to extensive mineral exploration in the 19th century. Starting in 1876, the Homestake Gold Mine in Lead, South Dakota, became the largest and deepest gold mine in North America until it ceased mining operations in 2001. Long before it was transformed into a dedicated underground laboratory, the Homestake Gold Mine had a notable scientific legacy [1]. Starting in the late 1960s, Dr. Raymond Davis Jr. counted neutrinos from the Sun in a laboratory on the 4850-foot level of the mine [2]. The experiment operated continuously from 1967 until 1994 and earned Davis a share of the 2002 Nobel Prize in Physics. Due to a

sharp decrease in the value of gold, Homestake was forced to close the operation of the mine; initially mining in 2001, and all other operations, including dewatering the underground, in 2003. However, discussions about the mine's future as a research facility were already underway. A few years later, with a generous donation from the facility's namesake T. Denny Sanford, a land donation from mine owner Barrick Gold Corporation and the formation of a governmental entity by the State of South Dakota, the South Dakota Science and Technology Authority (SDSTA), to manage the facility, the science facility was officially opened in 2007 and access for researchers to the 4850-foot level was restored in 2009.

1.2 SURF structure and affiliated organizations

SURF is operated by the SDSTA, under the direction of the SDSTA Board of Directors with funding from the U.S. Department of Energy's Office of Science. In 2020, the SDSTA established the SURF Foundation, a tax-exempt non-profit organization to raise funds in support of the science and education goals of the SDSTA. The SURF Foundation is separate from SURF and has its own Board of Directors. The Institute for Underground Science at SURF (The Institute), which aims to provide a space for intellectual communities to come together and have truly transformative conversations, was launched in June 2023 by the SDSTA. The Institute's inaugural event was the Center for Theoretical Underground Physics and Related Areas (CETUP*) conference[1] in June 2023. The conference, which had been held annually from 2011 through 2016, was revived under the umbrella of The Institute, to engage researchers from all areas of underground science, including physics, biology, geology, and engineering, to participate in conversations about the future of their research. The 2023 conference drew nearly 70 theorists, experimentalists, and students representing 47 institutions. The future program of The Institute, including conferences, graduate and undergraduate summer schools and expansion of collaborative programs with other institutions, are currently under development.

1.3 Science at SURF

Central to SURF's core institutional mission is the advancement of compelling underground and multidisciplinary research. Once underground access was re-established, science efforts have seen consistent growth [3]. Since then, a total of 64 groups have conducted underground research programs at SURF across a range of laboratory elevations from the surface to the 5000-foot level (with a major footprint on the 4850-foot level). At present, a total of 32 research programs are ongoing, with 22 of these programs maintaining a regular onsite presence. Excluding DUNE, the facility accommodates approximately 400 individual researchers from a larger pool of over 700 collaboration members contributing to the experiments at SURF. Nine U.S. National Laboratories are represented among a network of over 100 institutions from 9 countries.

Among the experiments at SURF are the LUX-ZEPLIN (LZ) dark matter experiment collecting WIMP search data since 2021, with world-leading results published recently [4]. The MAJORANA DEMONSTRATOR focusing on neutrinoless double-beta-decay published final results in 2023 [5] and is presently searching for the decay of ^{180m}Ta [6]. The Enhanced Geothermal System (EGS) Collab–SIGMA-V project completed two rock stimulation and flow tests in different rock formations [7], one of which will be repurposed starting late 2023 to conduct research in underground thermal energy storage technologies. The Compact Accelerator System for Performing Astrophysical Research (CASPAR) is concentrating on nuclear astrophysics research ([8], including recent results [9]). CASPAR is at present mothballed due to the excavation activities for the DUNE experiment, but is planning to resume activities in 2024.

Low background assays of materials, available to all users and experiments, not limited to SURF projects, are conducted through the Black Hill State University (BHSU) Underground Campus (BHUC). The BHUC is currently operating six radioassay instruments. In addition, local universities have supplemental material screening capabilities: ICP-MS (BHSU) and radon-emanation characterization (South Dakota Mines). Production of electroformed copper is also performed at SURF. The Majorana collaboration has produced electroformed copper since mid-2011, a total of 2,500 kg for the MAJORANA DEMONSTRATOR, and is presently continuing for LEGEND [10]. Upcoming, DUNE will investigate neutrino properties (oscillations, CP violation, mass hierarchy), nucleon decay and study supernovae neutrinos [11].

Due to the vast underground network of more than 600 km of tunnels extending to over 2,450 m below ground (not all currently accessible), a wide variety of environmental and geochemical conditions and a large network of legacy boreholes from Homestake mining exploration, researchers studying extremophilic organisms and biofilms represent a vital part of SURF's multidisciplinary community with high-impact scientific results.

2 SURF school education and curriculum development

An emphasis on education and public outreach is embedded in SURF's mission statement since its inception: "to advance world-class science and inspire learning across generations." The dedicated Education and Outreach (E&O) department at SURF has worked with schools (kindergarten to grade 12 or K-12) and post-secondary learning institutions across South Dakota. The SURF E&O department at its core mission believes that every student deserves high quality, rigorous, relevant, equitable, and engaging science learning opportunities. The efforts of the department include four main categories: 1) hosting school field trips to SURF and delivering in-school presentations (in-person or virtual); 2) the development and deployment of no-cost curriculum units to classrooms across the state, 3) the creation of career exploration opportunities, and 4) teacher professional development and support. Much of this work is done in partnership with BHSU.

1 https://indico.sanfordlab.org/event/53

2.1 Field trips and in-school presentations

SURF field trips include tours of surface facilities, including the Yates hoistroom (one of the two available hoists at SURF), where students see the large machinery that powers travel in and out of the underground, and SURF's own wastewater treatment plant, which manages water pumped from the underground before it is returned to local waterways. Field trips also include hands-on activities which engage students with the scientific and engineering concepts being studied at the facility. In-school presentations delivered to individual classrooms or large-group auditoriums, also include hands-on learning experiences for students. These presentations are predominantly given in person, by members of the SURF E&O team traveling to schools (including very remote schools in rural counties in South Dakota). Although, the inherent time, distance, and frequency restrictions of these presentations and field trips may limit the impact of these programs, the E&O team leverages these to establish connections with educators and school districts, which in turn can lead to sustained, high-impact relationships.

2.2 Curriculum modules

The SURF E&O team develops and ships school curriculum modules addressing science, technology, engineering, and math (STEM) concepts to classrooms across South Dakota and the surrounding region. The curriculum modules are provided at no cost to the educators, who often are required to purchase their own materials for classroom instruction. These modules leverage phenomena being studied at SURF—from dark matter and neutrinos to hoist engineering challenges—to connect students with the world-class research being pursued in their home state of South Dakota. Each module includes all the tools a school teacher needs for 10–20 h of instruction. The modules are developed with input from teachers across the state, aligned with South Dakota's K-12 Science Standards, and employ best practices in pedagogy, including phenomena-based, three-dimensional instruction [12]. This approach shifts science education from rote memorization to thinking like a scientist, investigating scientific concepts and solving problems.

2.3 Educator professional development

The SURF E&O team creates and hosts professional development workshops that use tested teaching techniques and innovative science to transform the teaching of K-12 science in South Dakota. These workshops utilize a three-dimensional teaching and learning approach; employ real phenomena and unsolved questions being explored underground; shift students from "learning about" a topic to "figuring out" for themselves; and connect teachers to the innovative science at SURF. Through grants and partnerships with several statewide entities, the E&O team offers no-cost programming, lodging, and, in some cases, stipends to workshop participants, especially important for rural and underserved communities. Upon completion of workshops, participants qualify for graduate credits from BHSU. Since 2020, the E&O team has implemented in-person, virtual, and hybrid options for workshops; these flexible options help remove cost, time, and travel barriers for participants.

2.4 Career exploration

The SURF E&O team creates career exploration opportunities for South Dakota's post-secondary students, including an internship program, the Davis-Bahcall Scholars Program, and pre-service educator training. SURF's summer internship program[2] offers paid, 10-week internships in a variety of disciplines, including science, engineering, education, communications, operations, underground access, and environment, health and safety. Undergraduate and graduate interns work with experts from around the globe, gaining real-world experience while helping SURF meet the challenges of operating the facility. The Davis-Bahcall Scholars program[3] is an all-expense-paid, 4-week tour of university, laboratory, and industry research centers throughout the United States and abroad. The program is designed to help first- and second-year university students who are entering science, technology, engineering, and math fields to gain insight of potential career paths. The E&O team partners with faculty from five South Dakota universities to provide training to pre-service teachers. These trainings familiarize future teachers with best practices for science education, as well as the resources available to them through SURF.

2.5 Results

The SURF E&O team collects quantitative data on K-12 student participation in field trips and in-school presentations; university student participation in career exploration programs; educator participation in professional development workshops; and curriculum module usage; as well as the percentage of school districts reached in South Dakota. The team also collects qualitative data through presentations from career exploration participants; real-time discussions and surveys from professional development participants; and feedback from education faculty whose classes are involved in preservice teacher training programs. In 2022–23 (July to July), the E&O team reached via the various avenues, over 17,000 students, covering every, even the remotest county of a mostly rural and sparsely populated state of South Dakota (and nearby counties of some neighboring states); see also Figure 1. These numbers follow a trend of steady, significant growth over the last 15 years, despite the unique challenges since 2020 introduced by the COVID-19 pandemic, which necessitated a swift adaptation to virtual in-school presentations. Since then, the E&O team has resumed its focus on in-person field trips and presentations with the focus on more rural and historically underserved communities, and often schools with very small student enrollments.

2 https://sanfordlab.org/internships

3 https://sanfordlab.org/dbs

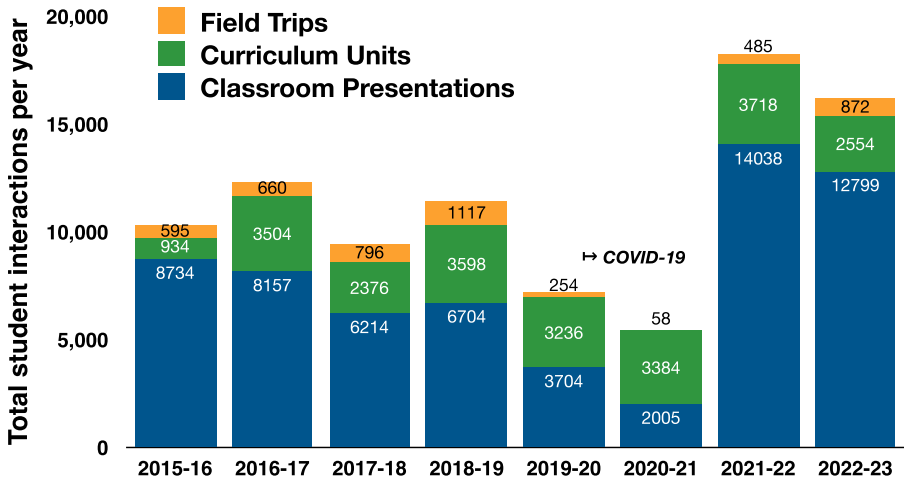

FIGURE 1
Total student interaction numbers per year (July to July) constituted by the number of students on field trips visiting SURF, students participating in curriculum units developed by the SURF E&O team, and students reached by SURF E&O classroom presentations (in person and virtual).

Several strategies and lessons learned have emerged that may be helpful for other institutions looking to expand their education programming.

- Identifying high-leverage opportunities:
  The E&O team continually evaluates the relative impacts of their program offerings in order to focus on high-leverage, transformational efforts. For example, while field trips and in-school presentations generate an impressive number of direct interactions with students, the short-term nature of those interactions do not create sustained, long-term impacts. Rather than striving to increase those numbers, the E&O team sees these programs as an opportunity to establish relationships with educators and school districts. The team focuses their efforts on curriculum modules, which generate up to 20 h of classroom science instruction, and on professional development workshops, which train cohorts of educators with a sustained impact towards student science education.
- Designing "place-based" content:
  SURF increased audience engagement and relevance by designing content with direct connections to our local community and environment. South Dakota is a rural state that is widely known for its agriculture and tourism industries. The E&O team leverages science taking place at SURF by tying content to research at a world-leading research facility located in their home state. This inspires a sense of ownership and relevance to audiences.
- Increasing accessibility:
  The E&O team uses state demographic data and self-reported data from educators to target efforts to those who need it most. In South Dakota, rural and remote school districts often have fewer resources than school districts in urban areas. Though giving presentations in urban schools results in higher student interaction numbers, the E&O team chooses to focus their efforts in rural and remote districts. Additionally, in many US schools, teachers in classrooms with students under the age of 12 typically have less time to devote to science education than middle and high school educators do; thus, the E&O team focuses their efforts on designing curriculum models and professional development programs for educators working with younger students.

3 Sanford Lab Homestake Visitor Center

In 2015, the Sanford Lab Homestake Visitor Center (Visitor Center) was built with SDSTA funds to commemorate the history of Lead, South Dakota, and to highlight scientific discoveries related to SURF. The approx. 750 m^2 (8,000 sq ft) building features a gift shop, conference rooms, and an exhibit hall that highlights the history of the Lead area, as well as the research taking place at SURF.

The Visitor Center was owned and operated by the Lead Area Chamber of Commerce from 2015 until 2022. In January 2022, ownership transferred to the SDSTA. Since 2022, the SDSTA has updated facility infrastructure, updated exhibits, and increased tour offerings and event programming. The location of the Visitor Center on Main Street in Lead, has uniquely positioned it to be both a hub for outreach of the laboratory, as well as a vital community information resource and tourism destination attracting nearly a total 55,000 visitors in the year 2022. The Visitor Center exhibits include panels with photography, graphics, and information about the Black Hills's unique geology, the 1870s gold rush, the Homestake Gold Mine and its influence on the region, the history of science at the mine, the Nobel Prize-winning Solar Neutrino Experiment of Dr. Raymond Davis Jr., and current science taking place underground. Exhibits also include a suspended scale model of the underground workings, a cage conveyance that once transported people and equipment in and out of the underground, the LUX

FIGURE 2
The Sanford Lab Homestake Visitor Center is located on the southern edge of the historic mining pit ("Open Cut") of the Homestake Gold Mine in downtown Lead, South Dakota. It is a space for SURF to connect with the local community, host events and tours, and provide information to locals and tourists. Reproduced with permission from Stephen Kenny (SDSTA), Sanford Underground Research Facility, June 2023.

FIGURE 3
SURF's Artists in Residence create a collection inspired by the science, history, and community of SURF. Reproduced with permission from Ashley Beguin (SDSTA), Sanford Underground Research Facility, July 2023.

detector, which was the world's most sensitive dark matter detector from 2013 until 2017, and the "Davis Ring", an original piece of the experiment's water tank now displayed outside next to the building. The Visitor Center also offers a view of Homestake Gold Mine's historic mining pit ("Open Cut") from an observation deck (see Figure 2).

Among the many offerings of the Visitor Center are trolley tours of the City of Lead, which include a visit to one of two hoistrooms on SURF property. Built in the 1930s to support gold mining operations, the hoists are still in use today to transport scientists and research equipment to laboratories up to the 5000-foot level, approx. 1.5 km below the surface. The Visitor Center hosts events for a variety of audiences, from locals to tourists, technical and non-technical alike. "Deep Talks", a monthly lecture series, invites local audiences of scientific and non-scientific backgrounds to learn more about research taking place underground and across the state. The

FIGURE 4
At SURF's Neutrino Day, visitors of all ages get hands-on science experiences. Reproduced with permission from Stephen Kenny (SDSTA), Sanford Underground Research Facility, July 2023.

monthly "Ask-A-Scientist" series gives audiences the opportunity to chat informally with a scientist who conducts research at SURF. Other community events include book signings with local authors, a Fourth of July fireworks viewing party near the Open Cut, and "Trunk-or-Treat", a Halloween-themed event which invites children to dress up and "trick-or-treat" safely in the Visitor Center parking lot as well as participation in many other City of Lead events. Furthermore, due to its unique location and scenic backdrop near the Open Cut, the Visitor Center is also a popular venue for private events.

3.1 Impact and insights

The Visitor Center has become a very popular tourism destination by itself in the Black Hills of South Dakota, attracting solo travelers and families to organized charter tours. Key performance indicators for public outreach include length of time of visits, return visitation, number of visits, event attendance, informal surveying, online reviews (Google, Facebook, Yelp, etc.), number of bus tours that seek this location out, and the frequency of private rentals.

For other institutions seeking to expand their outreach programming, here are several strategies and lessons learned that have emerged from the operation of the Sanford Lab Homestake Visitor Center.

- Intergenerational learning:
  As a general public visitor center, guests often travel in family units, meaning each group includes visitors of various ages and a range of technical backgrounds. To create an engaging attraction, a visitor center must offer a range of experiences. To appeal to diverse audiences, the Visitor Center offers scavenger hunts for young guests, 3-D virtual reality headsets offering virtual underground tours, and exhibits that capture the attention of adult visitors. Some offers, such as the "Ask-a-Scientist" series or guided tours can be adjusted to engage visitors of diverse ages and backgrounds, as determined by the scientist and/or guide.
- Dynamic offerings:
  The Visitor Center seeks to offer a new experience to people every time they visit. This has inspired the Visitor Center staff to think outside the box, offering talks with experts, interactive exhibits, and increased tour offerings that are captivating, even for repeat visitors.
- Focus on audience needs:
  The Visitor Center's location on Main Street in Lead, along with its history as the city's sole visitor center, has uniquely positioned it to be both a hub for lab outreach, as well as a vital community information resource and tourism destination. This multi-purpose space has enhanced SURF's ability to communicate and build relationships within its local community.
- Room for future growth:
  SURF leadership acknowledges that more work can be done to acknowledge the complex history and cultural significance of the Black Hills area, especially to the indigenous population. A strategy is currently under development to achieve this mission.

4 SURF artist-in-residence program

SURF's unique location in the Black Hills of South Dakota and history as a former gold mine and home to Nobel Prize-winning physics experiment make it an ideal place for creative work. The SURF Artist-in-Residence (AiR) program invites artists to create work inspired by SURF, leveraging the unique characteristics of the underground facility and the science experiments it hosts to create awareness and encourage interdisciplinary work. The program is open to artists in all media; this includes, but is not limited to, visual artists, filmmakers, writers, and musicians. The program has a rigorous application and selection process. The selection committee considers each applicant's professional record including major regional, national or international exhibitions, or similarly documented experience. The SURF AiR program provides

transportation, housing, per diem for visits, studio space, and stipends for their work.

4.1 Outcome

This program includes several key deliverables, including the exhibition, artwork in SURF's permanent collection, and public outreach events, such as artist talks and open studio days, see Figure 3. The SURF AiR includes a 4-week on-site visit during the summer and a 1-week art installation/guest lecture visit during the fall. The artist will have an art exhibition and up to two lectures based on the artist's proposal during the fall. In addition to the lectures, each artist will provide promotional or outreach events within the local community. Each artist will donate at least one piece of artwork to the facility to be included in the SURF permanent art collection. In previous years, artists also secured exhibitions and events at universities across South Dakota as well as other institutions with a strong connection to underground science, further increasing the impact of the program, as described below.

Since the creation of this program in 2019, several best practices have enhanced SURF's AiR program, including the following.

- Leveraging partnerships with the arts to engage new audiences:
  As research facilities strive to attract attention to STEM subjects, partnerships with artists or art institutions can broaden the appeal of facility offerings, connect new audiences to the research taking place at a facility, and even propel new discoveries through inter-departmental collaboration.
- Extending the life of an exhibit:
  The impact of an art exhibit can be strengthened by advertising the collection and advancing opportunities for repeat exhibitions at partner institutions. Gina Gibson, SURF's 2019 artist in residence, created her original SURF-inspired exhibit in 2020. The exhibition was hosted virtually, due to the COVID-19 pandemic. Through SURF's continued promotion of the collection, Gibson was invited to bring the collection to the University of Michigan for a 1-year exhibition. This extended life of the exhibit is now inviting audiences in Michigan to learn about science at SURF through art.
- Engaging the general public:
  In addition to attending a final exhibition, there are ample opportunities for the general public to engage with the artist. SURF has hosted open studio sessions, meet-and-greets, and virtual Q&A sessions to increase the visibility and impact of a visiting artist.

5 SURF Neutrino Day

Neutrino Day is SURF's signature public outreach event, a free science festival that takes place annually throughout Lead on the second Saturday of July. The event invites attendees to take part in hoistroom tours, science activities and exhibits for all ages, live video chats with scientists underground at SURF, and engaging talks about the research happening deep underground beneath their feet, see Figure 4. Over the past 15 years, Neutrino Day has grown to include dozens of activities in several locations within the community. Building on that success, SURF is envisioning Neutrino Day to become one of the world's premiere science festivals and establishing Lead and the South Dakota Black Hills as a science destination. As the SURF team works toward that vision, Neutrino Day efforts build brand recognition for the organization as a whole; offer greater opportunities to partner with local, regional and international communities, create additional opportunities for fundraising, bring greater attention to the Visitor Center, the SURF Foundation, and the Institute for Underground Science at SURF; and foster planned and organic interactions between the arts and sciences.

5.1 Participation and review

SURF tracks the number of in-person and virtual attendees, as well as attendee feedback, volunteer feedback, and repeat partner participation rate. In 2023, more than 2,000 visitors participated in the activities at Neutrino Day, as estimated by free wrist-bands given to each visitor checking in at multiple welcome stations. (For context, the total population of Lead-Deadwood and surrounding communities is approximately 5,000).

After 15 years celebrating Neutrino Day, SURF as the coordinating organization learned that large-scale events are largely more successful when the planning achieves the following:

- Achieving brand recognition:
  For all previous years, Neutrino Day had a unique theme and brand each year. As the event grew, drawing reliably more than 1,000 attendees from around the globe each year, the planning committee acknowledged the need for a consistent, recognizable brand. In 2022, SURF trademarked the name "Neutrino Day" and developed a new brand identity and website for the event with the help of a third-party design group[4]. By adopting a high-quality, consistent brand, SURF hopes to increase brand recognition and spur repeat attendance.
- Strong partnerships with local, regional, and international communities:
  Neutrino Day would not be possible without the contribution of our donors and partners. Each year, the event is supported by volunteers who host booths, give talks, set up and tear down, and help guests navigate the event. These partnerships range from local businesses and regional education organizations to international science partners, like STFC in the United Kingdom and CERN in Switzerland.

6 Conclusion

The Sanford Underground Research Facility, in addition to being home to a large variety of world-leading research in multiple science

4 https://neutrinoday.com

disciplines, strives to improve public outreach and community engagement. SURF aims to meet audiences where they are. That means leveraging their curiosity and making the science approachable to the general public, to teachers and to students. With every outreach activity, SURF tries to make the learning relevant and engaging to science-curious learners of all ages by connecting the science to South Dakota—and to people's interests, including art, history, and culture. In this way, SURF reaches a much broader audience. This approach and the methods described, may serve as examples for effective science education, public outreach, and community engagement to research facilities and underground laboratories specifically.

Data availability statement

The original contributions presented in the study are included in the article/Supplementary Material, further inquiries can be directed to the corresponding author.

Ethics statement

Written informed consent was obtained from the individual(s), and minor(s)' legal guardian/next of kin, for the publication of any potentially identifiable images or data included in this article.

Author contributions

MH: Writing–original draft. EW: Writing–original draft.

Funding

The author(s) declare that financial support was received for the research, authorship, and/or publication of this article. This material is based upon work supported by the U.S. Department of Energy Office of Science under award number DE-SC0020216.

Conflict of interest

The authors declare that the research was conducted in the absence of any commercial or financial relationships that could be construed as a potential conflict of interest.

Publisher's note

Supplementary material

The Supplementary Material for this article can be found online at: https://www.frontiersin.org/articles/10.3389/fphys.2023.1310451/full#supplementary-material

References

1. Mitchell S. *The Riches of our universe: the Homestake Legacy at the Sanford underground research facility*. Lead, South Dakota: Sanford Underground Research Facility (2023).

2. Bahcall JN, Davis R. Solar neutrinos: a scientific puzzle. *Science* (1976) 191:264–7. doi:10.1126/science.191.4224.264

3. Heise J. The Sanford Underground Research Facility (2022). Contribution to Snowmass 2021. doi:10.48550/arXiv.2203.08293

4. Aalbers J, Akerib DS, Akerlof CW, Al Musalhi AK, Alder F, Alqahtani A, et al. (2023). FFirst dark matter search results from the LUX-ZEPLIN (LZ) experiment. *Phys Rev Lett* 131:041002. doi:10.1103/PhysRevLett.131.041002

5. Arnquist IJ, Avignone F, Barabash A, Barton C, Barton P, Bhimani K, et al. Final result of the MAJORANA DEMONSTRATOR'S search for neutrinoless double-β decay in ^{76}Ge. *Phys Rev Lett* (2023) 130:062501. doi:10.1103/PhysRevLett.130.062501

6. Arnquist IJ, Avignone F, Barabash A, Barton C, Bhimani K, Blalock E, et al. Constraints on the decay of ^{180m}Ta. *Phys Rev Lett* (2023) 131:152501. doi:10.1103/PhysRevLett.131.152501

7. Kneafsey TJ, Dobson PF, Ulrich C, Hopp C, Rodríguez-Tribaldos V, Guglielmi Y, et al. The EGS Collab project – stimulations at two depths. In: Proceedings of the Paper presented at the 56th U.S. Rock Mechanics/Geomechanics Symposium; June 2022; Santa Fe, New Mexico, USA (2022). doi:10.56952/ARMA-2022-2261

8. Robertson D, Couder M, Greife U, Strieder F, Wiescher M. Underground nuclear astrophysics studies with CASPAR. *EPJ Web of Conferences* (2016) 109:09002. doi:10.1051/epjconf/201610909002

9. Borgwardt TC, deBoer RJ, Boeltzig A, Couder M, Görres J, Gula A, et al. Deep underground measurement of ^{11}B$(\alpha,n)^{14}$N. *Phys Rev C* (2023) 108:035809. doi:10.1103/PhysRevC.108.035809

10. Abgrall N, Abramov A, Abrosimov N, Abt I, Agostini M, Agartioglu M, et al. The large enriched germanium experiment for neutrinoless double beta decay (LEGEND). In: Proceedings of the workshop on calculation of double-beta-decay matrix elements (medex'17); June 2017; Prague, Czech Republic. American Institute of Physics Conference Series (2017). doi:10.1063/1.5007652

11. Abi B, Acciarri R, Acero M, Adamov G, Adams D, Adinolfi M, et al. Volume I. Introduction to DUNE. *J Instrumentation* (2020) 15:T08008. doi:10.1088/1748-0221/15/08/T08008

12. NGSS Lead States. *Next generation science Standards: for states, by states*. Washington, DC: The National Academies Press (2013).

frontiers | Frontiers in Physics

TYPE Original Research
PUBLISHED 03 January 2024
DOI 10.3389/fphy.2023.1290449

OPEN ACCESS

EDITED BY
Sean M. Paling,
Science and Technologies Facilities Council, United Kingdom

REVIEWED BY
Marzio De Napoli,
National Institute of Nuclear Physics of Catania, Italy
Giulia D'Imperio,
Istituto Nazionale di Fisica Nucleare, Sezione di Roma, Italy

*CORRESPONDENCE
Alessandro Razeto,
razeto@infn.it
Nicola Rossi,
nicola.rossi@lngs.infn.it

RECEIVED 07 September 2023
ACCEPTED 07 November 2023
PUBLISHED 03 January 2024

CITATION
Razeto A and Rossi N (2024), Challenges for dark matter direct search with SiPMs. *Front. Phys.* 11:1290449. doi: 10.3389/fphy.2023.1290449

Challenges for dark matter direct search with SiPMs

Alessandro Razeto* and Nicola Rossi*

Gran Sasso National Laboratory (INFN), L'Aquila, Italy

Liquid xenon and liquid argon detectors are leading the direct dark matter search and are expected to be the candidate technology for the forthcoming generation of ultra-sensitive large-mass detectors. At present, scintillation light detection in those experiments is based on ultra-pure low-noise photo-multipliers. To overcome the issues in terms of the extreme radio-purity, costs, and technological feasibility of the future dark matter experiments, the novel silicon photomultiplier (SiPM)-based photodetector modules seem to be promising candidates, capable of replacing the present light detection technology. However, the intrinsic features of SiPMs may limit the present expectations. In particular, interfering phenomena, especially related to the optical correlated noise, can degrade the energy and pulse shape resolutions. As a consequence, the projected sensitivity of the future detectors has to be reconsidered accordingly.

KEYWORDS

noble gas detectors, time projection chamber, light yield, dark matter, silicon photomultiplier, optical cross-talk

1 Introduction

Indirect astrophysics observations from galactic to large structure scales imply the presence of a non-luminous and hidden mass, commonly named *dark matter*, accounting for approximately 85% of the matter content of the Universe (for a review, see, e.g., [1]). Although the nature of this missing ingredient is still unknown, many particle candidates have been proposed over the recent decades, with masses ranging from fractions of eV/c^2 to the grand unification mass scale. Weakly interacting massive particles (WIMPs), with mass in the range from 1 GeV/c^2 up to 1 TeV/c^2 [2, 3], have been considered promising candidates, as originating from natural high-energy extensions of the Standard Model of particle physics. However, the lack of observation in many direct and indirect searches has led to the questioning of their theoretical foundations recently [4].

Since the beginning of the new millennium, the direct dark matter search has been attracting a lot of interest in the astroparticle physics community, with a substantial effort in terms of engagement and funding. Since the majority of the experiments searching for WIMPs are providing null results, a quest is ongoing for the deployment of the ultimate hundred-ton-scale targets. The latter effort requires experimental technology that is easily scalable while preserving a very low level of background, high detection efficiency, and stable behavior over time exposures of tens of years.

One of the most successful and scalable detection technologies is based on liquid noble gas, in particular on xenon and argon. Both targets show clear *pros and cons*, and at the moment, the scientific community is split down the middle, and there is no clear choice for the ultimate experiment capable of reaching the so-called *neutrino floor* limit in the forthcoming decades [5, 6]. The experiments based on the xenon double-phase time projection chamber (TPC), as LZ [7], XENON1T [8], and PANDAX-4T [9], reported

independently the strongest bound on the spin-independent (SI) WIMP–nucleon interaction (for a review of dark matter refer to [10]). DEAP-3600 [11], a single-phase liquid argon detector, reported an independent, even if less stringent, limit for the same interaction. Finally, DarkSide-50, using ultra-pure underground argon in a double-phase TPC, has set a corresponding limit, constraining especially the region down to a few GeV/c^2 [12, 13].

Recently, LZ has reported the strongest SI limit [7], and XENONnT has shown a very low background in the first physical data collection of its multi-ton target [14]. Meanwhile, DarkSide-20k [15], which will exploit approximately 20 ton (fiducial mass) of ultra-pure underground argon in a gigantic double-phase TPC, is under construction and should start data collection by the end of the present decade. The argon and xenon scientific communities are already designing the next iteration of experiments: the xenon community is converging on a future detector, called DARWIN, based on a target of 50 ton [6], while the argon community is planning a future detector, called ARGO-300, based on a target of 300 ton of ultra-pure argon naturally depleted in ^{39}Ar [5].

At present, the scintillation light of the aforementioned experiments is detected using ultra-pure low-noise photomultiplier tubes (PMTs) [7, 9, 11, 12, 14]. To overcome possible issues in terms of the extreme radio-purity, costs, and technological feasibility, many projects are planning to replace PMTs with novel photodetectors. In particular, the DarkSide-20k experiment, designed to reach 200 ton·y exposure, will install approximately 22 m^2 of silicon photomultiplier (SiPM) arrays [15–17].

In this work, extensive studies on the SiPM performances prove that the intrinsic features of the SiPM units, in addition to the well-known internal correlated noise, may limit the present expectations. In particular, interfering phenomena related to the optical correlated noise, i.e., the light emission of fired SiPMs triggering nearest SiPMs, produce an irreducible degradation of the resolution of the fundamental reconstructed observables as energy and pulse shape. As a consequence, the projected sensitivity on the dark matter parameter space of the future detectors, especially based on liquid argon, needs a corresponding revision.

The article is structured as follows: in Section 1, the main argon- and xenon-based characteristics concerning light detection are described; in Section 2, the main feature of the SiPM-based photodetector module at cryogenic temperature is reviewed, and the noise classification and the impact on the event reconstruction are largely discussed; in Section 3, a toy Monte Carlo simulation for a multi-ton liquid argon TPC is performed, and the impact of the correlated noise in the final dark matter analysis is outlined. Finally, in Section 4, the implication of the irreducible correlated noise on the dark matter sensitivity plots is discussed.

2 Liquid noble gas detectors

Noble liquid detectors can be designed to exploit either single- [11] or double-phase TPC [7, 9, 14, 15, 18]. The first type has a simpler design and shows fewer technological challenges. In those detectors, like DEAP-3600 [11], the liquid noble gas fills up a spherical vessel whose surface is instrumented with PMTs to detect the scintillation light. The reconstructed position is less accurate than in double-phase detectors, and it is, in principle, difficult to reject the pile-up events. In contrast, the second type shows a more complex design but features many advantages in terms of event reconstruction. A double-phase TPC is typically a cylindrical-shaped vessel filled with a noble liquid. On top of the liquid free surface, there is a thin gas pocket, separated by a conductive grid. On the bottom and on the top of the cylinder, there are a cathode and an anode, respectively, able to set the so-called *drift* and *extraction* fields. For each ionizing particle hitting the detector, two signals are produced: the first scintillation signal is originated in the liquid by the primary interaction and is typically called S1, whereas the second signal (S2) is produced by electro-luminescence of the gas pocket when ionization electrons, pulled upward by the drift fields, are accelerated in the gas pocket by the extraction field. The double signal allows to increase the spatial resolution and exploit the pulse shape discrimination between electron recoils (ERs) and nuclear recoils (NRs) using the ratio S2/S1.

Among the available noble gases in nature, at present, only argon and xenon have shown a reasonable feasibility in terms of costs and performances. Both technologies have proven to be easily scalable to multi-ton scales, with no insuperable obstacles and with reasonable economical effort. However, the two gases have very different physical properties being, to some extent, complementary. This is especially true as well for the design of PMT- and SiPM-based photodetectors.

The use of PMTs in liquid argon has experienced a very critical performance in terms of electronics stability, due to the very low cryogenic temperature of 87 K. In addition, the 128-nm scintillation light does not match the PMT photo-cathodic sensitive window, and therefore, a wavelength shifter-coated reflector is needed (typically made of tetraphenyl butadiene (TPB) at 420 nm [18]). On the contrary, in liquid argon, the use of SiPMs is encouraged by the low dark rate at 87 K and by the easy detection of visible shifted scintillation light that matches the high photon detection efficiency (PDE) of commercial SiPMs [19, 20].

For the xenon-based detector, instead, the use of PMTs is much convenient since they operate steadily at the xenon cryogenic temperature (165 K) and are highly sensitive to the scintillation light at 178 nm without the need for a wavelength shift. Concerning the use of SiPMs in xenon, in principle, photo-cathodic surfaces with a reasonable PDE to vacuum ultraviolet light are already available. However, the higher cryogenic temperature could not be sufficiently low to bring the dark rate down to an acceptable threshold.

3 SiPM-based photodetectors

SiPMs are solid-state devices based on single-photon avalanche diode (SPAD) micro-cells on silicon substrates [21]. The dimension of each single SPAD ranges between 10 and 100 μm. Each SPAD operates in the Geiger mode, coupled with the others by means of a quenching circuit. For analog SiPMs, the signal of the micro-cells is summed in parallel by appropriate quenching resistors; this results in a dynamic range spanning from one to thousands of photo-electrons (for mm^2) with an intrinsic photon-counting resolution exceeding few percent [22]. SiPMs produce a signal proportional to

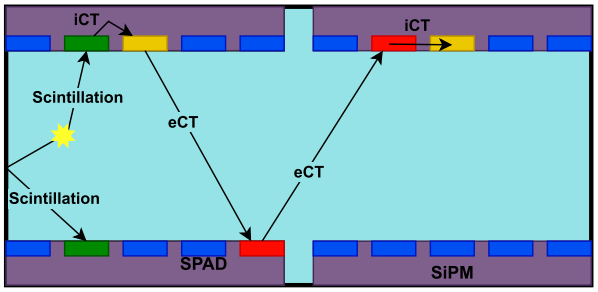

FIGURE 1
Photon detection in a high-coverage detector with SiPMs: scintillation photo-electron may be followed by a cascade of internal and external cross-talks. The SiPMs are drawn in gray with blue SPADs that become green/red/yellow when triggered, respectively, by a primary photon, eCT, and iCT (see text). All surfaces of the chamber are highly reflective; the scintillation medium is shown in cyan. For simplicity, after-pulsing is not shown.

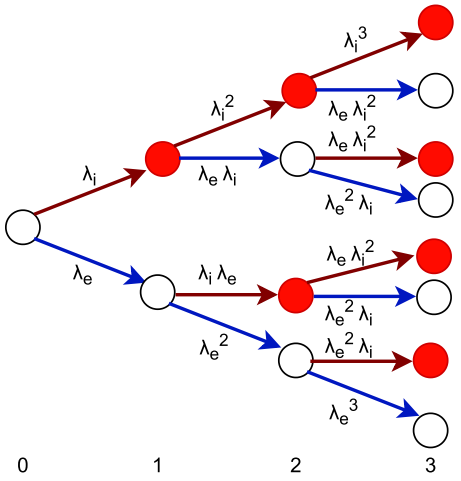

FIGURE 2
Optical cross-talk cascade in the presence of both internal and external processes. For level n of recursion, the average number of avalanches is $N^n = (\lambda_{iCT} + \lambda_{eCT})^n$ (for brevity, the CT pedix has been removed in the figure), while the number of iCT-only photo-electrons (red circles) is $N^n_{iCT} = N^{n-1}\,\lambda_{iCT}$ (n > 0). The sum over i converges to $\mathcal{G}_{oCT}$, defined in Equation 2, and $N_{iCT} = \mathcal{G}_{oCT}\,\lambda_{iCT}$.

the bias exceeding the breakdown voltage (typically between 20 and 50 V) with over-voltages (OV) in the range 2–10 V [23].

Since first measurements at cryogenic temperature [24], Fondazione Bruno Kessler intensified the effort for the development of SiPMs for cryogenic particle detectors. The current cryogenic near-ultraviolet high-density (NUV-HD-Cryo) family is capable of stable operation in liquid nitrogen/argon at over-voltages in excess of 10 V [25]. These devices are optimized for the detection of NUV and blue light with a peak photon detection efficiency close to 60% [19], measured at room temperature. The primary dark rate is lower than few counts per square centimeter per second at 77 K [26].

Beyond the dark rate, SiPMs exhibit correlated noises: after-pulsing (AP) occurs when, during an avalanche, a carrier is temporarily trapped by impurities in the medium. When released, a second avalanche is generated. If detrapping happens before SPAD is fully recharged, the after-pulse will have a charge lower than that of the single photo-electron. *Optical cross-talk* (oCT) is triggered by photons generated as the secondary process during the avalanche. These photons can interact with a neighbor micro-cell and generate *internal cross-talk* (iCT), or escape the silicon bulk and generate *external cross-talk* (eCT) in the nearest SiPMs. Figure 1 shows the optical-crosstalk cascade in case of high photo-detection coverage. Consider that in TPCs, due to the high reflectivity of the chosen materials, the collection efficiency for photons can typically exceed 90% [27]. Furthermore, the final signal is inevitably affected by electronic noise amplified and shaped by the read-out electronics.

At Laboratori Nazionali del Gran Sasso (LNGS), large integrated photodetectors for cryogenic applications have been developed [16, 22]. It is now possible to aggregate the signals of 96 SiPMs into a single analog output covering a surface of 100 cm^2 [17]. As a result, it is now possible to plan for large dark matter experiments using SiPMs for light detection [15].

3.1 Optical cross-talk models

The scientific literature reports many measurements of optical cross-talk for SiPMs (see, for example, [28–31]). In a highly reflective environment, the optical cross-talk cascade process leads to an information-less multiplication of the number photo-electron, defined here as detection *noise gain* $\mathcal{G}_{oCT}$ (not be confused with the charge gain of the SiPM avalanche). In other words, the apparent light yield of a particle detector can be significantly larger than the real one since for each real photo-electron associated with the scintillation photon, a number $\mathcal{G}_{oCT}$ (> 1) is, in average, actually detected.

As described in [32], iCT follows a recursive process in which the primary avalanche is followed by secondaries, which, in turn, can produce other avalanches. The process is theoretically limited to the very large number of micro-cells in the detector (between millions and billions), but for mathematical convenience, the geometric progression is approximated with a series. Let λ_{iCT} be the mean number of secondaries for each primary avalanche ($\lambda_{iCT} < 1$); the noisy detection gain converges to $\mathcal{G}_{iCT} = 1/(1 - \lambda_{iCT})$ with an excess noise factor $\mathcal{E}_{iCT} \simeq 1 + \lambda_{iCT}$ [32]. The fluctuations in the cascade have a strong impact on the resolution of a particle detector using SiPMs: it is possible to introduce a generalized Fano factor ($\mathcal{F}_{iCT} = \mathcal{G}_{iCT}\,\mathcal{E}_{iCT}$) that directly correlates the number of detected photons with its variance.

The modeling of iCT is further complicated by the neighbors effect, for which already triggered micro-cells reduce the acceptance for new photons; therefore, both the “Branching Poisson” and the “Geometric Chain” models introduced in [33] show inaccurate results.

For a simplified symmetric detector (where all SiPMs are identical and the optical acceptances for external cross-talk are uniform), using positive feedback theory, it is possible to write

$$N_G^{pe} = N_N^{pe} + \lambda_{iCT}\,N_G^{pe} + \lambda_{eCT}\,N_G^{pe}, \tag{1}$$

where N_G^{pe} and N_N^{pe} represent the detected (gross) and scintillation (net) number of photo-electrons, respectively. Equation 1 implies only the additive and independence properties of iCT and eCT

TABLE 1 Input parameters for the toy Monte Carlo simulation extracted from [27] at 5, 7, 9 over-voltages: the last column quantifies the relative uncertainty for each parameter at one sigma. eCT includes the contribution of the feedback cross-talk measured in STAR (see text). The light yield and the external cross-talk are rescaled by the light losses of the STAR chamber (13%).

Parameter	5 OV	7 OV	9 OV	Unit	$\Delta p/p$
Scintillation light yield	11.0	12.3	13.1	*pe/keV*	10%
λ_{iCT}	18.3	29.7	41.8	%	3%
λ_{eCT}	9.2	14.9	20.9	%	3%
$P_{\mathrm{AP}}^{(1/2)}$	3.2	4.6	5.9	%	10%
Electronic noise	14	10	7.8	-	5%

photons. Under these assumptions, the oCT gain becomes by extension:

$$\mathcal{G}_{\mathrm{oCT}} = \frac{1}{1 - \lambda_{\mathrm{iCT}} - \lambda_{\mathrm{eCT}}} \tag{2}$$

that is valid for $\lambda_{\mathrm{oCT}} = \lambda_{\mathrm{iCT}} + \lambda_{\mathrm{eCT}} < 1$; otherwise, the system diverges. It may be interesting to know how many eCT photo-electrons are generated in average for each physical scintillation photo-electron, discarding the contribution of iCT. The solution is simply

$$\begin{aligned} N_{\mathrm{iCT}}^{\mathrm{pe}} &= \mathcal{G}_{\mathrm{oCT}}\, \lambda_{\mathrm{iCT}}\, N_N^{\mathrm{pe}} \\ N_{\mathrm{eCT}}^{\mathrm{pe}} &= \mathcal{G}_{\mathrm{oCT}}\, \lambda_{\mathrm{eCT}}\, N_N^{\mathrm{pe}} \end{aligned} \tag{3}$$

as the iCT and eCT probabilities are additive. Figure 2 reports a visual demonstration of these formulas for the geometric chain hypothesis. However, these are valid as well in the branching Poisson model, as application of the multinomial theorem.

For a highly reflective large-particle experiment, it is impossible to distinguish scintillation photo-electrons from the external cross-talk. The eCT emission happens with subnano-second timing [26] (significantly lower than the path spread in the detector), and photons are emitted isotropically from the surface of SiPM. As a matter of fact, eCT cannot be disentangled from scintillation photons reflected on the SiPM surface, whose reflectivity can reach 30% [34].

3.2 After-pulsing

AP adds another positive feedback contribution to the process, thus increasing the overall noise gain. Modifying Eq. 2 to include after-pulsing is not trivial because the charge gain of the avalanches depends on the delay from the primary photo-electron. At a leading order, one can write

$$\mathcal{G}_{\mathrm{oCT+AP}} = \frac{1}{1 - \lambda_{\mathrm{iCT}} - \lambda_{\mathrm{eCT}} - \lambda_{\mathrm{AP}}^{\star}}, \tag{4}$$

where $\lambda_{\mathrm{AP}}^{\star}$ is an effective parameter.

The AP probability (P_{AP}^{T}) in the literature is measured above a fixed signal amplitude, typically T = 50%. The amplitude of after-pulsing is proportional to the status of the recharge of the fired micro-cell. The signal half-life for the photodetectors in consideration is about $T^{(1/2)} = 100$ ns [17]. This means that for after-pulsing closer than $T^{(1/2)}$, the charge of the avalanche is more than halved.

The probability of emitting oCT photons is proportional to the charge of the avalanche; therefore, after-pulsing with low amplitude will not contribute significantly to $\mathcal{G}_{\mathrm{oCT+AP}}$. For NUV-HD-Cryo SiPM at the highest over-voltage, $P_{\mathrm{AP}}^{(1/2)}$ is less than one-tenth of the combined oCT lambdas (see Table 1); therefore, (at a leading order) it can be assumed $\lambda_{\mathrm{AP}}^{\star} = P_{\mathrm{AP}}^{(1/2)}$.

3.3 Streamers

In addition to the correlated noises, SiPMs are subject to stability issues at cryogenic temperatures. The DUNE collaboration has recently reported for Hamamatsu SiPMs a burst of photo-electrons at a very high rate in liquid nitrogen [35]. In analogy to discharges in Geiger–Muller tubes, such events are called *streamers*. It is sensible to suppose that NUV-HD-Cryo SIPMs could be subjected to the same problem.

These events would represent a potential problem for highly reflective detectors equipped with many SiPMs. Although it is easy to identify and exclude a streamer in the analysis, all events during the burst may contain extraneous photo-electrons, indeed due to external cross-talk triggering other photodetectors. Assuming an incidence of one streamer event per SiPM per year with a duration of approximately 10 s, for a detector with 200,000 SiPMs, the probability of having a streamer for any event is approximately 7%.

4 Toy Monte Carlo simulations

To properly account for all noise contributions, a dedicated toy Monte Carlo (tMC) simulation was developed: the code is based on the simulation used in the STAR R&D facility at LNGS [27], i.e., a down-scaled liquid argon detector, instrumented with the aforementioned NUV-HD-Cryo SiPMs. The tMC was extended to a large homogeneous liquid argon detector with $N_{\mathrm{pd}} \simeq 2000$ readout channels based on SiPM photodetectors. The SiPM parameters and scintillation light yield were extracted from STAR (Table 1).

The simulation does not include scintillation photon tracking (as for a full chain physical Monte Carlo simulation), and the light collection efficiency is considered uniform in the fiducial volume: all photodetectors have the same probability of being hit by scintillation or cross-talk photons. As a consequence of the simplification, the following results have to be considered a pure and ideal case, as just driven by the statistical features of the SiPM intrinsic noise. The real physical performances will further be reduced by the detector imperfections, such as detector reflectivity, scintillation light absorption, TPB re-emission, electronics flaws, and all other possible systematic effects.

For each detected photo-electron (from primary argon scintillation or from correlated noises), a recursive oCT + AP cascade is applied. This is implemented by a set of recursive functions, each describing one possible correlated noise. Each function generates the correlated noise using a binomial extraction (or two binomials for iCT, as in [27]). If an avalanche

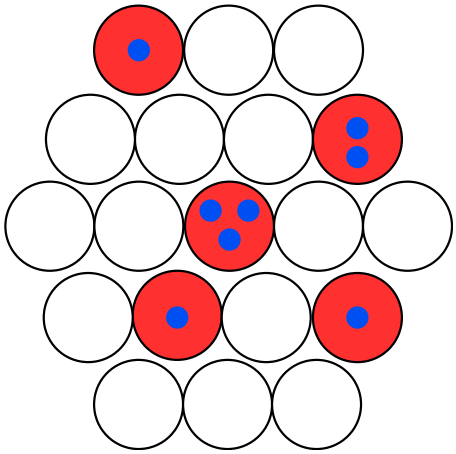

FIGURE 3
Example of an energy estimator during the event reconstruction. For both SiPM and PMTs, the energy of an event producing several photo-electrons can be estimated by counting the number of total photo-electrons (*N*, blue circles) or counting the number of total photodetectors (*B*, red circles).

is generated, a recursion on all correlated noises is activated. In case of eCT, the avalanche is applied to another readout channel, randomly picked. All the oCT and AP components are accounted for individually. It is important to notice that tMC does not depend on the models described in the previous section that describe the average cascade behavior (Eq. 3, 4): tMC propagates each photo-electron independently.

tMC keeps track of photo-electrons (both primaries and secondaries) generated by the singlet and triplet argon states for electron and nuclear recoils (for a review of the scintillation in noble gasses, refer to [36]). The median values for the fast-to-total light yield (typically referred to as f_{90} or f_{prompt}) are extracted from [37, 38]. As discussed above, after-pulsing closer than $\tau_{1/2}^{\text{AP}}$ has a smaller amplitude and reduced probability of triggering oCTs. It is safe to assume that after-pulsing, as well as its secondaries, does not contribute to the detected singlet photo-electrons with a timing of few nanoseconds. Note that, for large experiments, the propagation time of the photons in the liquid argon chamber can increase the spread of the singlet photo-electrons beyond $\tau_{1/2}^{\text{AP}}$. In such cases, after-pulsing can affect the singlet too. Since in any case the AP probability is very small for NUV-HD-Cryo, this case is not particularly interesting.

The region of interest (RoI) for the analysis is in the range 5–35 keVee; tMC simulates a wider window to avoid border effects due to statistical fluctuations of the simulated resolution.

4.1 Energy reconstruction

In the absence of correlated noises, it is possible to define three estimators for the *net* energy of the scintillation event. N_N is calculated as the total number of avalanches detected by photodetectors. B_N is the number of read-out channels with at least one avalanche. In the first approximation, B_N behaves as a binomial distribution with the success probability $1 - e^{-N_N/N_{\text{pd}}}$ with N_{pd} extractions (i.e., the total number of read-out channels). Therefore,

$$\langle B_{\text{N}} \rangle = N_{\text{pd}}\left(1 - e^{-N_N/N_{\text{pd}}}\right), \tag{5}$$

where the mean value is required because the binomial extraction introduces an irreducible spread in the data. To overcome the inherent non-linearity of B_N as a function of energy, the L_N (linearized binomial) variable is introduced with the following definition:

$$L_N = -N_{\text{pd}} \ln\left(1 - \frac{B_{\text{N}}}{N_{\text{pd}}}\right). \tag{6}$$

Figure 3 intuitively depicts the meaning of the binomial counting. For B_N, the information on piled-up photo-electrons in the same read-out channel is lost. The information loss leads inevitably to a spoiled

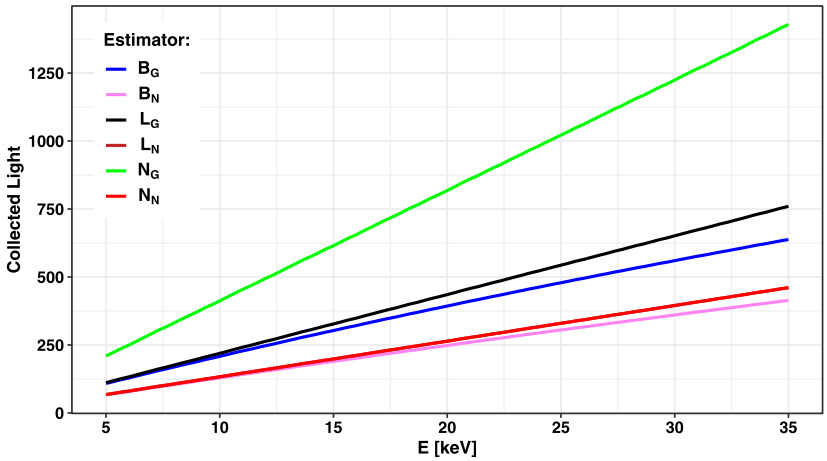

FIGURE 4
Average collected light for electron recoils for the different estimators described in the text. The L_N curve is completely overlapped by the N_N line. With the exception of the B^* variables, the curves are a straight line with a slope defined by the light yield at 9 OV multiplied by the correlated noise gain (Eqs 4, 3). In the rest of the article, N_N, N_G, L_N, and L_G will be used as energy estimators by implicitly inverting this plot.

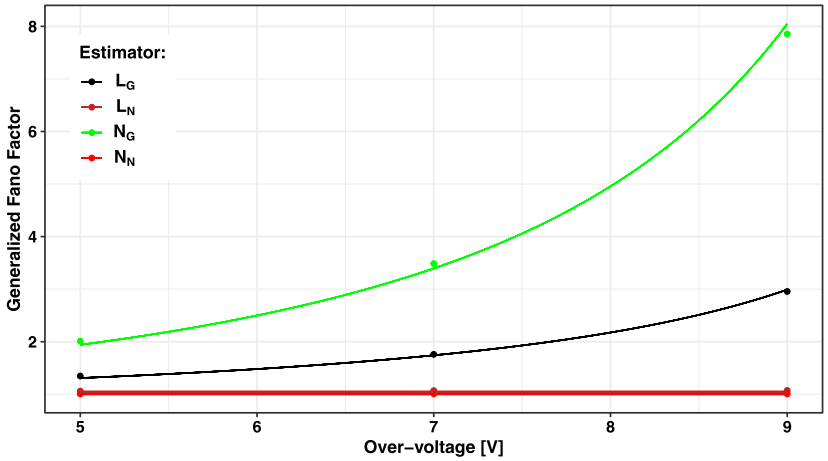

FIGURE 5
Average generalized Fano factor for electron recoil events *versus* SiPM over-voltages for the energy estimators described in the text. As expected, $\mathcal{F}_{N_N}$ has a unity value, the process being purely Poissonian. The generalized Fano factor for the *L* estimators ($\mathcal{F}_{L_N}$ and $\mathcal{F}_{L_G}$) is inherently not constant as a function of the energy. Since in the region of interest it changes by less than 7%, the mean value is used. The lines for $\mathcal{F}_{N_G}$ and $\mathcal{F}_{L_G}$ represent the best-fit described in the text, while for $\mathcal{F}_{N_N}$ and $\mathcal{F}_{L_N}$, a constant line at 1 is drawn to guide the eye.

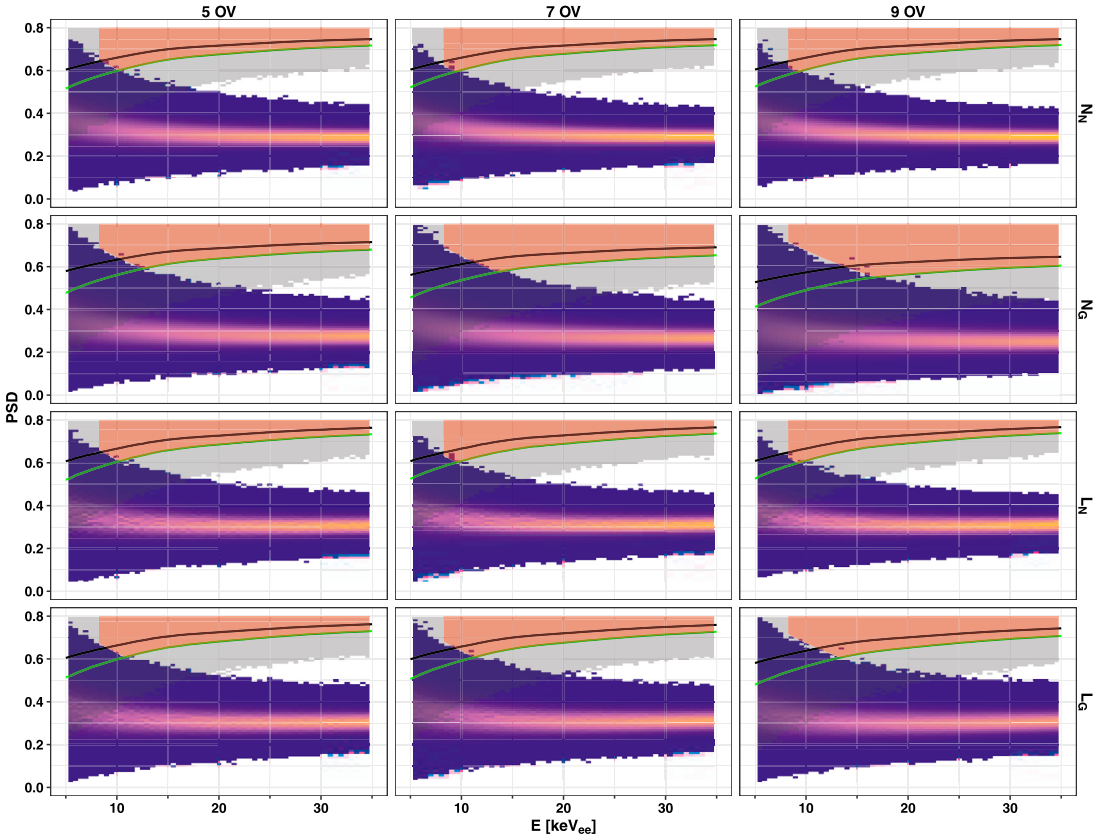

FIGURE 6
Pulse shape discrimination *versus* reconstructed energy for several SiPM over-voltages and different energy estimators. The blue–gold heatmaps correspond to 3×10^{10} electron-like events uniformly distributed between 5 and 35 keVee. The gray-shaded bands correspond to approximately 1×10^{9} nuclear recoil events: 50% (black) and 90% (green) quantiles are shown. The red ribbons identify the dark matter acceptance area with a leakage of about 10 electron-like events.

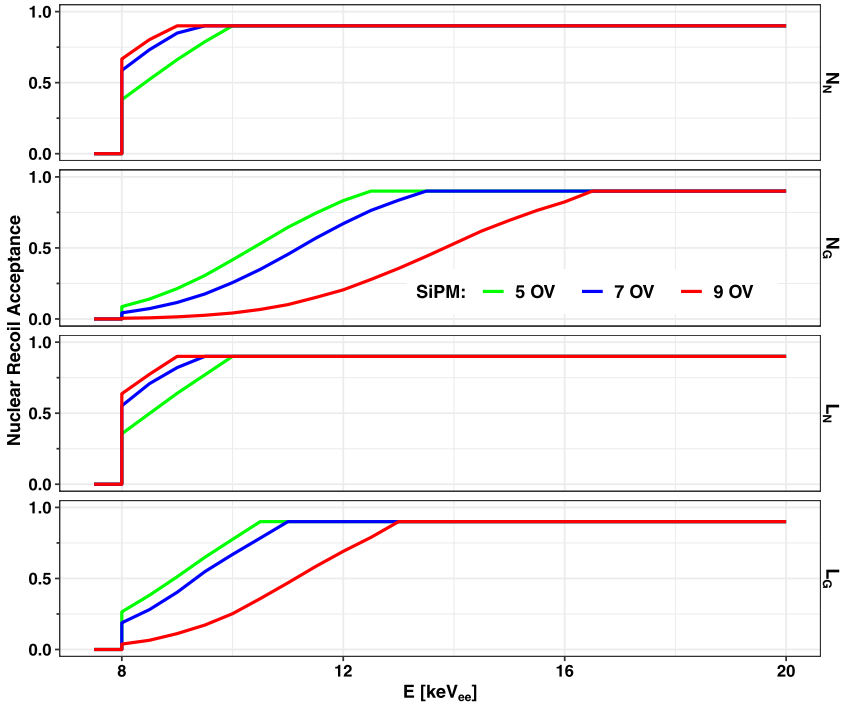

FIGURE 7
Nuclear recoil acceptances as a function of collected energy for the different estimators discussed in the text and at several over-voltages. Above 20 keVee, the acceptance remains at 90%. Below 8 keVee, it is set to zero.

resolution; however, the fluctuations introduced by the correlated noise are strongly reduced as it will be shown later. As hinted earlier, the binomial extraction is only an approximation because the number of photo-electrons is set to N_N, and only the pile-up can fluctuate. This is clearer for an event with $N_N = 1$; the binomial extraction allows non-physical events with $B_N \neq 1$. The tMC simulation correctly simulates the pile-up, and the reported results are unaffected by the binomial approximation used to simplify the description.

For a real detector, the net estimators cannot be observed directly; similar quantities can be calculated in the presence of correlated noises (oCT and AP), obtaining N_G, B_G, and L_G for modeling the *gross* energy seen by the detector. Figure 4 reports the reconstructed values of N, B, and L (net and gross) as a function of the deposited energy for electron recoil events (E_e) in keVee. Both L and N provide a linear scale to measure the released energy (once a calibration is performed) and will hence be used as energy estimators. It is interesting to note that the L_G estimator is less affected by an internal cross-talk and after-pulsing than N_G since only the first photo-electron from scintillation (or from eCT) is accounted for by each photodetector. As a result, the noisy gain of the correlated processes (the slope of Figure 4) is unequivocally lower then N_G; from Eq. 3, $\mathcal{G}_{L_G} = 1 + \mathcal{G}_{\text{oCT+AP}}\,\lambda_{\text{eCT}}$.

Figure 5 reports the generalized Fano factor (defined as the variance over mean of the collected number of photo-electrons) for different energy estimators. It is possible to express the energy resolution of the experiment as a function of the correlated noise gains. A non-linear regression analysis on the simulated data shows an exponential dependence of the Fano factors upon the noise gains, namely, $\mathcal{F}_{N_G} = (\mathcal{G}_{\text{oCT+AP}})^{-1.84\pm0.02}$ and $\mathcal{F}_{L_G} = (\mathcal{G}_{L_G})^{-2.18\pm0.04}$, with a standard deviation of the relative residuals of ~3%.

The lower generalized Fano factor for L_G with respect to N_G, and hence the better energy resolution in RoI, is directly linked to the lower noise gain of the oCT process, affecting the linearized binomial energy estimator. For example, at 9 OV, $\mathcal{G}_{L_G} \simeq 1/2\ \mathcal{G}_{\text{oCT+AP}}$.

4.2 Pulse shape

The tMC simulation keeps track of which photon corresponds to the singlet or triplet emission in liquid argon scintillation. The pulse discrimination parameter (PSD) is defined as the ratio between the number of singlet photo-electrons collected divided by the total number of photo-electrons. Figure 6 reports PSD as a function of the reconstructed energy for 3×10^{10} electron-like events for the energy estimators discussed earlier and with three SiPM over-voltages, namely, 5 V, 7 V, and 9 V. As expected, these plots are affected by the presence of correlated noise with a spread in PSD and by a lower resolution on the energy scale.

4.3 S2

As mentioned before, S2 plays a crucial role in the position and energy reconstruction of the double-phase argon TPCs and is fundamental for the pulse shape of the double-phase xenon TPC. Typically, S2 is much greater than S1 and depends on applied drift and extraction fields. For the reasons discussed above, S2 is indeed not free from all of the issues concerning the presence of oCTs. Furthermore, in S2, the scintillation photo-electrons are not

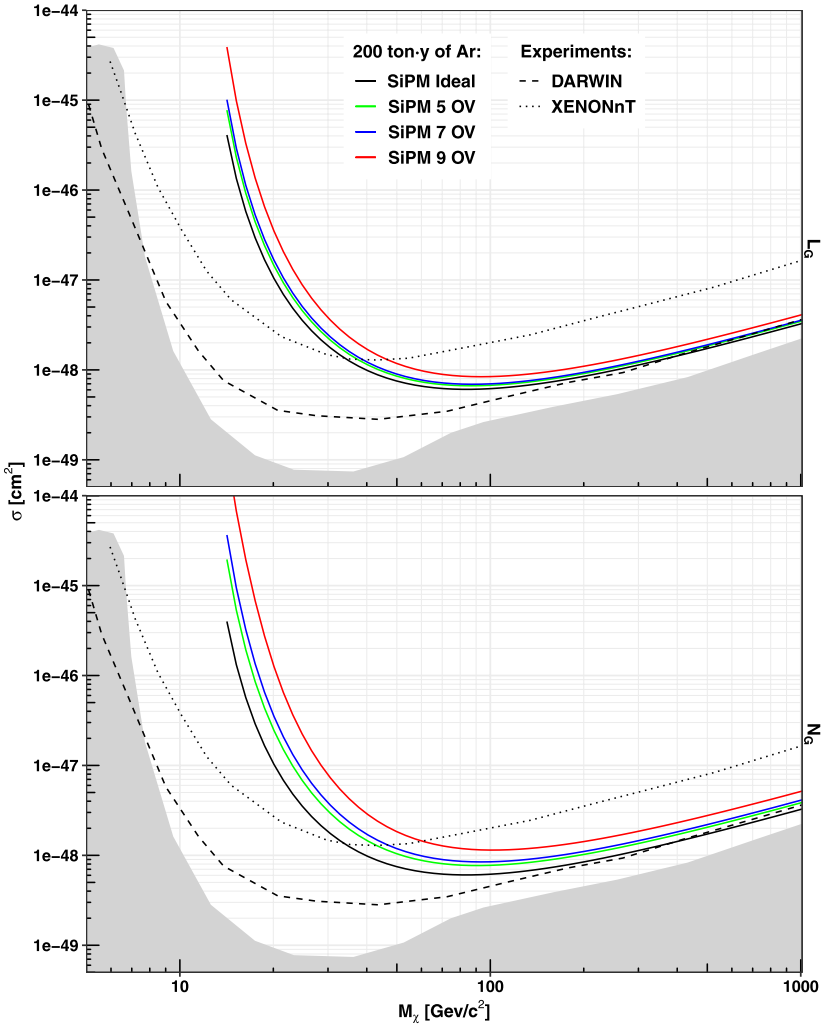

FIGURE 8
Sensitivity curve (90% CL) for a 200-ton·y exposure of a liquid argon detector using a SiPM-based photodetector module for different over-voltages and using two different energy estimators for S1: linearized binomial counting (top) and number of detected photo-electrons (bottom). The ideal curves refer to the absence of noises (oCT, AP, and electronic). As a reference, the projected sensitivity curves for XENONnT [39] and DARWIN [6] are added with dotted and dashed lines. The neutrino floor [1] with the gray area is also shown. As explained in the text, the projected sensitivity for the argon detector with SiPMs is overestimated by a factor 2 ÷ 3 with respect to a realistic experiment.

uniformly distributed; only a few photo-detectors, just above the S2 position, will see the largest fraction of the emitted light. In these conditions, the use of binomial estimators is not possible. The full description of eCT effects on S2 would anyway require a detailed Monte Carlo analysis, e.g., for the position reconstruction algorithm, that goes beyond the scope of the present work.

5 Implications on the projected sensitivity

Assuming the SI WIMP–nucleon interaction, under the galactic Standard Halo model, it is possible to extract the projected sensitivity of the simulated experiment. The number of background events is considered zero; the suppression of nuclear recoil events is demanded to a proper detector design, including active neutron veto and low background materials. For a leaking electron recoil, this is obtained by tuning the NR acceptance regions. This process depends strongly on the correlated noise contribution and on the used energy estimator, as discussed in Section 3.

5.1 Acceptance regions

Based on the data shown in Figure 6, the acceptance regions are defined as the areas in which only approximately 10 ER leaking events are present over the aforementioned exposure. The acceptance regions are defined between 5 and 35 keV by the intersection of the 90% quantile for NR events and a segment of a rectangular hyperbola $(1/(1 + \xi E))$ in the pulse shape parameter. The scale parameter (ξ) is tuned to satisfy the requirement of having 10 ER outliers in the acceptance for each SiPM OV and energy estimator. The resulting NR acceptance as a function of energy is shown in Figure 7.

This number of leaking events over the 200 ton·y exposure corresponds to 0.10 ± 0.01. Indeed, neglecting the contribution of all possible γ backgrounds in the detector fiducial volume, the only source of internal ER events is the ^{39}Ar β decay and amounts to

$$N_{^{39}\mathrm{Ar}} = 3.15 \cdot 10^{10} \times \frac{\mathrm{mass}}{[\mathrm{ton}]} \times \frac{\mathrm{time}}{[\mathrm{y}]} \times \frac{\delta_{\mathrm{RoI}}}{\mu}, \quad (7)$$

where μ is the ^{39}Ar depletion factor, reasonably assumed to be approximately 1/1,500 [38], with respect to the specific activity of atmospheric argon (1 Bq/kg); and δ_{RoI} is the fraction of the ^{39}Ar beta decays falling in RoI (calculated by integrating the normalized β–spectrum over RoI). For the chosen exposure, one obtains $N_{^{39}\mathrm{Ar}} \simeq 3 \times 10^8$ events.

5.2 Dark matter sensitivity plots

To calculate the dark matter sensitivity plot, the standard WIMP-halo model with v_{esc} = 544 km/s [40], v_0 = 220 km/s [40], v_{earth} = 232 km/s [41], and ρ_{DM} = 0.3 GeV/(c^2 cm^3) [42] is assumed. The SI WIMP–nucleon differential interaction rate, as a function of the kinematic parameters and of the dark matter velocity distribution, is convoluted with the energy resolution for each energy estimator. The number of interactions is given by the exposure multiplied by the differential rate integrated over RoI, scaled by the acceptance of Figure 7 and by the exposure. NR quenching, as a function of the energy for liquid argon, is taken from [38]. Assuming the null result and neglecting the 0.1 ^{39}Ar background events, the 90% CL exclusion curves, corresponding to the observation of 2.3 events for the SI WIMP–nucleon interactions, are derived for each energy estimator.

Figure 8 shows the corresponding sensitivity curves for the energy estimators described earlier for different SiPM over-voltages. The figures show a progressive decrease in the sensitivity, depending on the operating over-voltage. In other words, the optical correlated noise produces a sizeable effect on the final analysis that may reduce the projected sensitivity even by a factor two, especially in case a large OV is used. This effect can be mildly reduced using the linearized binomial energy estimator but not completely removed.

It should be noted that the ideal sensitivity curves are tangibly better than a realistic experimental situation because, as explained in Section 3, the tMC simulation does not take into account a further broadening of the energy and the pulse shape resolutions, due to the scintillation properties and detector geometry. Considering the acceptance of a real liquid argon detector as DarkSide-50 [12], one can easily estimate that sensitivity is overestimated by a factor 2 ÷ 3 or even more. For this reason, the distortion caused by the correlated noise with respect to the ideal Poisson baseline must be considered in a relative and not in an absolute way, and its real impact could be dramatically large, depending on how large is the difference between the reconstruction of the physical observables and their ideal expectations.

6 Conclusion

The direct dark matter search, especially concerning the WIMP-like detection in the mass interval 1 GeV–1 TeV, starts exploiting the multi-ton scale. For future detectors, scalable and reliable photodetectors are required. The argon community decided to use SiPMs, taking advantage of high PDE and low background. SiPMs have been developed at Fondazione Bruno Kessler for operation in liquid argon, and large photodetectors have been proven at LNGS, opening the path to the deployment of large experiments. However, as largely discussed in the present work, the presence of correlated noise can spoil the full scientific reach of future detectors if not properly managed.

We introduced a new energy estimator, based on the number of the fired module, which is capable of mitigating the noise caused by optical cross-talk and after-pulsing. Differently, the external optical cross-talk is irreducible and becomes dominant for high over-voltages. We have shown, as an example, a multi-ton liquid argon detector with 200-ton·y exposure. A dedicated simulation shows that the presence of the irreducible correlated noise can even divide the ideal projected sensitivity (Figure 8), basically doubling the needed experiment live time. A recent pre-print [43] demonstrates the effects of eCT for xenon-based detectors. In principle, with respect to argon, xenon-based detectors should be less affected by this issue as the sensitivity for an optical cross-talk of vacuum ultraviolet-sensitive SiPMs is lower.

Beyond analysis optimizations, it is possible to mitigate in the detectors the effects of correlated noise. A first solution could be the introduction of colored optical filters capable of attenuating wavelengths above 500 nm in front of the SiPM-based modules. More elaborate options require modifications to SiPM to reduce iCT, emission probability, and PDE above the green wavelength.

As we have shown in our toy Monte Carlo simulations, the correlated noise largely applies for high over-voltage settings, where the effect is strongly amplified. Therefore, a natural solution could be operating the detectors at very low over-voltage, to reduce the cascade gain down to some acceptable value. However, reducing the SiPM charge gain may require a very low electronic noise condition that cannot be easily achieved in very big detectors.

The dark matter search is entering a critical and challenging phase, in which old technological solutions may not be sufficient any longer, and novel and promising solutions have to be carefully tested and validated in dedicated prototypes. In addition, SiMP detectors are a clear example in this sense.

Data availability statement

The original contributions presented in the study are included in the article/Supplementary Material; further inquiries can be directed to the corresponding authors.

Author contributions

AR: conceptualization, formal analysis, software, writing–original draft, and writing–review and editing. NR: investigation, software, validation, writing–original draft, and writing–review and editing.

Funding

The author(s) declare that no financial support was received for the research, authorship, and/or publication of this article.

Acknowledgments

The authors would like to thank the LNGS computing center and Dr. C. Pellegrino at CNAF for providing the CPU required to run the simulations. The authors acknowledge the support of Dr. G. Rannucci and Prof. V. Caracciolo, in the discussion of the statistical models and for proofreading.

Conflict of interest

The authors declare that the research was conducted in the absence of any commercial or financial relationships that could be construed as a potential conflict of interest.

Publisher's note

All claims expressed in this article are solely those of the authors and do not necessarily represent those of their affiliated organizations, or those of the publisher, the editors, and the reviewers. Any product that may be evaluated in this article, or claim that may be made by its manufacturer, is not guaranteed or endorsed by the publisher.

References

1. Zyla PA, Barnett RM, Beringer J, Dahl O, Dwyer DA, Groom DE, et al. Review of particle physics. *PTEP* (2020) 2020(8):083C01. doi:10.1093/ptep/ptaa104

2. SteigmanTurner GMS. Cosmological constraints on the properties of weakly interacting massive particles. *Nucl Phys B* (1985) 253:375–86. doi:10.1016/0550-3213(85)90537-1

3. Bertone G, Silk DHJ. Particle dark matter: evidence, candidates and constraints. *Phys Rept* (2005) 405:279–390. doi:10.1016/j.physrep.2004.08.031

4. Tait GBT. A new era in the search for dark matter. *Nature* (2018) 562(7725):51–6. doi:10.1038/s41586-018-0542-z

5. Ajaj R. Low radioactivity argon for dark matter and Rare event searches, in *Proc XXIX Int Symp Lepton Photon Interactions High Energies — PoS(LeptonPhoton2019)* 367 (2019), 084. doi:10.22323/1.367.0084

6. Aalbers, Agostini F, Alfonsi M, Amaro FD, Amsler C, Aprile E. *JCAP* (2016) 11:017. doi:10.1088/1475-7516/2016/11/017

7. Aalbers J, Akerib DS, Akerlof CW, Al Musalhi A, Alder F, Alqahtani A, et al. First dark matter search results from the LUX-ZEPLIN (LZ) experiment. *Phys Rev Lett* (2023) 131:041002. doi:10.1103/PhysRevLett.131.041002

8. Aprile E, Aalbers J, Agostini F, Alfonsi M, Althueser L, Amaro F, et al. Constraining the spin-Dependent WIMP-nucleon cross sections with XENON1T. *Phys Rev Lett* (2019) 122(14):141301. doi:10.1103/PhysRevLett.122.141301

9. Meng Y, Wang Z, Tao Y, Abdukerim A, Bo Z, Chen W, et al. Dark matter search results from the PandaX-4T Commissioning run. *Phys Rev Lett* (2021) 127(26):261802. doi:10.1103/PhysRevLett.127.261802

10. LewinSmith JDPF. Review of mathematics, numerical factors, and corrections for dark matter experiments based on elastic nuclear recoil. *Astropart Phys* (1996) 6:87–112. doi:10.1016/S0927-6505(96)00047-3

11. Ajaj R, Amaudruz PA, Araujo GR, Baldwin M, Batygov M, Beltran B, et al. Search for dark matter with a 231-day exposure of liquid argon using DEAP-3600 at SNOLAB. *Phys Rev D* (2019) 100:022004. doi:10.1103/PhysRevD.100.022004

12. Agnes P, Albuquerque IFM, Alexander T, Alton A, Araujo G, Ave M, et al. DarkSide-50 532-day dark matter search with low-radioactivity argon. *Phys Rev D* (2018) 98:102006. doi:10.1103/PhysRevD.98.102006

13. Agnes P, Albuquerque IFM, Alexander T, Alton A, Ave M, Back H, et al. Search for low-mass dark matter WIMPs with 12 ton-day exposure of DarkSide-50. *Phys Rev D* (2023) 107:063001. doi:10.1103/PhysRevD.107.063001

14. Aprile E, Abe K, Agostini F, Ahmed Maouloud S, Althueser L, Andrieu B, et al. First dark matter search with nuclear recoils from the XENONnT experiment. *Phys Rev Lett* (2023) 131:041003. doi:10.1103/PhysRevLett.131.041003

15. Aalseth CE, Acerbi F, Agnes P, Albuquerque IFM, Alexander T, Alici A, et al. DarkSide-20k: a 20 tonne two-phase LAr TPC for direct dark matter detection at LNGS. *Eur Phys J Plus* (2018) 133(3):131. doi:10.1140/epjp/i2018-11973-4

16. D'Incecco M, Galbiati C, Giovanetti GK, Korga G, Li X, Mandarano A, et al. Development of a novel single-channel, 24 cm^2, SiPM-based, cryogenic Photodetector. *IEEE Trans Nucl Sci* (2018) 65(1):591–6. doi:10.1109/TNS.2017.2774779

17. Razeto A, Acerbi F, Camillo V, Carlini M, Consiglio L, Flammini A, et al. Very large SiPM arrays with aggregated output. *J Instrumentation* (2022) 17(05):P05038. doi:10.1088/1748-0221/17/05/p05038

18. Agnes P, Alexander T, Alton A, Arisaka K, Back H, Baldin B, et al. First results from the DarkSide-50 dark matter experiment at Laboratori Nazionali del Gran Sasso. *Phys Lett B* (2015) 743:456–66. doi:10.1016/j.physletb.2015.03.012

19. Gola A, Acerbi F, Capasso M, Marcante M, Mazzi A, Paternoster G, et al. NUV-sensitive silicon Photomultiplier technologies developed at Fondazione Bruno Kessler. *Sensors* (2019) 19(2):308. doi:10.3390/s19020308

20. Zappalà G, Acerbi F, Ferri A, Gola A, Paternoster G, Regazzoni V, et al. Study of the photo-detection efficiency of FBK High-Density silicon photomultipliers. *J Instrumentation* (2016) 11(11):P11010. doi:10.1088/1748-0221/11/11/p11010

21. Buzhan P, Dolgoshein B, Ilyin A. *Advanced Technology and Particle Physics* (2002). doi:10.1142/9789812776464_0101

22. D'Incecco M, Galbiati C, Giovanetti GK, Korga G, Li X, Mandarano A, et al. Development of a very low-noise cryogenic Preamplifier for large-area SiPM devices. *IEEE Trans Nucl Sci* (2018) 65(4):1005–11. doi:10.1109/TNS.2018.2799325

23. Piemonte C. A new Silicon Photomultiplier structure for blue light detection. *Nucl Instr Methods Phys Res Section A: Acc Spectrometers, Detectors Associated Equipment* (2006) 568(1):224–32. doi:10.1016/j.nima.2006.07.018

24. Collazuol G, Bisogni M, Marcatili S, Piemonte C, Del Guerra A. Studies of silicon photomultipliers at cryogenic temperatures. *Nucl Instrum Methods Phys Res A* (2011) 628(1):389–92. doi:10.1016/j.nima.2010.07.008

25. Boulay MG, Camillo V, Canci N, Choudhary S, Consiglio L, Flammini A, et al. Direct comparison of PEN and TPB wavelength shifters in a liquid argon detector. *Eur Phys J C* (2021) 81(12):1099. doi:10.1140/epjc/s10052-021-09870-7

26. Acerbi F, Davini S, Ferri A, Galbiati C, Giovanetti G, Gola A, et al. Cryogenic Characterization of FBK HD near-UV sensitive SiPMs. *IEEE Trans Elec Dev* (2017) 64(2):521–6. doi:10.1109/TED.2016.2641586

27. Boulay MG, Camillo V, Canci N, Choudhary S, Consiglio L, Flammini A, et al. SiPM cross-talk in liquid argon detectors. *Front Phys* (2023) 11. doi:10.3389/fphy.2023.1181400

28. Mirzoyan R, KosyraMoser RHG. Light emission in Si avalanches. *Nucl Instrum Methods Phys Res A* (2009) 610(1):98–100. doi:10.1016/j.nima.2009.05.081

29. Nepomuk Otte A. On the efficiency of photon emission during electrical breakdown in silicon. *Nucl Instr Methods Phys Res Section A: Acc Spectrometers, Detectors Associated Equipment* (2009) 610(1):105–9. doi:10.1016/j.nima.2009.05.085

30. Nagai A, Alispach C, Berghöfer T, Bonanno G, Coco V, della Volpe D, et al. SENSE: a comparison of photon detection efficiency and optical crosstalk of various SiPM devices. *Nucl Instr Methods Phys Res Section A: Acc Spectrometers, Detectors Associated Equipment* (2018) 912:182–5. doi:10.1016/j.nima.2017.11.018

31. McLaughlin JB, Gallina G, Retière F, De St. Croix A, Giampa P, Mahtab M, et al. Characterisation of SiPM photon emission in the dark. *Sensors* (2021) 21(17):5947. doi:10.3390/s21175947

32. Vinogradov S, Vinogradova T, Shubin V. In: *2009 IEEE nuclear science Symposium Conference Record (NSS/MIC)* (2009). p. 1496–500. doi:10.1109/NSSMIC.2009.5402300

33. Gallego L, Rosado J, Arqueros FBF. Modeling crosstalk in silicon photomultipliers. *J Instrumentation* (2013) 8(05):P05010. doi:10.1088/1748-0221/8/05/p05010

34. Wagenpfeil M, Ziegler T, Schneider J, Fieguth A, Murra M, Schulte D, et al. Reflectivity of VUV-sensitive silicon photomultipliers in liquid Xenon. *J Instrumentation* (2021) 16(08):P08002. doi:10.1088/1748-0221/16/08/P08002

35. Guarise M, Andreotti M, Calabrese R, Cotta Ramusino A, Cicero V, Fiorini M, et al. A newly observed phenomenon in the characterisation of SiPM at cryogenic temperature. *J Instrumentation* (2021) 16(10):T10006. doi:10.1088/1748-0221/16/10/t10006

36. Lippincott WH, Coakley KJ, Gastler D, Hime A, Kearns E, McKinsey DN, et al. Scintillation time dependence and pulse shape discrimination in liquid argon. *Phys Rev C* (2008) 78:035801. doi:10.1103/physrevc.78.035801

37. Cao H, Alexander T, Aprahamian A, Avetisyan R, Back H, Cocco A, et al. Measurement of scintillation and ionization yield and scintillation pulse shape from nuclear recoils in liquid argon. *Phys Rev D* (2015) 91:092007. doi:10.1103/PhysRevD.91.092007

38. Agnes P, Addendum. *Phys Rev D* 93(8), 081101 (2016). DOI doi:10.1103/PhysRevD.93.081101

39. Aprile E, Aalbers J, Agostini F, Alfonsi M, Althueser L, Amaro F, et al. Projected WIMP sensitivity of the XENONnT dark matter experiment. *J Cosmology Astroparticle Phys* (2020) 2020(11):031. doi:10.1088/1475-7516/2020/11/031

40. Smith MC, Ruchti GR, Helmi A, Wyse RFG, Fulbright JP, Freeman KC, et al. The RAVE survey: constraining the local Galactic escape speed. *Mon Not Roy Astron Soc* (2007) 379:755–72. doi:10.1111/j.1365-2966.2007.11964.x

41. Savage C, Gelmini G, Freese PGK. *JCAP* (2009) 04:010. doi:10.1088/1475-7516/2009/04/010

42. Savage C, FreeseGondolo KP. Annual modulation of dark matter in the presence of streams. *Phys Rev D* (2006) 74:043531. doi:10.1103/PhysRevD.74.043531

43. Gibbons R, Chen H, Haselschwardt SJ, Xia Q, Sorensen P *e-print: 2309* (2023) 07913. doi:10.48550/arXiv.2309.07913

frontiers | Frontiers in Physics

TYPE Technology and Code
PUBLISHED 11 January 2024
DOI 10.3389/fphy.2023.1319879

OPEN ACCESS

EDITED BY
Osvaldo Civitarese,
National University of La Plata, Argentina

REVIEWED BY
Olga Gileva,
Institute for Basic Science (IBS), Republic of Korea
Giorgio Arcadi,
University of Messina, Italy

*CORRESPONDENCE
Wolfgang Rau,
wrau@triumf.ca

†PRESENT ADDRESSES
Philippe Camus,
Institut Néel, CNRS, Grenoble, France
Richard Germond,
Institute for Quantum Computing, University of Waterloo, Waterloo, ON, Canada
Muad Ghaith,
Zayed University, Dubai, United Arab Emirates
Adam Mayer,
Lancaster University, Lancaster, United Kingdom
Silvia Scorza,
Univ. Grenoble Alpes, CNRS, Grenoble INP*, LPSC-IN2P3, Grenoble, France

RECEIVED 11 October 2023
ACCEPTED 04 December 2023
PUBLISHED 11 January 2024

CITATION
Camus P, Corbett J, Crawford S, Dering K, Fascione E, Gerbier G, Germond R, Ghaith M, Hall J, Hong Z, Kubik A, Mayer A, Nagorny S, Pakarha P, Rau W, Scorza S and Underwood R (2024), CUTE: A Cryogenic Underground TEst facility at SNOLAB.
Front. Phys. 11:1319879.
doi: 10.3389/fphy.2023.1319879

CUTE: A Cryogenic Underground TEst facility at SNOLAB

Philippe Camus[1†], Jonathan Corbett[1], Sean Crawford[1], Koby Dering[1], Eleanor Fascione[1,2], Gilles Gerbier[1], Richard Germond[1,2†], Muad Ghaith[1†], Jeter Hall[3,4,5], Ziqing Hong[4], Andrew Kubik[3,4], Adam Mayer[2†], Serge Nagorny[1], Payam Pakarha[1], Wolfgang Rau[1,2]*, Silvia Scorza[3,4,5†] and Ryan Underwood[1,2]

[1]Department of Physics, Engineering Physics and Astronomy, Queen's University, Kingston, ON, Canada, [2]Department of Particle Physics, Physical Science Division, TRIUMF, Vancouver, BC, Canada, [3]Research Division, SNOLAB, Lively, ON, Canada, [4]Department of Physics, University of Toronto, Toronto, ON, Canada, [5]School of Natural Sciences, Laurentian University, Sudbury, ON, Canada

Low-temperature cryogenics open the door for a range of interesting technologies based on features like superconductivity and superfluidity, low-temperature phase transitions or the low heat capacity of non-metals in the milli-Kelvin range. Devices based on these technologies are often sensitive to small energy depositions as can be caused by environmental radiation. The Cryogenic Underground TEst facility (CUTE) at SNOLAB is a platform for testing and operating cryogenic devices in an environment with low levels of background. The large experimental chamber ($\mathcal{O}$(10) L) reaches a base temperature of ~ 12 mK; it can hold a payload of up to ~ 20 kg and provides a radiogenic background event rate as low as a few events/kg/keV/day in the energy range below about 100 keV, as well as a negligible muon rate ($\mathcal{O}$1)/month). CUTE was designed and built in the context of the Super Cryogenic Dark Matter Search experiment (SuperCDMS) that uses cryogenic detectors to search for interactions of dark matter particles with ordinary matter. The facility has been used to test SuperCDMS detectors since its commissioning in 2019. In 2021, it was handed over to SNOLAB to become a SNOLAB user facility after the completion of the testing of detectors for SuperCDMS. The facility will be available for projects that benefit from these special conditions, based on proposals assessed for their scientific and technological merits. This article describes the main design features and operating parameters of CUTE.

KEYWORDS

cryogenic, low radiation background, underground science, SNOLAB, dark matter, rare event searches, CUTE

1 Introduction

Cryogenic particle detectors are among the detectors with the best energy resolution, capable of reaching eV-scale thresholds in small (typically gram-scale) devices (see, e.g., [1–4]). When combined with intrinsic amplification, this can extend to devices up to the kilogram scale [5, 6]. In small devices, intrinsic amplification can push the threshold well below an eV [7]. Hence, this is often the technology of choice for detecting sub-keV interactions. One important consideration when using cryogenic detectors is that thermal processes are generally slow (ms time scale) compared to other particle-detection technologies (e.g., ionization or scintillation with time scales of μs or faster). In massive detectors (kg scale) the typical

environmental radiation background generates interactions at rates of tens of Hz. The combination of high event rate and slow response time would lead to overlapping events (pile-up) which in turn would severely limit the usefulness of such detectors. Hence, a low-radiation environment is required for experiments using this technology. Finally, high energy cosmogenic radiation is not only a direct source of background, but can also generate long-lived radioactive isotopes in the detector or surrounding material (cosmogenic activation, see, e.g., [8]). Thus, extended exposure of the detector material to cosmogenic radiation may limit the sensitivity of experiments that rely on very low background.

The Super Cryogenic Dark Matter Search experiment (SuperCDMS) [9] is presently under construction at SNOLAB, a deep underground laboratory hosted inside the active Vale Creighton mine near Sudbury, ON, Canada. It combines all the above requirements: massive cryogenic detectors with a low energy threshold are used to search for rare interactions of dark matter particles, and the detectors and the experimental apparatus of SuperCDMS are comprised of materials that get easily activated by cosmogenic radiation [8]. This motivated the design and construction of the Cryogenic Underground TEst facility (CUTE) at SNOLAB [10, 11]. CUTE enables the testing of the new SuperCDMS detectors under low-background conditions while mitigating the risk of cosmogenic activation.

From the beginning, consideration was given to a possible use of the facility after the primary goal of testing SuperCDMS detectors would be concluded. This informed a number of design choices that now make this a convenient facility for testing and operating not only particle detectors, but also other devices with low operating temperature that benefit from (or require) very low levels of background radiation. In 2021, SNOLAB has taken on the responsibility of maintaining and upgrading the facility and will be making it available to new users based on the merit of their proposals.

In this paper, we introduce the design considerations for the facility and describe its different components and subsystems and their performance, before ending with a short discussion of possible uses that might benefit from the special conditions provided by CUTE. The focus is on the facility as such, but where appropriate we will give examples of specific solutions implemented for SuperCDMS.

2 Design requirements and considerations

The original motivation for the CUTE facility was to test the new detectors that will be used in the upcoming SuperCDMS SNOLAB experiment [12]. Besides understanding basic detector parameters, a number of calibration measurements are planned, including a measurement to study the neutron-gamma discrimination power of the detectors with a sensitivity of better than 10^{-6} (meaning that the measurement would reveal if more than one in 10^6 gamma interactions were misidentified as neutron interactions). The minimal requirements for the facility are defined by the needs for operating these detectors and the necessity that the calibration measurements can be conducted without major interference from background radiation.

The SuperCDMS detectors consist of cylindrical germanium or silicon crystals, 10 cm in diameter and 3.3 cm thick (corresponding to a mass of 1.4 and 0.6 kg respectively), instrumented with superconducting transition-edge sensors (TESs) that require an operational temperature below about 30 mK [12]. Extended operation at such temperatures require a dilution refrigerator. The detectors come in two denominations: interleaved Z-sensitive Ionization and Phonon (iZIP) detectors and high-voltage (HV) detectors. iZIP detectors measure both phonons and charges for optimal background identification and discrimination An earlier incarnation of this detector type is described in [13]. HV detectors are operated with a bias voltage on the order of 100 V (compared to just a few Volts for the iZIPs). The Neganov-Trofimov-Luke effect [14, 15] leads to a significant increase of the phonon signal which in turn yields a low effective energy threshold. The detectors are arranged in stacks of six, attached to a structure that provides the mechanical, thermal and electrical connections and includes the central elements of the first-stage amplifiers. The complete assembly has a mass of up to ~20 kg and is referred to as a *tower*. The tower without the detectors is called the *tower body* and the electronic elements attached to the tower are referred to as *cold electronics*. The sensors and some elements of the cold electronics require a low magnetic field of ideally $\lesssim 1\ \mu$T.

For calibrating these detectors, the maximum beneficial rate is about 7 Hz before being limited by pile-up. To enable a good signal-to-background rate during calibration, the overall background rate would therefore need to be $\ll 1$ Hz. The limitation on the detector rate means that the maximum number of gamma interactions accumulated per day is a few times 10^6. Therefore, to achieve the goal sensitivity of 10^{-6} for the neutron-gamma discrimination measurement, the background neutron rate needs to be less than one neutron interaction per day per detector in the energy range of interest (~1–50 keV).

To reduce the rate of cosmogenic radiation, the facility is located 2 km underground at SNOLAB near Sudbury ON. This in turn reduces the otherwise prohibitively high cosmic-ray induced neutron flux [16] and protects the detectors from cosmogenic activation. Additional shielding is necessary to reduce the environmental radiogenic neutron and gamma flux [17]. Also, measures were taken to avoid introducing contaminants into the experimental setup. We decided early on in the planning process to take further steps towards a considerably lower background level. The additional effort to accomplish this was modest and it gives the best perspective for a useful life of the facility after the completion of the SuperCDMS tests.

Other considerations during the design process included the strong susceptibility of the SuperCDMS detectors to mechanical vibration, due to their large mass, and the susceptibility of the readout electronics to electromagnetic interference. In addition to providing the right environment for the measurement, it is essential that the installation of the detectors into the facility does not significantly increase their exposure to contaminants such as dust or radon. Hence, a dedicated cleanroom with a low-radon air supply to host the cryostat for payload changes is an important part of the facility.

3 Cryogenics

The CUTE cryostat is cooled by a cryogen-free (dry) dilution refrigerator from CryoConcept, with a base temperature of

approximately 12 mK. The cryostat has six thermal stages with nominal temperatures of 300 K, 50 K, 4 K, 1 K, 100 mK, and 10 mK, respectively. The lowest three stages are referred to as the *Still* (ST), *Cold Plate* (CP) and *Mixing Chamber* (MC) stages, after the respective functional components of the dilution refrigerator. The other two cold stages are referred to as 4K and 50 K stages. Mechanical connections between the stages are made by stainless steel or G10 standoffs which provide solid structural connections with low thermal conductivity. The room-temperature stage consists of a stainless-steel vacuum vessel referred to as the *Outer Vacuum Can* (OVC). Copper cans acting as thermal radiation shields are mounted on the 50K, 4K, and Still stages. The 50 K can is wrapped in multiple layers of aluminized Mylar super-insulation to reduce the thermal load from the OVC. A separate experimental stage is mechanically and thermally anchored to the MC stage with three copper bars, providing a large volume (~25 cm diameter and 30 cm high) for the experimental payload.

The 50K and 4 K stages are cooled by a pulse-tube cryocooler (PTC), while the lower thermal stages are cooled by the dilution unit (DU). In order to minimize the coupling of vibrations from the PTC into the cryostat, CryoConcept developed a technique that avoids mechanical connections between the cold stages of the PTC and the cryostat (the Ultra-Quiet Technology™, UQT). Thermal contact is instead provided by the helium mixture that pumped out of the Still. This is achieved by installing the PTC's cold head inside the Still pumping line of the DU. Gold-plated copper disks with a concentric ring structure mounted on the cold head stages are interleaved with corresponding disks that are connected to the 50K and 4 K stages of the cryostat. This compact design provides a large effective heat transfer surface and a narrow gas gap (~1 mm) as the circulating gas meanders through the ring structure.

The cool-down process includes two distinct steps, the *precooling* and the *condensation*. During the precooling, helium is circulated past the PTC before infusing the DU while bypassing the main impedance. This step takes roughly 3 days and cools the DU to $\lesssim 4$ K. In the second step, the ^{3}He/^{4}He-mixture is condensed in to the refrigerator, starting the main cooling cycle. The base temperature (11–12 mK without any payload) is reached about 8 h after the start of the condensing step. With a payload installed, the temperature typically settles at around 15 mK, before dropping slowly (time scale of weeks) to ~ 12 mK (owed likely to not, or imperfectly, annealed Cu parts in the setup). The cooling power at 100 mK is ~ 200 μW. The warm-up to room temperature takes nearly a week if the cryostat is left under vacuum; however, introducing of nitrogen gas into the OVC can reduce the warm-up time to less than 3 days.

The SuperCDMS detector tower body includes three thermal stages mirroring the three lower stages of the cryostat (MC, CP and ST). This allows the cold electronics and the wiring between the MC and ST stages to be mounted directly to the tower. The tower is installed by attaching its MC stage to the experimental stage of the cryostat. The detectors are above, and the tower body with the warmer thermal stages is below the experimental stage. A copper can (referred to as *top hat*) is mounted on the experimental stage, surrounding the detector stack to shield it against infrared radiation (IR) from higher temperature stages. It is made entirely from copper, held together and connected to the experimental stage by a total of only four screws; brazing or soldering was avoided as these techniques are known to add noticeable levels of radio-contaminants.

The thermal connection to the CP stage of the tower is provided by a braided and annealed copper heat-sink strap attached to a long copper bar which reaches from the CP stage of the cryostat to below the experimental stage. The Still stage of the tower is thermally connected to the bottom of the Still can by means of a ~ 0.3 mm-thick copper membrane. This membrane also closes the Still can volume to prevent thermal radiation from the 4 K stage from entering. An undulation in the membrane halfway between the tower and the rim of the can allows for a few millimeter of relative vertical movement to avoid differential thermal contraction between the tower and the cryostat causing stress on the tower.

An extension to the 4 K can was designed and built out of copper and held together by screws only, again to avoid brazing and the related increase in radioactive background. This extension has a removable bottom lid and includes feedthroughs for the six readout cables for the SuperCDMS towers. These cables are guided up along the outside of the 4 K can. The feedthrough and the connection to the can provide the heat sinking to that stage. The cables are further heat-sunk at the 50 K stage before they are connected to the room-temperature vacuum feedthrough.

Figure 1 shows pictures of the MC top hat together with the experimental stage mounted on the MC bars, the Still membrane, and the 4 K extension with the IR blocking cable feedthroughs.

The dilution refrigerator was delivered with the thermometry required for its operation and an additional unused twelve-pin vacuum feedthrough installed. This is being utilized for custom wiring for three additional thermometers. The wiring is routed to the MC stage of the cryostat and heat-sunk at the different thermal stages using custom-designed printed circuit boards that also act as IR blocking feedthroughs. Four-pin connectors at each feedthrough allow for easy connection of auxiliary thermometry at the desired thermal stage. In addition, a coaxial wiring solution for the future operation of sensors that require the transmission of high-frequency signals has been developed. An initial test showed that this wiring does not impact the cryogenic performance.

For payload changes, the cryostat needs to be moved from its operating location inside the shielding to the facility's cleanroom. For this, all electrical, gas and vacuum connections need to be removed. The high-pressure helium hoses for the PTC are connected to the rotary valve using quick-connect style connections that automatically seal when disconnecting and minimize air inclusion when connecting. When the cryostat is placed inside the shielding, many of the other standard connection points are difficult to reach. Hence, all connections for the helium mixture and the cryostat vacuum were routed to a conveniently located *connection plate* which has manual valves to close off all the lines going to the cryostat. All lines that may get cold during operation (primarily during the precooling stage) are thermally insulated to minimize frost production and the subsequent dripping water after warming up. A multi-connector is used for conveniently connecting and disconnecting simultaneously all air-pressure lines for the pneumatic valves.

The turbomolecular pump which is part of the circulation system for the helium mixture is mounted on top of the refrigerator and requires cooling. The most common method of cooling with water bears a non-negligible risk of leaks due to the

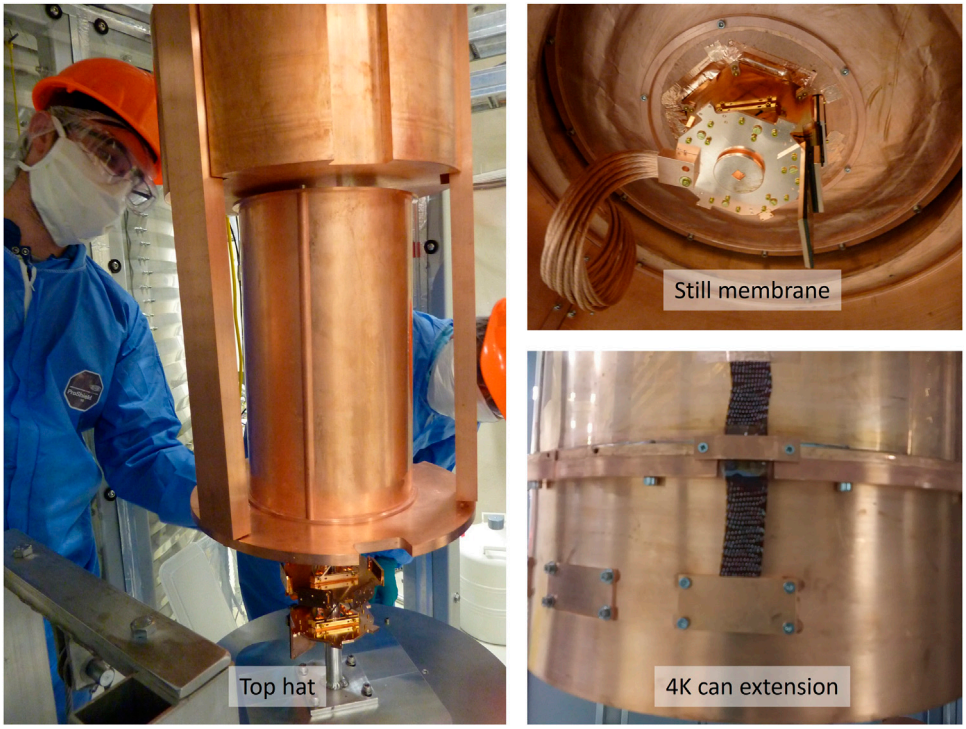

FIGURE 1
Left: The IR shield at the MC stage (*top hat*) is mounted on the experimental stage which in turn is attached to the cryostat by the 3 MC bars. Directly above the top hat is the internal lead shield (see Section 5 for more detail on the shield). The half-pipe shaped walls of the top hat sit in grooves in its top plate, the bottom ring and the connecting vertical rods, The whole assembly is held together with the two screws connecting the top plate to the rods and two screws that attach the top hat to the experimental stage (connecting through the bottom ring to the rods). Top right: The Still membrane with the visible circular undulation is mounted, connecting the bottom of the Still can to the Still stage of the SuperCDMS tower, acting as thermal link as well as closing off the Still volume to IR from the warmer thermal stages. Bottom right: The 4 K extension, consisting of a wall section with screwed-on flange and bottom plate. When needed, the cover plates in the walls are replaced by the easy-to-install IR-blocking cable feedthroughs (also shown in the picture).

regular need to disconnect the lines. Therefore, cooling is provided instead by a Peltier cooler. The temperature of the cooler is regulated by a feedback control system. The original control circuit was based on medium-frequency switching of a high power line, leading to significant electromagnetic emission that interfered with the readout electronics. To mitigate this effect an alternate control was implemented that instead uses voltage control. The power supply is a high-frequency switching power supply where the switching frequency is above the bandwidth of the presently used readout electronics. This avoids the electromagnetic interference introduced by the original control circuit. If a future use of the facility is also susceptible to the interference from the high-frequency switching power supply, it can easily be replaced by a non-switching power supply. Figure 2 shows a top-view of the refrigerator when fully connected at its operating location inside a drywell in the centre of the shielding water tank (for more details of the facility layout see Section 5).

4 Vibration isolation

The laboratory environment or the cryogenic equipment mounted on top of the refrigerator can be sources of vibrations. Several strategies are utilized to mitigate the transmission of such vibrations to the experimental stage. Typically, the pulse tube cooler's rotary valve is the largest source of vibrations in a dry dilution refrigerator. The refrigerator used at CUTE features a double-frame design to effectively decouple the top with the rotary valve and the turbo pump from the lower part where the detectors are installed. The upper part is rigidly connected to the drywell, while the lower part is connected to a stainless steel frame, the *suspension frame*. The latter sits on three soft elastomer cup dampers (Newport ND20-A) as shown in Figure 3. The upper and lower parts of the refrigerator are connected only by the outer wall of the Still pumping line in form of a bellows with very low stiffness (16 N/mm along its axis and 167 N/mm laterally), effectively decoupling the two parts. The UQT discussed in Section 3 further minimizes the transmission of vibrations from the rotary valve of the PTC to the lower part of the cryostat.

The low pressure inside the pumping line (< 1 mbar during normal operation) together with its large diameter leads to a strong upwards force from the atmospheric pressure in the lab acting on the lower (floating) part of the refrigerator. With no stiff mechanical connection between the two parts, this would compress the soft bellows. Hence, extra weights are placed on the suspension frame to counteract this force.

Due in part to the design of the ventilation system at SNOLAB, the pressure in the lab can fluctuate by up to ~ 20% over the course of twenty to 30 minutes. The resulting time-varying force would lead to a change in position of the cryostat relative to the top part of the

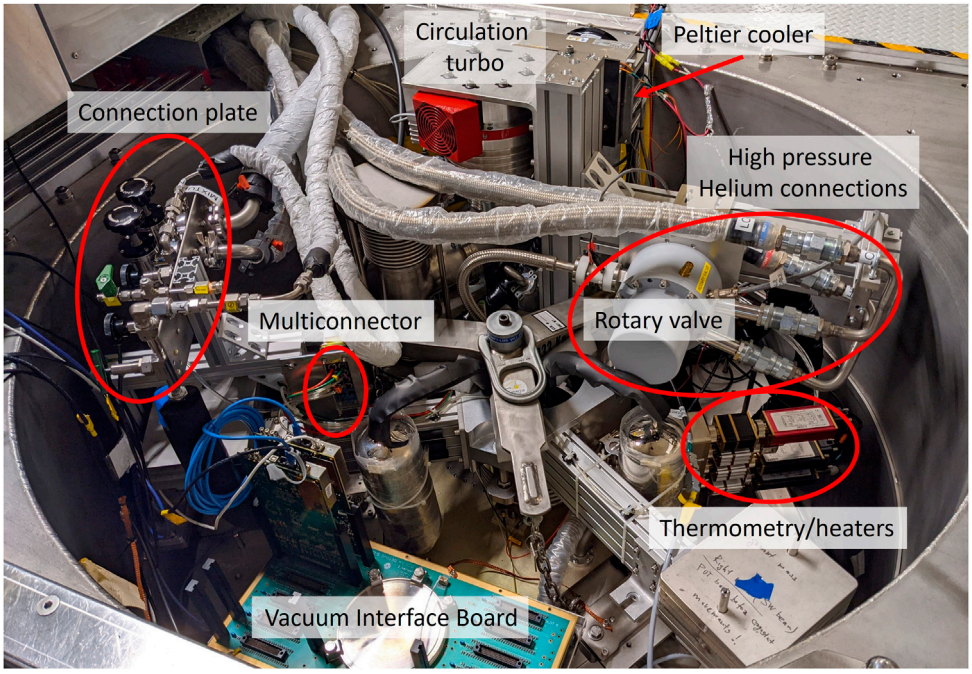

FIGURE 2
Top view of the cryostat when installed and fully connected in its operating location inside the drywell. Labelled in the picture are (starting near the centre and going clockwise): the multiconnector for the pressurized air lines for the pneumatic valves; the connection plate collecting all vacuum and helium-mixture lines that need to be disconnected for moving the fridge; the turbo pump for the helium mixture, and attached behind it the Peltier cooler; the connection points for the high-pressure helium lines, next to the rotary valve the thermometry and heater connections; and the Vacuum Interface Board (VIB) for connecting the SuperCDMS readout electronics.

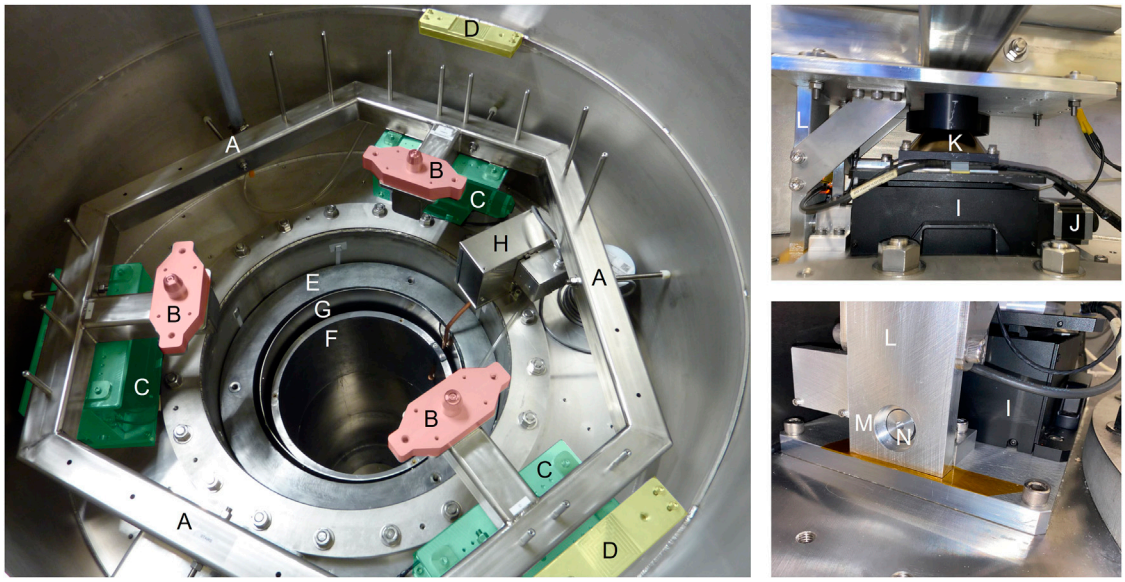

FIGURE 3
Left: The suspension system's steel frame **(A)** with the mounting points for the cryostat [**(B)**, red highlights] sits on three dampers (damper assemblies **(C)** highlighted in green) to mechanically isolate the cryostat from the vibrations transmitted through the drywell. Also visible are two of the mounting points **(D)** for the upper part of the refrigerator on the drywell (yellow highlights), as well as the shielding inside the lower part of the drywell (outer **(E)** and inner **(F)** layers of lead with a thin magnetic shield **(G)** in between; see Sec. 5). Located on the top right in the left picture is the gamma calibration system **(H)** (see Sec. 6). Top right: one of the three damper assemblies. A labjack **(I)** (black) driven by a stepper motor **(J)** (to the right of the labjack) sits on the drywell; the elastomer cup damper **(K)** is mounted on the movable stage of the labjack and carries the suspension frame. The positions of both, the movable labjack stage and the suspension frame are measured relative to the drywell (see text). Visible to the left of the labjack is a vertical aluminum bar **(L)** rigidly attached to the suspension frame. Right bottom: The vertical aluminum bar has a circular cutout **(M)**. A rod **(N)** attached to the drywell penetrates this cutout with a nominal clearance of 1.0 mm all around, limiting the movement of the suspension frame relative to the drywell.

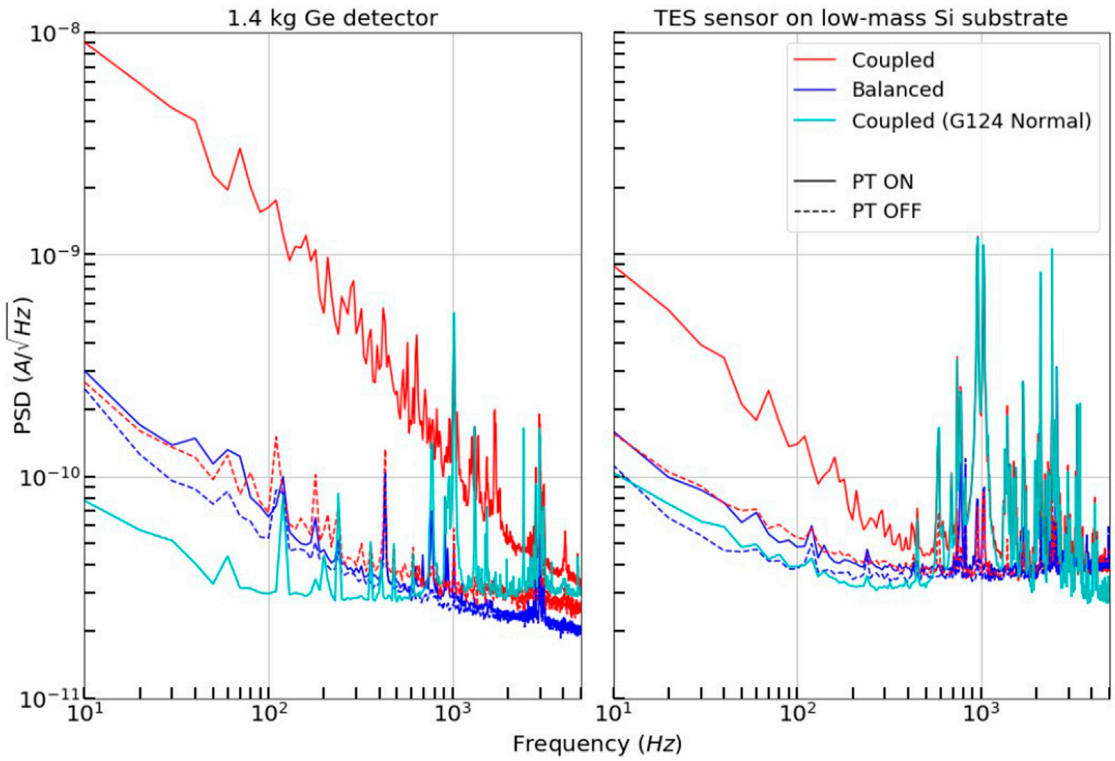

FIGURE 4
Noise power spectra under various conditions of the experimental setup from a 1.4-kg germanium detector (G124) and a small silicon substrate with a transition edge sensor (figure from [18]). Operating conditions include our main source of vibrations, the PTC (PT in the legend) being on and off with the suspension system in its normal operating mode (*balanced*) as well as tilted to introduce a mechanical (as well as electrical) connection between the PTC cold head and the cryostat (*coupled*). The latter condition was tested with G124 sensitive (sensor in its superconducting transition) as well as insensitive (sensor in normal-conducting state) but no change in the readout conditions of the small device. There is a drastic increase in noise in G124 in the coupled state when the PTC is turned on. The small sample also shows a significant increase, but only when G124 is sensitive, producing a large signal. When G124 is insensitive and thus does not produce a signal, the small device sees no significant difference between the coupled and balanced state. This shows that the increase in noise in the small sample is induced by the large signal from G124 (cross talk) rather than by the coupling. These findings support the hypothesis that the noise is indeed coupled through vibrations rather than electrically (the latter would have affected the small devices as much or more than the big one) and thus show the effectiveness of the suspension system.

refrigerator given by the stiffness of the dampers (~80 N/mm). This would change the cross section of the gas gap and hence impact the thermal profile of the cryostat: an increased gas gap improves the Still pumping efficiency, cooling it down, but reduces the thermal link between cold head and the 4K and 50 K stages of the cryostat. To compensate for the pressure variation, each of the three dampers supporting the suspension frame is mounted on the movable stage of a labjack. These stages are driven by stepper motors operated by a micro-controller. On one side of each damper assembly, there is a vertical aluminum bar mounted to the suspension system. Each of these bars has a cutout for a rod that is mounted on the drywell. The cutout is only marginally larger than the rod's cross section, allowing for a maximal deviation of the actual position of the suspension frame from its nominal position by 1 mm (vertically and laterally). Such a tight tolerance is necessary to avoid a touch inside the cryostat between the cold stages of the PTC and the cryostat stages. In the lowest possible position, the three aluminum bars carry the full weight of suspension frame and cryostat, and the cryostat is no longer floating. To monitor the position of the suspension system and the state of the dampers, each damper assembly has an optical sensor and a Hall effect sensor. The optical sensors track the distance between the suspension frame and the drywell and thus the relative position of the two parts of the refrigerator. The Hall effect sensors are used to measure the position of the movable stage of the labjack. Together with the optical sensors, they are used to determine the compression of the dampers. This information is important as the performance of the dampers depends on their compression. A software-based feedback system maintains the relative position of suspension system and drywell and thus of the upper and lower parts of the cryostat; more information about the control algorithm of the suspension system is presented in Section 9.

The performance of the vibration isolation was verified using a prototype 1.4 kg, germanium SuperCDMS HV detector (referred to as G124), as these large sized detectors have been observed to be sensitive to vibration-induced noise. To separate vibrational noise from noise caused by electromagnetic interference, a transition-edge sensor (similar to the TESs of the SuperCDMS detectors) on a small silicon substrate (chip) was operated alongside G124. This device is far less sensitive to vibrational noise but more sensitive to electromagnetic interference. For these tests, the state of the suspension system was changed between its normal (balanced) configuration, and a coupled configuration where it was intentionally tilted to introduce a contact between the cold stage of the PTC and the cryostat. The presence and absence of the touch

was verified by checking the electrical continuity between the pulse tube's cold head and the cryostat which are normally electrically isolated. For each configuration, data from the detectors were collected with the PTC running and switched off. Figure 4 shows the noise power spectra of these tests for both G124 and the TES sensor on the chip. In the coupled state there is a noise difference at low frequency in G124 of almost a factor of forty between PTC on and off. In contrast, only a very small difference (order of 10%–20%) is observed in the balanced state. The noticeable difference for the TES chip between PTC on and off in the coupled state can be traced back to cross-talk in the readout between the two devices and is not related to actual noise in the TES chip: the excess noise disappeared when the sensor on G124 was made insensitive by increasing the readout current until the sensor went into its normal-conducting state, while no change was applied to the TES chip. The fact that the PTC-induced noise couples strongly to G124 and only weakly to the TES chip confirms that the majority of the effect is indeed caused by mechanical vibration; all other effects would be as strong if not stronger in the smaller device when compared to G124. The fact that the excess noise essentially disappears when the suspension system is balanced demonstrates the effectiveness of the system, even though this test is not suited to quantify the level of vibration reduction or residual vibrations.

For a more direct measurement of vibrations, a triaxial and a single-axis accelerometer are available. However, they are presently mounted on top of the cryostat (not inside), show a relatively high electronic noise level and there is indication that they pick up acoustic noise. Hence, some improvements will have to be implemented in order to use them for sensitive diagnostics. However, they were used to demonstrate that a high flow of purge gas in the drywell causes the cryostat to vibrate. The purge gas streams from the bottom to the top of the drywell past the cryostat to prevent radon-rich air from the lab to enter that space (see Section 5). The purge gas flow was reduced to a level where the vibrations caused are negligible (assessed by measurements with the accelerometer as well as a detector) while the radon level in the drywell stayed low [19].

5 Shielding and background

Background radiation comes from various sources. Natural radioactive contaminants—mainly potassium (^{4} K) and the uranium U) and thorium (Th) decay chains—in the environment and the experimental setup itself produce high-energy gamma rays as well as neutrons via (α,n)-reactions and spontaneous fission. In the immediate vicinity of the sensitive components of the experiment, also short-range radiation such as alphas, betas, and low-energy gammas need to be considered. Lastly, cosmic radiation contributes muons, high-energy neutrons generated by muon interactions, and hadronic showers.

The approximately 2 km of rock-overburden at SNOLAB completely remove the hadronic component of the cosmic radiation and reduce the cosmic-ray muon flux by several orders of magnitude (to $< 0.27\ \mu/\mathrm{m}^2/\mathrm{day}$ [13]), and with it the high-energy neutron flux. The experimental space inside the CUTE cryostat is further protected by layers of passive shielding to absorb or moderate the environmental radiation. In addition, efforts were made to minimize the level of contaminants inside the facility itself.

The CUTE shielding was designed based on Monte Carlo simulations considering the attenuation of external radiation as well as the acceptable levels of contamination of the shielding materials. The outer layer of shielding consists of a water tank with a stainless steel drywell in the centre to host the cryostat. The water tank is filled with Ultra Pure Water (UPW) from the SNOLAB water purification plant and provides a shielding thickness of ~1.5 m on the side and ~1.0 m at the bottom, reducing the external gamma radiation by about a factor of 200 [20]. In regular intervals, the UPW is circulated through a container with bromine tablets to avoid biological growth in the water tank. This is scheduled for times when no measurements are taken with the facility to prevent possible electromagnetic interference caused by the water circulation pump. A deck structure holds the drywell in place and provides access to the top of the cryostat.

Inside the drywell, surrounding the cryostat, are two layers of lead. The outer layer has a thickness of 8.7 cm on the sides and 13 cm at the bottom and made from lead with a low activity of ^{210}Pb; the inner layer (2 cm sides and bottom) is made from very-low activity lead[1]. Located between the two layers of lead is a μ-metal shield (from Amuneal, Philadelphia, USA) which reduces the static magnetic flux by about a factor of fifty at the centre of the cryostat. This is necessary because the full strength Earth magnetic field would impact the detectors' performance and make it difficult or impossible to operate the SQUID-based preamplifiers used by SuperCDMS. The space between the inner lead layer and the cryostat is flushed with low-Rn air ($< 10\ \mathrm{Bq/m}^3$) by means of a purge gas line going down to a diffuser at the bottom of the inner lead layer. An aluminum collar plate is installed around the OVC just a few millimeters above the upper end of the lead shield. It covers the gap between the cryostat and the lead shield (without mechanical contact between the cryostat and the shield) to ensure that a low air flow is sufficient to prevent the high-Rn air from the lab (~130 $\mathrm{Bq/m}^3$) from diffusing into that space.

The setup as described so far shields the experimental space inside the cryostat well from radiation from the floor and walls, but the presence of the refrigerator necessarily generates a big opening on the top. This opening is closed by a 20 cm-thick polyethylene (PE) lid on the deck, mitigating neutrons from the top. The PE is encased in a stainless steel box and moves on rails to the side to provide access to the top of the refrigerator. Inside the cryostat, directly above the experimental volume is a 15 cm-thick layer of lead encased in copper. It shields the experimental volume from gamma radiation from above, including from contaminants inside the dilution refrigerator. The internal lead is thermally connected to the Still stage of the cryostat to avoid excess heat load on the experimental stage. A sketch of the experimental setup and a picture of the internal lead shielding are shown in Figure 5.

Most of the materials in use at CUTE were screened to assess their radioactive contamination levels. For the materials which were not screened, contamination levels of comparable materials from previous screening campaigns within the SuperCDMS experiment were considered.

1 "Faible Activite" (FA) lead with about 40 Bq/kg, and "Tres Faible Activite" (TFA) lead with about 6 Bq/kg of 210Pb, from the Fonderie de Gentilly, France.

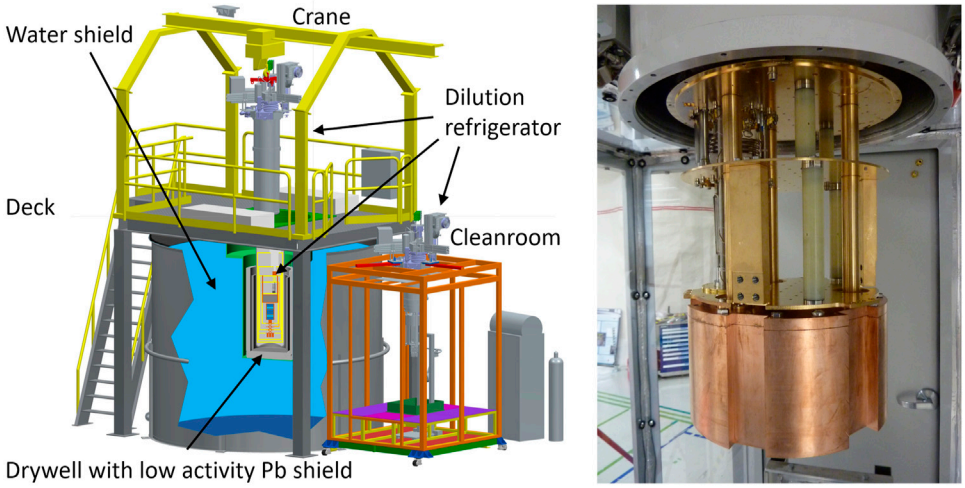

FIGURE 5
Left: Layout of CUTE facility. While in operation, the dilution refrigerator hosting the payload is located inside the drywell at the center of the ~3.5 m-diameter water tank and surrounded by about 11 cm of lead for shielding against environmental radiation. The deck structure holds a 20 cm-thick polyethylene shield moderating neutrons coming from the top. It consists of two-halves and is mounted on rails so it can be moved to the sides, giving access to the top of the cryostat. A monorail crane moves the cryostat between the drywell and the low-radon cleanroom for payload changes. Right: Internal lead shield encased in copper, to block external gammas from the top. As it sits below the MC plate, and thus below all functional parts of the dilution refrigerator, it also block radiation from the dilution unit to the payload which would be mounted below the internal lead (see Figure 1). Mechanically and thermally the lead it is attached to the Still stage of the cryostat by three gold-plated copper rods that clear openings in the CP and MC plates of the fridge.

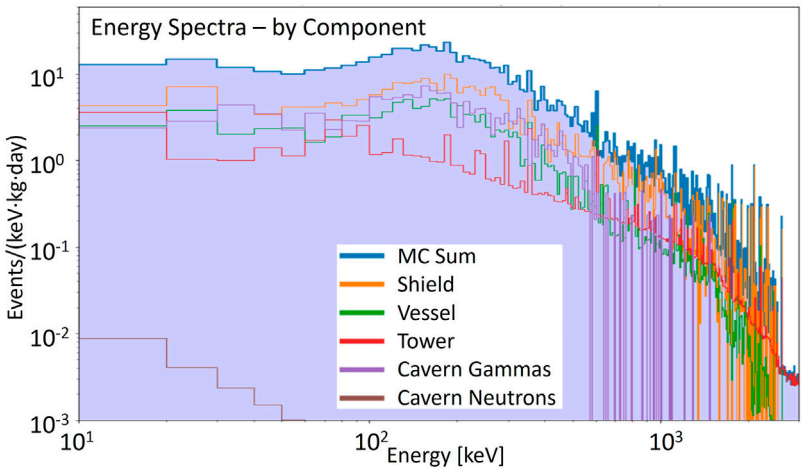

FIGURE 6
Energy spectra from Geant4 Monte Carlo simulations for different components of the background radiation in the CUTE facility for a 600-g SuperCDMS germanium detector. The sum of the contribution is shown in blue. "Vessel" refers to the cryostat components (including the internal shielding) while "Shield" includes all shielding components external to the cryostat. Note that most of the cryostat components had contamination levels below the sensitivity of the screening measurements and the values used in the simulation are the upper contamination limits from those measurements. The "Tower" energy spectrum refers to the radioactive background induced by the detector target material itself and the components of the detector tower structure. Nuclear recoils from radiogenic neutrons originating from the cavern wall contribute only a very small rate.

To estimate the background budget of the facility, extensive Geant4 [21] Monte Carlo simulations were carried out. All the components of the facility were simulated considering all contaminants that were identified in the screening measurements. The gamma and neutron flux from the walls of the SNOLAB cavern are also simulated, considering the measured U, Th and ^{4} K contamination. The simulations framework was set to generate gammas and neutrons from the bulk of the materials inside the facility and the surfaces of the SNOLAB cavern walls.

While the Geant4 Monte Carlo simulation propagates the radiation particles through the different components of the setup, the normalization and conversion of simulated spectra into event

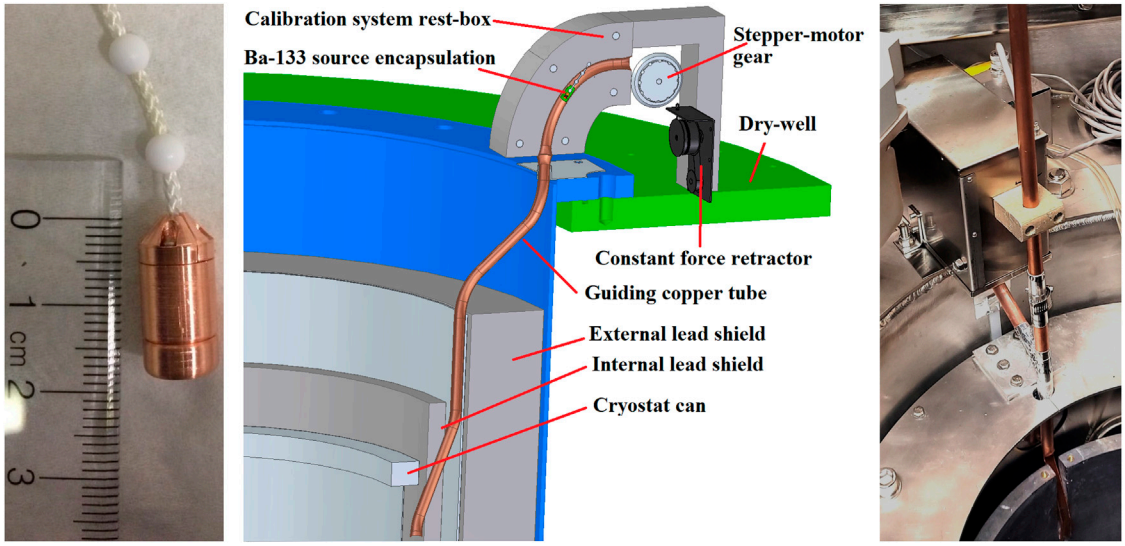

FIGURE 7
Left: Gamma calibration source (^{133}Ba, 37 kBq nominal activity) with double encapsulation added beyond the manufactures encapsulation and attached to the beaded string. Middle: Gamma calibration system schematic. The source is stored in a lead housing located inside the drywell near the top of the cryostat. It is attached to a beaded string that is moved by a stepper motor (only its gear is shown) and spooled by a constant-force retractor. The copper tube guides the source into the space between the cryostat and its lead shielding (Figure adapted from [18]) Right: The gamma calibration system as presently implemented: installed at the rim of the lower part of the drywell, the stainless-steel box houses the lead shielding and the retraction and deployment system. Visible underneath is the copper tube that guides the source into the space between the cryostat (not in place when picture was taken) and the lead shielding (the inner layer of the lead shielding is clearly visible while the outer layer is covered by an aluminum plate). As an upgrade, an additional vertical guide tube was installed to allow the manual deployment of alternate sources into the same space.

rates is handled by Background Explorer [22], a tool originally developed by SuperCDMS and then adopted for CUTE. The energy spectra of events in a 600-g SuperCDMS germanium detector from the different simulated sources are shown in Figure 6.

The sum of all components results in an event rate of 6.7 ± 0.8 events/keV/kg/day in the energy range from 1 to 1,000 keV which is in reasonably good agreement with initial measurements. About 10% of the rate is contributed by the detector stack itself. The major contributors to the background budget are the gammas from the SNOLAB cavern (~30%), the inner layer of the external lead shield (~20%) and the stainless steel of the OVC (~13%). The nuclear recoil rate is expected to be less than half an event/kg/day in the range from 1 to 50 keV.

Most of the external gammas enter through the gaps between the external and internal lead shielding. If a lower gamma background is required for future measurements, an upgrade to the facility could improve the situation by adding additional gamma shielding to reduce those gaps, and replacing the highest contributors from the facility (inner layer of the external lead shield and OVC) with lower activity materials (lower activity lead for the shield and, e.g., copper for the OVC).

6 Calibration systems

CUTE has two dedicated systems for the delivery of radioactive sources that can be used for calibration. A gamma calibration system was installed when the facility was first established; a neutron calibration system is presently in the process of being completed. In addition to these two systems that are both external to the cryostat, there is the possibility to install sources of radiation with low penetration inside the cryostat. An ^{55}Fe X-ray source (~6 keV) with an aluminum foil to generate X-ray fluorescence (~1.5 keV) is presently available and has been used in CUTE. The use of other sources is possible as long as they comply with the SNOLAB-specific requirements for radioactive sources.

The gamma calibration system is based on a ^{133}Ba source with a design activity of 37 kBq. It emits gammas at different energy with the most prominent emission at 356 keV. According to SNOLAB requirements, the source is doubly encapsulated in addition to the manufacturer's encapsulation, and it is attached to a beaded string (see left panel of Figure 7). This string in turn is attached to a constant-force retractor and its movement is controlled by a stepper motor. The system is installed inside the drywell, near the top of the cryostat. It includes a lead housing where the source is located when not in use. The source is pulled into the housing through a curved channel to ensure that there is no direct line of sight to the outside world when the source is in the storage location. With the ≥4 cm of Pb surrounding the source in all directions, the radiation outside is negligible (≪1 nSv/h). A sketch of the calibration system set up is shown in the middle panel of Figure 7.

When being deployed, the source is pulled by gravity, and after exiting the lead shielding it is guided by a copper tube past the top flange of the cryostat into the space between the cryostat and the lead shielding where it can be lowered as low as the bottom of the cryostat. When the source is fully retracted into the shielding, it activates a sensor referred to as *home sensor*, indicating that the sources is in the storage location. An IR reflection sensor package (IR LED and light sensor) is installed next to the chain, between the stepper motor and the lead shield where it detects the beads on the chain moving past to give feedback on the actual motion of the source.

As an upgrade to the original design, the copper guiding tube was modified to allow the deployment of alternate sources by hand. Such sources need to fit into the tube (1/2 inch ID) and be securely attached to a string. The right panel of Figure 7 shows the present guide tube configuration; the system prior to this modification can be seen in the top right of Figure 3.

Neutron sources are of particular concern at SNOLAB as there are several experiments searching for nuclear recoils induced by dark matter particles which could potentially be mimicked by neutrons. Therefore, neutron sources must be stored in a way that ensures that their presence does not increase the neutron flux in those experiments at a measurable level. Additionally, each time a neutron source is moved through the lab, this action needs to be announced a week ahead of time, so the concerned experiments can take the presence of that source into account, or object to the move if the experiment is in a critical phase. This restricts the flexibility when using neutron sources.

Therefore, the neutron source system for CUTE is designed such that during normal use the source ($a^{252}Cf$ with a nominal activity of 37.5 kBq) never leaves the shielding. It is stored within the CUTE water shielding tank, at the bottom near the edge of the tank, and when deployed it is located at the outside wall of the drywell, still inside the water tank, but close to the detectors with no or very little water in between the source and the detectors. The lead shielding inside the drywell is still in place. This diffuses the neutron flux, but modifies the neutron energy spectrum only modestly. An option is built into the system to move the source away from the drywell in a controlled way, increasing the water layer between the source and the drywell from zero up to about 10 cm to moderate the neutron spectrum at the cost of a reduced flux. This is of interest if lower interaction energies or a lower rate are desired, and is also a powerful tool for the validation of Monte Carlo simulations of neutron interactions.

When in the storage location, the source is surrounded by additional shielding. A modest gamma shield reduces the flux of high-energy photons, and a polyethylene (PE) box with about 30 cm of PE all around except towards the bottom moderates the neutrons. The residual dose rate outside the water tank is less than 50 nSv/h even with the water removed from the tank. This mitigates all possible safety concerns.

Both sides of the source are attached to a beaded string (same type as used in the gamma calibration system). The string with the source forms a loop that moves inside a plastic tube through the water tank. Both ends of the tube extend to above the lid of the tank where they end at a box that houses a stepper motor which controls the movement of the source. Special beads are attached to the chain at defined distances away from either side of the source. When one of these beads is detected by a sensor inside the motor box, the source is in its storage location. When the other one is detected, the source is deployed near the drywell, the farthest away from the storage location the source will travel during normal operation. If necessary, however, the source can be brought all the way up into the motor box where it can be accessed and removed from the system. Figure 8 shows a schematic of the neutron calibration system.

7 Payload changes

In a low-background experiment, the most critical part that needs to be protected from contamination is the payload itself. This means the installation or removal of the payload in CUTE must happen under especially clean conditions. While SNOLAB is operated as a class-2000 cleanroom, extended exposure of the SuperCDMS detectors to the lab air would still lead to an accumulation of dust, contributing to the detector background. An even more important contribution to the background would come from the high radon concentration of typically 130 Bq/m^3 in the air at SNOLAB [17]. To protect the payload from exposure to dust and radon, a dedicated cleanroom was installed next to the CUTE water tank. This cleanroom is supplied with low-radon air, either compressed air brought into the lab from the surface with a typical Rn concentration of < 10 Bq/m^3, or air from the SuperCDMS radon reduction facility with a Rn concentration of $\ll 1$ Bq/m^3. The cleanroom is operated at a slight over-pressure to minimize ingress of dust or high-radon air when opening the door or the ceiling. The air quality is constantly monitored by a NUVAP monitor [23], recording among other parameters the particulate rates and the concentration of Rn. The cleanroom class is roughly 200, and for operation with surface compressed air, the radon concentration is at or below 10 Bq/m^3. For safety reasons, there is also an oxygen monitor inside the cleanroom with the possibility to read the oxygen concentration from outside before entering.

A monorail crane is used to lift the cryostat from its operating position in the drywell to the cleanroom, where it is inserted through an opening in the roof. The centre section of the cleanroom roof has two sliding panels, each with a semi-circular cutout fitting tightly around the top part of the OVC can. When closed, the two-halves are locked together. When the cryostat is not in the cleanroom, a plastic lid closes the hole. When the cryostat is in the cleanroom, the various cans can be removed and installed using a hand-operated lifting platform in the centre of the cleanroom, directly underneath the cryostat. When the cryostat is open, the lower sections of the cryostat cans sit on that platform, nested within each other. Plastic collars are used to prevent the inner cans from sliding into the outer ones thus keeping the flanges easily accessible for remounting. Cover plates are available to be placed on top of the cans, providing a working surface directly underneath the cryostat to facilitate the payload installation. Dedicated sets of cryostat and detector tools are located permanently in the cleanroom for convenience. A small movable table is available inside the cleanroom for preparing the payload.

Full cleanroom gear (cleanroom suit, double gloves, booties, hair nets and face masks) must be worn when entering the cleanroom to ensure the best cleanliness standards. In the absence of an airlock, the air quality (particulates and Rn concentration) is compromised when the door is opened to enter the room. It is therefore important to let the air conditions settle (typical time for this process is ~ 10–20 min) before exposing any critical components. Given the small size of the cleanroom, only two people are allowed to work inside at any given time. A third crew member is often located outside to aid with the work planning, coordination, and helping the crew inside with operating procedures and logging of activities. Communication is facilitated by means of a phone line, video conferencing technology and the fact that the walls of the cleanroom are transparent for instantaneous full visual feedback. Figure 9 shows the transfer of the cryostat into the cleanroom and a snapshot of the payload installation into CUTE.

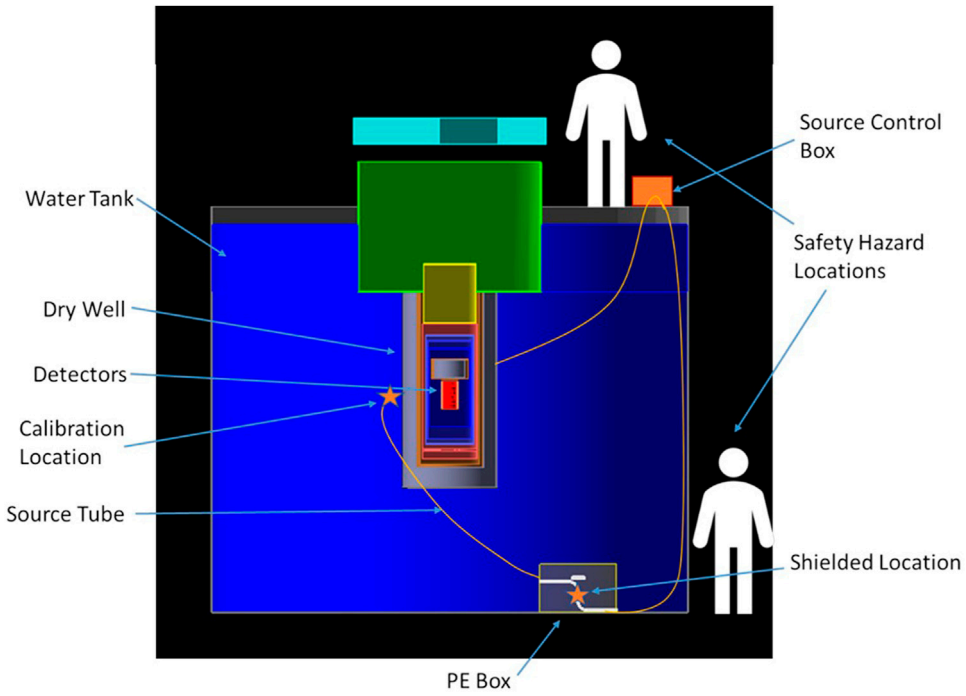

FIGURE 8
Schematic of the neutron calibration system from [19]. The source is moved by a stepper motor (orange box on the top right) through a tube that is installed inside the water shielding tank. The main locations of the source (inside the storage box, bottom right, and in the calibration position, next to the drywell) are indicated by orange stars. Monte Carlo simulations have been performed to asses the radiation exposure to personnel in the two indicated locations, demonstrating that any exposure would be negligible.

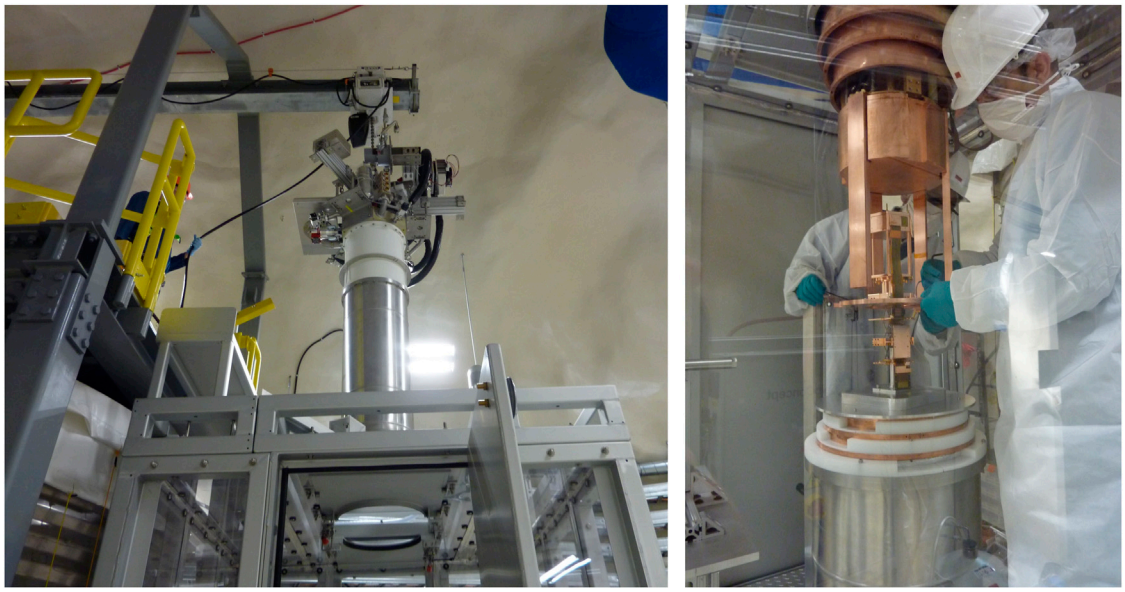

FIGURE 9
Left: The Dilution refrigerator is being moved from the drywell into the cleanroom by the monorail crane. The plastic disk in the ceiling of the cleanroom has been removed and the sliding panels are open, ready for the cryostat to be lowered. Right: A SuperCDMS tower with a single detector about to be mounted to the refrigerator is resting on a cover plate atop the nested cans.

8 Network and electronics

The computer network for the facility is integrated into the SNOLAB network and is protected by a firewall. Access from the outside world is only possible by connecting to a virtual private network (VPN). This allows direct or indirect access to all network-enabled devices that are part of the facility. The present setup of the computer network makes use of two subnets: one is exclusive to the devices needed for the detector operation and readout and the other serves all other devices. A total of four computers are part of the network: one for the operation of the dilution refrigerator, one for all other slow-control activities, one for the data acquisition and one for data handling and transfer. In addition, CUTE has dedicated resources available at the SNOLAB surface facility, for data handling (receiving data from underground and sending them to partner institutions) and for some modest amount of data processing primarily for data quality control.

The facility has two uninteruptable power supplies (UPS). One unit (Eaton 93 E, 40 kW) can power the whole facility including the pumps and compressors of the dilution refrigerators for about 10 minutes. This is usually enough to bridge the facility until SNOLAB's backup generator is able to restore power to the whole laboratory. In case the power restoration fails, a second smaller UPS (Eaton 9PX 6000) keeps the computing and network infrastructure of CUTE alive for about an hour. It comes with an extension module with eighteen 120 V power outlets, and allows for online oversight of the UPS performance and manual switching of individual outlets.

The slow-control system will be discussed in more detail in Section 9. The rest of this section is dedicated to a short description of the SuperCDMS-specific electronics and detector readout solutions.

As discussed in Section 2, the SuperCDMS detectors are mounted on a structure that includes the wiring between the three lowest temperature stages as well as key components of the first-stage amplifier electronics. For each detector installed, a cable with 100 individual conductors (wire loom with 50 twisted pairs) is attached to the tower-wiring and makes the connection to the 4 K stage of the cryostat; this cable is superconducting to minimize the conductive thermal load on the Still stage. From here another cable carries the signals to the room-temperature vacuum interface at the top of the cryostat. The vacuum feedthrough is achieved by a custom-designed printed circuit board (the Vacuum Interface Board, VIB) sandwiched between an ISO160 stainless steel flange. On the outside, custom-designed Detector Control and Readout Cards (DCRCs) attach directly to the VIB. These DCRCs hold the complete control and readout electronics including the signal digitization. They communicate directly with the data acquisition computer via an Ethernet connection and are powered by a 48-V Power-over-Ethernet (PoE) power supply. High voltage for the detector bias is provided by two ISEG HV modules (up to 500 V positive and negative respectively with eight outputs each) and brought to the boards through a dedicated connector on the VIB. The 24-port PoE as well as the HV power supply are identical to those used in SuperCDMS and will be available as backup for SuperCDMS if needed; otherwise they are part of the facility and available for other users of CUTE. Both devices can be addressed and controlled remotely.

9 Slow-control system

A crucial aspect of the CUTE facility is its slow-control system which encompasses the monitoring and control for the cryogenic subsystems, the suspension system, the calibration source deployment systems and all other devices and sensors at the facility except the payload and its readout system. All of the available facility data are recorded and stored in a MySQL database on the slow-control computer.

The control and logging software for the dilution refrigerator and its auxiliary systems was developed and provided by the manufacturer of the dilution refrigerator, CryoConcept, and is installed on the fridge control PC. This software provides functionality to start and stop the pumps and compressors, open and close valves, control thermometry and heater settings, read out and log the thermometry and pressure gauges, and set parameters for automated tasks like "cool down" or "warm up". While it provides the necessary functionality for normal fridge operations, it leaves room for improvements with regards to the monitoring and control of the compressor that drives the pulse tube cooler. In particular, the CryoConcept software cannot reset the compressor which is necessary after the occurrence of certain types of errors (e.g., when the cooling water temperature is out of range) or after a power outage. It also does not log the information from the compressor, such as water, oil and helium temperatures. Python scripts were developed to make those functionalities available so issues can be diagnosed easily and the system can be recovered remotely after faults.

The fridge control PC also runs a program monitoring the liquid nitrogen (LN) cold trap system: a 30-L LN Dewar containing the trap sits on a scale which is continually read out by a Python script. The weight can then be translated into the amount of LN in the Dewar. The setup also includes a LN-refill system (Norhof LN2 microdosing system) with a separate 100-L low-pressure LN Dewar. A heater inside this Dewar builds up pressure for transferring LN to the cold-trap Dewar when needed.

The Peltier cooler for the turbo pump is operated by a hardware controller to maintain its temperature. A Python script was developed to interface with the controller to start and stop the cooler, set the temperature and log the temperature and the output power of the controller.

The suspension system and the calibration systems are both operated through AVR microcontrollers. To communicate with the AVRs, a server written in Node. JS is running on the slow-control computer. Each AVR microcontroller is flashed with a C code that handles the driving of the stepper motors, the I/O of the digital pins, the measurements of the ADCs, and the USB communications. The actual logic used by the suspension and calibration systems is implemented in the Node server, and the microcontroller code only handles the low level hardware control. This provides an additional layer of flexibility by being able to easily add new functionality to the system without having to reprogram the AVR. The Node server creates the USB connection to the microcontrollers, and allows clients to connect to and communicate with the server via a websocket interface.

The logic for the suspension system control software is based on continually reading out the optical sensors via an ADAM-6017 module. A nominal position for the suspension system is set by the

user. While the original design anticipated this to be in the centre of the 2 mm-vertical range of the suspension system (that is at 1.0 mm), it can be set to any value between 0 and 2 mm. If a sensor reading deviates from the nominal position by more than a predefined amount, the respective stepper motor is driven in the appropriate direction to adjust the damper position and thus bring it back into range. The tolerance is presently set to 0.04 mm which offers a good compromise between stability of operation and adjustment frequency. A safety feature stops the automation if an extended adjustment by the stepper motor does not lead to a significant change in the measured position of the suspension system. In addition to the automated position control, each stepper motor can be individually controlled by the user to move up or down with an adjustable speed.

The compression of the dampers as determined by the Hall effect sensor together with the optical sensor is converted to an equivalent mass that should be added to or removed from each damper to bring it to its nominal operating point. This is mostly relevant when a new payload with a significantly different mass has been installed. Weights can be added to or removed from the suspension frame to bring the compression into the desired range.

The Node server also controls the stepper motor that deploys and retracts the gamma calibration source. Via the web interface, users can send the sources to specific positions. The feedback sensors (see Section 6) are used to confirm that the source is moving as intended (optical sensor) or to confirm it is in the housing (home sensor). This is useful after a power outage (in which case the information on the present position can get lost) or as a quick feedback if the source is not moving as intended.

The monitoring and control for the various subsystems is conveniently brought together on a single webpage. The status of the cryogenic systems, suspension system, the Ba calibration system and the Peltier cooler are prominently featured, and key parameters from across the facility are displayed in a ribbon along the top of the page. The suspension system, the calibration system and the Peltier cooler can also be controlled through this webpage. In addition, it includes a feature for plotting and downloading data from the database for easy monitoring of the performance of the facility over time. The slow-control webpage is accessible for all users of the facility while the operation of the dilution refrigerator is limited to a small number of experts; hence, most of the functionality of the fridge control software was deliberately not included in this webpage. Figure 10 shows a screen shot of this webpage.

10 Remote operation

Accessing SNOLAB comes with considerable extra effort compared to most other work places, due to its location 2 km underground in an active mine and the cleanliness requirements in the lab. In addition, there is no regular access during weekends and holidays, including extended no-access periods during the winter holidays and typically for several weeks during the summer for maintenance work by the mining company. Therefore it is important to be able to remotely monitor and control various aspects of the facility and experiment. Significant effort was made to ensure that CUTE can operate without operators present at the lab for an extended period.

The fridge control software operates on a remotely accessible PC and includes all functionality that is required for operating the dilution refrigerator. With the above mentioned custom additions, this also includes a restart after a loss of power. The nitrogen refill system can also be operated remotely; thus, the dilution refrigerator can operate for up to about 2 months without personnel underground. As discussed in Section 9, all relevant systems are remotely controllable and all facility data are accessible through the database. In addition to the aforementioned systems, a remote controlled power distribution unit with five outlets is located at the deck, for connecting and switching auxiliary devices on and off. Finally, the PoE and the HV power supplies are fully remotely controllable.

If all services are available, the period for complete remote operation is limited by the LN supply. Power interruptions can be bridged for about 10 minutes (see Section 8). If the facility loses power, it can be recovered remotely, provided the other systems are operating. However, depending on the length of the outage the cryostat may have warmed up significantly in which case the recovery would take an extended period and may consume significantly more LN than in steady state operations. Compressed air is required for switching the valves of the dilution refrigerator. As a backup in case of a loss of compressed air, there is presently a small buffer tank. In steady state operation when no valves are changing state, this lasts for several hours, but runs quickly out when valves are operated. The backup is sufficient to collect and secure the helium mixture in case an extended outage is expected. For cooling water, CUTE is connected to the low-pressure cooling water loop installed for SuperCDMS. This system presently has no backup in case of failure (either of the low-pressure loop itself, or the primary high-pressure cooling loop operated by SNOLAB). In case the cooling water fails, the compressor for the pulse tube cooler will stop operating after roughly a minute or two. SuperCDMS is exploring options to ensure the long-term stability of the system.

11 Use of CUTE

As discussed earlier, the original motivation for building this facility was the testing of the new SuperCDMS detectors under low-background conditions. However, CUTE provides an ideal environment for testing and operating a wide range of cryogenic devices that are known or suspected to be affected by radiation and vibrations. Prime examples are cryogenic detectors for rare event searches such as the direct detection of dark matter, neutrinoless double beta-decay or other rare nuclear decays (see, e.g., [24–26]) for the reasons discussed in Sec. 1. Depending on the expected event rate, the size and background of the CUTE facility may also be sufficient to carry out actual rare event searches. Even though the facility background of CUTE is noticeably higher than what is expected for the SuperCDMS experiment, operating one of the SuperCDMS HV detector towers for a few months could push the sensitivity of SuperCDMS a good fraction of the way towards the final goal of SuperCDMS SNOLAB.

The special environment provided by CUTE may also benefit cryogenic devices being developed in the fields of quantum information and quantum sensing. A leading platform to form

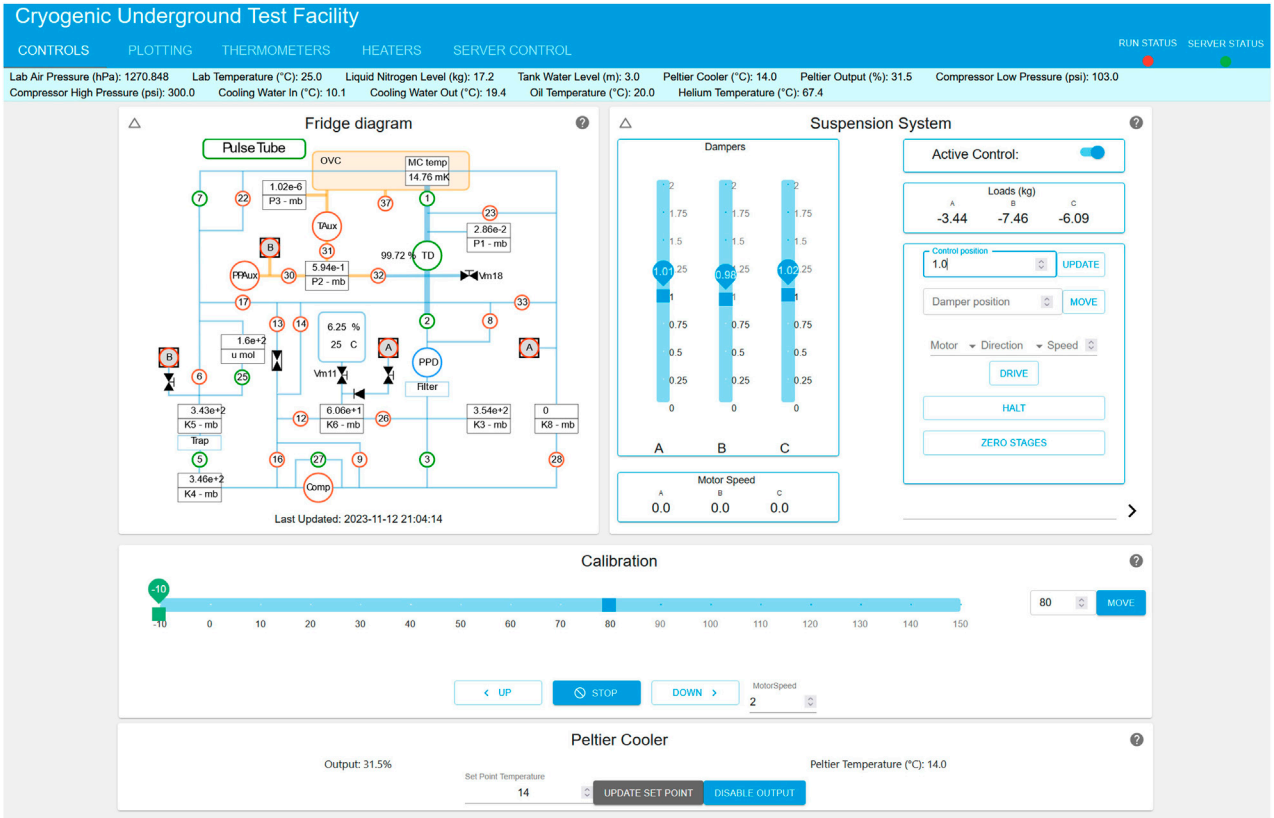

FIGURE 10
Screen-shot of the main slow-control webpage. In the top half are the fridge monitoring panel (left) and the panel for the monitoring and control of the suspension system (right). Active elements in the fridge monitoring panel (pumps, valves) are green, while inactive ones are red. The gamma calibration source is controlled through the first horizontal panel in the lower half; it indicates that the source is located inside the shielding box ("–10 cm"; 0 is just outside the lead shielding and level with the top rim of the lower part of the drywell). The lower horizontal bar controls the Peltier cooler. The cyan-colored banner above the panels shows various facility parameters (including lab air temperature and pressure). The blue top-banner allows the user to choose the alternate tabs for plotting and data downloading, control of the fridge thermometers and heaters, and an interface to easily check the status of (and if necessary restart) the servers for the suspension and calibration systems, the Peltier cooler and the compressor monitoring.

the basis of a practical quantum computer are superconducting quantum bits (*qubits*), due to their modular design and the fact that they can be easily fabricated using techniques developed by the semiconductor industry. It has been shown recently that ionizing radiation could generate excess quasiparticles in superconducting qubits, thereby degrading their performance in a way that would not be easily handled by error correcting codes [27, 28]. Operating such devices in a low-background environment would reduce the error rate due to particle interactions significantly and open the door to studying (and potentially resolving) more fundamental limitations.

The low radiation environment provided by CUTE is not only of interest for testing cryogenic devices in the near absence of radiation, but also allows for dedicated tests of their response to radiation in a controlled way. For particle detectors this is important for calibration measurements as discussed in Section 6, but is, for example, also relevant to understanding and quantifying the impact of ionizing radiation on the coherence time and correlated error rates of superconducting qubits [27, 28].

While quantum computing has the potential to revolutionize a variety of fields, the most mature area of quantum technology is currently that of quantum sensors, which also have the most promise for applications in the near future. Mechanical force sensors based on levitated superconductors currently find use in industry as gravimeters [29], and there is growing interest to improve the sensitivity of this technology by coupling the levitated superconductor to a superconducting qubit and demonstrating cooling to the quantum mechanical ground state [30]. One of the main technical limitations of this technology is mechanical vibrations, which can be mitigated by operating such a device in the low-vibration environment as provided by the CUTE facility. Moreover, if this technology reaches its projected sensitivity it could become difficult to operate in a regular laboratory due to minute environmental gravitational disturbances such as could be induced, e.g., by vehicles driving near the laboratory. A controlled remote environment such as provided by CUTE would significantly reduce the level of such disturbances.

Other devices that could benefit from the low-vibration environment provided by CUTE are small-scale gravitational wave detectors, sensitive to frequencies above 1 kHz [31]. Such devices could be sensitive to millisecond pulsars and exotic signatures produced by decays or annihilations of axions [31]. If this technology is to reach its full potential, an environment with low-vibrations, including low levels of seismic vibrations, would be essential.

After the end of detector testing for SuperCDMS, CUTE will be available to other interested projects. Time will be allocated based on scientific and technological merits of submitted proposals[2], and the CUTE team will work with users on the installation plan and help with all facility interfaces. Some basic equipment will be available to the users, and the aim is to constantly improve the facility to provide more support. For example, a microwave setup consisting of cryogenic coaxial cables, attenuators, filters, and amplifiers is planned to be installed in the near future for a specific experiment, but will stay at CUTE and be available afterwards for other users.

12 Summary and conclusion

CUTE is an underground facility at SNOLAB, built for the purpose of testing cryogenic detectors and other devices in a low-background and low-vibration environment. The underground location together with a composite shielding of water, low-activity lead and polyethylene drastically reduce the flux of cosmogenic and radiogenic radiation. A layer of magnetic shielding reduces the Earth's magnetic field by about a factor of fifty at the location of the payload, and the mechanical decoupling of the cryostat from the upper part of the dilution refrigerator (which includes the pulse tube cooler cold head) together with the cryostat's suspension system significantly reduces the level of vibrations which otherwise might negatively impact the performance of the devices being operated in CUTE. The CUTE facility currently includes a ^{133}Ba source delivery system that can be used for detector calibrations and other studies of the impact of gamma radiation on devices, and a ^{252}Cf neutron source delivery system is planned to be installed and commissioned soon; certain other sources may be made available upon request. Overall, the CUTE facility provides an excellent environment for cryogenic experiments that require low levels of radiation. While the primary motivation for the facility was to test SuperCDMS SNOLAB detectors in an environment with a similar background level as the main experiment, once the testing of SuperCDMS detectors in CUTE is complete, the facility will be available for other experiments on a proposal basis.

Data availability statement

The raw data supporting the conclusions of this article will be made available by the authors, without undue reservation.

Ethics statement

Written informed consent was obtained from the individual(s) for the publication of any potentially identifiable images or data included in this article.

2 Send proposals via e-mail to cute_proposals@snolab.ca or contact SNOLAB management.

Author contributions

PC: Conceptualization, Formal Analysis, Investigation, Methodology, Project administration, Writing–review and editing, Validation, Visualization. JC: Formal Analysis, Investigation, Methodology, Writing–review and editing, Validation, Visualization. SC: Methodology, Writing–review and editing. KD: Methodology, Project administration, Writing–review and editing, Visualization. EF: Formal Analysis, Investigation, Writing–review and editing, Validation, Visualization, Supervision. GG: Conceptualization, Formal Analysis, Funding acquisition, Investigation, Methodology, Project administration, Supervision, Writing–review and editing, Validation, Visualization. RG: Conceptualization, Formal Analysis, Investigation, Methodology, Software, Supervision, Writing–original draft, Writing–review and editing, Validation, Visualization. MG: Formal Analysis, Investigation, Methodology, Writing–original draft, Writing–review and editing, Validation, Visualization. JH: Funding acquisition, Investigation, Methodology, Writing–review and editing, Resources. ZH: Funding acquisition, Investigation, Project administration, Writing–review and editing, Supervision, Visualization. AK: Investigation, Project administration, Writing–review and editing, Supervision, Visualization. AM: Investigation, Writing–review and editing, Data curation, Formal Analysis, Validation, Methodology. SN: Investigation, Methodology, Project administration, Writing–review and editing, Supervision. PP: Methodology, Writing–review and editing. WR: Conceptualization, Funding acquisition, Investigation, Methodology, Project administration, Supervision, Writing–original draft, Writing–review and editing, Formal Analysis, Validation, Visualization. SS: Formal Analysis, Investigation, Project administration, Validation, Writing–original draft, Writing–review and editing, Software, Supervision, Visualization. RU: Investigation, Methodology, Writing–original draft, Writing–review and editing, Data curation, Formal Analysis, Software, Validation, Visualization.

Funding

This research was financially supported by the Canada Excellence Research Chair program (grant held by Dr. Gerbier), Queen's University (Special Research Grant held by Dr. Rau), the Natural Sciences and Engineering Research Council of Canada (SuperCDMS project grant SAPPJ-2017-00030, and grant SAPPJ-2021-00024 held by Dr. Hall), the Canada First Research Excellence Fund through the Arthur B. McDonald Canadian Astroparticle Physics Research Institute (grant CFREF-2015-00009), and the University of Toronto (Special Research Grant held by Dr. Hong). In-kind contribution were provided by SNOLAB, with SNOLAB operations being funded by the Canada Foundation for Innovation and the Province of Ontario, and supported by Vale Canada.

Acknowledgments

The construction of CUTE was made possible through the provision of funds by Dr. Gilles Gerbier (Queen's University) from his Canada Excellence Research Chair grant and generous support from SNOLAB. Additional funds were provided by

Queen's University through a Special Research Grant held by Dr. Wolfgang Rau. The operation and a variety of upgrades were funded largely by the Natural Sciences and Engineering Research Council of Canada (SuperCDMS project grant and an individual grant held by Dr. Jeter Hall), the Arthur B. McDonald Canadian Astroparticle Physics Research Institute, through support for research groups at TRIUMF, the University of Toronto, and the University of British Columbia as well as through engineering and technical support, and by the University of Toronto through a Special Research Grant held by Dr. Ziqing Hong. A contribution to the ^{3}He-contingent was made by Dr. Matt Pyle (University of California, Berkeley). During the construction, the technical and engineering support at Queen's University was invaluable; we thank in particular Chuck Hearnes, Robert Gagnon and Phil Harvey for their contributions. We would like to thank SNOLAB and its staff for support through underground space, logistical and technical services. SNOLAB operations are supported by the Canada Foundation for Innovation and the Province of Ontario, with underground access provided by Vale Canada Limited at the Creighton mine site. Particular thanks for on-site support go to Jasmine Gauthier and José Marco Olivares. A lot of students contributed during their internship at SNOLAB to the Monte Carlo simulations and CUTE detector payload changes; we especially thank Melissa Baiocchi, Scarlett Gauthier, Sabrina Cheng, Jordan Ducatel and Alexander Pleava for their strong commitment. We also thank the group of students from the British Columbia Institute of Technology, Sean Green, Karel Chanivecky Garcia, Gurden Singh Angi and Johnathon Gordon Scott who helped develop the slow-control webpage, and all other undergraduate summer and Co-op students who were involved in the project over the years. Last but not least we thank the SuperCDMS Collaboration: for validating the performance of the facility, the operation of SuperCDMS devices was invaluable. We thank SuperCDMS for providing these devices as well as personnel to operate them and assess their performance.

Conflict of interest

The authors declare that the research was conducted in the absence of any commercial or financial relationships that could be construed as a potential conflict of interest.

The author declared that they were an editorial board member of Frontiers, at the time of submission. This had no impact on the peer review process and the final decision.

Publisher's note

References

1. Petricca F, Angloher G, Bauer P, Bento A, Bucci C, Canonica L, et al. First results on low-mass dark matter from the CRESST-III experiment. *J Phys Conf Ser* (2020) 1342: 012076. doi:10.1088/1742-6596/1342/1/012076

2. Mantegazzini F, Kovac N, Enss C, Fleischmann A, Griedel M, Gastaldo L. Development and characterisation of high-resolution microcalorimeter detectors for the ECHo-100k experiment. *Nucl Instrum Methods A* (2023) 1055:168564. doi:10.1016/j.nima.2023.168564

3. Alkhatib I, Amaral D, Aralis T, Aramaki T, Arnquist I, Ataee Langroudy I, et al. Light dark matter search with a high-resolution athermal phonon detector operated above ground. *Phys Rev Lett* (2021) 127:061801. doi:10.1103/physrevlett.127.061801

4. Rothe J, Angloher G, Ardellier-Desages F, Bento A, Canonica L, Erhart A, et al. NUCLEUS: exploring coherent neutrino-nucleus scattering with cryogenic detectors. *J Low Temp Phys* (2020) 199:433–40. doi:10.1007/s10909-019-02283-7

5. Agnese R, Anderson A, Aralis T, Aramaki T, Arnquist I, Baker W, et al. Low-mass dark matter search with CDMSlite. *Phs Rev D* (2018) 97:022002. doi:10.1103/physrevd.97.022002

6. Marnieros S, Armengaud E, Arnaud Q, Augier C, Benoît A, Bergé L, et al. High impedance TES bolometers for EDELWEISS. *J Low Temp Phys* (2023) 211:214–9. doi:10.1007/s10909-022-02899-2

7. Amaral DW, Aralis T, Aramaki T, Arnquist I, Azadbakht E, Banik S, et al. Constraints on low-mass, relic dark matter candidates from a surface-operated SuperCDMS single-charge sensitive detector. *Phys Rev D* (2020) 102:091101. doi:10.1103/physrevd.102.091101

8. Agnese R, Aralis T, Aramaki T, Arnquist I, Azadbakht E, Baker W, et al. Production rate measurement of tritium and other cosmogenic isotopes in germanium with CDMSlite. *Astropart Phys* (2019) 104(1):1–12. doi:10.1016/j.astropartphys.2018.08.006

9. Albakry MF A strategy for low-mass dark matter searches with cryogenic detectors in the SuperCDMS SNOLAB facility (2022). Available at: https://arxiv.org/abs/2203.08463.

10. Camus P, Cazes A, Dastgheibi-Fard A, Dering K, Gerbier G, Rau W, et al. CUTE: a low background facility for testing cryogenic dark matter detectors. *J Low Temp Phys* (2018) 193:813–8. doi:10.1007/s10909-018-2014-0

11. Rau W, Gerbier G, Camus P, Dering K, Cazes A, Scorza S, et al. CUTE - a cryogenic underground test facility at snolab. *J Phys Conf Ser* (2020) 1342:012128. doi:10.1088/1742-6596/1342/1/012128

12. Agnese R, Anderson A, Aramaki T, Arnquist I, Baker W, Barker D, et al. Projected sensitivity of the SuperCDMS SNOLAB experiment. *Phys Rev D* (2017) 95(8):082002. doi:10.1103/physrevd.95.082002

13. Smith N The SNOLAB deep underground facility. *Eur Phys J Plus* (2012) 127:108. doi:10.1140/epjp/i2012-12108-9

14. Neganov BS, Trofimov VN. Colorimetric method measuring ionizing radiation. *Otkryt Izobret* (1985) 146:215.

15. Luke PN Voltage assisted calorimetric ionization detector. *J Appl Phys* (1988) 64: 6858–60. doi:10.1063/1.341976

16. Mei D-M, Hime A. Muon-induced background study for underground laboratories. *Phys Rev D* (2006) 73:053004. doi:10.1103/physrevd.73.053004

17. SNOLAB. SNOLAB user's handbook revision 2 (2022). Available at: http://snolab2008.snolab.ca/snolab_users_handbook_rev02.pdf.

18. Germond R *Techniques and challenges in low-mass dark matter searches*. PhD Thesis. Kingston, Canada: Queen's University (2023).

19. Corbett J. *Neutron calibration system for the cryogenic underground TEst facility (CUTE)*. MSc Thesis. Kingston, Canada: Queen's University (2021).

20. Liu S. *The limiting background in a detector testing facility for SuperCDMS at SNOLAB*. MSc Thesis. Kingston, Canada: Queen's University (2011).

21. Agostinelli S, Allison J, Amako K, Apostolakis J, Araujo H, Arce P, et al. Geant4—a simulation toolkit. *Nucl Instrum Methods A* (2003) 506(3):250–303. doi:10.1016/s0168-9002(03)01368-8

22. Loer B. Background explorer (2023). Available at: https://github.com/bloer/bgexplorer.

23. Nuvap. company (2022). Available at: https://www.nuvap.com/en/.

24. Poda D. Scintillation in low-temperature particle detectors. *Physics* (2021) 3(3): 473–535. doi:10.3390/physics3030032

25. Alduino C, Alessandria F, Alfonso K, Andreotti E, Arnaboldi C, Avignone FT, et al. First results from cuore: a search for lepton number violation via $0\nu\beta\beta$ decay of ^{130}te. *Phys Rev Lett* (2018) 120(13):132501. doi:10.1103/PhysRevLett.120.132501

26. Armatol A, Broerman B, Dumoulin L, Giuliani A, Khalife H, Laubenstein M, et al. ZnO-based scintillating bolometers: new prospects to study double beta decay of ^{64}Zn. *J Inst* (2023) 18:P06026. doi:10.1088/1748-0221/18/06/p06026

27. Antti P, Karamlou AH, Orrell JL, Dogra AS, Loer B, Vasconcelos F, et al. Impact of ionizing radiation on superconducting qubit coherence. *Nature* (2020) 584(7822):551–6. doi:10.1038/s41586-020-2619-8

28. Cardani L, Colantoni I, Cruciani A, De Dominicis F, D'Imperio G, Laubenstein M, et al. Disentangling the sources of ionizing radiation in superconducting qubits. *Eur Phys J C* (2023) 83(1):94. doi:10.1140/epjc/s10052-023-11199-2

29. Goodkind JM The superconducting gravimeter. *Rev Sci Inst* (1999) 70(11):4131–52. doi:10.1063/1.1150092

30. Romero-Isart O, Clemente L, Navau C, Sanchez A, Cirac JI. Quantum magnetomechanics with levitating superconducting microspheres. *Phys Rev Lett* (2012) 109:147205. doi:10.1103/physrevlett.109.147205

31. Vadakkumbatt V, Hirschel M, Manley J, Clark TJ, Singh S, Davis JP. Prototype superfluid gravitational wave detector. *Phys Rev D* (2021) 104(8):082001. doi:10.1103/physrevd.104.082001

frontiers | Frontiers in Physics

TYPE Perspective
PUBLISHED 12 January 2024
DOI 10.3389/fphy.2023.1340272

OPEN ACCESS

EDITED BY
Salvatore Micciche',
University of Palermo, Italy

REVIEWED BY
Francesca Soramel,
University of Padua, Italy
Rosaria Bonito,
Osservatorio Astronomico di Palermo (INAF), Italy

*CORRESPONDENCE
Erica Caden,
erica.caden@snolab.ca

RECEIVED 17 November 2023
ACCEPTED 29 December 2023
PUBLISHED 12 January 2024

CITATION
Caden E, Kuula S and Zens R (2024), Enhancing equity, diversity, and inclusion in physics: perspectives from North American underground laboratories.
Front. Phys. 11:1340272.
doi: 10.3389/fphy.2023.1340272

Enhancing equity, diversity, and inclusion in physics: perspectives from North American underground laboratories

Erica Caden[1]*, Samantha Kuula[1] and Rochelle Zens[2]

[1]SNOLAB, Lively, ON, Canada, [2]Sanford Underground Research Facility, Lead, SD, United States

Equity, Diversity, and Inclusion (EDI) are important to drive innovation in many different fields, including particle physics. Underground labs are working on many different fronts to improve EDI in their host countries and within particle physics collaborations. Laboratories can institute policies to protect their staff and make improvements to their facilities to increase accessibility. Laboratories can encourage the scientific collaborations they host to have policies and plans for increasing EDI. SNOLAB and the Sanford Underground Research Facility (SURF) are each supporting their employees and user-bases in different ways. Some examples are targeted outreach, consultation with experimental collaborations on their own policies, EDI training, and Indigenous cultural recognition. These efforts are intended to enhance the equity and inclusion of their communities.

KEYWORDS

underground, physics, diversity, equity, inclusion

1 Introduction

Increasing the Equity, Diversity, and Inclusion (EDI) in any organization improves the output of that organization [1, 2]. For the purpose of this paper, we are operating under the following definitions [3]:

Equity: This ensures everyone has access to the same opportunities to grow, thrive, and do their best work. We recognize that advantages and barriers exist for some groups, and that therefore we do not all start from the same place.

Diversity: This encompasses all the ways that individuals or groups are uniquely different from one another. We embrace a broader definition of diversity that not only includes race, ethnicity, and gender but also age, national origin, religion, disability, sexual orientation, socioeconomic status, education, marital status, language, and other factors that influence our ideas, values, perspectives, and experiences.

Inclusion: This is fostered by creating an environment where any individual or group feels welcomed, respected, valued, and empowered to not only fully participate but also to succeed. We are committed to creating a workplace that respects and embraces the differences of every member of our team.

The importance of EDI has also been recognized by national funding agencies in Canada and the US [4–7]. Our objective is a moving target that needs to adjust to the evolving demographics of our society in a timely way. Host laboratories have many roles to play in improving the EDI culture of particle physics. As a laboratory that operates its entire underground space as a Class-2000 clean room, SNOLAB in Greater Sudbury, Ontario,

Canada has additional EDI challenges and opportunities to support its workforce. Sanford Underground Research Facility (SURF) in Lead, South Dakota, United States has taken a leading role in working with the Indigenous peoples who occupied the land for generations before the mine was built. Both North American laboratories' efforts are detailed here.

2 SNOLAB

SNOLAB is Canada's deep underground research laboratory, located in Vale's Creighton mine near Sudbury, Ontario Canada. It provides an ideal low background environment for the study of extremely rare physical interactions. SNOLAB's science program focuses on astroparticle physics, specifically neutrino and dark matter studies, though its unique location is also well-suited to biology and geology experiments. SNOLAB facilitates world-class research, trains highly qualified personnel, and inspires the next-generation of scientists. It is an expansion of the facilities constructed for the Sudbury Neutrino Observatory (SNO) solar neutrino experiment and has 5,000 m^2 of clean space underground for experiments and supporting infrastructure. A staff of over 140 work to support the science by providing business processes, engineering design, construction, installation, technical, and operational support. SNOLAB research scientists provide expert and local support to the experiments and undertake research in their own right as members of experimental collaborations.

SNOLAB is working to improve EDI in Canada through targeting different aspects of research. Within the field of astroparticle physics, SNOLAB plays a significant role hosting many experiments run by large collaborations of scientists. SNOLAB effects change in these groups as well as its own workforce through coordinated efforts in outreach, leadership, experimental policies, and improving its unique underground environment.

2.1 Outreach

SNOLAB's Education and Outreach Group reaches out to communities that are underrepresented in Canadian physics, including women, Indigenous groups, and the 2SLGBTQI+[1] community. SNOLAB provides master classes on analyzing physics data from the SNO experiment [8] and low-background, high-purity Germanium detectors [9] for the International Summer School for Young Physicists [10] and the Canadian Astroparticle Physics Summer School [11]. These annual schools are for high school and undergraduate students and show what a career in research can look like. SNOLAB provides support to a number of local high school robotics teams including the Wiikwemikoong high school team, First Nations STEM [12]. Specifically, SNOLAB donated equipment from its machine shop to assist their efforts in setting up their workshop space. As part of our public outreach, SNOLAB has partnered with Anishinaabe Akinomaagewin Bemwidoot (Knowledge Carrier) William Morin, to provide free, public planetarium shows at the Doran Planetarium at Laurentian University [13]. These events explore the night sky through traditional sky stories. SNOLAB also is a partner in the TRISEP summer school, a 2-week intensive summer program for graduate students [14]. TRISEP's location rotates between TRIUMF (Canada's accelerator lab), Perimeter Institute (a theoretical physics institute), and SNOLAB.

SNOLAB also presents at local career fairs, providing opportunities to engage with the local community at all levels. SNOLAB coordinates with the local boards of the Professional Engineers of Ontario and Women in Science and Engineering professional societies. SNOLAB also participates in the WISE Science Olympics, aimed at girls 9–12 years old to strengthen their interest in science. Education resources are available on the SNOLAB website, with material aimed at different grade ranges [15]. Since 2017, SNOLAB has hosted a booth in the local 2SLGBTQI + Pride festival. Volunteers explain the science of bubbles and rainbows and share information about the laboratory while showing our support for the community. SNOLAB employees have undergone gender inclusivity training through Safer Spaces [16]; this training improved organizational awareness understanding of why its important to show up and support our gender diverse community.

In 2019, SNOLAB partnered with Digital M'kmaq to host a high impact research experience for a group of Indigenous high school students from Nova Scotia. This facilitated a week of learning about science and research in Sudbury. The visit included a day at SNOLAB and travel to the underground facility followed by science talks [17]. Digital M'kmaq has transitioned to Ulnooweg Education Centre. The SNOLAB Education and Outreach Group has reengaged with this group in 2023 to bring the science of SNOLAB to the students in their programming.

2.2 Experiments

As a host lab for large international collaborative experiments, SNOLAB encourages collaborations to have policies that enhance diversity and inclusion in their own ranks. During the initial formation of an agreement between a new scientific collaboration and the lab, each collaboration must have a formal Code of Conduct that is approved by its scientific board. The Code of Conduct should include a path for escalation of issues, be reviewed regularly by the collaboration board, and shared with the collaboration at all large meetings. This is a good first step for many collaborations, but more can be done [18].

As the conceptual and technical designs of an experiment advances, so too should the plans for increasing EDI within the experimental collaboration. Collaborations are each unique, and the EDI plan should be developed by members who understand their own group dynamics and needs. This can include any number of initiatives and varies depending on the size of the collaboration. Ideas for initiatives can include mentorship programs, junior member board representation, including EDI-focused seminars at collaboration meetings, ensuring broad advertising of hiring

1 The recognized Canadian acronym for those who identify as Two-Spirit, Lesbian, Gay, Bisexual, Transexual, Queer, Intersex, and inclusive of other identities.

announcements, and performing a climate survey, among others. The plan should include measurable goals, and progress can be presented to the lab during design reviews and bi-annual experimental reviews.

2.3 Leadership

SNOLAB has incorporated EDI in its leadership through actions that reach into the structure of the lab. SNOLAB named an EDI officer in 2020, who then led a limited-time task force that developed an action plan [3] to be completed by 2023. Measurable indicators that can be used to assess the impact of action plan are:

- Number of complaints, annual reports, complaint trends and analysis;
- Number of EDI reviews, training sessions, barrier removals, policy and procedure changes;
- Increases/decreases in reporting, results and other representation data trends;
- Feedback from internal and external stakeholders (questionnaires, interviews, focus groups);
- Distinct Staff and User Engagement Surveys.

Data collection of these indicators will be crucial for informed decision making. These data will be collected through the engagement surveys, and will be shared in SNOLAB's annual report when statics are available. With inclusion in mind, SNOLAB supports its staff's personal safety in a number of different ways. EDI is written into policies for the lab staff. These include exempting travel to countries or areas wherein the laws and culture are harmful to people with certain identities. SNOLAB's Young Workers Program is required for all employees under 25 years of age, in both term and indefinite positions. This is to ensure that new workers are aware of all their rights and the safety protections that they should be afforded. SNOLAB has designated a quiet space in its office building, to be used for prayer, reflection, or a personal space for nursing/pumping parents.

All staff are encouraged to share their pronouns in their email signatures. This is a normalizing practice that ensures everyone is addressed in the manner they prefer. SNOLAB created stickers for sharing pronouns on name tags while at conferences.

In 2021, SNOLAB signed the Dimensions Charter. An initiative of the Natural Sciences and Engineering Research Council of Canada, the charter is foundational to the Dimensions pilot program that aims to transform post-secondary research experiences and contributions by achieving greater EDI across Canada's research community. By committing to the charter's principles and implementing actions to achieve the charter outcomes, institutions demonstrate their recognition that improving EDI strengthens our research communities. In turn, these efforts will improve the quality, relevance and impact of research, and the opportunities for the full pool of potential participants [19].

SNOLAB regularly conducts Pay Equity Assessments. These are a method of evaluating pay rates within an organization and assessing differences in relative to age, race, gender, seniority, among other criteria. Pay equity assessments are done to remove the effects of unintended biases and create a more equitable workplace.

Having implemented the action plan, in 2023 the task force was replaced with a standing committee. The standing committee membership will be selected to be more representative of the SNOLAB community and user base. EDI continues to be a pillar in the SNOLAB 2023–2029 Strategic Plan. SNOLAB has embraced and implemented these policies from the bottom-up, with support from the top-down, and worked to create a safe and inclusive workplace [20, 21].

2.4 Underground facility

SNOLAB operates its entire 5,000 m^2 underground facility as a Class-2000 clean room, inside an active mine site [22]. This obligates different requirements than other underground facilities might have in terms of the preparation that staff and users undergo to access the lab space. All persons entering SNOLAB underground must have a shower, to remove any dust from the travel through the mine drift. Currently the showering facilities are gendered, and SNOLAB supports all staff and users to choose the change room they feel most comfortable in.

There are plans to renovate the underground space to include a universal shower, for accommodating those who might not feel comfortable showering in a gendered space. This shower already exists in the surface building after recent renovations. SNOLAB is sourcing a mobile quiet space for providing a prayer/pumping space underground as well. The washrooms underground are all "universal", meaning that each one can be used by a person of any gender-identity.

2.5 Mural

In April 2023, SNOLAB worked with William Morin on the creation of a large mural in the lobby of the surface building. This mural, titled "Agaashiinyi: It is Small" is shown in Figure 1. The piece interweaves Indigenous and western knowledge into a cohesive and inspiring work explaining astronomy and particle physics that every person experiences when they enter the building [23].

The mural design begins with the Dream Catcher at the centre, where the spiral paths of the neutrinos emerge from within, out in all directions. For the Anishinaabek, the creation story begins among the stars. The North Star, also called the going-home star or Kiiwe-di-nong, is highlighted within the sky. The mural reminds us of our place in the world by depicting the Milky Way (Jiibay Miikana), the Northern Lights (Waasinoode), and the Boreal Forest (M'tigwaaki) which is the ancestral home of the Anishinaabek, the Ojibwa, Odawa, Potawatami, Algonquin, Cree, and Saulteaux [24]. The bottom right corner has the string of seven strawberries (Ode-min), to reflect many Anishinaabek teachings: the seven Grandfather teachings, women's berry fasting teachings, and our relationship and connection with all plant life [25]. On the outer edge of the Dream Catcher circle are the four colours of the medicine wheel: yellow, red, black, and white. Anishinabek knowledge tells us that these colours represent many things: the sacred medicines, the seasons, and the prophecy that all colours of people would one day inhabit Turtle Island (North America) [26]. For SNOLAB, this means diversity: people, voices, ideas, and world views are all represented—making for better science.

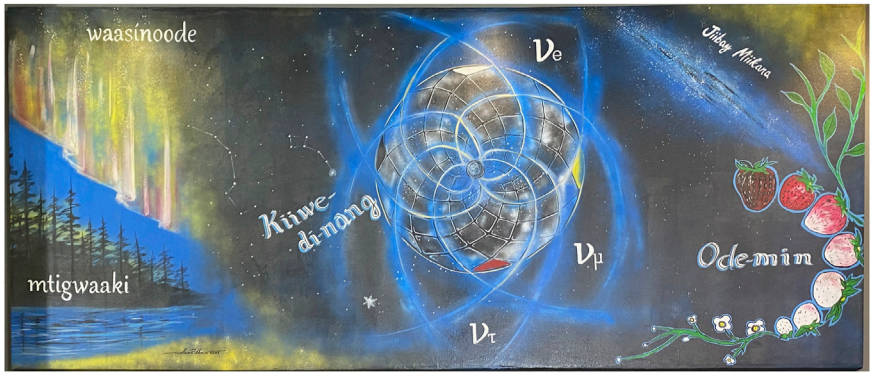

FIGURE 1
Mural by William Morin in the SNOLAB lobby. The themes include neutrinos, the stars, the northern nights, the local forest, the medicine wheel, strawberry teachings, and Anishinaabek names for these concepts. More information can be found in Section 2.5.

3 SURF

The Sanford Underground Research Facility (SURF) is governed by the South Dakota Science and Technology Authority (SDSTA) and hosts world-leading science experiments in a range of disciplines including physics, geology, biology, and engineering. SURF provides significant depth and rock stability—a near-perfect environment for experiments that need to escape the constant bombardment of cosmic radiation, which can interfere with the detection of rare physics events [27].

The history of SURF is complex and has shaped the SDSTA's approach to diversity, equity, and inclusion efforts. SURF is located at the site of the former Homestake Gold Mine in Lead, South Dakota. Homestake was established in 1877, when miners were drawn into the region after General George Armstrong Custer proclaimed the region to be laden with gold [28]. At the time, numerous Indigenous groups lived in and around the Black Hills, an area still held sacred by numerous Tribal Nations in the region today. Thereafter, mining and the desire to homestead led to incredible land loss for Indigenous peoples in the region. From 1851 to 1889, Indigenous groups in the area went from free reign over their traditional homelands to forced removal to the reservation boundaries we know today. Homestake officially closed in 2002, and by 2006 the mine transitioned into an underground research facility [27].

3.1 IDEA office

In light of this history and the need to build a welcoming environment at SURF, the Inclusion, Diversity, Equity and Access (IDEA) Office was formally established in January 2021. The SURF IDEA Office works to:

- create a sense of belonging among SDSTA employees;
- build relationships with under-served communities in South Dakota, with a focus on tribal communities;
- and ensure all visitors to SURF feel welcome.

There are several initiatives at SURF that aim to address the area's history with Indigenous populations, including communication with the Tribal Nations surrounding SURF, a Cultural Advisory Committee, Čhaŋgléška Wakȟáŋ: the ethnobotanical garden at SURF, and the Star Knowledge Working Group.

While the IDEA Office was not established until 2021, cultural efforts at SURF have been a priority since the beginning. The transition from the Homestake Gold Mine to the establishment of SURF led to extensive underground excavation. During this transition, SURF leadership recognized the importance of communicating these developments to regional tribes. In 2010, SURF created a culture and diversity position to lead these efforts and established the Cultural Advisory Committee (CAC), see Section 3.2.

3.2 Cultural advisory committee

The SURF CAC promotes cultural awareness at SURF and advises the SDSTA on topics such as diversity in the workforce, outreach to tribal communities, and creating cultural awareness opportunities for SDSTA staff and the surrounding community. The CAC's recommendations assist the SDSTA Board and key stakeholders in developing cultural awareness activities, including education and outreach programming and recruitment of underrepresented groups. The CAC is comprised of tribal members, educators, and community members and leaders [29]. Two recommendations from the CAC have had a particularly strong impact on the work of the IDEA Office, as outlined in Secs. 3.3 and 3.4.

3.3 Čhaŋgléška Wakȟáŋ

One recommendation was the creation of Čhaŋgléška Wakȟáŋ, the ethnobotanical garden at SURF. The garden's Lakota name roughly translates to "sacred hoop or circle." The garden was originally suggested by a CAC member who is an ethnobotanist and an enrolled member of the Cheyenne River Sioux Tribe. Located on a hilltop meadow at SURF, Čhaŋgléška Wakȟáŋ will serve as a space that inspires connection and collaboration across worldviews and differences. The garden will function as a physical reminder of the cultural significance of this region and SURF's pledge to build meaningful relationships with community partners. The garden will encourage its visitors to slow down and recognize the importance of stewarding the environment along with

FIGURE 2
An imange of Čhaŋgléška Wakȟáŋ, a sacred ethnobotanical garden on SURF grounds. More information can be found in Section 3.3.

relationships that are built in and around SURF. Construction of Čhaŋgléška Wakȟáŋ was completed in the fall of 2023, and is shown in Figure 2. Initial programming for the garden is being developed, and opportunities include presentations from tribal organizations and leaders, opportunities for community gardeners to connect, and teacher professional development on topics related to reclamation [30].

3.4 Star knowledge working group

The CAC also recommended the creation of a working group that would create public learning opportunities to highlight connections between the science conducted at SURF and indigenous ways of knowing. As a result of this recommendation, the Star Knowledge Working Group was formed in 2022. The Group examines topics such as Native star knowledge and understandings of the beginning of the Universe, looking for connections to the science taking place at SURF. Once developed, the Group will use these connections to share cultural and scientific concepts with SURF's internal and external communities.

Currently, the Group meets four times per year and is comprised of staff from the SURF IDEA Office, Education and Outreach Department, the Sanford Lab Homestake Visitor Center, and the Science Department. The Group is currently working to address several recommendations of the CAC, including the creation of programming that highlights cross-cultural attempts to understand the origins of the Universe in order to in order to strengthen relationships with the communities surrounding SURF. Successful programming will require SURF staff and scientists to work collaboratively alongside Indigenous elders and culture bearers to highlight traditional knowledge and draw connections to current research being conducted at SURF.

4 Summary and outlook

Implementing successful EDI programs at any organization, including underground laboratories, takes persistence and the willingness to change and adapt as necessary. Organizations with strong EDI programs ensure that everyone is included and can see their identities reflected in the space. Practitioners must pay special attention to their surrounding communities as well as the communities they serve—researchers, employees, contractors, and others. Incorporating cultural connections through artwork, shared spaces, and other venues can create space for productive dialogue for both scientific connections and belonging.

Demonstrating better outcomes by building more diverse teams is an important tool for top-level management to understand to ensure increased success. Development of policies and implementation of programming to promote cross-cultural learning are two complementary approaches to bolstering equity, diversity and inclusion. Both SNOLAB and SURF have made important steps to implement these approaches in their own organizations. The future work of both organizations will include evaluating and publishing the results of climate surveys and other feedback mechanisms to re-inform our work and update our actions accordingly. The people of underground laboratories, like any organization, are constantly changing and as a result EDI practitioners must be constantly prepared for adaptation.

Data availability statement

The original contributions presented in the study are included in the article/Supplementary Material, further inquiries can be directed to the corresponding author.

Author contributions

EC: Conceptualization, Resources, Writing–original draft, Writing–review and editing. SK: Conceptualization, Resources, Writing–review and editing. RZ: Conceptualization, Resources, Writing–original draft, Writing–review and editing.

Funding

The author(s) declare that no financial support was received for the research, authorship, and/or publication of this article.

Acknowledgments

SNOLAB acknowledges the Canadian Foundation for Innovation and the National Science and Engineering Research Council. SURF acknowledges the U.S. Department of Energy.

Conflict of interest

The authors declare that the research was conducted in the absence of any commercial or financial relationships that could be construed as a potential conflict of interest.

Publisher's note

References

1. Hong L, Page SE. Groups of diverse problem solvers can outperform groups of high-ability problem solvers. *Proc Natl Acad Sci USA* (2004) 101:16385–9. doi:10.1073/pnas.0403723101

2. Lorenzo R, Voigt N, Tsusaka M, Krentz M, Abouzahr K. How diverse leadership teams boost innovation (2018). Available at: https://www.bcg.com/publications/2018/how-diverse-leadership-teams-boost-innovation (Accessed May 24, 2023).

3. SNOLAB EDI Task Force. Snolab edi action Plan (2021). Available at: https://www.snolab.ca/wp-content/uploads/2022/07/SNOLAB-EDI-Action-Plan.pdf (Accessed May 24, 2023).

4. Canada Foundation for Innovation. Equity, diversity and inclusion in research infrastructure funding (2021). Available at: https://www.innovation.ca/sites/default/files/2021-09/CFI-EDI-Report-2021.pdf (Accessed May 8, 2023).

5. National Science Foundation. Broadening participation in STEM (2022). Available at: https://www.edc.org/broadening-participation-stem (Accessed May 8, 2023).

6. US Department of Energy. U.S. Department of Energy diversity, equity, inclusion, and accessibility (DEIA) strategic plan 2022 (2022). Available at: https://www.energy.gov/media/279976 (Accessed May 8, 2023).

7. Tri-Agency of Canada. Tri-agency statement on equity, diversity and inclusion (EDI) (2022). Available at: https://www.nserc-crsng.gc.ca/InterAgency-Interorganismes/EDI-EDI/index_eng.asp (Accessed May 8, 2023).

8. Aharmim B, Ahmed S, Anthony A, Barros N, Beier E, Bellerive A, et al. Combined analysis of all three phases of solar neutrino data from the Sudbury Neutrino Observatory. *Phys Rev C* (2013) 88:025501. doi:10.1103/PhysRevC.88.025501

9. Lawson I. Low background measurement capabilities at SNOLAB. *J Phys Conf Ser* (2020) 1342:012086. doi:10.1088/1742-6596/1342/1/012086

10. Perimeter Institute. International summer school for Young Physicists (2009). Available at: https://www2.perimeterinstitute.ca/outreach/students/programs/international-summer-school-young-physicists (Accessed May 24, 2023).

11. McDonald Institute. Canadian astroparticle physics summer school (2018). Available at: https://mcdonaldinstitute.ca/capss/capss-info/ (Accessed May 24, 2023).

12. First Nations STEM. *First Nations STEM, team 5672* (2014). Available at: https://team5672.weebly.com/ (Accessed 2 June, 2023).

13. Laurentian University. After more than fifty-five years, Laurentian's Doran Planetarium continues to educate and entertain astronomy enthusiasts (2023). Available at: https://laurentian.ca/news/after-more-than-fifty-five%20years-doran-planetarium-continues-educate-entertain-astronomy-enthusiasts.

14. TRISEP. Tri-institute summer school on elementary particles (2013). Available at: https://www.trisep.ca/ (Accessed May 24, 2023).

15. SNOLAB. *Educational resources* (2022) (Accessed 24 May 2023).

16. Safer Spaces. *Create an inclusive workplace environment* (2020). Available at: https://saferspaces.ca/ (Accessed 15 December, 2023).

17. Gemmill A. *Mi'kmaq students in Sudbury to learn about science and technology*. Toronto, Ontario: CBC News (2019). Available at: https://www.cbc.ca/news/canada/sudbury/mikmaq-students-visit-sudbury-1.5152629.

18. Sacco T, Norman D. Report on the review of ATP inclusion plans by DEI expert and science expert panels. *Bull AAS* (2022) 54. doi:10.3847/25c2cfeb.19262acc

19. Government of Canada. Dimensions: equity, diversity and inclusion Canada (2019). Available at: https://cihr-irsc.gc.ca/e/51463.html (Accessed May 8, 2023).

20. SNOLAB. *Strategic plan* (2023). p. 2023–9. Available at: https://www.snolab.ca/about/strategic-plan/.

21. Phillips KW. How diversity works. *Scientific Am* (2014) 311:42–7. doi:10.1038/scientificamerican1014-42

22. Duncan F, Noble AJ, Sinclair D. The construction and anticipated science of SNOLAB. *Annu Rev Nucl Part Sci* (2010) 60:163–80. doi:10.1146/annurev.nucl.012809.104513

23. SNOLAB. New mural unveiled at SNOLAB (2023). Available at: https://www.snolab.ca/news/new-mural-unveiled-at-snolab/ (Accessed June 22, 2023).

24. Union of Ontario Indians. *Anishinabek nation* (2023). Available at: https://www.anishinabek.ca/ (Accessed December 18, 2023).

25. Wabano Centre. Strawberry teachings (2023). Available at: https://wabano.com/product/strawberry-teachings/ (Accessed December 18, 2023).

26. Dumont J. *Culture, behaviour, identity of the Native person*. Sudbury: Laurentian University Press (1989).

27. Sanford Underground Research Facility. *Our history* (2020). Available at: https://sanfordlab.org/feature/our-history (Accessed May 8, 2023).

28. Ostler J. *The lakotas and the black Hills: the struggle for sacred ground*. New York: Penguin Books (2011).

29. Sanford Underground Research Facility. Cultural advisory committee (2020). Available at: https://sanfordlab.org/cultural-advisory-committee (Accessed May 8, 2023).

30. Sanford Underground Research Facility. *Čhaŋgléška Wakȟáŋ* (2023). Available at: https://sanfordlab.org/garden (Accessed May 8, 2023).

frontiers | Frontiers in Physics

TYPE Review
PUBLISHED 18 January 2024
DOI 10.3389/fphy.2024.1317659

OPEN ACCESS

EDITED BY
Sean M. Paling,
United Kingdom Research and Innovation, United Kingdom

REVIEWED BY
Olga Gileva,
Institute for Basic Science (IBS), Republic of Korea
Sandra Zavatarelli,
Universities and Research, Italy

*CORRESPONDENCE
Jari Joutsenvaara,
Jari.Joutsenvaara@oulu.fi

RECEIVED 10 October 2023
ACCEPTED 03 January 2024
PUBLISHED 18 January 2024

CITATION
Joutsenvaara J, Puputti J, Holma M and Kotavaara O (2024), Callio lab: an underground and above ground,laboratory—overview and prospects for high energy and applied physics. *Front. Phys.* 12:1317659.
doi: 10.3389/fphy.2024.1317659

Callio lab: an underground and above ground, laboratory—overview and prospects for high energy and applied physics

Jari Joutsenvaara*, Julia Puputti, Marko Holma and Ossi Kotavaara

Callio Lab, Kerttu Saalasti Institute, University of Oulu, Oulu, Finland

This overview provides a comprehensive insight into Callio Lab, a versatile multidisciplinary research platform, by describing the events and actions that have led to the development of the project-based, pay-by-service approach to organizing and economically running the research activities, a mandatory approach for a platform operating without governmental funding. The research platform has a maximum depth of 1.4 km underground, equivalent to approximately 4,100 m of water equivalent (m.w.e.). The flat-overburden mine configuration of Callio Lab minimizes cosmic-ray background interference, making it an ideal setting for low-background experiments, particularly in neutrino and dark matter research. The main-level galleries, with dimensions up to 12 m wide, 30–40 m long, and 8 m tall, provide ample space for research activities, with the potential for even more extensive galleries based on Laguna design studies. Callio Lab has a history with several small and medium-scale cosmic ray and low-background experiments. This overview highlights the site's inherent characteristics, revealing promising opportunities for high-energy and applied physics research and applications across various scientific domains.

KEYWORDS

Callio lab, research infrastructure, underground physics, underground laboratory, multidisciplinary

Introduction to the history of Callio lab

Since 1962, the Pyhäsalmi Mine in central Finland has been notable for scientific and technological advancements. Rich in zinc, copper, and pyrite, the underground extraction continued until August 2022, surpassing 60 years. Originally slated to close in the late 1990s, the discovery of additional ore beneath the existing mine extended its life by over two decades. The eventual closure of the mine has prompted the nearby Pyhäjärvi community to ponder the future beyond mining.

Underground particle physics was identified as key to revitalizing the Pyhäsalmi mine. In 1999, the University of Oulu, aided by Finnish universities including the University of Jyväskylä as a scientific advisor, founded the Centre for Underground Physics in Pyhäsalmi (CUPP) [1]. Aiming to make the site a leading Finland´s premier international research infrastructure, the team collaborated on neutrino experiment planning, positioning Pyhäsalmi as a candidate for European GLACIER, LENA, and MEMPHYS detectors

[2]. The feasibility of candidate sites was evaluated during the European Commission FP7 program -funded LAGUNA (Large Apparatus for Grand Unification and Neutrino Astronomy) and subsequent LAGUNA-LBNO (Long Base Line Neutrino Observatory) Design Studies [2–5]. Finland was identified as the ideal location to host all the proposed experiments. However, none of these experiments were ultimately constructed in Europe. While the design studies were ongoing, CUPP began its legacy with underground physics experiments, including cosmic ray experiments such as Muons UnderGround (MUG, 2000–2002 [1,6]), Movable Underground Detector (MUD, 2004–2005 [7]) and Experiment with MultiMuon Array (EMMA, 2005–2018 [8,9]). The low background experiment C14 (2016- [10]) is used to study liquid scintillators' 14C/12C ratios. These experiments have shown that Pyhäsalmi, Finland, is where scientific experiments can be conducted.

In 2015, with the Laguna LBNO's outcomes indicating a shift away from major physics experiments at Pyhäsalmi Mine, CUPP underwent a significant transition. It evolved from a dedicated particle physics research facility into Callio Lab, a multidisciplinary research center, to broaden its scientific scope and future potential [11]. The establishment of Callio Lab has broadened onsite research to encompass particle physics and geosciences, among other fields, including deep geothermal [12], deep bedrock microbiological research [13,14] to underground food production [15], and remote sensing [16,17], with more to come.

Callio Lab's collaboration has enhanced its role in Finnish and European research, exemplified by joining the European Plate Observation System (EPOS), which integrated it into broader Finnish, Nordic, and European research networks [18]. Current projects cherish the Pyhäsalmi mine's history as a leading technology adapter and test site for future mining technologies. Current Horizon-funded projects include H2020 GoldenEye [19] and Horizon Europe MINE.IO [20], which benefit from the underground and above-ground infrastructure.

Callio lab overview

Location

Callio Lab is one of the northernmost underground research infrastructures in Europe. It is in the Northern Ostrobothnia, Finland, in the town of Pyhäjärvi. It utilizes the mining environment of Pyhäsalmi Mine Oy. The mine infrastructure consists of a 1.4 km (~4,100 m water equivalent) deep underground mine and surface areas, including two open pits, an industrial area, and a 250 ha tailings area. The research activities benefit from the whole mine site, not just the underground.

The geographical coordinates are N 63.6593, E 26.0419 (WGS 84). It is located near the intersection of two main roads, E4 and VT27. There are three regional airports within a 2-h drive, and the Helsinki-Vantaa airport is only 5 hours away. The mine site can also be accessed by cargo train from the Ylivieska—Iisalmi rail connection. See Figure 1 for illustration.

FIGURE 1
Alt Text Finnish road network. The Pyhäsalmi mine, and thus Callio Lab research environment and CALLIO—Mine for Business, is easy to reach whether arriving by car, train, or plane. Picture by Callio Lab.

Organizational structure

The organizational structure at the Pyhäsalmi mine site involves three major entities. The aforementioned Callio Lab, coordinated by the University of Oulu´s Kerttu Saalasti Institute, facilitates scientific activities at the site utilizing both underground and surface infrastructure. Callio Lab operates on a project-based, pay-by-use approach, minimizing infrastructure costs. The Pyhäsalmi Mine Oy owns the mine site and is responsible for closure activities and safety monitoring. Pyhäjärven Callio [21], established by the Pyhäjärvi town in 2017, oversees the mine's repurposing into an industrial and energy park, including the key development project Pyhäsalmi Pumped Hydro Energy Storage (PPHES), which alone would be big enough to allow the future upkeep and development of the mine site [22] For more information see, e.g., [23].

Services

Callio Lab, like other underground laboratories, provides support services for scientific activities. As Callio Lab operates in a mining environment, there are clean rooms or no radioactivity screening facilities like in more established underground laboratories such as Gran Sasso and Canfranc [24]. However, what the Pyhäsalmi site has over other laboratories is a flat overburden of ~4,100 m water equivalent (m.w.e.) deep underground infrastructure, with the possibility to excavate and equip new underground tunnels and galleries, also at hundred-meter scales [25]. To support the scientific activities, Callio Lab staff can operate in many roles: facilitator of experiments [19,26], onsite operator of scientific instruments [27,28], or developer of needed infrastructure [29]in cooperation with the Pyhäjärven Callio [30].

Safety is paramount in every operation, whether underground, on the surface, or in the airspace above. All the pilots, trials, and experiments need safety documentation and risk analysis to evaluate the activity's safety and its effects on overall safety. Additionally, Callio Lab can provide various data sets, including ground truthing

FIGURE 2
Alt Text Pyhäsalmi Mine Aerial. Callio Lab's research environment is not limited to the underground but utilizes the whole industrial area for various research purposes. Picture by second author.

FIGURE 3
Alt Text Elevator Shaft. Access to the bottom of the mine takes less than 3 min by elevator. The journey is 1.4 km long. Picture by the second author.

data for air and satellite studies and geological and geochemical data from local sources or national data repositories.

Infrastructure

Connectivity

The site offers advanced connectivity and data security, crucial for testing and research. It features a fast wireless network alongside optical cabling for high-speed data transfer. Secure remote operations are enabled through VPN, supporting everything from drones to mining equipment. An industrial 5G network facilitates high data flow and mobile control, while the surrounding area is covered by public 3G and 4G networks [31,32].

Surface

The Pyhäsalmi mine's surface area, spanning several hundred hectares See Figure 2., includes a main industrial zone with a beneficiation plant, open pits, and a direct railway line. Accompanying facilities include offices, workshops, and a logistics center. Its varied topography and 250-ha tailings area are ideal for Earth Observation data verification and support vertical take-offs for helicopters and drones. An airfield nearby facilitates data gathering via fixed-wing platforms [32].

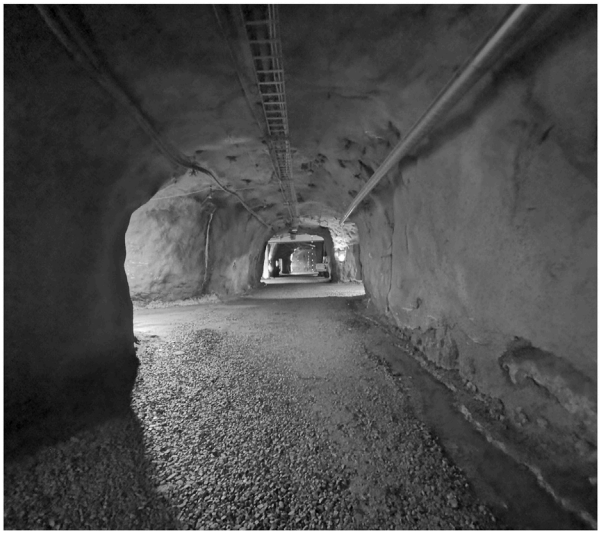

FIGURE 4
Alt Text Tunnel Cross-Section. The tunnel cross-section in the old part of the mine is roughly 5 × 5 m, allowing the transportation of mining equipment and up to 20′ marine containers. Picture by the first author.

Underground

The Pyhäsalmi mine's underground infrastructure expands over 100 km of tunnels and galleries. It features fast elevator access, an 11 km long vehicle incline, advanced ventilation, and a comprehensive safety system, including refuge chambers and a two-way radiophone network. The elevator takes 2.5 min from the surface to the main level at 1,410 m. Figure 3 shows the industrial mine elevator. The incline's crosssection is spacious enough (see Figure 4 for illustration) to transport everything safely, from mining equipment to 20-foot sea containers [32].

The ventilation and water pumping are crucial for safety, managed via a Supervisory Control and Data Acquisition (SCADA) computer system that monitors air quality and alerts for any oxygen or carbon dioxide level deviations. The mine's operational areas maintain an average temperature of 22°–28 °C and a humidity level of 30%–70%, achieved by continuously blowing fresh air from the surface and distributing it through the mine using auxiliary fans and ducting.

The main level of the Pyhäsalmi mine, at a depth of 1,410 m, prioritizes safety with a room for entire shifts, an ambulance, and transport for rescue teams. It features refuge chambers and a communication network for safety and open dialogue. This level includes an extensive maintenance facility, the world's deepest sauna, a restaurant for 100 people, and comprehensive social amenities. The maintenance area has extensive storage,

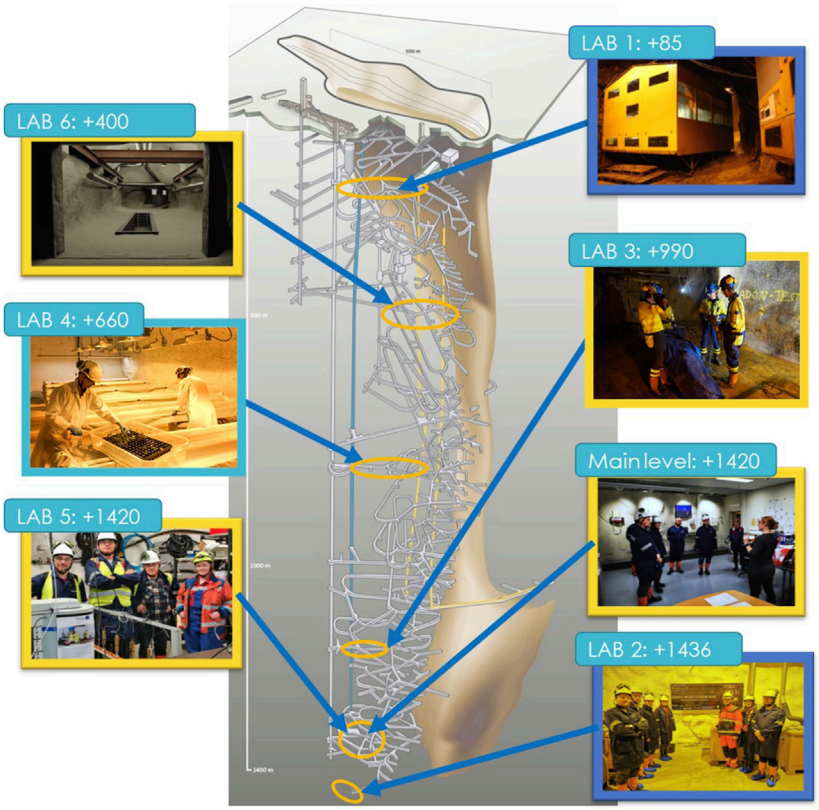

FIGURE 5
Alt Text Axonometric View With Lab Locations. Axonometric view of the Pyhäsalmi Mine and its ore body. The old orebody was carrot-shaped down to 990 m, and the new mine was from 990 m down to 1,400 m. Picture by Callio Lab.

workshops, and parking, supporting the mines' and Callio Lab´s operational needs [11].

The Pyhäsalmi mine includes specialized labs like the underground rescue and training center at 400 m depth (Lab 6) for high-risk training, including fire extinguishing and search and rescue in low visibility. Level 660 (Lab 4) focuses on underground farming technologies and mining machinery testing. Other labs, such as Lab 1*, 2, 3*, and 5, cater to varied projects, with Lab 5 currently hosting physics experiments. Decommissioned labs, marked with *, can be reactivated for new activities. See Figure 5 for the locations of labs within the Pyhäsalmi mine.

Callio lab site characteristics

Overburden

In physics, 'overburden' refers to the material layer above a specific point underground, such as a mine tunnel, and is measured in meters of water equivalent (m.w.e.). Geologically, it includes soil and rock layers. Surface features, composed of soil and bedrock, are monitored using laser scanning, producing digital elevation models with a 2 × 2 meter resolution [33]. Thus, the characteristics and changes in topography and their effect on overburden can be measured accurately; see Figure 6 for more details.

Located a few kilometers west of the mine, Lake Pyhäjärvi spans 122 km^2 with an average depth of 6.3 m and a maximum of 27 m. Its water level is stable and controlled, with an average annual maximum of 139.74 m over 61 years (1961–2022), a recorded maximum of 139.93 m, and a minimum of 139.42 m. The observed and predicted water levels are publicly available via a data dashboard provided jointly by the Finnish Environment Institute, the ELY Centers, the Finnish Meteorological Institute, and the Flood Centre in collaboration with water sector expert organizations [34]. The nearby small lake Komujärvi is characterized as shallow. See Figure 7 for the distances to topograhic anomalies including the water bodies Lake Pyhäjärvi and Lake Komujärvi.

In winter, a snow layer, typically about 40–60 cm thick, forms a fourth type of overburden [35]. The processes capable of causing alterations in the average densities of natural materials in Pyhäsalmi include the movements of underground water utilizing the fractures in bedrock, fluctuation of the water table within the soil overburden (where it surmounts the soil, it pools), and the seasonal [36] appearance of snow cover.

High-energy neutrons generated by muons pose a challenge for low-background experiments, necessitating accurate muon flux measurements to estimate neutron flux underground. From 2000 to 2005, cosmic-ray-induced muon flux was measured at seven different depths, see Figure 8 [7]. The analysis treated all muons similarly, without distinguishing between vertical and non-vertical directions. The average rock density is 2.85 g/cm3, which was used to convert vertical depth into meters of water equivalent. Effective

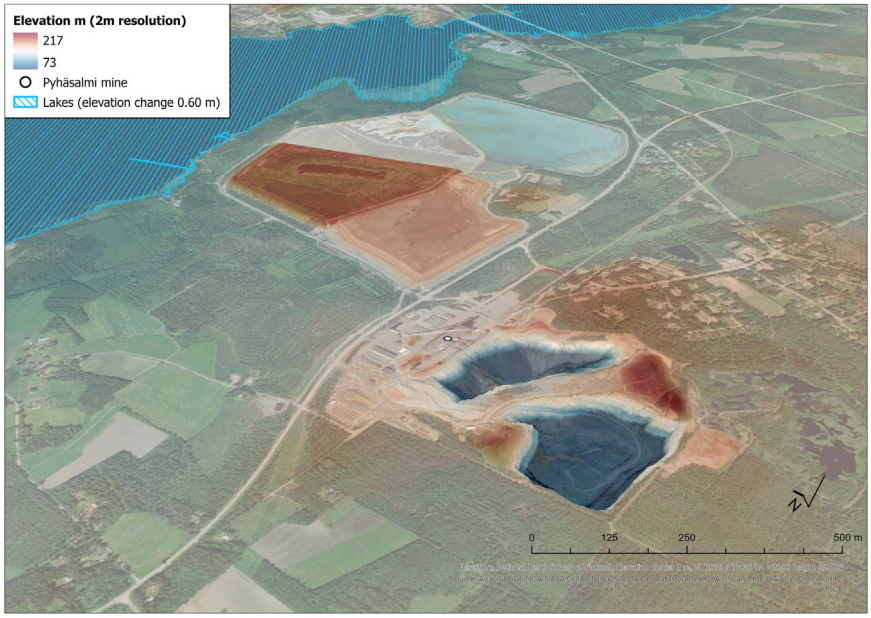

FIGURE 6
Alt Text Pyhäsalmi Digital Elevation Model. Overburden is related to the local topography, and its morphologic changes can be mapped and monitored with high resolution and accuracy to provide a stable environment for underground measurements—analysis and figure created by the fourth author.

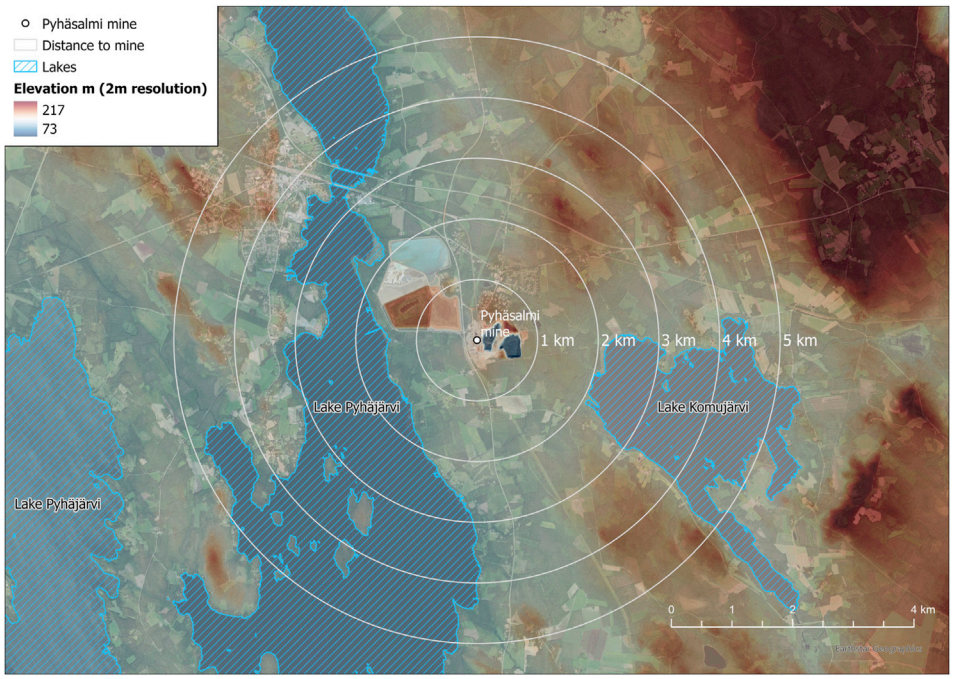

FIGURE 7
Alt Text Lakeside. The geography of the nearest water bodies near the Pyhäsalmi Mine. The surface level of Lake Pyhäjärvi varies by less than a meter as it has been regulated. Similarly, Lake Komujärvi, which flows into Lake Pyhäjärvi, has minor water level variations—the analysis and figure were created by the fourth author.

depths at 210 m and 400 m levels, located beneath the 100-m-deep open pit, were calculated using simulations to reflect flat surface geometry, as shown in Figure 8. Other levels, not under the open pit, were unaffected. Detailed measurement methods are in Ref. [7]. For comparisons of maximum overburden with other laboratories, see Figure 2 in Ref. [24].

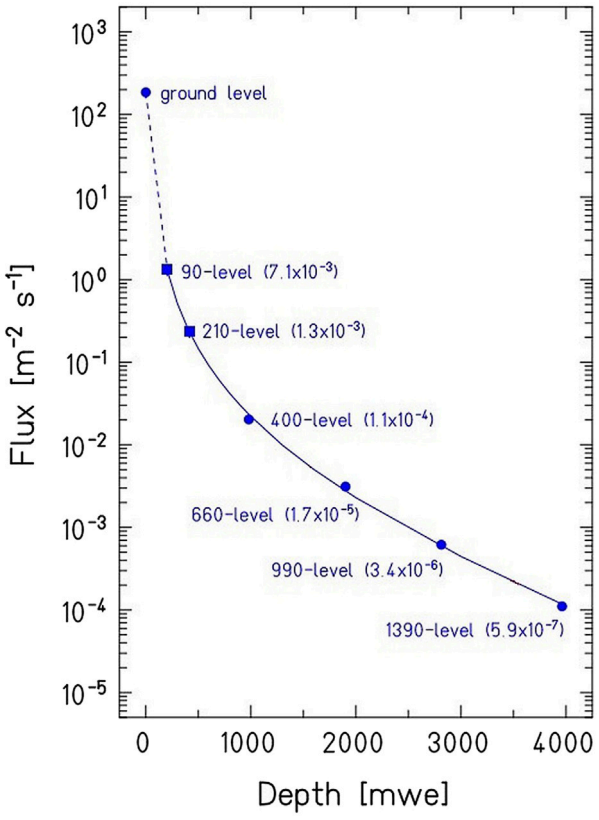

FIGURE 8
Alt Text Muon Flux. The measured muon flux at various levels of the mine. The corresponding reduction of the flux in parentheses compared with the flux at the surface. The deepest surveyed level was at 1,390 m (4,000 m.w.e). Lab 2, e.g., is located at a level of 1,436 m (~4,100 m.w.e.). For comparison, the depth of the Laboratori Nazionali del Gran Sasso (LNGS) underground laboratory, which hosts multiple particle physics experiments, is 3,800 m.w.e [7,37]. Published with the permission of the author.

Since these measurements date back to the early 2000s, updated muon flux measurements and overburden characterization are needed. This is particularly important considering potential changes in the rock mass density structure in the new mine (between 990 and 1,436 m) due to extraction and backfilling activities in the mining galleries.

Geology

The Pyhäsalmi ore deposit belongs to the Volcanogenic Massive Sulphide (VMS) class, originating from submarine volcanism. The Pyhäsalmi VMS deposit is around 1.93–1.92 billion years old [23]. Initially a horizontal sequence, the deposit and surrounding country rocks form a nearly vertical stack due to the Svecofennian Orogeny, a mountain-building event that altered their orientation. During this orogeny, the original marine volcano-sedimentary basin was closed, aligning with the natural sequence of events induced by plate tectonics. The Svecofennian Orogeny also played a significant role by facilitating the generation of magmatic rocks that intruded the original volcano-sedimentary sequence. Some of these intrusive rock bodies, such as pegmatites, may locally contain enriched quantities of U-bearing minerals. See, e.g., Table 10 from the Site characterization and data Callio Lab report[1] of the EUL project [38].

Before mining, the ore deposit at Pyhäsalmi contained significant amounts of chalcopyrite (copper), sphalerite (zinc), and pyrite (sulphuric acid) in a near-vertical formation. Traces of these minerals still exist around the underground laboratories. The surrounding rock mass is not uniform in density or radiation properties due to varying rock types and the presence of tunnels and voids.

Seismicity before and after the end of underground mining

The mine has an Integrated Seismic System (ISS) for microseismic monitoring, covering production areas from 810 m to 1,425 m. The applicable measuring range is from −2 to 2 on the local magnitude scale (M_L). The network consists of geophones with a characteristic frequency of 4.5 Hz capable of detection in a 3–2000 Hz range, allowing for identifying minimal seismic events. Each geophone is linked to a seismometer that converts weak voltage pulses into digital signals, which are then sent to an above-ground server. This server analyzes the data, correlating events across geophones based on timing, automatically pinpointing seismic occurrences, and storing them in a database. The monitoring operates on a trigger system, where the seismometer continuously receives signals but only records data when a predefined signal-to-noise threshold is surpassed.

Weekly data is available online for mine personnel, showing all events (magnitude, location, time) from the past 14 days. More in-depth monthly seismic reports from Australia's Institute of Mine Seismology (IMS) are provided to the mine. According to internal private communications with Pyhäsalmi Mine Oy, in 2021, when underground mining was still ongoing, the total number of recorded seismic events averaged around 95 per week. Any events larger than 0 M_L were singled out; only 10 were recorded out of almost 5,000 yearly events.

Since underground mining ceased in August 2022, including all related tunneling and blasting activities, there has been a notable decrease in seismic events. According to Pyhäsalmi Mine Oy's 2023 data, seismic events have dropped to a weekly average of seven, marking over a 90% reduction from 2021. It is yet to be determined what the final level of seismic activity will be or if it has already stabilized. The current geophone network, focused mainly on areas active from 2001–2022, could be expanded to cover the entire mine infrastructure, especially considering the planned pumped hydro storage construction. A comprehensive review and potential enlargement of the seismic monitoring network are under consideration.

Site characteristics: Natural background radiation

Rare-event searches necessitate significant rock overburden for shielding against cosmic rays and require deep underground laboratories to maintain low background conditions. Natural background radiation (NBR) can arise from various sources,

1 https://bsuin.eu/wp-content/uploads/2022/03/A3.3_report_Site-Description-Callio-Lab_final.pdf

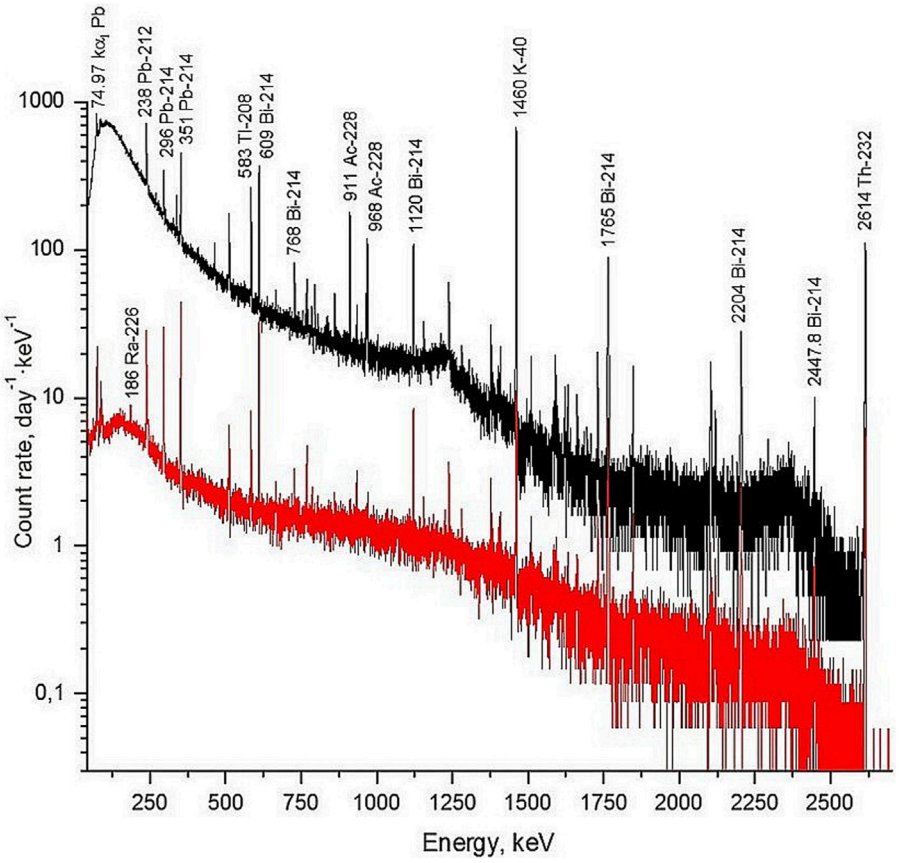

FIGURE 9
Alt Text Gamma-Ray Background Spectra At Lab2. During the Interreg Baltic Sea Region Programme funded BSUIN and EUL projects, detailed GRB measurements were conducted with a dedicated HPGe detector setup, both with the shield open (black) and closed (red) [28]. Published with the permission of the author.

including surrounding rock, concrete, building materials, equipment, and air.

Reactor neutrino background

During Laguna and Laguna LBNO design studies, a numerical study was conducted on the nuclear reactor-induced reactor antineutrino background at different underground laboratories, from which four are selected here as examples: Callio Lab, Canfranc, Frejus, and Boulby. The background calculations were made for the LENA (Low Energy Neutrino Astronomy) detector and are presented in Ref. [39].

The Terrestrial Neutrino Unit (TNU) is one neutrino flux-induced event per 10^{32} protons (~1 kiloton of liquid scintillator) per year. The values for 2014 load factors for the above sites were 72.4 ± 3.1, 222.3 ± 8.4, 550.6 ± 19.5 and 1,005 ± 119 TNUs, respectively [39]. These numbers are slightly higher than the ones presented in Ref. [40]. In 2014, there were four nuclear reactors in Finland, two in Olkiluoto (TVO-1 and TVO-2) with nominal thermal power of 5.0 GW and Loviisa 3.0 GW thermal power. The TVO-3, now operational, with 4.3 GW thermal power, is estimated to add 10% to the Pyhäsalmi reactor antineutrino flux. Olkiluoto and Loviisa sites are roughly 360 km away from Pyhäsalmi. Calculations and TVO-3 estimates are based on Ref. [39].

For more up-to-date reactor antineutrino datasets, visit the website A reference worldwide model for antineutrinos from reactors at https://www.fe.infn.it/antineutrino/. It updates the 2015 published Reference worldwide model for antineutrinos from reactors [40]. It provides updated data on Signal in the Low Energy Region (2003–2021), The worldwide map of reactor antineutrino signals (2003–2021), and Predicted reactor antineutrino signals (2013 reactor conditions).

Natural background radiation

The BSUIN project [41] developed and tested a method for Natural Background Radiation (NBR) measurements in underground labs, ensuring replicability and comparability across different labs. This approach, applied in Lab 2 and Lab 5, included measuring gamma-ray background, in-air radon concentration, and both thermal and fast neutron background. For detailed information on NBR characterization in BSUIN's underground labs, including Callio Lab, see the project's final reports on activity A2.2[2]. Lab 2, located at level 1,436 m, consists of Hall 1 (about 700 m^3) and Hall 2 (around 1,000 m^3)

2 http://bsuin.eu/wp-content/uploads/2021/01/Final_Report_A2.2.pdf

TABLE 1 Specific activities were measured from the samples from Lab 2 and Lab 5 [27,28].

Nuclide	Lab 5	Lab 5	Lab 2	Lab 2
	Wall shotcrete Bq/kg	Floor concrete Bq/kg	Shotcrete Bq/kg	Rock Bq/kg
Ra-226	37.2 ± 11	31.7 ± 9.5	162 ± 14.5	83 ± 7.47
Th-232	27.3 ± 8	17.8 ± 5.3	100 ± 11	47.6 ± 5.2
K-40	614 ± 184	402.8 ± 120.8	1,171 ± 257	1,513 ± 333

for experiments. Air flows from the elevator shaft into the labs at 10 m^3/s, first passing through an air filtration unit. The labs have concrete floors and 5–10 cm thick shotcrete walls. Designed as a multipurpose facility with a low-muon background, its initial use was for underground physics, specifically the C14 experiment, and later for circular economy and underground food production research.

NBR measurements were initially carried out at Lab 2, then at Lab 5. In Lab 2, local NBR was influenced by the radioactivity of the nearby rock and lab hall coating. The thermal neutron flux was assessed using Neutron helium proportional counters (type ZDAJ NEM425A50), sensitive to thermal neutrons, showing a peak at 764 keV. The thermal neutron flux recorded was 1.73 ± 0.10 × 10^{-5} cm^{-2} s^{-1}. The gamma-ray background was measured with a portable, liquid nitrogen-cooled HPGe detector (Canberra Industries, Inc.), covering a range of 7 keV to 3.15 MeV. The gamma-ray flux was 12.7 ± 1.5 cm^{-2} s^{-1}, with a dose of 0.158 ± 0.029 μSv/h. Radon concentration in the air, measured using a Rad7 detector (Durridge Company, Inc.), was 213.3 Bq/m3 ± 11%. Radionuclide analysis of surrounding rock, concrete, and water samples was also conducted. At Lab 5, liquid organic scintillators measured the flux of fast neutrons (0–1.5 MeV) at 37.5 × 10^{-7} cm^{-2} s^{-1}, and the neutron flux above 25 MeV was below 0.6 × 10^{-7} cm^{-2} s^{-1} [23,42].

Differences in background radiation were observed between Lab 2 (1,430 m) and Lab 5 (1,410 m), as evidenced by varying NBR levels. Gamma-ray background (GRB) measurements using a low-background HPGe gamma spectrometer with 100 mm lead shielding revealed distinct contrasts. In Lab 2, the GRB showed total integrated counts of 0.095 s^{-1} kg^{-1} ± 0.03 s^{-1} kg^{-1} (closed lid) in the 40 keV to 2.7 MeV range, significantly higher than Lab 5, which recorded 0.028 ± 0.0007 s^{-1} kg^{-1} in the same range. Open lid measurements were approximately 20 s^{-1} kg^{-1} in Lab 2 and around 10 s^{-1} kg^{-1} in Lab 5. This difference is attributed to local geology and construction materials variations, as Lab 5's area was built earlier than Lab 2. Table 1 details the radionuclide activities in the materials of both labs [27,28]. Figure 9 shows the HPGe detector measured GRB from Lab 2.

Lab 2's shotcrete coating shows higher specific activities of natural nuclides, with noticeable differences between wall shotcrete and floor concrete. This underscores the need for thorough screening of building materials in low-background laboratories. While crucial for such facilities, some screening is also advisable in general construction, especially with the trend of using industrial waste in materials like concrete, especially if the materials are to be used in habitats or more permanent working areas.

Lab 5, located on the main level, benefits from more efficient air ventilation compared to Lab 2 (see Figure 10). This is evident from the radon concentration levels: approximately 213 Bq/m^3 in Lab 2 and about 22 Bq/m^3 in Lab 5. Lab 5 receives fresh air from the surface, with fans blowing 130 m^3/s down to the main level, stabilizing air quality and minimizing annual fluctuations. While Lab 2 used additional air filtering for dust removal, Lab 5 did not require such methods. Both labs implemented dust shielding with mechanical structures and flushing with technical air or nitrogen. The low radon levels observed are notable, demonstrating that effective ventilation can achieve low concentrations underground. Callio Lab also has a 20-tonne, 5′ lead-lined sea container for additional shielding.

FIGURE 10
Alt Text Lab 2 with the C14 experiment is still in place. Lab 2 is the largest of the Labs developed to host various types of experiments at a depth of 1,436 m. The gallery is a former mine tunnel transformed into a research facility. Since C14 Lab 2 has been used for underground cricket farming and a site for underground rescue training and published with permission.

For the development of a low-background facility at Callio Lab, Lab 5 on the main level is the optimal location due to its NBR suitability. Lab 5, a former central underground storage space of about 3,000 m^3, is larger than Lab 2's 800 m^3. It is easily accessible, with just a 3-min elevator ride and a 2-min walk. Large materials can be transported directly into Lab 5 through the incline tunnel, with available lifting equipment for unloading. In contrast, Lab 2 would require upgrades, including new floor and wall coatings and an improved air ventilation system [28].

In characterizing the NBR, it is essential to recognize that no single measurement fully describes an underground infrastructure. Factors like overburden (muon flux), local geology, construction materials (affecting gamma rays and neutron background), and ventilation (radon levels)

significantly influence the NBR characteristics of each hall. Therefore, measurement approaches, like those in the BSUIN project, must be thoroughly detailed technically and in terms of location.

Possibilities for high energy and applied physics research

The initiative taken at Callio Lab has been and still is very multidisciplinary. The topics range from original underground physics to mining, Earth Observation, environmental and production monitoring of the mine, underground and surface safety, deep geothermal pilots, and underground simulated GNSS positioning. Despite the current project assortment having a limited scope for physics activities, these projects have kept Callio Lab operational. The feasibility of conducting physics experiments at the Pyhäsalmi mine site, acknowledged since 1999, remains unchanged.

Physics research

The terrain encompassing the mine's surface and its immediate vicinity is predominantly flat. For the Pyhäsalmi mine, notably Lab 2, the overburden is estimated at approximately 4,100 m.w.e., significantly attenuating the muon background. See Figure 10. for Lab 2. This, coupled with the low radon levels and standard natural background radiation in Lab 5, propels the site forward as a promising ground for further development into underground physics and even a low background physics laboratory. The characterization measurements done during the BSUIN and EUL project at Lab 5 demonstrate that the site can be relatively easily transformed into a low background facility. The bedrock is still well understood and excavatable, potentially hosting small, medium, or even large-scale physics experiments, which was confirmed during the Laguna Design studies and extended site investigations [5,43]. The low reactor antineutrino background is also advantageous for locating various neutrino experiments at Callio Lab [39].

High energy physics

The distance from Cern to Pyhäsalmi is 2,300 km, making it a good candidate for accelerator beam-based long baseline neutrino studies, especially linked to open questions in neutrino mass hierarchy and CP violations [44,45]. The long baseline measurements and the 2,450 km baseline magics could determine the mass hierarchy independent from the CP phase [44]. The Laguna Design studies investigated a large-scale Liquid Argon-based Time Projection Chamber called GLACIER [2].

The Callio Lab, as described in its characteristics section, offers a lower reactor antineutrino background compared to other underground laboratories in mainland Europe. This reduced background is advantageous for studying solar, supernova, and geoneutrinos, whose energy regions intersect with those of reactor antineutrinos. During the Laguna era, the LENA detector was identified as a feasible project for implementation in Pyhäsalmi [2].

Low reactor antineutrino background at Pyhäsalmi also benefits geosciences. Geoneutrinos, emitted from β decaying isotopes like U-238 and Th-232 in the Earth, are detectable via inverse beta decay. Although K-40 is a significant emitter, its neutrinos are undetectable. Studying geoneutrinos at Pyhäsalmi would help to estimate the distribution of these isotopes on average on Earth and as a part of a network of geoneutrino detectors, in more detail the mantle and crust, which is essential for understanding Earth's heat budget and thermal history. Over 99% of the Earth's internal heat is from the decay of these isotopes, influencing plate tectonics and magnetic field generation. Geoneutrinos offer insights into the Earth's deep interior, complementing seismic data and overcoming limitations of traditional rock sampling methods [36,39].

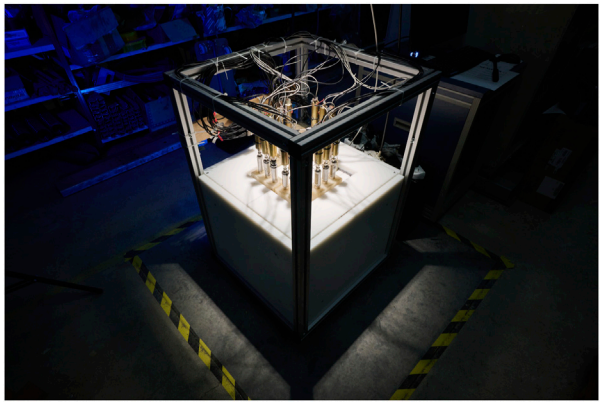

FIGURE 11
Alt Text NEMESIS1.4 At Lab 5. NEMESIS1.4. the pilot experiment for dark matter is located at a depth of 1,410 m in Lab 5. The setup consists of neutron detectors embedded within the lead target of 1,130 kg. The NEMESIS1.4 aims to search for anomalies in high-multiplicity neutron spectra emitted from massive, metallic targets placed deep underground. Photo by S. Trzaska. Published with permission.

Callio Lab could host experiments to detect dark matter particles, which are hypothesized to constitute a significant portion of the universe's mass. With reduced background noise, the underground setting is ideal for deploying sensitive detectors that search for weakly interacting massive particles (WIMPs) or axions. This has been one of the original options since the dawn of CUPP, but it has also been piloted at Callio Lab with the NEMESIS experiment [46,47]. See, e.g., [47], for more information on the NEMESIS, located at Lab 1, and its successor, NEMESIS1.4, located at Lab 5. See Figure 11 for NEMESIS1.4 at Lab 5.

Applied physics research

Muography

Callio Lab's known geology and structured spaces are ideal for muography, which uses cosmic muons to image Earth's interior. This environment is suitable for testing and improving muography. Its mine, with various tunnels, is well-suited for muon radiography and tomography, making Callio Lab an ideal location for exploring and advancing muography research. Surface structures can also be used in experiments, benefiting from an average muon flux of ~150 muons per square meter [48].

Atom interferometric observatory and network

Researching gravitational variations in a mine, especially near a potential pumped-hydro energy storage site, presents a valuable chance for applied physics studies. The consistent overburden,

minor water level fluctuations in Lake Pyhäjärvi and Lake Komujärvi, and data from the energy storage facility help pinpoint gravitational anomalies. Predictable gravitational changes caused by water movements in the underground pumped-hydro facility make it an ideal site for precise gravimetric studies.

The Atom Interferometric Observatory and Network (AION) project could greatly benefit from this environment. It is a multidisciplinary effort to investigate complex physics phenomena using advanced ultra-cold atom and laser technologies. Ultra-cold atoms, cooled to near absolute zero, allow for highly accurate measurements, aiding in detecting phenomena like ultra-light dark matter and gravitational waves, thus significantly contributing to our understanding of the universe [49].

Ultra-light dark matter lacks interaction with electromagnetic radiation and is detectable only through its gravitational effects. However, gravitational waves, which are space-time ripples from cosmic events like black hole collisions, provide a window into the universe's dynamic processes. AION aims to precisely utilize these phenomena precisely, exemplifying applied physics [49].

Given the substantial overburden at Callio Lab and the observable local environmental gravitational changes, it emerges as a suitable venue for hosting various developmental phases of AION, whether in horizontal tunnels or vertical shafts, thus presenting a real-world application of applied physics principles in a controlled environment [49].

Discussion

Despite not receiving governmental funding like other established underground labs, Callio Lab has thrived by supporting science and research through its unique, cost-effective, multidisciplinary approach. With a 4,100 m.w.e. flat overburden, stable bedrock, distance from nuclear reactors, and the capability to expand or excavate new tunnels, Callio Lab is recognized for its potential to host large-scale underground detectors in Finland and Europe, as noted already in the LAGUNA and LAGUNA LBNO design studies.

National and international network support and the University of Oulu's backing have been crucial in transitioning Callio Lab to a multidisciplinary research infrastructure. This collaboration has yielded successes in various European projects, including H2020 GoldenEye, Horizon Europe MINE.IO, and numerous ERDF projects. While this approach has ensured Callio Lab's sustainability, it has also impacted long-term infrastructure development, particularly for underground physics. The lab's future in underground, high-energy, and applied physics depends on the direction and scale of funded projects.

Author contributions

JJ: Conceptualization, Methodology, Visualization, Writing–riginal draft, Writing–review and editing. JP: Visualization, Writing–original draft, Writing–review and editing. MH: Writing–original draft, Writing–review and editing. OK: Conceptualization, Methodology, Writing–original draft, Writing–review and editing.

Funding

The author(s) declare financial support was received for the research, authorship, and/or publication of this article. This work has been partially supported by the H2020 project GoldenEye (GA ID: 869398).

Conflict of interest

The authors declare that the research was conducted in the absence of any commercial or financial relationships that could be construed as a potential conflict of interest.

Publisher's note

References

1. Jämsen T, Elo AM, Kangas J, Mursula K, Peltoniemi J, Usoskin I~G, et al. A new multilevel experiment MUG for observing muon fluxes underground. *Int Cosmic Ray Conf* (2001) 3:1250.

2. Trzaska WH, Enqvist T, Joutsenvaara J, Kalliokoski T, Kokko E, Kuusiniemi P, et al. Advantages of locating LAGUNA in Pyhäsalmi mine. *Prog Part Nucl Phys* (2011) 66(2): 463–7. doi:10.1016/j.ppnp.2011.01.052

3. Trzaska WH, Kalliokoski T, Loo K, Maalampi J, Enqvist T, Joutsenvaara J, et al. LAGUNA in Pyhäsalmi. *Acta Physica Pol B* (2010) 41(7).

4. Nuijten GA. LAGUNA DESIGN STUDY, Underground infrastructures and engineering. *J Phys Conf Ser* (2011) 308(1):012029. doi:10.1088/1742-6596/308/1/012029

5. Tonazzo A. The LAGUNA-LBNO project. *Nucl Part Phys Proc* (2015) 265–266: 192–4. doi:10.1016/j.nuclphysbps.2015.06.049

6. Jämsen T, Usoskin IG, Räihä T, Sarkamo J, Kovaltsov GA, Jämsén T, et al. Case study of Forbush decreases: energy dependence of the recovery. *Adv Space Res* (2007) 40(3):342–7. doi:10.1016/j.asr.2007.02.025

7. Enqvist T, Mattila A, Föhr V, Jämsén T, Lehtola M, Narkilahti J, et al. Measurements of muon flux in the Pyhäsalmi underground laboratory. *Nucl Instrum Methods Phys Res A* (2005) 554(1–3):286–90. doi:10.1016/j.nima.2005.08.065

8. Enqvist T, Föhr V, Joutsenvaara J, Jämsén T, Keränen P, Kuusiniemi P, et al. EMMA: a new underground cosmic-ray experiment. *J Phys Conf Ser* (2006) 34. doi:10.1088/1742-6596/39/1/125

9. Kuusiniemi P, Bezrukov L, Dzaparova I, Enqvist T, Fynbo H, Inzhechik L, et al. Performance of tracking stations of the underground cosmic-ray detector array EMMA. *Astroparticle Phys* (2018) 102:67–76. doi:10.1016/j.astropartphys.2018.05.001

10. Enqvist T, Barabanov IR, Bezrukov LB, Gangapshev AM, Gavrilyuk YM, Vyu G, et al. Towards ^{14}C-free liquid scintillator. *J Phys Conf Ser* (2017) 888:012098. doi:10.1088/1742-6596/888/1/012098

11. Jalas P, Enqvist T, Isoherranen V, Joutsenvaara J, Kutuniva J, Kuusiniemi P. Callio lab, a new deep underground laboratory in the Pyhäsalmi mine. *J Phys Conf Ser* (2017) 888(1):012156. doi:10.1088/1742-6596/888/1/012156

12. Ahonen L, Ala-Rämi K, Lehtinen U, Leppäharju N, Martinkauppi A. *Pyhäsalmen kaivos hiilivapaan lämpöenergiatuotannon mahdollistajana Mikroyrittäjyyden tutkimusryhmä MicroENTRE ja Geologian tutkimuskeskus*. Oulu, Finland: University of Oulu (2023).

13. Kietäväinen R, Ahonen L, Kukkonen IT, Niedermann S, Wiersberg T. Noble gas residence times of saline waters within crystalline bedrock, Outokumpu Deep Drill Hole. *Finland Geochim Cosmochim Acta* (2014) 145:159–74. doi:10.1016/j.gca.2014.09.012

14. Kietäväinen R, Purkamo L. The origin, source, and cycling of methane in deep crystalline rock biosphere. *Front Microbiol* (2015) 6(JUL):725. doi:10.3389/fmicb.2015.00725

15. Callio P. Edible insects (2023). Available from: https://callio.info/natural-resources-business/edible-insects/ (Accessed December 11, 2023).

16. Puputti J, Holma M, Kotavaara O, Joutsenvaara J, Magyar M. Callio Lab – a GoldenEye field trial site at the Pyhäsalmi mine in Finland. In: *EGU general assembly*. Vienna, Austria: Copernicus GmbH (2023).

17. GoldenEye. GoldenEye (2021). Available from: http://www.goldeneye-project.eu/ (Accessed December 11, 2023).

18. Elger K, Lauterjung J, Ulbricht D, Cocco M, Atakan K, Bailo D, et al. *Implementation of the European plate observing system*. Norwich, England, UK: EPOS Infrastructure (2016).

19. Havisto J, Matselyukh T, Paavola M, Uusitalo S, Savolainen M, González AS, et al. Golden AI data acquisition and processing platform for safe, sustainable and cost-efficient mining operations. In: 2021 IEEE International Geoscience and Remote Sensing Symposium IGARSS; July, 2021; Brussels, Belgium (2021). p. 5775–8.

20. European Commission. MINE.IO (2023). Available from: https://ec.europa.eu/info/funding-tenders/opportunities/portal/screen/how-to-participate/org-details/999756982/project/101091885/program/43108390/details (Accessed December 11, 2023).

21. Callio. Callio - mine for business (2021). Available from: https://callio.info (Accessed December 11, 2023).

22. Karhinen S, Huuki H. Private and social benefits of a pumped hydro energy storage with increasing amount of wind power. *Energy Econ* (2019) 81:942–59. doi:10.1016/j.eneco.2019.05.024

23. Joutsenvaara J, Holma M, Puputti J, Szkliniarz K, Kisiel J. *SITE DESCRIPTION AND DATA OF THE CALLIO LAB Site services*. Characteristics and Data (2021). Available from: https://bsuin.eu/wp-content/uploads/2022/03/A3.3_report_Site-Description-Callio-Lab_final.pdf.

24. Ianni A. Considerations on underground laboratories. *J Phys Conf Ser* (2020) 1342(1):012003. doi:10.1088/1742-6596/1342/1/012003

25. Salmelainen J, Ström J, Cristiá S, Hatakka L, Tirinen J, Westerlund G, et al. *LAGUNA-LBNO EXTENDED SITE INVESTIGATION AT PYHÄSALMI, Finland Deliverable 9 Site investigation summary* (2014).

26. European Commission. Mine.IO consortium. Horizon Europe project MINE.IO (2023). Available from: https://ec.europa.eu/info/funding-tenders/opportunities/portal/screen/how-to-participate/org-details/999756982/project/101091885/program/43108390/details (Accessed December 13, 2023).

27. Pohuliai S, Sokolov A, Gostilo V, Joutsenvaara J, Puputti J. Measurements of gamma-ray background radiation in Pyhäsalmi mine. *Appl Radiat Isot* (2020) 161:109166. doi:10.1016/j.apradiso.2020.109166

28. Gostilo V, Sokolov A, Pohuliai S, Joutsenvaara J. Characterisation of the natural gamma-ray background in the underground Callio Lab facility. *Appl Radiat Isot* (2020) 156:108987. doi:10.1016/j.apradiso.2019.108987

29. Joutsenvaara J. *Deeper understanding at Lab 2: the new experimental hall at Callio Lab underground centre for science and R & D in the Pyhäsalmi Mine*. Master´s Thesis. Finland: University of Oulu (2016).

30. Callio. Callio lab (2021). Available from: https://calliolab.com (Accessed December 11, 2023).

31. Callio. Callio FUTUREMINE (2022). Available from: https://callio.info/2017/wp-content/uploads/Callio-FutureMINE-press-release-1.11.2022.pdf (Accessed December 11, 2023).

32. Joutsenvaara J, Holma M, Kotavaara O, Puputti HJ. Callio Lab - the deep underground research centre in Finland, Europe. *J Phys Conf Ser* (2021) 2156(1):012166. doi:10.1088/1742-6596/2156/1/012166

33. National Land Survey of Finland. *National land survey of Finland (2023) elevation model 2 m*. Helsinki, Finland: National Land Survey of Finland (2023).

34. FMI. *Water body predictions - vesistöennusteet: pyhäjoen vesistö alue- Pyhäjärvi -Junttiselkä* (2023).

35. FMI. *Talvien lumista ja lumisuudesta [About the Winter snow and snow cover]* (2023).

36. Sammon LG, McDonough WF. Quantifying Earth's radiogenic heat budget. *Earth Planet Sci Lett* (2022) 593:117684. doi:10.1016/j.epsl.2022.117684

37. Bellini G, Benziger J, Bick D, Bonfini G, Bravo D, Avanzini MB, et al. Cosmic-muon flux and annual modulation in Borexino at 3800 m water-equivalent depth. *J Cosmology Astroparticle Phys* (2012) 2012(05):015. doi:10.1088/1475-7516/2012/05/015

38. Konieczna-Fuławka M, Szumny M, Fuławka K, Jaśkiewicz-Proć I, Pactwa K, Kozłowska-Woszczycka A, et al. Challenges related to the transformation of post-mining underground workings into underground laboratories. *Sustainability* (2023) 15(13):10274. doi:10.3390/su151310274

39. Loo K. Extending physics potential of large liquid scintillator neutrino detectors (2016). Available from: https://jyx.jyu.fi/bitstream/handle/123456789/52317/978-951-39-6812-0.pdf.

40. Baldoncini M, Callegari I, Fiorentini G, Mantovani F, Ricci B, Strati V, et al. Reference worldwide model for antineutrinos from reactors (2015). Available from: www.fe.infn (Accessed December 12, 2023).

41. Joutsenvaara J, BSUIN - Baltic Sea underground innovation network. *EGUGA* (2020):11212 (Accessed December 12, 2023).

42. Polaczek-Grelik K, Walencik-Łata A, Szkliniarz K, Kisiel J, Jędrzejczak K, Szabelski J, et al. Natural background radiation at lab 2 of Callio lab, Pyhäsalmi mine in Finland. *Nucl Instrum Methods Phys Res A* (2020) 969:164015. doi:10.1016/j.nima.2020.164015

43. Angus D, et al. The LAGUNA design study-towards giant liquid based underground detectors for neutrino physics and astrophysics and proton decay searches. In: European strategy for future neutrino physics Proceedings, Workshop; October, 2009; Geneva, Switzerland (2009).

44. Agarwalla S, Agostino L, Aittola ag M, Alekou A, Andrieu B, Angus af D, et al. Published for SISSA by Springer the mass-hierarchy and CP-violation discovery reach of the LBNO long-baseline neutrino experiment the LAGUNA-LBNO collaboration. *JHEP* (2014) 94.

45. Raut SK, Singh RS, Uma Sankar S. Magical properties of a 2540 km baseline superbeam experiment. *Phys Lett B* (2011) 696(3):227–31. doi:10.1016/j.physletb.2010.12.029

46. Peltoniemi J, Group C. Underground physics in the Pyhäsalmi mine. *Phys Scr* (2001) 2001(T93):102.

47. Trzaska WH, Barzilov A, Enqvist T, Jedrzejczak K, Joutsenvaara J, Kasztelan M, et al. NEMESIS setup for indirect detection of WIMPs. *Nucl Inst Methods Phys Res* (2022) 1040:167223. doi:10.1016/j.nima.2022.167223

48. Joutsenvaara J, Holma M, Hynynen I. Thoughts about an ideal validation environment for muography applications. *J Adv Instrumentation Sci* (2022) 2022:2022. doi:10.31526/jais.2022.282

49. Badurina L, Bentine E, Blas D, Bongs K, Bortoletto D, Bowcock T, et al. AION: an atom interferometer observatory and network. *J Cosmology Astroparticle Phys* (2020)(05) 2020:011. doi:10.1088/1475-7516/2020/05/011

frontiers | Frontiers in Physics

TYPE Brief Research Report
PUBLISHED 08 March 2024
DOI 10.3389/fphy.2024.1320097

OPEN ACCESS

EDITED BY
Jeter Hall,
SNOLAB, Canada

REVIEWED BY
Gioacchino Ranucci,
Universities and Research, Italy
Jaret Heise,
Sanford Underground Research Facility,
United States

*CORRESPONDENCE
Paolo Cavalcante,
paolo.cavalcante@lngs.infn.it

RECEIVED 11 October 2023
ACCEPTED 23 February 2024
PUBLISHED 08 March 2024

CITATION
Cavalcante P and Bucciarelli G (2024), An adaptive evacuation system for the Gran Sasso underground laboratory.
Front. Phys. 12:1320097.
doi: 10.3389/fphy.2024.1320097

An adaptive evacuation system for the Gran Sasso underground laboratory

Paolo Cavalcante* and Gabriele Bucciarelli

INFN Laboratori Nazionali del Gran Sasso, Technical and General Service Division, L'Aquila, Italy

The Gran Sasso National Laboratory (LNGS) is, at present, the largest deep underground laboratory in operation for astroparticle physics and rare event research. The LNGS was created to carry out this research exploiting an overburden of 1,400 m of rock to reduce the flux of muons from cosmic rays. Operating an underground laboratory and its facilities implies a high level of risk. To mitigate risks at the LNGS, a crucial aspect is represented by the evacuation of people from an underground environment during emergencies. The connection between the underground facilities and the outside infrastructure is limited, and the intervention by rescue teams is complicated. This paper reports the study of an adaptive evacuation system to improve the evacuation performance in underground laboratories. The system proposed is composed of a combination of passive, dynamic, and adaptive signage that is able to adapt itself to lead the laboratory occupants to the safe location for evacuation (assembly point). The system collects information from all safety plants, and the data are processed using a customized path-finding algorithm. In the computational algorithm, the underground laboratory is represented as a grid, and the customized path-finding algorithm discovers all available paths to reach the identified evacuation assembly point.

KEYWORDS

adaptive evacuation route, underground safety, Dijkstra algorithm, decision making, Gran Sasso National Laboratory

1 Introduction

The Gran Sasso National Laboratory (LNGS) is located between the towns of L'Aquila and Teramo in Italy [1]. The LNGS has two sites: an underground facility along the highway tunnel connecting Teramo to L'Aquila and a surface headquarters on the L'Aquila side. The underground complex consists of three huge experimental halls (each 100 m long, 20 m wide, and 18 m high) and bypass tunnels, for a total volume of about 180,000 m^3. The access to the experimental halls is horizontally provided by the highway tunnel. The halls are outfitted with all the technical and safety equipment plus monitoring systems necessary for experimental activities, as well as ensuring proper environmental conditions for the people involved. The main hazards are due to fire (inside the laboratory or outside in the highway tunnel), oxygen deficiency, and earthquakes. Based on these hazards, an internal emergency plan has been developed with three defined evacuation assembly points. Assembly point #1 is the default assembly point, but other assembly points may be more appropriate depending on the emergency scenario. During an emergency situation, part of the laboratory may be not accessible; moreover, the hazard may evolve over time, such as during a fire event. In such circumstances, a static evacuation sign may not help people

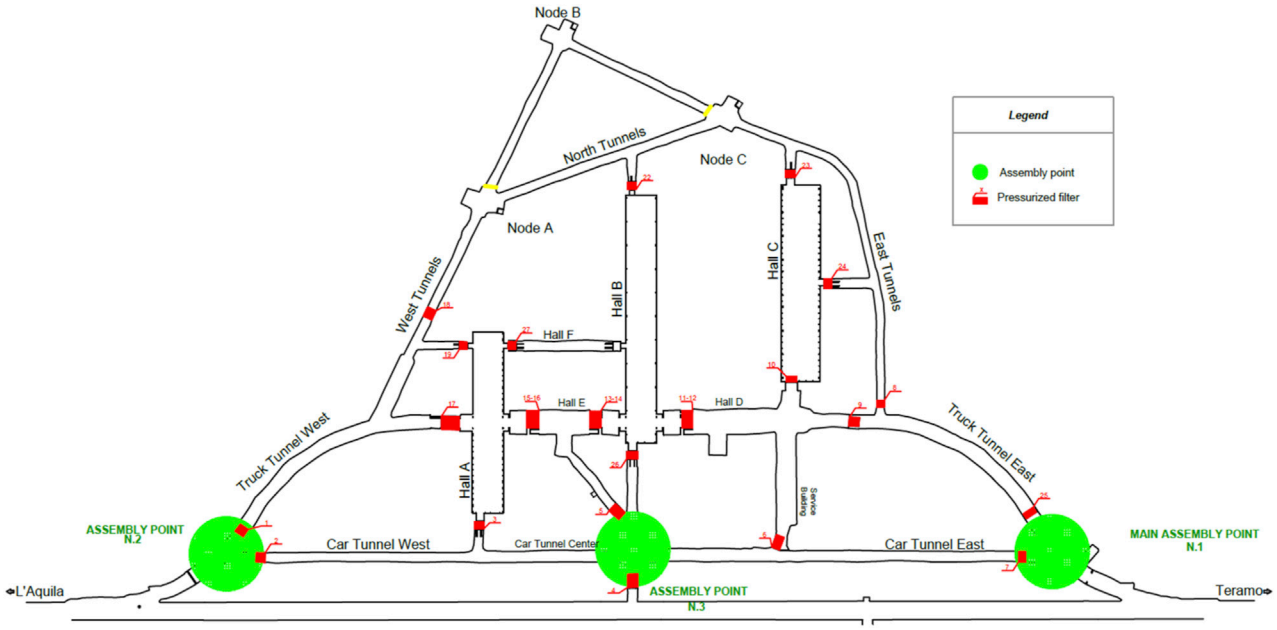

FIGURE 1
The Gran Sasso underground laboratory and its evacuation assembly points.

evacuate in the most effective and efficient manner, especially considering people who may not be very familiar with the local environment.

In this paper, we present an evacuation algorithm that is adaptive to specific dynamic situations in case of an emergency, where real-time environmental data are automatically gained from the safety alarm systems. The underground laboratory and the evacuation assembly points are shown in Figure 1.

Evacuation strategies have already been studied for different risk scenarios. The work in [2] presents a tsunami evacuation strategy; [3] evaluates an adaptive evacuation system that monitors situations in real time and controls the evacuation route dynamically, applicable to large underground areas; and [4] proposes an algorithm that minimizes the total evacuation time of all evacuees for multi-exit buildings.

2 Risk scenarios

The main hazard at the LNGS is fire inside the laboratory or in the highway tunnel. In the event of a fire, there is only a short window of time available for evacuation to the designated safe assembly point. In the area or compartment which is directly affected by fire, only few minutes are available after the alert to evacuate the zone. Indeed, smoke from fire can quickly cause reduced visibility making it difficult for people to safely evacuate the area. Moreover, toxic substances generated by combustion, such as carbon monoxide or hydrocyanic acid, are harmful for people and may affect their perception. Another possible danger is an oxygen deficiency hazard (ODH), since in the Gran Sasso laboratory, a number of experimental facilities make use of large quantities of cryogenic liquids and the associated boil-off gas. Other types of danger exist, such as spills of water or dangerous substances and natural events such as earthquakes.

3 From a static to adaptive evacuation system

According to the LNGS emergency plan, three evacuation assembly points are defined (assembly point #1, assembly point #2, and assembly point #3). Only one assembly point is designed during an evacuation. Assembly point #1 is the default one, but the emergency team can decide to change the evacuation assembly point after assessing the situation. In addition, we underline that having a clear evacuation route during an emergency is critical in an underground environment since the connection between underground facilities and outside infrastructure is limited.

Static evacuation systems are unable to react to temporary events and may guide the occupants directly to the hazard in the worst case or to the wrong assembly point.

Due to the complexity of the LNGS structure, an adaptive evacuation system offers the advantage of optimizing the escape routing according to the development of the hazardous situation, routing people to a safe escape path and reducing the evacuation time.

4 General behavior of the system

The system proposed in this work combines passive and adaptive signs that adapt based on information from an array of safety sensors to lead laboratory occupants to the designed assembly point. The system is an intelligent system able to get information from safety plants. At the LNGS, there are many safety monitors

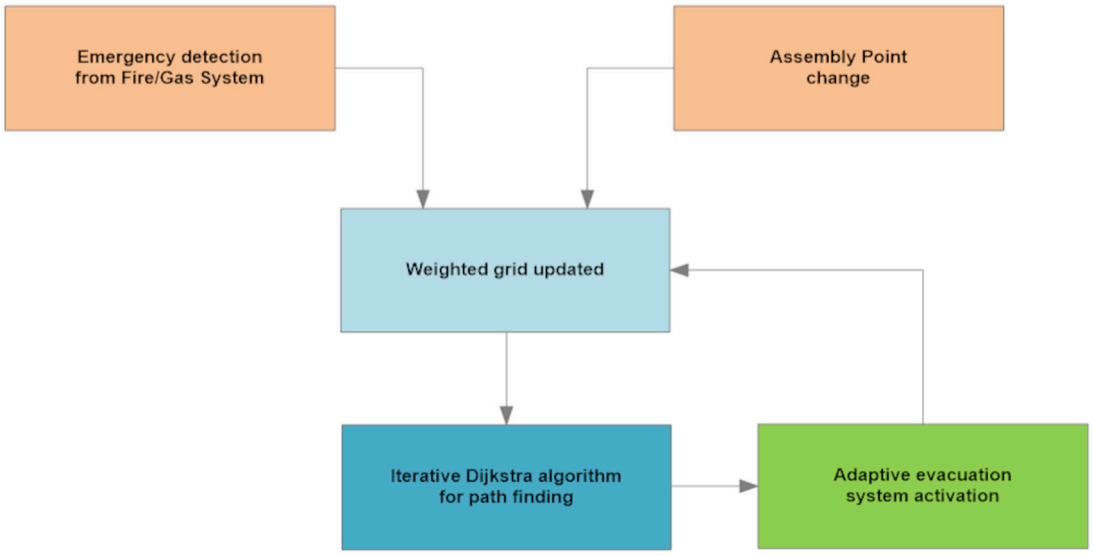

FIGURE 2
Adaptive evacuation system workflow.

with sensors for detecting fire, gas, and leaking liquid, as well as safety PLC systems, etc. The system collects all the information from the alarm panels and analyzes it to determine the location and intensity of the event. In the computational algorithm, the underground laboratory is represented as a grid, with nodes that are updated in real time to reflect areas that may be not accessible due to a critical event. According to the resulting grid, a customized path-finding algorithm will discover all safe paths to reach the identified evacuation assembly point. The results of this computation is communicated to the field elements (dynamic emergency and evacuation signs), providing occupants the exit route based on the best available information at the time. The system workflow is represented in Figure 2.

5 Mapping the underground laboratory into a weighted grid

In order to develop the algorithm to determine an adaptive evacuation route, we represent the underground laboratory as a weighted grid. Each node (or vertex) is positioned at every change of direction or any decision point in the escape route. Each edge (or link between two nodes) has an associated weight, which represents the path length (in meters) between two nodes. Paths may be assigned a correction factor to define a preferred evacuation path according to various criteria. For example, the weight is increased to minimize the usage of the experimental hall as an evacuation route or to reduce the number of firefighting lobbies crossed during the evacuation. The calculation begins with all possible starting nodes and changes weights as the situation evolves. The resulting grid is a grid where all possible starting vertices, intermediate vertices, and final vertices are determined to perform the calculation. In our case, any node (except the final assembly point nodes) may be a starting node or an intermediate node since people may be located in any part of the laboratory. The baseline grid (without any emergency scenario) is represented in Figure 3.

6 Fire compartments and firefighting lobbies

The LNGS has access to nine fire compartments. A fire compartment is a confined section of the laboratory that is isolated in case of a critical event inside it to prevent its propagation to other areas. Each fire compartment is controlled by a dedicated fire control panel connected to several field detection and extinguishing systems as part of active fire protection. Each control unit generates a “fire alarm in the compartment” and implements both the local and remote signaling procedures and automatic fire extinguishment in the zones where it is foreseen. Moreover, each fire control panel controls the firefighting lobby doors of its fire compartment. In case of fire, the air ventilation stops, all fire dumpers and doors close, and all firefighting lobbies are pressurized by the nearest compartment’s air. This implementation allows all nine compartments to be isolated in case of fire by exploiting the 27 firefighting lobbies. Personnel will not be allowed into the area that triggered the emergency, nor will that area be available for the evacuation route.

7 Best evacuation route algorithm

The evacuation route algorithm is based on Dijkstra’s algorithm for undirected weighted graphs [5]. Dijkstra’s algorithm is an algorithm to find the shortest path between nodes in a weighted

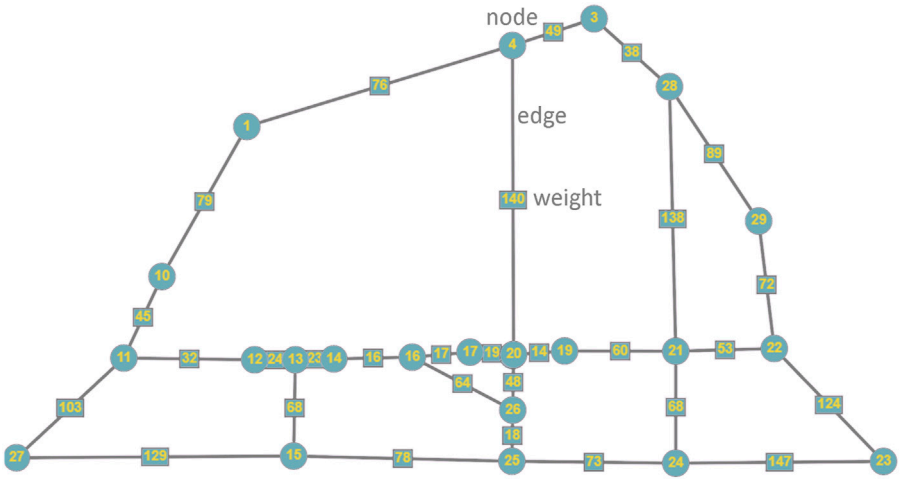

FIGURE 3
Representation of the Gran Sasso underground laboratory as a weighted grid as the input for the computational algorithm for evacuation path finding.

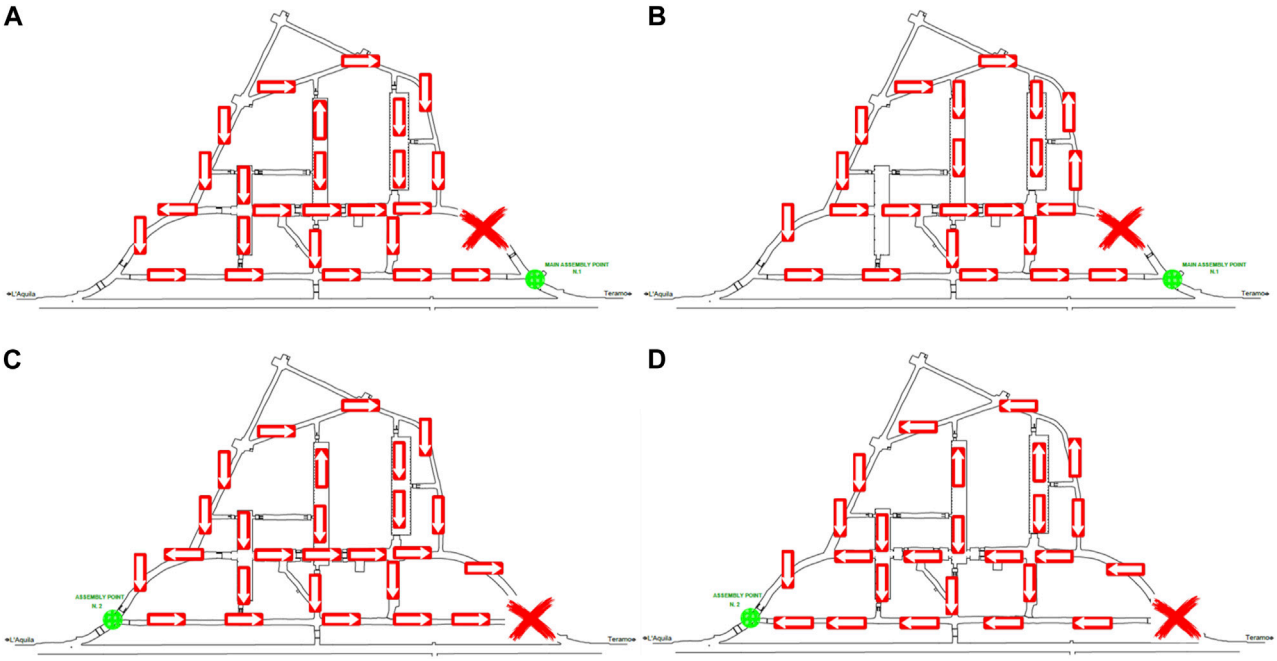

FIGURE 4
Comparison between the actual static evacuation system **(A)** and the evacuation route generated by the adaptive system for a specific scenario, with the forbidden compartment highlighted by a red cross **(B)**. In **(D)**, the evacuation route from the adaptive system is illustrated for another emergency scenario in which the default evacuation assembly point is inaccessible due to an accident, while in **(C)**, the static evacuation system is depicted.

graph. In our implementation, Dijkstra's algorithm is reiterated until every node of the graph is part of the solution. The process begins with the baseline grid that has no access restrictions, as described previously. The initial graph is the resulting graph without any compartment denied by the access that has been presented in paragraph 5. The final node is the assembly point designated for that evacuation. The graph is updated in real time according to the latest events detected.

The following are the steps of the implemented algorithm:

1) One node is randomly picked as the starting node (not the final node).
2) Dijkstra's algorithm is run, and the resulting path is identified.
3) Another node which is not in any of the previously identified solutions is run, and step 2 is re-run until all nodes belong to one of the result paths.

4) Step 1 is re-run if the weighted graph has changed. The final result is the best evacuation route identified based on using all the nodes of the graph.

8 Testing the algorithm and system behavior

Prototype software is developed using LabVIEW [6] to test the customized algorithm presented in Section 7. Based on the restricted (emergency) area and the designated assembly point, the software generates all possible evacuation solutions, and analysis of the solutions indicates a clear advantage when using adaptive versus static systems. Figure 4A shows the current static system compared to one evacuation route coming from the adaptive system (Figure 4B); this scenario is one of all the possible emergency scenarios. In this case, one of the nine fire compartments is denied due to an accident. In this scenario, an emergency situation is presented where part of the laboratory is not accessible, and the evacuation assembly point remains the default one. The adaptive system calculates all the available paths to reach the assembly point based on the real-time emergency information, while the static system shows evacuation issues near the accident area.

In other emergency scenarios, where the designated assembly point is not the default one but is another one (assembly points #2 or #3), the advantage of an adaptive system becomes even more relevant, as the static system continues to direct occupants to the default assembly point. At the LNGS, where the evacuation assembly point may change based on emergency assessment as defined in the emergency plan, the use of an adaptive system is crucial despite the existing static system. In fact, the use of the presented adaptive evacuation system provides significant advantages not only in terms of evacuation time but also for better overall performance in terms of the safety and accuracy of the evacuation. For example, in emergency scenarios where the designated evacuation assembly point is assembly point #2, the current evacuation system proves to be entirely inadequate for a proper evacuation. This results in laboratory occupants heading to the default assembly point, which is situated on the opposite side of assembly point #2, with a distance of approximately 400 m between them. Figure 4D shows the evacuation route from the adaptive system for the emergency scenario just described previously, where the main assembly point becomes unavailable due to an accident in close proximity. In this scenario, assembly point #2 is designated for evacuation. The advantage of the adaptive system is evident in the presented scenario, offering a correct evacuation route for occupants, despite the inadequacy of the current evacuation system for this specific case (Figure 4C). Currently, in the event of evacuation to an assembly point other than the default one, occupants can only rely on our voice evacuation system, which is utilized by the emergency team during emergencies.

9 System realization

The system realization is part of a comprehensive recovery project called NextGenerationEU [7], which is funded and currently in the final design phase. The algorithm presented and its solutions are adopted as the input for an industrial adaptive evacuation system that is able to change sign directions according to a set of preconfigured scenarios. Different companies have already developed emergency adaptive evacuation systems. The core of these systems is a central unit that will take care of the scenario changes—evacuation signs are able to change direction or show a red arrow to deny access to a specific area. Different scenarios or sign combinations are activated by closing a predetermined set of dry contacts in the adaptive system central unit. A specific emergency scenario is described by the type of situation and location (provided by the alarm panels and closed contacts) as well as the chosen assembly point (provided by the emergency team). Communication between all nine alarm panels at Gran Sasso is demonstrated, and logic programming meets the relevant EN 54 European Standards for fire detection and fire alarm systems [8].

10 Conclusion

In this paper, we present an algorithm to determine an adaptive evacuation route in a complex environment such as the Gran Sasso National Laboratory or any underground laboratory. A static evacuation may not be the best solution in terms of evacuation time and correctness in these peculiar environments. On the contrary, the presented algorithm and the whole implemented evacuation system are able to direct people to the safest evacuation route more quickly than a traditional static system. Moreover, it is able to adapt to changing scenarios and avoid leading people to gather at an inappropriate assembly point or area. Indeed, the evacuation route is calculated based on the current emergency situation obtained from the alarm systems. The presented system is fully integrated with the LNGS safety and security systems and is able to detect an emergency situation and activate the safest evacuation route, avoiding critical and dangerous situations. The tests and performance of the adaptive system based on the presented algorithm are discussed. At the Gran Sasso laboratory, we regularly conduct evacuation drills, simulating various emergency situations to assess both emergency and evacuation management. The presented system will be fully tested during the commissioning phase and evacuation drills to verify the accuracy of evacuations and determine whether there is a need to add monitoring sensors to enhance evacuation performance.

Data availability statement

The raw data supporting the conclusion of this article will be made available by the authors, without undue reservation.

Author contributions

PC: validation, software, methodology, conceptualization, and writing–original draft. GB: conceptualization and writing–review and editing.

Funding

The authors declare that financial support was received for the research, authorship, and/or publication of this article. This work

was supported by the NextGenerationEU, Mission 4 Component 2 Investment 3.1.

Conflict of interest

The authors declare that the research was conducted in the absence of any commercial or financial relationships that could be construed as a potential conflict of Interest.

Publisher's note

All claims expressed in this article are solely those of the authors and do not necessarily represent those of their affiliated organizations, or those of the publisher, the editors, and the reviewers. Any product that may be evaluated in this article, or claim that may be made by its manufacturer, is not guaranteed or endorsed by the publisher.

References

1. Ianni A. Underground laboratories. *Phys.Proc.* (2023) 12:007. doi:10.21468/SciPostPhysProc.12.007

2. Pratiwi AF, Riyanto SD, Listyaningrum R, Aji GM. The shortest path finder for tsunami evacuation strategy using Dijkstra algorithm. *IOP Conf Ser Mater Sci Eng* (2020) 854:012035. doi:10.1088/1757-899X/854/1/012035

3. Kasahara Y, Ito A, Tsujiuchi N, Horii H, Kitano K. Evaluation of adaptive evacuation guide sign by using enlarged evacuation simulation at an actual floor plan of underground area. *Int J Saf Security Eng* (2020) 10(1):35–40. doi:10.18280/ijsse.100105

4. Han L, Guo H, Zhang H, Kong Q, Zhang A, Gong C. An efficient staged evacuation planning algorithm applied to multi-exit buildings. *ISPRS Int J Geo-Information* (2020) 9(1):46. doi:10.3390/ijgi9010046

5. Khan MA. *A comprehensive study of Dijkstra's algorithm* (2020). doi:10.2139/ssrn.4559304

6. National Instruments. Design and prototype (2023). Available at: https://www.ni.com/en/solutions/design-prototype.html (Accessed November 9, 2023).

7. European Union. NextGenerationEU (2023). Available at: https://next-generation-eu.europa.eu/index_en (Accessed November 3, 2023).

8. EN 54-1:2021. Fire detection and fire alarm systems – Part 1: introduction (2023). Available at: https://standards.iteh.ai/catalog/standards/cen/1198d5fc-b3d2-48a2-9721-e0dcd3b3772b/en-54-1-2021 (Accessed October 20, 2023).

frontiers | Frontiers in Physics

TYPE Perspective
PUBLISHED 26 March 2024
DOI 10.3389/fphy.2024.1378254

OPEN ACCESS

EDITED BY
Aldo Ianni,
Gran Sasso National Laboratory (INFN), Italy

REVIEWED BY
Paolo Lombardi,
National Institute of Nuclear Physics of Milano, Italy

*CORRESPONDENCE
Ko Abe,
abe@km.icrr.u-tokyo.ac.jp
Hide-Kazu Tanaka,
thide@km.icrr.u-tokyo.ac.jp

RECEIVED 29 January 2024
ACCEPTED 26 February 2024
PUBLISHED 26 March 2024

CITATION
Abe K and Tanaka H-K (2024), Hyper-Kamiokande construction status and prospects. *Front. Phys.* 12:1378254.
doi: 10.3389/fphy.2024.1378254

Hyper-Kamiokande construction status and prospects

Ko Abe[1,2]* and Hide-Kazu Tanaka[1,2]* on behalf of the Hyper-Kamiokande collaboration

[1]Kamioka Observatory, Institute for Cosmic Ray Research, University of Tokyo, Kamioka, Gifu, Japan, [2]Kavli Institute for the Physics and Mathematics of the Universe (WPI), The University of Tokyo Institutes for Advanced Study, University of Tokyo, Kashiwa, Chiba, Japan

The Hyper-Kamiokande (Hyper-K) project is the world's leading international neutrino and nucleon decay experiment comprising a next-generation underground water Cherenkov detector and upgraded Japan Proton Accelerator Research Complex (J-PARC) neutrino beam. It will provide an enormous potential to discover the leptonic charge-parity violation, to investigate the Grand Unified Theory by proton decay exploration, and to determine the neutrino mass ordering. Further, Hyper-K will significantly enhance the capability to observe solar neutrinos and neutrinos from other astronomical sources in comparison with its predecessors. After the budget approval in January 2020, the Hyper-K project officially began, and the operation is expected to start in 2027. The excavations of a 2.0 km long access tunnel and the tunnels for the detector facility have been completed. In October 2022 it was started the excavation of one of the world's largest underground caverns to suite the HK detector. This article discusses the status and the prospects of the Hyper-K detector construction.

KEYWORDS

Hyper Kamiokande, super kamiokande, water cherenkov detector, underground, construction, excavation

1 Introduction

The Hyper-Kamiokande (Hyper-K) project Abe et al. [1] is the world-leading international scientific research project hosted by the university of Tokyo and High Energy Accelerator Research Organization (KEK) consisting of a next-generation underground water Cherenkov detector and upgraded Japan Proton Accelerator Research Complex (J-PARC) neutrino beam. The Hyper-K international collaboration consists of about 560 researchers from 101 institutes in 21 countries (at the time of writing this article). The detector technology has been developed based upon the successful Super-K experiment Fukuda et al. [2] and feasibility studies have been completed by international groups. The Hyper-K operation plans to start in 2027. The supplementary budget for FY2019, including the first-year construction budget for Hyper-K project, was approved by the Japanese Diet on January 2020 and the Hyper-K project was officially started.

The Hyper-K detector will be built in one of the world's largest underground caverns, which is being excavated ~600 m underground beneath the Kamioka Mine in Kamioka-cho, Hida City, Gifu Prefecture. Figure 1 shows an overview of the Hyper-K underground facility and a schematic view of the area around the detector. The overburden at the top of the main cavern is 592m and 650 m at the center of the detector. The detector, 71 m high and 68 m diameter, will be filled with 0.260 million metric tons of ultra pure water, corresponding to an order of magnitude larger fiducial mass (0.188 million metric tons) than Super-K. It will

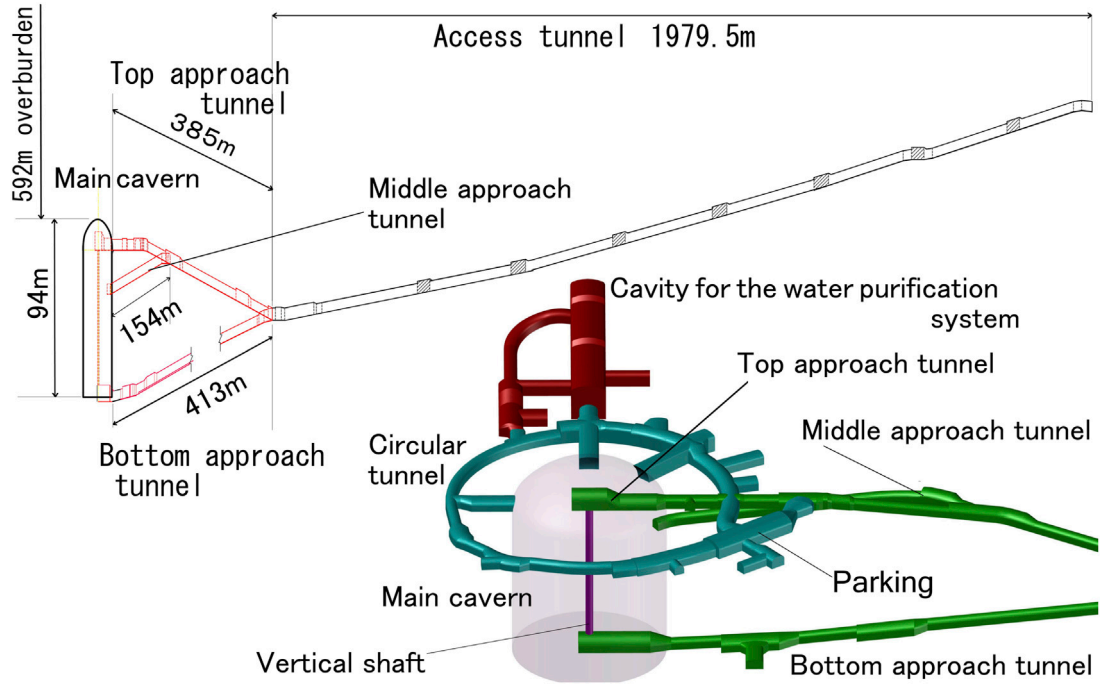

FIGURE 1
The Hyper-K underground facility overview (top) and the schematic view of the detector area (bottom).

be equipped with newly developed high-sensitivity photosensors, and it will use a high-intensity neutrino beam produced by the upgraded J-PARC accelerator facility. It will provide an enormous potential to discover leptonic charge-parity (CP) violation by observing neutrino and anti-neutrino particles from J-PARC, to investigate the Grand Unified Theory by exploring proton decay, and to determine the neutrino mass ordering by observing atmospheric neutrinos and combining beam data. Hyper-K will also have far better capabilities to observe solar neutrinos and neutrinos from other astronomical sources than those of predecessor experiments based on water.

Hyper-K will have capability to measure the magnitude of the CP violation with high precision, which could explain the baryon asymmetry in the Universe. By 10 years operation with predicted systematic error improvement, Hyper-K is expected to cover the 60% of the parameter space with a 5σ significance or better. More than 8σ significance will be expected if $\delta_{CP} = -\pi/2$ as suggested by T2K Abe et al. [3]. The observation of the decay of the proton in the channel $p \rightarrow e^{+}\pi^{0}$ is a strong signature favored by many Grand Unified Theory models, with a prediction close to the current limit of the proton decay life time. Hyper-K, thanks to the new high sensitive photomultiplier tubes (PMTs), will be able to strongly reduce the background induced by atmospheric neutrinos. This will help a lot the $p \rightarrow e^{+}\pi^{0}$ search that is expected to be almost "background-free" (particularly in the free-proton enhanced signal region). Hyper-K is the only proposed experiment with the potential to go beyond and explore proton lifetimes larger than of 1×10^{35} years. Supernova burst neutrinos, once observed by Kamiokande, and undiscovered supernova relic neutrinos are also interesting targets to explore the history of elements and the Universe.

2 Construction overview

The Hyper-K underground facility consists of the main cavern, in which Hyper-K detector will be built, a cavity for the water purification system, tunnels, and a few small sub-cavities. The tunnel between the tunnel portal and the Hyper-K detector area is called the "access tunnel" which is approximately 2.0 km long with ~6% downward slope. The access tunnel is split into three branches, called the "approach tunnels", to allow to access the main cavern at diverse levels of the barrel section: the top, the middle, and the bottom section. Another "circular tunnel" surrounds the main cavern at the top level of the barrel section, and it is connected to additional cavities (e.g., the cavity for the water purification system) and to other smaller sub-cavities for auxiliaries systems.

All components of the Hyper-K underground facility are newly excavated. The first access tunnel excavation work started in 2021, while the excavations of the approach tunnels and sub-cavities were conducted subsequently. At the time of writing this article, all tunnels, sub-cavities and the cavity for the water purification system have been completed, while the excavation of the main cavern is still in progress. The following sections describe the details of the excavation work and their current status.

3 The tunnel excavation

3.1 Construction yard

The tunnel excavation started on 6 May 2021, immediately after the preparation of a construction yard in front of the portal of the access tunnel. The large excavation project required many

specialized facilities, such as temporary storage for the excavated rock, a concrete plant, and a wastewater treatment facility for the water employed for the excavation. The construction yard and all the above facilities were prepared and installed in a ~10,000 m^2 area in approximately 6 months, including a breaktime due to snowfall.

For improve excavation safety, the yard preparation included the switchover of the prefectural road in front of the portal to separate construction traffic from civilian traffic. A new, temporary prefectural road was built so that the construction road could pass under that road without any interference.

3.2 Access tunnel

The access tunnel was first excavated; it is approximately 2.0 km long and connects the tunnel portal to the Hyper-K underground facility area. The end of the tunnel is approximately 100 m lower than the portal. The tunnel cross-section is 5 m wide and 5 m high, these dimensions were determined by considering sizes of required construction vehicles and facilities such as ventilation pipes. Widening sections are prepared every 200 m and employed for passing-each-other of vehicles.

The excavation was completed in only 9 months using long-hole blasting, which can cover a length of 4 m in a single blast. Initially, the schedule was delayed due to poor bedrock conditions, but as the bedrock conditions improved, the excavation speed was greatly improved. The speed reached a maximum of 15 m/day in the later part of the excavation, and the 1979.5 m excavation was completed as scheduled by February 2022.

3.3 Approach tunnel

The excavation of the approach tunnels, which connect the access tunnel to the main cavern, was the next step in the construction process. The approach tunnel splits into two tunnels at first; the "top approach tunnel" and "bottom approach tunnel", which are connected to the top and the bottom, respectively, of the main cavern, each with a 10% slope. Thereafter, the "middle approach tunnel" branches from the top approach tunnel and connects to the middle level of the main cavern. The lengths of the top, bottom, and middle approach tunnels are 385 m, 413 m, and 154 m, respectively. From the first branch point of the approach tunnel, the excavation was implemented by two teams to expedite the process. The excavation started in March 2022 and ended in August 2022.

3.4 Circular tunnel and the sub-cavities

The circular tunnel surrounds the main cavern with a lap of 445 m. The width and height of the tunnel differ by area. The area with the highest width is the southeast area for parking as shown in the bottom of Figure 1. The length of that area is approximately 40 m, with a cross-section that is 12.5 m wide and 7.3 m high. The numbers were determined based on actual use in the Super-K experiment and expected number of vehicles in the Hyper-K experiment. In addition to its use for housing the experimental facilities, the circular tunnel was used to verify the condition of the bedrock around the main cavern in detail. During the excavation, collection of Measurements While Drilling data (logging the information related to drilling blast holes) and detailed observations of the tunnel surface were carried out.

The excavation of the circular tunnel started by branching from the top approach tunnel. In approximately 4 months, the excavation of the circular tunnel, including the sub-cavities arranged along with the circular tunnel, was completed as scheduled.

3.5 Cavity for the water purification system

Among the cavities attached to the circular tunnel, the largest is the cavity for the water purification system. The cavity is 101 m long, 17 m high, and 16 m wide. The excavation started from the work tunnel to the top of this large cavity. The main body was excavated in parallel with the dome excavation (see Figure 2), and completed May 2023.

4 Cavern excavation

The Hyper-K main cavern consists of a rooftop portion, which is called a "dome section," and a cylindrical "barrel section" under the dome section. The main cavern of Hyper-K is approximately 94 m high (the dome section is 21 m high, and the barrel section is 73 m high) with a diameter of 69 m[1]. The total excavation volume of the main cavern is approximately 330,000 m^3.

Various geological investigation such as bore-hole drilling, laboratory rock test using drilled rock cores, seismic exploration in the adit, is-situ tests, measurement of initial state of underground stress, were carried out prior to the excavation of the Hyper-K main cavern Abe et al. [1]. The bedrock surrounding the main cavern is mainly composed of Hida gneisses (fine-grained paragneisses accompanied by coarse-grained migmatitic granitoids so-called Inishi migmatite). From the *in-situ* measurements and rock tests, a typical value of Young's modulus and the Geological Strength Index Hoek [4] of the bedrock were evaluated to be 40 GPa and 73, respectively. Based on the results of the geological survey, we conducted cavern-stability analyses, including a three-dimensional elasto-plastic finite difference model analysis considering multi excavation steps, and designed the rock support, e,g., selection of rock-supporting materials, layout of the rock supports, and their specifications. The selected rock-supporting materials are shotcrete (thickness: ~30 cm), rock bolts (length: 4–7 m), and pre-stressed anchors so-called "PS-anchors" (length: 8–22 m with applying pre-stress of 300–600 kN). The area density, length, and applied pre-stress (for the PS-anchors) of the rock support vary with the expected depth of the plastic zone and the geological conditions.

Since the Hyper-K main cavern is an underground cavern excavation of unprecedented scale worldwide, an "information-oriented design and excavation" method was employed. This method optimizes the rock support design and the excavation plan based on the latest geological information obtained as the excavation progresses and the data from the bedrock monitoring

1 A 50 cm thick lining concrete is placed after the cavern excavation.

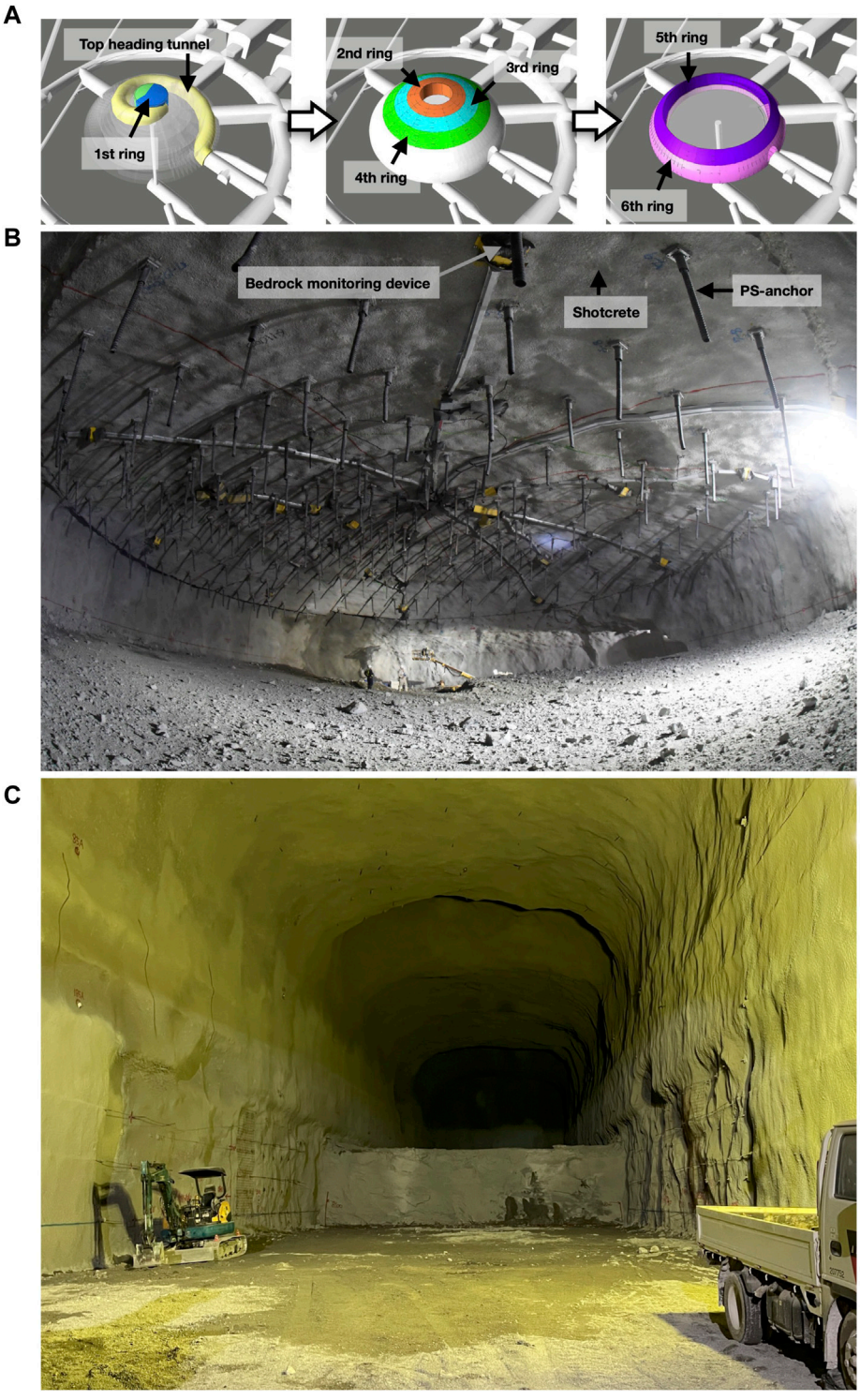

FIGURE 2
(A) Schematic of the excavation step of the dome section, **(B)** picture of the dome section as of the third ring excavation completed, early April 2023, **(C)** picture of the cavity for the water purification system as of early May 2023.

devices, e.g., bedrock displacement gauges (multiple stage extensometers) and PS-anchors load cells.

The main cavern excavation has started in October 2022. The main cavern is excavated step by step from the dome section through the bottom of the barrel section. For the dome section, a first pilot tunnel (called the "top heading tunnel") was excavated to approach the dome zenith part. The dome section is being excavated with six excavation steps, called "rings". The first ring is the dome zenith part with a diameter of 16 m, and the second to the sixth rings are excavated outward in an annular shape, as shown in Figure 2A.

Notably, the diameter of the third ring is 40 m (see Figure 2B) which is the same as the diameter of the Super-K detector tank. At the time of writing this article, the excavation work for the fourth ring is underway. After the completion of the dome section, expected by end of 2023, the excavation of the barrel section will commence. The 73 m high barrel section is divided into 19 excavation steps in the vertical direction called "benches"; each one of these steps is 3–4 m deep. A vertical shaft with a diameter of 3.4 m was excavated with "raise boring" method through the entire barrel section from the top to the bottom and connected to the bottom approach tunnel as shown in Figure 1. The vertical shaft is used to transport the excavated rock of the barrel section to the bottom of the main cavern to be finally transported to the above ground via the bottom approach tunnel. This allows us to expedite the excavation by avoiding interference between the excavation work and the transportation of the excavated rocks. Furthermore, the excavation time for the barrel section is roughly identical to that for the dome section, despite that the excavation volume of the barrel section is 5.6 times higher than the dome section.

5 Summary and prospect

The excavation work for the Hyper-K underground facility, the first step in constructing the Hyper-K detector, is in progress. The tunnel, sub-cavity, and the cavity for the water purification system excavations have been completed, and the excavations of the Hyper-K main cavern is underway. The Hyper-K main cavern excavation is expected to be completed in 2024. The Hyper-K detector lining construction, PMT installation, and ultrapure water filling will be implemented subsequently. The Hyper-K collaboration aims to start the operation of the Hyper-K detector in the Japanese fiscal year of 2027.

Data availability statement

The original contributions presented in the study are included in the article/Supplementary Material, further inquiries can be directed to the corresponding author.

Author contributions

KA: Writing–original draft, H-KT: Writing–original draft.

Funding

The author(s) declare that no financial support was received for the research, authorship, and/or publication of this article.

Conflict of interest

The authors declare that the research was conducted in the absence of any commercial or financial relationships that could be construed as a potential conflict of interest.

Publisher's note

References

1. Abe K, Aihara H, Aimi A, Akutsu R, Andreopoulos C, et al. *Hyper-kamiokande design report* (2018). arXiv , 1805.04163 Available at: https://arxiv.org/abs/1805.04163 (Accessed January 29, 2024).

2. Fukuda S, Hayakawa T, Ichihara E, Ishitsuka M, Itow Y, Kajita T, et al. The super-kamiokande detector. *Nucl Instr Methods Phys* (2003) A501:418–62. doi:10.1016/S0168-9002(03)00425-X

3. Abe K, Akutsu R, Ali A, Alt C, Andreopoulos C, Anthony L, et al. Constraint on the matter-antimatter symmetry-violating phase in neutrino oscillations. *Nature* (2020) 580:339–44. doi:10.1038/s41586-020-2177-0

4. Hoek E, Kaiser PK. Use of rock mass classifications for estimating GSI. In: *Support of underground excavations in hard rock 102–105*. Rotterdam: Balkema (1995).

frontiers | Frontiers in Physics

TYPE Brief Research Report
PUBLISHED 02 April 2024
DOI 10.3389/fphy.2024.1323991

OPEN ACCESS

EDITED BY
Jeter Hall,
SNOLAB, Canada

REVIEWED BY
Xavier Bertou,
Bariloche Atomic Centre (CNEA), Argentina
Osvaldo Civitarese,
National University of La Plata, Argentina

*CORRESPONDENCE
K. S. Park,
heppark@ibs.re.kr

RECEIVED 18 October 2023
ACCEPTED 26 February 2024
PUBLISHED 02 April 2024

CITATION
Park KS, Kim YD, Bang KM, Park HK, Lee MH, So J, Kim SH, Jang JH, Kim JH and Kim SB (2024), Construction of Yemilab.
Front. Phys. 12:1323991.
doi: 10.3389/fphy.2024.1323991

Construction of Yemilab

K. S. Park[1]*, Y. D. Kim[1,2], K. M. Bang[1], H. K. Park[3], M. H. Lee[1,2], J. So[1], S. H. Kim[1], J. H. Jang[1], J. H. Kim[1] and S. B. Kim[1]

[1]Center for Underground Physics, Institute for Basic Science (IBS), Daejeon, Republic of Korea, [2]IBS School, University of Science and Technology (UST), Daejeon, Republic of Korea, [3]Department of Accelerator Science, Korea University, Sejong, Republic of Korea

The Center for Underground Physics of the Institute for Basic Science (IBS) in Korea has been planning the construction of a deep underground laboratory since 2013 to search for extremely rare interactions such as dark matter and neutrinos. In September 2022, a new underground laboratory, Yemilab, was finally completed in Jeongseon, Gangwon Province, with a depth of 1,000 m and an exclusive experimental area spanning 3,000 m^3. The tunnel is encased in limestone and accommodates 17 independent experimental spaces. Over 2 years, from 2023 to 2024, the Yangyang Underground Laboratory facilities will be relocated to Yemilab. Preparations are underway for the AMoRE-II, a neutrinoless double beta decay experiment, scheduled to begin in Q2 2024 at Yemilab. Additionally, Yemilab includes a cylindrical pit with a volume of approximately 6,300 m^3, designed as a multipurpose laboratory for next-generation experiments involving neutrinos, dark matter, and related research. This article provides a focused overview of the construction and structure of Yemilab.

KEYWORDS

UL, underground Facility, Yemilab, Korea UL, underground laboratory, Asian underground laboratory

1 Introduction

The Institute for Basic Science (IBS) is a Korean national research institute established in 2011 to conduct basic scientific research. As of 2023, IBS includes 31 independent centers, each focusing on different research themes. The Center for Underground Physics (CUP) is one of the centers and, as indicated by its name, is a research center dedicated to astroparticle physics, conducting primary experiments underground. CUP started in 2013, and approximately 70 researchers are engaged in research activities to measure extremely rare interactions, such as dark matter and neutrinos. Since its inception, CUP planned to construct a new underground laboratory to expand the existing Yangyang Underground Laboratory (Y2L), which has a limited experimental space of ~200 m^2 at a depth of ~700 m. In September 2022, a new underground experimental facility with a depth of 1,000 m (2,500 m w. e.) and an exclusive experimental area of ~3,000 m^2 was finally completed in Jeongseon-gun, Gangwon province, named the Yemilab. All tunnels in the experimental area are predominantly surrounded by limestone, providing more than ten independent experimental sections.

2 Site selection

The implementation of extremely low background radiation, a crucial aspect in underground experiment research, can only be achieved by thoroughly understanding

FIGURE 1
The red pin indicates Yemilab's location in Gangwon province, South Korea.

and addressing various complex factors. One of the most essential factors is the shielding of muons. Several locations were considered for the site of the new underground experimental facility. Firstly, existing closed or operational mines were investigated. Another option involved excavating tunnels on high mountains to secure deep underground spaces. Candidate sites were selected, considering tunnel length and lab depth. After a comprehensive investigation spanning about 3 years, the options narrowed down to two locations in Gangwon province: Mt. Duta (peak height 1,357 m) located in Samcheok-city and Mt. Yemi (peak height 989 m) encompassing SM Handuk Iron Mine Co., Ltd (Handuk) in Jeongseon-gun. Both sites allowed for the construction of underground experimental facilities at depths exceeding 1,000 m. Subsequently, after conducting a feasibility study that considered geological conditions, excavation and construction costs, permission issues, and more, Mt. Yemi was confirmed as the final site for the new underground research facility.

The primary reason for choosing Mt. Yemi was its high muon shielding effect compared to the construction cost and a relatively simple permission process. Firstly, when considering construction costs, it was estimated that the construction cost for Mt. Yemi was nearly half of that for Mt. Duta. It was attributed to the 627 m long shaft owned by Handuk near the top of Mt. Yemi. By utilizing this shaft, the access tunnel length to be excavated was only about half compared to Mt. Duta, resulting in significant cost savings. Secondly, permission issues related to construction were a concern. For Mt. Duta, excavating a new tunnel was subject to multiple regulations concerning natural preservation, necessitating careful consideration of numerous procedures and restrictions. On the other hand, as the Mt. Yemi site employed the existing operational Handuk, construction could proceed without any environmental damages, and there were no significant legal restrictions or permission issues. Lastly, the third reason was muon shielding performance. The possible depths of the underground experimental facilities at Mt. Duta and Mt. Yemi were 1,400 and 1,000 m, respectively, resulting in a difference. When calculating muon rates using the topographies of both mountains, the muon flux at the depth just under the summit of the mountains was reduced to approximately 1.8×10^{-6} at Mt. Duta and 3×10^{-6} at Mt Yemi compared with the muon rate at sea level. The difference between the two is less than a factor of 2. Despite the depth difference, which might suggest a factor of five to six, the influence of omnidirectional coverage reduces the expected factor. It could be attributed to better omnidirectional coverage in Yemi compared to Duta. While Mt. Duta had about 40% higher shielding capability compared to Mt. Yemi, both have over five times the shielding efficiency of the Y2L. Thus, they deemed suitable as potential new sites. After considering all these factors, it was decided in mid-2015 to construct a new deep and spacious underground research facility at Mt. Yemi at a depth of 1,000 m. Immediately, construction plans were formulated to secure the budget. The following year, after passing the National Facility Equipment Committee review, construction of the Yemilab began in September 2017, starting with the installation of an elevator for personnel access called man-cage. The construction took place over a 5-year period until 2022.

2.1 Geology overview

Handeok is located in Jodong-ri, Sindong-eup, Jeongseon-gun, Gangwon province, South Korea. It is situated west of the Mt. Taebaek mineralized zone. The surrounding terrain is characterized by east-west oriented ridges such as Mts. Yemi (989.2 m), Baejae (740 m), and Jilun (1,171.8 m). The southern slope, delineated by these ridges, is steep, while the northern slope features a gentler rugged terrain. The variation in slope gradient is attributed to the distribution of rock types, with sandstone and shale predominantly found on the northern side, whereas limestone predominates on the southern side. In the south part of the area, the geological composition includes the upper layer of the Makdong limestone formation, part of the Paleozoic Joseon Supergroup, overlain by the Hongjom series from the Pyeongan Supergroup, and intrusions of quartz diorite/quartz diorite gneiss of unknown age. The upper part of the Makdong limestone formation is overlain by a Jikunsan shale formation, characterized by its color ranging from black to dark gray.

3 Construction timeline

Since 2013, CUP has been exploring potential sites to construct a new underground research facility. In early 2016, construction proceeded in stages at the final location at Mt. Yemi (Figure 1). By the end of 2016, funding for the first construction phase was secured. The first phase involved the installation of the man-cage and primary tunnel excavation. The cage installation was completed in December 2018, and the first construction phase was concluded with the tunnel construction in August 2020. In early 2021, funding for the second phase of construction was secured, and work for the

FIGURE 2
A view of the experimental zone. A photo was taken from the main hallway towards the end of the tunnel.

second phase resumed at the end of 2021. The second phase included excavation work for a pit to accommodate a 6,200 m^3 Large Scintillation Counter (LSC) and the installation of electrical, ventilation, communication, and fire safety facilities underground. The second construction phase was completed in August 2022, establishing the basic framework of Yemilab. With the completion of the fundamental structure of Yemilab, interior enhancements took place in 2023 (Figure 2). They involved the installation of equipment such as cranes, vehicle washing systems, dustproof doors, and coating for floors and walls. Finally, Yemilab acquired the necessary infrastructure for the beginning of experiments. Starting in September 2023, the relocation of various facilities from Yangyang to Yemilab began. By the end of 2024, once all the relocations are completed, each experiment will enter a new phase at Yemilab.

4 Tunnel

In February 2019, the first blast for tunnel excavation started. The Yemilab tunnel starts approximately 100 m away from the shaft. The tunneling progressed towards the peak of Mt. Yemi. While some sections of the rock at the excavation site exhibited quartzite and traces of iron ore, most of the experimental section was composed of limestone.

4.1 Design

Yemilab consists of seventeen dedicated and independent experimental rooms. The basic structure is designed with two exits for experimental rooms exceeding a length of over 20 m to ensure that researchers can safely and swiftly escape in the event of a fire. Therefore, it inherently features a ladder-type design. In this structure, creating clean rooms according to users' preferences is more efficient than the structure of a large hall.

The starting point of the Yemilab tunnel is situated at an elevation of −35 m in the Handuk area, with a depth of 604 m. Therefore, the Yemilab tunnel does not extend to connect with any other public roads. From the tunnel front, an entry tunnel was excavated with a standard cross-section of 5 m (width) by 5 m (height), featuring a downward slope of 12% and a length of 782 m. This slope was intentionally designed to achieve a greater depth, aiming for a descent of approximately 100 m at the end of the tunnel. Turning shelters were established every 90 m to facilitate the rotation of large construction vehicles. There are six turning shelters in the access tunnel, four of which can be repurposed as experimental spaces. A horizontal tunnel for experiments was excavated from the end of the access tunnel. In the experimental area, 23 independent spaces were excavated, with 16 dedicated to experiments or housing equipment directly supporting experiments and the remainder serving operational purposes.

Focusing only on the experimental spaces, the largest laboratory is the LSC Hall, combining a square dome measuring 22 m (width) by 22 m (length) by 8 m (height) on top, with a cylindrical pit having a diameter and depth of 20 m. The pit has a volume of 6,200 m^3 and serves as a multipurpose space for detectors. The second largest space, the AMoRE Hall, was excavated with dimensions of 21 m (width) by 21 m (length) by 16 m (height). Additionally, there are intermediate-sized spaces: one measuring 12 m (width) by 17 m (length) by 10 m (height), three measuring 8 m (width) by 15 m (length) by 8 m (height), and two measuring 7 m (width) by 25 m (length) by 7 m (height). The remaining spaces comprise sections with cross-sections of 5 m (width) by 5 m (height).

4.2 Excavation

The New Austrian Tunneling Method (NATM) was employed to ensure the safety and stability of the underground experimental spaces during rock excavation. The excavation of NATM tunnels involves a cyclical process consisting of five stages. Before the tunnel excavation, ground surveys were conducted, followed by dynamite blasting. Subsequently, excavation face reinforcement was carried out using rock bolts and shotcrete. Precise measurements of rock deformation were then conducted. If no deformation was detected, this process was repeated to proceed with the excavation.

Reinforcement methods (Type 1–5) were selected based on the Rock Mass Rating (RMR) grades (grade 1 to grade 5) [1]. Rock bolts and standard shotcrete, as detailed in Table 1, were applied, and stability measurements were taken before and after the blast. The table provides information on the radioactive isotope of the shotcrete components. The rock conditions at the excavation face were relatively advantageous, exhibiting RMR grades of 2 and 3. In addition to ensuring the safety of the experimental spaces, we took a conservative approach in applying reinforcement methods to protect the people working in the tunnel. Across the entire underground excavation tunnel, reinforcement methods corresponding to RMR grade 2 were applied in 38% of the area, and RMR grade 3 reinforcement methods were applied in 62%. All sections of the experimental spaces were reinforced using RMR grade 3 methods. Most of the rock in the experimental area is composed of limestone, with some sections showing signs of metamorphic and quartz veins.

TABLE 1 The isotopic composition measurements and results of bedrock and aggregates of Yemilab.

Rock	U (mg/kg)	Th (mg/kg)	K (mg/kg)	Remark
Access tunnel	1.21	9.62	24,267	@ sump pit
AMoRE-Hall	0.84	3.27	11,800	
LSC pit	1.58	7.15	24,600	
Shotcrete	U (mg/kg)	Th (mg/kg)	K (mg/kg)	Mixture Ratio (%)
Sand	1.98	13.05	27,384	49
Gravel	0.72	2.17	1,768	27
Cement	2.10	5.24	6,977	22
Steel fiber	0.22	0.39	610	2
Concrete for expr. room's floor	U (mg/kg)	Th (mg/kg)	K (mg/kg)	Mixture Ratio (%)
Sand	0.50	2.05	4,300	50
Gravel	0.82	1.41	4,900	28
Cement	2.10	5.24	6,977	22

The rock samples collected during the blasting process and the primary aggregates used for reinforcement were analyzed for the isotopic concentrations of U, Th, and K using ICP-MS, and the values are presented in Table 1.

The deepest point in the experimental tunnel is the AMoRE Hall, with a depth from the surface to the hall floor at 1,029 m (~2,500 m w. e.). The LSC Hall reaches a depth of 980 m, and most other spaces in the experimental area have depths exceeding 1,000 m (Figure 3). The total volume of excavation is approximately 65,000 m^3, and all excavation work was completed by August 2022.

5 Infrastructures

5.1 Safety

We conducted fire spread simulations using the "ANSYS Fluent" [2] program to analyze the tunnel's structure, electrical systems, and ventilation facilities. Based on the results, we employed the "Simulex" program [3] to devise effective evacuation strategies within the underground experimental space. Subsequently, we determined the refuge locations within the experimental area and installed a refuge from MINEARC Co., Ltd (Australia) [4] to accommodate up to 40 individuals during evacuation. In addition, we installed fire detection sensors such as smoke and flame detectors and high-definition cameras at regular intervals for early fire detection. It allows for effective environmental monitoring within the tunnel. Through these facilities, we aim to suppress the occurrence and spread of fires. As we operate the facilities, we will continuously work to enhance safety measures by addressing any weak points.

5.2 Electricity

Yemilab's underground facilities have a total power supply capacity of 1,600 kW (2,000 kV A) to support the power requirements for experiments. Approximately 200 kW is allocated for the operation of facilities such as lighting, ventilation, exhaust systems, etc., with the remaining 1,400 kW available for experiments. Critical facilities and primary experimental equipment are continuously supported by a 260 kW UPS (Uninterrupted Power Supply) unit and a surface emergency generator in preparation for power outages. In the event of a power outage, the surface emergency generator activates within a few seconds. This emergency generator can supply an instantaneous power of 360 kW until regular power is restored. Depending on the criticality of the facility, emergency power can be dynamically distributed as needed.

5.3 Ventilation

Due to its sealed structure, natural ventilation is impossible within Yemilab's underground spaces. However, the entrance of the Yemilab access tunnel is connected to the mine's shaft and the rampway, which is 6 km long to the surface. Under normal circumstances, ventilation in the mine operates in a natural circulation system, where surface air is drawn in through the vertical access tunnel, passes through the mine's rampway, and exits back to the surface.

Yemilab's ventilation system introduces air from the vertical access tunnel, utilizing a 1-m diameter duct to deliver 39,000 m^3/h of air into every corner of the Yemilab tunnel. Among this, 12,000 m^3 is supplied to the outdoor unit room where the outdoor units of the air conditioning systems located in the experimental area are gathered. The heat load of the outdoor unit room is assumed to be approximately 100 kW to maintain an indoor temperature below 40°C. The remaining 27,000 m^3 is supplied to the experimental area, providing about ten air exchanges daily for the entire Yemilab volume. Due to this ventilation system, the underground temperature can be maintained at 26°C, and the radon concentration remains below 50 Bq/m^3. However, during the summer months, usually June to September, when surface temperatures are high, the natural ventilation within the mine

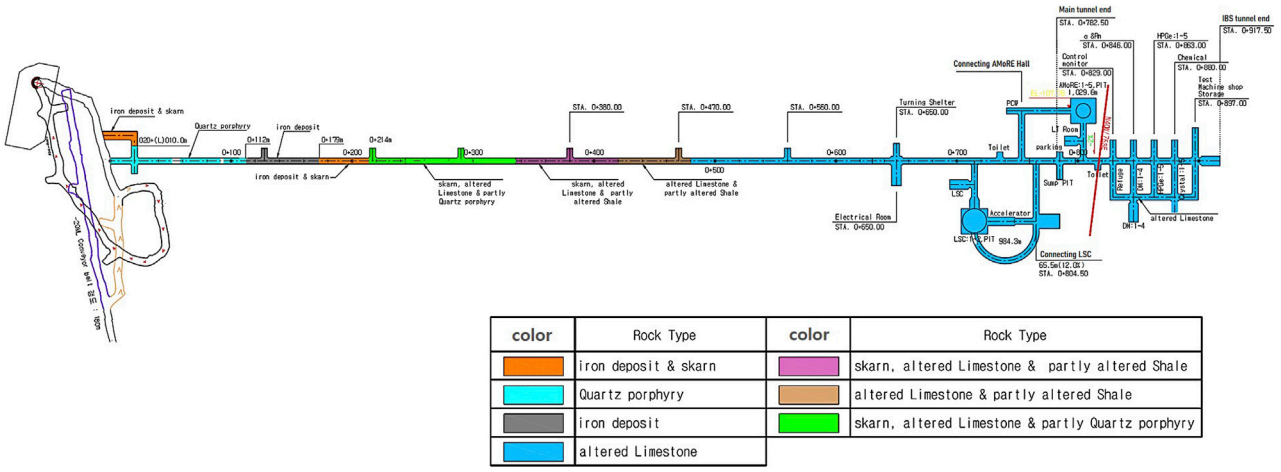

FIGURE 3
The structure of the underground experimental zone of Yemilab. The deepest point is the AMoRE hall floor with 1,029 m of overburden. The distance from the left end (Electrical Room) to the right end (IBS tunnel end) is approximately 260 m.

slows down significantly. As a result, the radon concentration within Yemilab rises to ~2,000 Bq/m^3. To reduce this level to below 150 Bq/m^3, a radonless air supply system is currently being installed to supply surface air directly into the underground. Once this facility is completed in 2024, the radon concentration within Yemilab during the summer will be maintained below 150 Bq/m^3. Furthermore, investigations are underway to improve the natural ventilation system of the mine tunnel to address the high radon concentrations during the summer.

5.4 Communication and network

Anywhere within Yemilab's underground facilities, users can access all commercial mobile phone services available in South Korea. By November 2023, first step network installation for data transmission connecting the underground to the surface office was completed. The transmission speed is approximately 1 Gbps, enabling remote control of underground experimental equipment such as AMoRE-II and COSINE-200 from the surface office and facilitating the transmission of large volumes of experimental data. By 2025, there are plans to implement an automatic access control system for users of the underground laboratory utilizing the network facilities.

5.5 Groundwater

The groundwater within Yemilab's underground is discharged at approximately 4 tonnes daily. This groundwater is collected in a 90-tonne capacity reservoir at the end of the access tunnel beneath the entrance. This amount is sufficient to serve as domestic water for up to 40 individuals utilizing the underground, although it is not used for drinking. The collected groundwater in Yemilab is sent to the main reservoir in the mine via a pumping system. After combined with all other groundwater within the mine, it is discharged to the surface through drainage pipes installed in the shaft. This entire process is automated but can be operated manually if necessary.

5.6 Sustaining cleanliness

Due to its proximity to mining facilities, Yemilab is inevitably affected by the high-concentration dust generated in the mine. To minimize dust contamination, we installed two main dustproof doors at the access tunnel, physically separating the experimental area, access tunnel, and mine tunnel. The floor of the experimental area is coated with epoxy, and each laboratory's wall is painted to block dust generated from shotcrete. Vehicles and equipment operate separately for each designated area. Vehicles requiring access to the experimental area go through cleaning before entering each section. Personnel entering also follow specific paths, changing shoes and clothing. The dust level in the experimental area shows a PM10 (≤10 μm) under about 10 μg/m^3 after the epoxy floor coating, which is lower than the Korean government's recommended limit of 50 μg/m^3 for office environments. After completing Y2L's relocation, strict management will reduce it to below 5 μg/m^3. Yemilab is specially equipped with a Radon Reduction System (RRS). It can provide air with a very low radon concentration level, typically below 100 mBq/m^3 at a rate of 50 m^3/h, suitable for experimental spaces requiring low radon levels. Furthermore, the RRS air meets approximately Class 1,000 cleanroom standard. An additional RRS, with a capacity of 250 m^3/h, will be installed in 2025.

6 Radiation background and measurements

There were several measurement systems to understand the radiation environment of the Yemilab and monitor the seasonal variation. First, RAD7, the most popular radon detector, has been used to measure the radon levels in the Yemilab. The RAD7 was installed at AMoRE Hall, refuge, HPGe, and IBS tunnel end in Figure 3 to see the difference through the Yemilab tunnel. Fortunately, all the values were consistent in each place because of the proper ventilation in the Yemilab. However, as mentioned in

section 5.3, the limited ventilation caused a high radon level of up to 2000 Bq/m^3 during the summer. There are additional systems to improve this high radon level, like Rn-less air supply and permanent air circulation system through the Handuk iron mine. To confirm the performances of the additional systems, ionization-type radon detectors are installed at AMoRE Hall, HPGe room, and the end of the IBS tunnel. We continuously provide the radon levels from the radon detectors on the online monitoring system.

The second is the external gamma rays and neutrons. We have collected rock samples through the Yemilab tunnels to measure the amount of elements using the ICP-MS and radioactivity using the HPGe detector. The compositions of the light elements in the rock samples are especially essential to understanding the origin of the neutrons [5]. Several ^{3}He detectors with different thicknesses of the moderators, already used to measure the neutron flux at Y2L [6], have been installed at AMoRE Hall, IBS tunnels end, and LSC PIT in Figure 3 and measured for 2 months at each place. The ongoing analysis will be compared with the simulation using the element compositions of the rock samples.

The last is the muon flux at the Yemilab. The AMoRE-II muon veto system is installed, and the bottom array of the system can be used to measure the muon flux at the Yemilab. This bottom array of the muon veto system comprises twenty-two plastic scintillators, each with dimensions of 1,680 × 310 × 61 mm^3, and accumulated data for a week. A preliminary muon flux was measured to be 1.0×10^{-7} μ/cm^2·s, four times less than the muon flux at Y2L, 3.8×10^{-7} μ/cm^2·s [7]. The measured value is consistent with an expectation value of 8.2×10^{-8} μ/cm^2·s using a GEANT4 simulation [8]. To profile the muons for each cavern precisely, we plan to install a thick plastic (or liquid) scintillator for long-time measurements at different caverns and provide the values to the experiments, which want to avoid the muon background.

7 Experimental programs at Yemilab

AMoRE experiment is to search the neutrino-less double beta decay of Mo-100 isotopes. It will use about 160 kg of $Li_2{}^{100}MoO_4$ crystals cooled at about 10 mK and coupled with low-temperature sensors. It has 25 cm Pb and 70 cm polyethylene and water shielding. The estimated background level at ROI of the signal induced by muons at Yemilab is below 10^{-5} counts/keV/kg/year. AMoRE requires a Class 100 cleanroom for crystal assembly on site and low humidity below 1% RH due to the hygroscopicity of the crystals. The dilution refrigerator will be installed at the center of the shielding in 2024 [9].

The COSINE-100 experiment will be upgraded to COSINE-100U after reassembling the crystals used in the COSINE-100 experiment. The copper box containing about 2 tonnes of liquid scintillator will be reused, and the shielding will be remade. The whole setup will be cooled to about −30°C in a refrigerator. The background is dominated by internal components, and radon-reduced air will be flown continuously to the copper box. COSINE-200 experiment with new NaI crystals containing a lower internal background will begin after the crystals are successfully grown [10].

A large liquid scintillator detector will be installed at the LSC pit. The pit will be laminated, and the laminated cylinder will be 19.5 m in diameter and 22 m in height. A detector of about two kilo-tonne liquid scintillator capable of separating Cherenkov light from scintillator light is planned for solar neutrino studies and sterile neutrino searches.

A general-purpose dilution refrigerator and cryostat will be installed for low-mass dark matter searches and R&D for detector tests. In addition to the dark matter and neutrino physics, a microgravity experiment, an experiment for anomaly searches with Na-22 sources, and other rare phenomena searches will be conducted.

8 Conclusion

While Yemilab construction was completed in October 2022, an expansion of essential facilities to support experiments is needed. After relocating Y2L facilities to Yemilab in 2024, the focus will be on the operation of Yemilab, with a particular emphasis on the operation of experiments such as AMoRE-II and COSINE-200. Step-by-step improvements will be implemented as needed. Additionally, we aim to contribute to various international underground experiment facilities worldwide by sharing information about resources and environments.

Data availability statement

The raw data supporting the conclusion of this article will be made available by the authors, without undue reservation.

Author contributions

KP: Conceptualization, Data curation, Funding acquisition, Investigation, Methodology, Project administration, Supervision, Validation, Visualization, Writing–original draft, Writing–review and editing. YK: Conceptualization, Funding acquisition, Investigation, Methodology, Project administration, Supervision, Validation, Writing–review and editing. KB: Conceptualization, Investigation, Methodology, Project administration, Validation, Writing–review and editing. HP: Conceptualization, Writing–review and editing, Investigation, Methodology. ML: Conceptualization, Methodology, Writing–review and editing. JS: Writing–original draft, Data curation. SHK: Writing-review and editing, Data curation. JJ: Writing–review and editing, Project administration. JK: Project administration, Writing–review and editing. SBK: Writing-origainal draft.

Funding

The author(s) declare financial support was received for the research, authorship, publication of this article. This work was supported by the Institute for Basic Science (IBS), funded by the Ministry of Science and ICT, Korea (Grant id: IBS-R016-D1).

Conflict of interest

The authors declare that the research was conducted in the absence of any commercial or financial relationships that could be construed as a potential conflict of interest.

Publisher's note

References

1. Nata RA, Murad MS. Stand up time in tunnel base on rock mass rating Bieniawski 1989. *AIP Conf Proc* (2017) 1903:090005. doi:10.1063/1.5011608

2. Rybdylova O, Al Qubeissi M, Braun M, Crua C, Manin J, Pickett L, et al. A model for droplet heating and its implementation into ANSYS Fluent. *Int J Heat Mass Transfer* (2016) 76:265–70. doi:10.1016/j.icheatmasstransfer.2016.05.032

3. Thompson PA, Marchant EW. Testing and application of the computer model 'SIMULEX'. *Fire Saf J* (1995) 24:149–66. doi:10.1016/0379-7112(95)00020-T

4. MINEARC. *Chambers and safety shelters*. Australia: MINEARC Co, Ltd (2024). Available at: https://minearc.com/products/chambers-and-safety-shelters/(Accessed February 8, 2024).

5. Kudryavtsev VA, Zakhary P, Easeman B. Neutron production in (a,n) reactions. *Nucl Inst Meth Phys Res A* (2020) 972:164095:164095. doi:10.1016/j.nima.2020.164095

6. Yoon YS, Kim J, Park H. Neutron background measurement for rare event search experiments in the YangYang underground laboratory. *Astroparticle Phys* (2021) 126:102533. doi:10.1016/j.astropartphys.2020.102533

7. Prihtiadi H, Adhikari G, Adhikari P, de Souza EB, Carlin N, Choi S, et al. Muon detector for the COSINE-100 experiment. *J Instrumentation* (2018) 13:T02007. doi:10.1088/1748-0221/13/02/T02007

8. Bae HW, Jeon EJ, Kim YD, Lee SW. Neutron and muon-induced background studies for the AMoRE double-beta decay experiment. *Astroparticle Phys* (2020) 114:60–7. doi:10.1016/j.astropartphys.2019.06.006

9. Oh Y. AMoRE-II preparation status. *PoS TAUP* (2024) 2023:214. doi:10.22323/1.441.0214

10. Lee HS. Status of the COSINE-100 experiment. *PoS TAUP* (2024) 2023:039. doi:10.22323/1.441.0039

frontiers | Frontiers in Physics

TYPE Perspective
PUBLISHED 24 April 2024
DOI 10.3389/fphy.2024.1397799

OPEN ACCESS

EDITED BY
Frank Franz Deppisch,
University College London, United Kingdom

REVIEWED BY
Maria Antonella Tabocchini,
National Institute of Health (ISS), Italy

*CORRESPONDENCE
Laura Cid-Barrio,
lcid@lsc-canfranc.es

RECEIVED 08 March 2024
ACCEPTED 04 April 2024
PUBLISHED 24 April 2024

CITATION
Hernández-Antolín R, Cid-Barrio L and Peña-Garay C (2024), Canfranc biology platform: exploring life in cosmic silence. *Front. Phys.* 12:1397799.
doi: 10.3389/fphy.2024.1397799

Canfranc biology platform: exploring life in cosmic silence

Rebecca Hernández-Antolín, Laura Cid-Barrio* and Carlos Peña-Garay

Laboratorio Subterráneo de Canfranc, Huesca, Spain

Deep underground laboratory infrastructures have extensively been used for exploring rare events, such as proton decay, dark matter searches or neutrino interactions, taking advantage of their large muon flux reduction. However, only very few investigations have evaluated the effects of low background radiation environments on living organisms. With this purpose, the Canfranc Underground Laboratory (LSC) launched the Biology Platform in 2021, which provides lab space for approved biology experiments. Two identical laboratories have been built (underground and on surface) to replicate biology experiments under the same conditions, with the main difference being the cosmic radiation background. The access protocol to use the LSC facilities includes two open calls per year and assigned time windows for executing the experimental program, which led to the first eight approved and already running experiments. We describe the scientific program of the Canfranc Biology Platform, which explores extremophiles, viral infection, immune system, multicellularity, development or aging in cosmic silence, and the first experimental results. The Platform also allows to observe the response of life to microgravity in absence of radiation, a key condition to explore life in space.

KEYWORDS

underground laboratories, underground biology, radiobiology, LSC, low radiation environment

1 Introduction

Living organisms have evolved under constant exposure to natural environmental radiation, which has been demonstrated to play an important role in the development of life and contributes to many biological defense mechanisms [1]. In fact, the dose to which humans are exposed has been evaluated by international bodies. In particular, the UNSCEAR (United Nations Scientific Committee on the Effects of Atomic Radiation) in its 2008 report [2] describes that most of the radiation we receive comes from natural sources, such as cosmic or external terrestrial radiation. Surprisingly, the man-made sources present a very low contribution to the total ionizing radiation. In order to assess the risks of ionizing radiation exposure the Linear No-Threshold (LNT) model has been widely used, based on the extrapolation of high-dose and low-dose exposure on the effects of living organisms suggesting that even low doses of radiation can be harmful [3]. However, a limited understanding of the biological effects induced by ionizing radiation at low radiation background continues to be a challenge to predict the human health risk associated with low radiation exposure.

In this sense, several biological investigations have been carried out under low background radiation conditions taking advantage of the existence of deep underground laboratories (DULs). These DULs, traditionally used for astroparticle or nuclear physics

purposes, have unique location features, shielding from cosmic radiation and reduction of natural radioactivity, which make them the ideal scenario for performing these radiobiological experiments [4, 5]. In fact in recent years, research carried out in these DULs has expanded into new fields, such as biology or radiobiology experiments, demonstrating negative effects induced on the development of the tested organisms in response to the reduction of ionization radiation [6, 7].

Regarding biological evidence, some experiments focused on evaluating the influence of cosmic radiation reduction, were performed at underground facilities of the Gran Sasso National Laboratory (LNGS, Italy) [8]. The first experiment called Pulex, demonstrated, employing yeast as a model organism, that this low background environment affects the defense mechanisms against radiomimetic compounds [9]. More recently, other complex organisms were investigated. *Drosophila melanogaster* was selected as a model for the evaluation of the effect of low doses of radiation. In this research, Morciano *et al* showed that the reduced radiation influences *Drosophila* development and the viability of flies [10]. Following these progresses carried out at LNGS, other underground laboratories have begun to develop their own biological research programs. Experiments at the Modane Underground Laboratory (LSM, France) have investigated the effect of different radiation conditions on *Escherichia coli* [11]. Several biological assays have been carried out at LBRE Laboratory hosted by the WIPP (United States) since 2011 [12, 13]. The REPAIR project started at SNOLAB (Canada) through using a combination of cell culture and whole organisms models [14]. With the aim of testing new prediction models that are direct competitors of the LNT model, the Surface Astrobiology Laboratory located in Boulby (United Kingdom) has performed bacterial growth assays as part of SELLR project [15]. As a result of all these relevant developments in the biology field, some specific workshops were organized by LSC and LNGS in 2015 and 2019 respectively. In these conferences, called DULIA-Bio, the most relevant progress of the different biology experiments performed at DULs facilities were exposed. The latest DULs to introduce its Biology platform was the LSC, whose construction and development started in 2021, both on surface and in the underground facility. The Bio-platform allows international research groups to submit experimental proposals and perform their research activities in the LSC underground facilities. So far, eight research proposals have been approved to study the influence of low-dose radiation exposure on different model organisms.

The Biology platform available at Canfranc is presented herein, offering an overview of the Canfranc facilities for the study of the influence of low radiation environment on living organisms, as well as the current experimental program.

2 Muons in biology

The LSC is located on the Spanish side of the Pyrenees, at a maximum depth of 800 m, under the Tobazo mountain. It is situated between the international Somport road tunnel (which connects Spain and France) and the historical train tunnel. The rock overburden is equivalent to approximately 2400 m water equivalent (mwe), which reduces the cosmic muon flux underground to 5 10^{-7} cm^{-2} s^{-1} [16]. The total area of the underground laboratory is about 1600 m^2, divided in various experimental rooms, with clean rooms, mechanical workshop and the biolab. Several services are available, such us radiopurity service, with high purity germanium detectors and a high sensitivity elemental mass spectrometer, copper electroforming service, the radon abatement system (RAS) [17] or liquid nitrogen production, among others.

Muons are the dominant energetic charged particles at sea level. Muon flux is about one muon per square centimeter per minute at surface with mean energy of 4 GeV. Its flux and energy is affected by solar activity, the geomagnetic field and the amount of matter traveled to the observer. Two facts are important to qualitatively understand the influence of muons in life. Muon energy spectrum above GeV rapidly decreases with energy, with a power law with index close to three, and muon energy losses are dominated by ionization below 500 GeV [18]. Therefore, muons dominantly ionize the medium with a mean energy deposited of 2 MeV per column density units in g/cm^2 [19]. Another ionization contribution is due to natural radioactivity, through the decay of the radioactive isotopes of Uranium, Thorium and Potassium and their radioactive products, occurring since the origin of life at the Earth's surface. In summary, life on the Earth surface has been exposed and adapted to these sources of ionizing radiation. The mainstream question posed to the experiments discussed here is on the biological implications of the drastic reduction of the environmental ionization, i.e., exploring life in cosmic silence.

3 Biology platform at LSC

The LSC Biology Platform was created with the aim of hosting biology experiments in a low background radiation environment. This platform offers the opportunity to develop scientific studies in a multidisciplinary environment, where researchers working with very different microorganisms can share their results and ideas, promoting the development of knowledge and expanding the field of study.

The laboratory is prepared to host experiments with a variety of biological models. Underground and surface facilities are available to replicate experiments, the same model and brand was selected for the equipment and incubators used, to reduce variables that could influence the experiments. The main goal of the experimental proposals is to be able to compare above ground experiments, which are considered as reference radiation, and underground experiments where the muon flux is reduced. In addition, shielding for other types of radiation and a radon-free air system can be included in the experimental setup to study how the reduction of a particular radiation affects metabolism.

3.1 Biology laboratory facilities

At present, both laboratories have been equipped with microbiological and cell biology instruments. There are Class II biological safety cabinets, bacteriological incubators and CO_2 incubators, autoclave, orbital incubators, spectrophotometers and a water purification equipment. In addition, the underground

FIGURE 1
(A) Photograph of the above ground biology laboratory containing some of the equipment described. **(B)** Underground Biology Laboratory, as a replica of the external laboratory, except for a flow cytometer instrument, which is only located in this location.

laboratory has a −80°C ultra-freezer, a bench-top flow cytometer, a stereomicroscope, and a clinostat, which allows experiments to be carried out in microgravity conditions. On surface, an inverted fluorescence microscope, which contains the necessary filters and objectives typically used for biological samples, is also available under request. In Figure 1, two pictures of the external and underground biology laboratories are shown, where some of the available instruments can be seen.

In the underground facilities, the LSC can provide researchers its extensive experience in the design of physics experiments. In this vein, similar to rare event research, radiobiology experiments could require different types of shielding, such as lead castles, copper and polyethylene shields, in order to block gammas and neutrons A dedicated control of the radioactive background (background model) is a standard practice in low background physics experiments, but not yet common in biology experiments. This is one of the well-established coordinated efforts with other underground biology laboratories carried out during DULIA meetings, hosted by LSC (https://indico.cern.ch/event/436589) in 2015 and LNGS (https://agenda.infn.it/event/19116/) in 2019, to reach solid conclusions. A compilation of low background facilities, in comparison with underground labs worldwide, has been recently shown [4, 20].

Concerning this radioactive background characterization, continuous monitoring of ambient radiation is carried out at the LSC since 2011. Firstly, the incident radiation is monitored using thermoluminescent dosimeters (TLD), model TLD UD-802A supplied by Panasonic. These dosimeters consist of two different crystals ($Li_2B_4O_7$ and $CaSO_4$), placed in four independent areas, which are sensitive to different sources of radiation. These TLD are placed in 14 different locations of LSC and are replaced every month. After their exposure, the dose rate is measured employing a UD-716 instrument from Panasonic. The average results obtained for the TLD during 2022 show dose rates of 0.71 ± 0.03 and 1.36 ± 0.03 mSv/year, for Underground and above ground biological areas, respectively (2022 annual LSC data, not published).

Another relevant radiological parameter that must be taken into account is Radon environmental concentration, which is the main source of natural radiation [2]. Radon varies throughout the year and is continuously monitored with calibrated instruments located at six different sites in the LSC facilities. Alphaguard P30 portable radon detectors from Genitron Instruments are used for its determination. The current values obtained for underground facilities (60–100 Bq/m^3) are shown to be one-third of the surface levels (200–280 Bq/m^3). To improve these values, a Radon Abatement System was put into operation in the underground lab [17] and good ventilation in the surface laboratory is being implemented to match the lower levels of radon in the underground laboratory Background radiation of experiments hosted underground is reduced by eliminating the radon present in air next to the detector or, in this case, the biological samples. The radon abatement system is capable of providing levels of 1 mBq/m^3, which

are much lower than the Rn levels measured in the above ground laboratory. Taking advantage of this system, the radon-free dry air produced underground can in future be used directly in the microorganism incubators, making sure humidity is correctly added to the air, to explore life in radon-less air conditions.

3.2 Biology platform operation

Research groups or collaborations must submit a written proposal for an experimental activity through an Expression of Interest (EOI) to use the LSC Biology Platform services. This proposal is subject to evaluation by the LSC Scientific Committee, whose members are scientists of international repute. Their role is to give advice on the experimental proposals as well as to monitor the progress of the experiments that have already been approved. The LSC Scientific Committee meets twice a year, so any proposal for evaluation at the following committee meeting must be submitted to the LSC by the deadline specified in the call for proposals.

The EOI must contain the scientific, economic and operational elements necessary for the laboratory to initiate the evaluation process with the assistance of the Scientific Committee. These elements include the title of the project, the spokesperson and structure of the collaboration, the scientific proposal with objectives and work plan or the requirements it implies for the LSC. For more information on this section, please consult the official website of the laboratory (https://lsc-canfranc.es/en/rules-for-bio-proposals/).

3.3 Experiments currently hosted

Several national research groups have expressed interest in hosting their experiments in the underground facilities since the LSC decided to launch the Biology Platform. Between 2021 and 2023, 8 proposals from different research groups of Spanish universities have been approved and have become experiments. All of them have extensive experience of working under reference radiation conditions with the microorganisms selected for the experiments that are being carried out at Canfranc. In underground conditions, they are going to study such important parameters in biology as growth and viability, mutation rate, aging or fitness to the environment. According to the microorganisms studied, the experiments' proposals have been classified in four groups: bacteria, yeast, cell culture and nematodes. A more detailed explanation of each of the proposals and their status, following this ranking, is given below.

3.3.1 Bacteria

Among all the biological characteristics that can be studied, the growth rate and viability of microorganisms are two of the most remarkable characteristics that can be measured most easily. Focusing on these parameters, the first of the proposals hosted by the LSC, which has been taking data since the platform's inception in 2021 can be named as bacteria in D_2O water. Before bacteria began to be studied at the LSC facilities, the bacteria communities present in D_2O were analysed using 16S sequencing showing a low diversity of bacterial populations, dominated by yet uncultivated species of the *Nitrosomodaceae* family and microorganisms such as *Curvibacter* sp (non-photosynthetic). This experiment aims to evaluate the effect of reduced cosmic radiation on the viability of bacterial communities recovered from high purity D_2O in the absence of externally added nutrients. With this purpose and taking advantage of the underground facilities, this research activity is analyzing bacterial growth and simultaneously determining the elemental content variations in the growth media by ICP-MS on samples taken from the D_2O water every 2 months.

Another parameter that can be explored under low radiation conditions is the mutation rate. Selecting this parameter as a target, one of the approved experiments propose to revisit the classical experiment of Luria and Delbrück fluctuation test [21] to evaluate the possible role of cosmic radiation in the mutation rate of bacteria. The directed vs. random character of mutations will be also evaluated. The main hypothesis of this project is that under similar conditions, changes in the rate of point mutation should be observed depending on the radiation level. To perform this research, *E. coli* was selected as model organisms.

On the other hand, the effects of radiation on DNA damage, already explained in previous sections, can also be analyzed. Some microorganisms have shown to be very versatile by naturally surviving extreme conditions. These extremophiles organisms present natural mechanisms to resist DNA damage such as ionizing and non-ionizing radiation, extreme temperatures or low pressures. Recently, *Deinococcus radiodurans*, have been studied showing resistance to several extreme environments compatible with outer space [22]. In this sense, other representative microorganisms have been investigated such as *Ramazzottius varieornatus* or *E. coli* [23, 24]. At the same time, research developed in underground laboratories has shown that the absence of radiation may result in inefficient DNA repair mechanisms, therefore having a negative impact on cellular growth and survival. For all these reasons, one of the experimental proposals intends to prove if there is a minimum of radiation under which cellular growth can be deemed optimal, while above and below this level, cellular survival decreases. To do that, bacteria cultures will be exposed to increasingly higher levels of radiation analyzing the bacteria growth and response. In particular, the Dsup protein involved in efficient DNA repair mechanisms [24] will be characterized, in the first step of this project, on protecting *E. coli* from high levels of radiation and, in the following steps, its beneficial effects on mammalian cell cultures will be tested.

3.3.2 Yeast

Another interesting parameter that is under investigation is human aging. Yeast, and more specifically *Saccharomyces cerevisiae*, is one of the most important model organisms for the study of molecular mechanisms related to human aging and disease. It has played a central role in the discovery of important conserved longevity factors and pathways [25, 26]. The two paradigms to study aging in *S. cerevisiae* are the chronological and the replicative life span (CLS and RLS, respectively). Following this research, one of the approved experiments currently working at LSC, is focused on the determination of CLS, i.e., the measurement of the mean and maximum survival time of non-dividing yeast populations,

aiming to gain insight into the biological impact of low levels of background radiation on the chronological aging of yeast. To achieve this goal, the results of CLS in reference radiation will be compared to those obtained under low radiation conditions. Previous investigations of yeast metabolism performed at Grand Sasso Underground facilities, showed that these decreased radiation levels impair the biological defense of *S. cerevisiae* against radiomimetic chemical agents [6]. However, no results on yeast lifespan under these conditions have been reported. Therefore, the main objective of the project is to understand the biological impact of low background radiation levels on yeast chronological aging and mutation rate. The experimental measurement of mutation rate in *S. cerevisiae* is based on the study of certain genes such as CAN1, because of the selectable phenotypes that are produced when the function of this gene is lost due to mutations. In particular, CAN1 is the transporter for the amino acid arginine, which can also be used by its toxic analogue L-canavanine. The presence of L-canavanine in the growth media is used to select yeast mutants. In this way, only mutants that have lost CAN1 functionality are able to grow on plates containing canavanine, as it cannot be introduced into the cells [27].

Finally, the latest yeast-based research accepted to date is focused on the evaluation of the influence of low background radiation on the alteration in subcellular enzymatic reactions, cell mitochondrial function, direct (DNA-repair mechanisms) and indirect (protective mechanisms by antioxidant activity) DNA damage. Most of the experiments carried out in low radiation environments show that, once the cultures have been conditioned, their ability to repair DNA after exposure to DNA-damaging agents (chemical substances, irradiation) is reduced [9, 28, 29]. Focus on those results, this research proposal seeks to determine whether this low radiation conditioned organisms to DNA damage is direct, due to the impairments of DNA-repair mechanisms, or indirect, due to the reduced efficiency of Reactive Oxygen Species (ROS)-scavenging species. The effect of low radiation on enzymatic chemical reactions involved in cellular protection against oxidative damage will be study through the employment of well-established biochemical assays focusing on glutathione peroxidase (GPx) and the determination of mitochondrial functions tests in *S. cerevisiae*.

3.3.3 Cell cultures

As explained for yeast-based experiments, human aging can also be investigated taking cell cultures as model organisms. Aging is a major risk factor for a wide range of human pathologies. There are two long-argued causes for human aging, namely, epigenetic aging and senescence. Cellular senescence is physiologically beneficial in several contexts. It was originally observed in normal human diploid fibroblasts, which were no longer able to divide after a finite number of cell divisions in culture. Subsequent research has shown that cellular senescence is a state of stable cell cycle arrest that occurs in response to irreparable damage and can be considered a hallmark of aging [30].

Epigenetic aging, which can be measured with so-called "epigenetic clocks," is due to deterministic processes embedded in the mammalian genome. Stochastic (random) damage, which may be due to wear and tear and/or malfunctioning of stress response mechanisms, leads to cellular senescence. Epigenetic clocks are a maintenance system that appears to be conserved in all model organisms, including humans [31]. Thus, although the relationship between cellular senescence and aging is undisputed, epigenetic aging appears to act independently of the common stressors that induce senescence. Making use of the absence of background radiation from the LSC, the last experiment, which is currently taking data at Canfranc, aims to study the primordial nature of the epigenetic clocks of aging and senescence by measuring their functioning and timing capability in a low background radiation environment. The main objective is to examine the longitudinal aging trajectories of aging clocks across the replicative lifespan to senescence of primary human cells from healthy and premature aging syndromes in cosmic silence.

Apart from aging determination purposes, the reduced radiation observed in underground laboratories has been also correlated to alterations on the growing kinetics in several organisms including bacteria [32], unicellular eukaryotes [9], mammalian cell lines [33] or small multicellular organisms [34, 35]. The difference in growth phenotypes observed in unicellular *versus* multicellular organisms suggests a distinct response to this particular low background environment that may be influenced by the cellular organization state. Taking this into account, a research group proposed an experiment based on the study of the contribution of cellular organization in the response to low background radiation, by investigating this response in the context of models of unicellular relatives of animals which form multicellular structures during clonal stages in their life cycle (*Sphaeroforma arctica*) or by aggregation in response to environmental stimuli (*Capsaspora owczarzaki*) [36, 37]. These selected organisms have been well characterized in its laboratory, offering the opportunity to evaluate the changes that have occurred in cell division and grow of these unicellular organisms, their transition through stages of multicellular formations, and the associated genomic and/or transcriptomic while they are cultured in underground conditions.

3.3.4 Nematodes

To conclude, several studies demonstrated that environment is a critical factor in the virus-host interactions which modifies the outcome of the infection and its severity. Abiotic stresses cause changes in host susceptibility to infection and reduce innate and adaptive immune responses, modifying the infection evolution and the virulence of pathogens. Among these abiotic factors microgravity has been shown to be one that affects immunity [38, 39] and gene regulation [40].

Astronauts can experience various forms of stress during space missions, caused by environmental factors such as radiation, pressure and microgravity. These factors can significantly affect the human physiological state and cause a decline in their immune system [41], but the underlying causes are still not well understood. In this context, DULs become the perfect scenery to study the effects of microgravity as an isolated factor, independently of radiation effects.

For that purpose, *Caenorhabditis elegans (C. elegans)* and its natural pathogen, *Orsay nodavirus* have been selected to study the progression of viral infections in those conditions. Experiments assessing the fertility and viability of eggs are being carried out under conditions of infection, absence of muons and microgravity.

4 Preliminary results

The evidence obtained so far in underground radiobiology experiments, oxidative stress and impact on DNA reparation

mechanisms, confirm that DULs offer an opportunity to advance in these scientific quests in a multidisciplinary environment, helped by the existing infrastructures for low background experiments exploring neutrino properties and searching for dark matter. Four experiments have already taken data in the underground and on surface labs: 1) Microorganisms observed in heavy water show different count rates when compared to replicas on the surface. Metagenomic content is under analysis [42] 2) Development of *C. elegans* and response to infection has been explored. The first experiments show differences in the development underground, with observed significant variations in the total number of eggs per generation and in the fraction of viable ones. Infection progress also shows significant differences. Very interestingly, cosmic silence stress is very important when compared to microgravity influence [43]. 3) The experiments studying the primordial nature of the epigenetic clocks of aging and senescence have completed the first phase of data taking. Data are currently under methylation analysis and epigenetic clocks characterization [44]. 4) The de Luria-Delbruck experiment completed underground shows different statistics than the one performed on the surface. Analysis of the results and more statistics are needed to reach firm conclusions [45].

5 Future and perspectives

DULs have been the ideal location for astroparticle physics experiments that require a well-characterized low background environment for many years, but their use for hosting biological experiments is a relatively new field of study that is gaining momentum. With regard to this new research field in underground laboratories, mechanisms underlying the effects observed in living organisms at low levels of radiation are not yet well understood, as the different experiments conducted to date have used different species and different conditions. In order to unify methodologies and results among the different, already established, biology programs, future experiments carried out in underground laboratories should involve the selection of a common model organism evaluated in the different bio-platforms. Further investigations testing different radiation environments over a long period of time should be performed. These steps will allow a deep knowledge of the selected organisms by comparing the results between different DULs, whose radiation doses and environment are different and the evolution of the microorganisms with time.

In addition to the undoubted advances in understanding the role of radiation in life, exploring life in underground labs has further implications on future experiments and applications. In the exploration of life in space (or in other planets), the impact of microgravity (or reduced gravity) on biological processes has been widely explored in experiments on surface and in space missions. The muon flux reduction and, in general, the lack of cosmic and natural radiation in underground laboratory conditions is able to isolate the influence of microgravity on life, from other important influences like cosmic protons and heavier nuclei [46, 47]. Therefore, installations in underground laboratories could serve to simulate specific conditions in space valid to perform biology experiments in long space trips or life on other planets.

Author contributions

RH-A: Conceptualization, Investigation, Writing–original draft, Writing–review and editing. LC-B: Conceptualization, Investigation, Supervision, Writing–original draft, Writing–review and editing. CP-G: Conceptualization, Supervision, Writing–original draft, Writing–review and editing.

Funding

The author(s) declare that financial support was received for the research, authorship, and/or publication of this article. Funding for this work was provided by Spanish Ministry of Science and Technology.

Conflict of interest

The authors declare that the research was conducted in the absence of any commercial or financial relationships that could be construed as a potential conflict of interest.

Publisher's note

References

1. Chew MT, Bradley DA, Jones B, Nisbet A, Hill M. Review of the effect of reduced levels of background radiation on living organisms. *Radiat Phys Chem* (2022) 200: 110273–5. doi:10.1016/j.radphyschem.2022.110273

2. United Nations. *Scientific committee on the effects of atomic radiation. Sources and effects of ionizing radiation: united Nations scientific committee on the effects of atomic radiation: UNSCEAR 2008 report to the general assembly, with scientific annexes*. New York, New York, United States: United Nations (2010).

3. Tubiana M, Feinendegen LE, Yang C, Kaminski JM. The linear no-threshold relationship is inconsistent with radiation biologic and experimental data. *Radiology* (2009) 251:13–22. doi:10.1148/radiol.2511080671

4. Ianni A. Science in underground laboratories and DULIA-bio. *Front Phys* (2021) 9: 7–10. doi:10.3389/fphy.2021.612417

5. Smith GB, Tabocchini MA, Garay CP. The biogeochemistry, biophysics, radiobiology, and technical challenges of deep subsurface. *Front Phys* (2021). doi:10.3389/978-2-88966-892-2

6. Liu J, Ma T, Liu Y, Zou J, Gao M, Zhang R, et al. History, advancements, and perspective of biological research in deep-underground laboratories: a brief review. *Environ Int* (2018) 120:207–14. doi:10.1016/j.envint.2018.07.031

7. Lampe N, Breton V, Sarramia D, Sime-Ngando T, Biron DG. Understanding low radiation background biology through controlled evolution experiments. *Evol Appl* (2017) 10:658–66. doi:10.1111/eva.12491

8. Esposito G, Anello P, Ampollini M, Bortolin E, Angelis CD, Imperio GD, et al. Underground radiobiology: a perspective at gran Sasso national laboratory. *Front Public Heal* (2020) 8:611146–7. doi:10.3389/fpubh.2020.611146

9. Satta L, Augusti-Tocco G, Ceccarelli R, Esposito A, Fiore M, Paggi P, et al. Low environmental radiation background impairs biological defence of the yeast *Saccharomyces cerevisiae* to chemical radiomimetic agents. *Mutat Res Lett* (1995) 347:129–33. doi:10.1016/0165-7992(95)00031-3

10. Morciano P, Iorio R, Iovino D, Cipressa F, Esposito G, Porrazzo A, et al. Effects of reduced natural background radiation on *Drosophila melanogaster* growth and development as revealed by the FLYINGLOW program. *J Cel Physiol* (2018) 233: 23–9. doi:10.1002/jcp.25889

11. Lampe N, Biron DG, Brown JMC, Breton V, Marin P, Maigne L, et al. Simulating the impact of the natural radiation background on bacterial systems: implications for very low radiation biological experiments. *PLoS One* (2016) 11:e0166364–19. doi:10.1371/journal.pone.0166364

Smith, GB, Grof, Y, Navarrette, A, and Guilmette, RA. Exploring biological effects of low level radiation from the other side of background. *Health Phys* (2011) 100:263–5. doi:10.1097/hp.0b013e318208cd44

13. Zarubin MP, Kuldoshina OA, Kravchenko EV. Biological effects of low background radiation: prospects for future research in the low-background laboratory DULB-4900 of baksan neutrino observatory INR RAS. *Phys Part Nucl* (2021) 52:19–30. doi:10.1134/S1063779621010056

14. Thome C, Tharmalingam S, Pirkkanen J, Zarnke A, Laframboise T, Boreham DR. The REPAIR project: examining the biological impacts of sub-background radiation exposure within SNOLAB, a deep underground laboratory. *Radiat Res* (2017) 188: 470–4. doi:10.1667/RR14654.1

15. Wadsworth J, Cockell CS, Murphy ASJ, Nilima A, Paling S, Meehan E, et al. There's plenty of room at the bottom: low radiation as a biological extreme. *Front Astron Sp Sci* (2020) 7:1–14. doi:10.3389/fspas.2020.00050

16. Trzaska WH, Slupecki M, Bandac I, Bayo A, Bettini A, Bezrukov L, et al. Cosmic-ray muon flux at Canfranc underground laboratory. *Eur Phys J C* (2019) 79:721–6. doi:10.1140/epjc/s10052-019-7239-9

17. Pérez-Pérez J, Amare JC, Bandac IC, Bayo A, Borjabad-Sanchez S, Calvo-Mozota JM, et al. Radon Mitigation Applications at the Laboratorio Subterráneo de Canfranc (LSC). *Universe* (2022) 8:112. doi:10.3390/universe8020112

18. Group. WRL particle D. Review of particle physics. *Prog Theor Exp Phys* (2022) 15: 1–878. doi:10.1093/ptep/ptac097

19. Groom DE, Mokhov NV, Striganov SI. Muon stopping power and range tables 10 MeV-100 TeV. *Data Nucl Data Tables* (2001) 78:183–356. doi:10.1006/adnd.2001.0861

20. Kamaha A, Mount B, Schnee R. Supporting capabilities for underground facilities. *AIP Conf Proc* (2023) 2908. doi:10.1063/5.0161437

21. Luria SE, Delbrück M. Mutations of bacteria from virus sensitivity to virus resistance. *Genetics* (1943) 28:491–511. doi:10.1093/genetics/28.6.491

22. Kawaguchi Y, Shibuya M, Kinoshita I, Yatabe J, Narumi I, Shibata H, et al. DNA damage and survival time course of deinococcal cell pellets during 3 Years of exposure to outer space. *Front Microbiol* (2020) 11:2050. doi:10.3389/fmicb.2020.02050

23. Jönsson KI, Rabbow E, Schill RO, Harms-Ringdahl M, Rettberg P. Tardigrades survive exposure to space in low Earth orbit. *Curr Biol* (2008) 18:729–31. doi:10.1016/j.cub.2008.06.048

24. Kirke J, Jin XL, Zhang XH. Expression of a tardigrade Dsup gene enhances genome protection in plants. *Mol Biotechnol* (2020) 62:563–71. doi:10.1007/s12033-020-00273-9

25. Longo VD, Shadel GS, Kaeberlein M, Kennedy B. Replicative and chronological aging in saccharomyces cerevisiae. *Cell Metab* (2012) 16:18–31. doi:10.1016/j.cmet.2012.06.002

26. Jung PP, Zhang Z, Paczia N, Jaeger C, Ignac T, May P, et al. Natural variation of chronological aging in the *Saccharomyces cerevisiae* species reveals diet-dependent mechanisms of life span control. *Aging Mech Dis* (2018) 4:3–11. doi:10.1038/s41514-018-0022-6

27. Whelan WL, Gocke E, Manney TR. The CAN1 locus of Saccharomyces Cerevisiae: fine-structure analysis and forward mutation rates. *Genetics* (1979) 91:35–51. doi:10.1093/genetics/91.1.35

28. Satta L, Antonelli F, Belli M, Sapora O, Simone G, Sorrentino E, et al. Influence of a low background radiation environment on biochemical and biological responses in V79 cells. *Radiat Environ Biophys* (2002) 41:217–24. doi:10.1007/s00411-002-0159-2

29. Carbone MC, Pinto M, Antonelli F, Amicarelli F, Balata M, Belli M, et al. The Cosmic Silence experiment: on the putative adaptive role of environmental ionizing radiation. *Radiat Environ Biophys* (2009) 48:189–96. doi:10.1007/s00411-008-0208-6

30. Song S, Lam EWF, Tchkonia T, Kirkland JL, Sun Y. Senescent cells: emerging targets for human aging and age-related diseases. *Trends Biochem Sci* (2020) 45:578–92. doi:10.1016/J.TIBS.2020.03.008

31. Lowe D, Horvath S, Raj K. Epigenetic clock analyses of cellular senescence and ageing. *Oncotarget* (2016) 7. doi:10.18632/oncotarget.7383

32. Castillo H, Li X, Schilkey F, Smith GB. Transcriptome analysis reveals a stress response of Shewanella oneidensis deprived of background levels of ionizing radiation. *PLoS One* (2018) 13:e0196472–22. doi:10.1371/journal.pone.0196472

33. Liu J, Ma T, Gao M, Liu Y, Liu J, Wang S, et al. Proteomic characterization of proliferation inhibition of well-differentiated laryngeal squamous cell carcinoma cells under below-background radiation in a deep underground environment. *Front Public Heal* (2020) 8:584964. doi:10.3389/fpubh.2020.584964

34. Van Voorhies WA, Castillo HA, Thawng CN, Smith GB. The phenotypic and transcriptomic response of the *Caenorhabditis elegans* nematode to background and below-background radiation levels. *Front Public Heal* (2020) 8:581796–12. doi:10.3389/fpubh.2020.581796

35. Pirkkanen J, Zarnke AM, Laframboise T, Lees SJ, Tai TC, Boreham DR, et al. A research environment 2 km deep-underground impacts embryonic development in lake whitefish (*Coregonus clupeaformis*). *Front Earth Sci* (2020) 8:1–9. doi:10.3389/feart.2020.00327

36. Sebé-Pedrós A, Irimia M, del Campo J, Parra-Acero H, Russ C, Nusbaum C, et al. Regulated aggregative multicellularity in a close unicellular relative of metazoa. *Elife* (2013) 2013:e01287–20. doi:10.7554/eLife.01287

37. Dudin O, Ondracka A, Grau-Bové X, Haraldsen AAB, Toyoda A, Suga H, et al. A unicellular relative of animals generates a layer of polarized cells by actomyosin-dependent cellularization. *Elife* (2019) 8:e49801–26. doi:10.7554/eLife.49801

38. Zhu L, Nie L, Xie S, Li M, Zhu C, Qiu X, et al. Attenuation of antiviral immune response caused by perturbation of TRIM25-mediated RIG-I activation under simulated microgravity. *Cell Rep* (2021) 34:108600. doi:10.1016/j.celrep.2020.108600

39. Gilbert R, Torres M, Clemens R, Hateley S, Hosamani R, Wade W, et al. Spaceflight and simulated microgravity conditions increase virulence of *Serratia marcescens* in the *Drosophila melanogaster* infection model. *npj Microgravity* (2020) 6:4–9. doi:10.1038/s41526-019-0091-2

40. Corydon TJ, Schulz H, Richter P, Strauch SM, Böhmer M, Ricciardi DA, et al. Current knowledge about the impact of microgravity on gene regulation. *Cells* (2023) 12:1043. doi:10.3390/cells12071043

41. Garrett-Bakelman FE, Darshi M, Green SJ, Gur RC, Lin L, Macias BR, et al. The NASA twins study: a multidimensional analysis of a year-long human spaceflight. *Science* (2019) 80(364):eaau8650–52. doi:10.1126/science.aau8650

42. Sobrino F *Private Communication (F Sobrino) to be published elsewhere* (2024).

43. Elena SF *Private Communication (S F Elena) to be published elsewhere* (2024).

44. Menendez J *Private Communication (J Menendez) to be published elsewhere* (2024).

45. Buceta J *Private Communication (J Buceta) to be published elsewhere* (2024).

46. Durante M, Cucinotta FA. Physical basis of radiation protection in space travel. *Rev Mod Phys* (2011) 83:1245–81. doi:10.1103/RevModPhys.83.1245

47. Durante M, Cucinotta FA. Heavy ion carcinogenesis and human space exploration. *Nat Rev Cancer* (2008) 8:465–72. doi:10.1038/nrc2391

frontiers | Frontiers in Physics

TYPE Original Research
PUBLISHED 28 May 2024
DOI 10.3389/fphy.2024.1398070

OPEN ACCESS

EDITED BY
J. W. F. Valle,
Spanish National Research Council (CSIC), Spain

REVIEWED BY
Gu Chen,
Guangzhou University, China
Olga Gileva,
Institute for Basic Science (IBS), Republic of Korea

*CORRESPONDENCE
S. Carbajal,
scarbajalv@pucp.edu.pe

RECEIVED 08 March 2024
ACCEPTED 02 May 2024
PUBLISHED 28 May 2024

CITATION
Carbajal S and Gago AM (2024), Indirect search of heavy neutral leptons using the DUNE near detector.
Front. Phys. 12:1398070.
doi: 10.3389/fphy.2024.1398070

Indirect search of heavy neutral leptons using the DUNE near detector

S. Carbajal* and A. M. Gago

Sección Física, Departamento de Ciencias, Pontificia Universidad Católica del Perú, Lima, Peru

We evaluate the potential of the DUNE near detector (DUNEND) for establishing bounds for heavy neutral leptons (HNLs). This is achieved by studying how the presence of HNLs affects the production rates of active neutrinos, therefore creating a deficit in the neutrino charged current (CC) events at the LArTPC of the DUNEND. The estimated bounds on HNLs are calculated for masses between 1 eV and 500 MeV. We consider 10 years of operation (five in neutrino and antineutrino modes) and obtain limits of $|U_{\mu 4}|^2 < 9 \times 10^{-3}$ (4×10^{-2}) and $|U_{e4}|^2 < 7 \times 10^{-3}$ (3×10^{-2}) for masses below 10 MeV and a 5% (20%) overall normalization uncertainty in the neutrino charged current event rate prediction. These limits, within the region of masses below 2 (10) MeV, are better than those that can be achieved by DUNE direct searches for the case of a 5% (20%) uncertainty. When a conservative 20% uncertainty is present, our limits can only improve current constraints on $|U_{e4}|^2$ by up to a factor of 3 in a small region of approximately 5 eV and set limits on $|U_{\mu 4}|^2$ in a mass region free of constraints (40 eV–1 MeV).

KEYWORDS

neutrino physics, heavy neutral leptons, DUNE experiment, flavor physics, beyond the standard model physics

1 Introduction

Heavy neutral leptons (HNLs) are singlet (right-handed) fermion states introduced for explaining the non-zero neutrino masses, interacting via Yukawa coupling with the Higgs boson and the leptonic doublet, a Dirac mass term, and also appearing in the Majorana mass term. The nearly sterile states that arise after the diagonalization of the mass terms interact with matter via suppressed mixing to the active neutrinos of the Standard Model (SM) [1, 2].

The HNLs are candidates to solve important particle physics and cosmological issues [1]. They can help explain the smallness of the active neutrino masses via the seesaw mechanism [3], act as possible dark matter candidates [4], and also explain the baryon asymmetry of the universe through their role in leptogenesis (see [1, 5] and references therein). On the other hand, neutrino oscillations involving light sterile states have been proposed to explain the excess of electron antineutrino and neutrino events at LSND and MiniBoonE, respectively, as well as the deficit of electron antineutrino events at reactor experiments [6]. The HNL masses required for solving the previously mentioned problems fall within a mass range that spans from keV to TeV. As a consequence of their relevance, there have been several HNL searches in this wide mass range, placing limits on the possible values of the HNL mass m_N and its mixing to the SM neutrinos $|U_{\alpha 4}|^2$ [2, 7].

In particular, searches of HNLs in the range of masses of 1–400 MeV have been conducted in accelerator-based experiments through searches for low-energy peaks in the energy spectrum of the muons resulting from pion ($\pi^{\pm} \to \mu^{\pm}\nu_H$) and kaon decays ($K^{\pm} \to \mu^{\pm}\nu_H$) [8–11]. With no positive results found so far, they obtain upper bounds for $|U_{\mu 4}|^2$ such as 10^{-6} for $m_N \sim 10$ MeV and 10^{-9} for $m_N \sim 300$ MeV.

This work aims to assess the sensitivity of the DUNE in setting upper limits for $|U_{\mu 4}|^2$ and $|U_{e4}|^2$ for masses below 500 MeV. We achieved the latter by comparing the energy distributions of the neutrino CC event rates with and without HNLs at the DUNE near detector (DUNEND) [12]. We found that the presence of HNLs creates a deficit of CC events that is not generated by neutrino oscillations but instead by the combination of kinematic effects in the production and decay chains of HNLs: the decrease in the branching ratios of active neutrino production, the large lifetimes of HNLs, and the fact that active neutrinos born from HNLs have angular distributions spanned outside the detector coverage. We consider the decrease in CC events as an indirect signal of HNLs and use it to set limits on the mixing parameters. Additionally, we present an analysis of the possibility of finding confidence regions for the values of (m_N, $|U_{\alpha 4}|^2$) if a deficit of CC events is found at DUNE [13].

This paper is summarized as follows: in Section 2, we discuss the theoretical framework of HNL production and decay. Then, in Section 3, we describe the experimental setup. In Section 4, the details of our simulation are given, while in Section 5, our results are presented. We draw our conclusion in the final section.

2 Theoretical framework

As we already mentioned, the nearly sterile mass eigenstates couple to the active flavor states via an extended version of the Pontecorvo–Maki–Nakagawa matrix (PMNS) [14], which can be expressed as follows:

$$\nu_\alpha = \sum_{i=1,2,3} U_{\alpha i}\nu_i + U_{\alpha 4}N,$$

where N represents the HNL field. It is also helpful to write the new active neutrino flavor states in terms of the flavor states of the SM ν_α^{SM}, which represent the neutrino flavor states when the values of the 3×3 PMNS mixing matrix are assumed. This can be done by the approximation [15].

$$\nu_\alpha \approx \nu_\alpha^{\mathrm{SM}}\left(1 - \frac{|U_{\alpha 4}|^2}{2}\right) + U_{\alpha 4}N.$$

Due to the connection mentioned above, the HNLs can be produced in any weak decay involving active neutrinos. The production rate of HNLs depends kinematically on its mass m_N, the strength of its mixing to active neutrinos $|U_{\alpha 4}|^2$, and the nature of the decaying particle that produces it, which, from now on, is referred to as its parent. In this work, we are interested in HNLs with masses below the kaon mass (m_K). The production of HNLs from kaon and pion decays, followed by the muon decays, dominates at the typical energies of beam dump experiments such as DUNE. Their production from heavier particles, such as D mesons or τ leptons, is also possible, but it is rare since the production of the latter is heavily suppressed in comparison to the light mesons. Table 1 shows the dominant HNL production channels from light leptons and mesons, along with the maximum kinematically allowed values of the masses for the HNLs. A rough estimation of these values is obtained by subtracting the total rest mass of the particles produced, other than the HNLs, from the corresponding mass of their parent particles.

TABLE 1 Channels considered for the production of HNLs. The maximum possible value of m_N is shown for each channel. Charged conjugate channels were also considered.

	Channel	m_N (MeV)
$\mu^+ \to$	$e^+\nu_e\bar{\nu}_\mu$	105.14
$\pi^+ \to$	$\mu^+\nu_\mu$	33.91
	$e^+\nu_e$	139.06
$K_L^0 \to$	$\pi^+e^-\nu_e$	357.12
	$\pi^+\mu^-\nu_\mu$	252.38
$K^+ \to$	$\mu^+\nu_\mu$	387.81
	$\pi^0e^+\nu_e$	358.19
	$\pi^0\mu^+\nu_\mu$	253.04
	$e^+\nu_e$	493.17

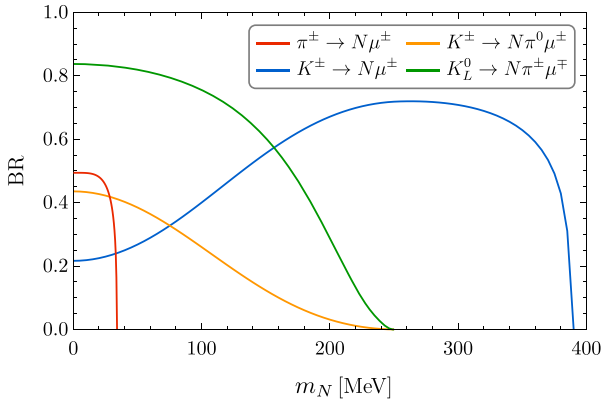

FIGURE 1
Branching ratios of the dominant HNL production channels for $|U_{\mu 4}|^2 = 1$.

We calculated the branching ratios for HNL production by using the formulas from [16]. For instance, Figure 1 shows the branching ratios of the dominant HNL production channels below the kaon mass for $|U_{\mu 4}|^2 = 1$. We can note that almost all the branching ratios decrease with m_N, with the only exception being the leptonic decays of charged kaons, $K^{\pm} \to N\mu^{\pm}$. Above 34 MeV, the production from pions is kinematically forbidden; this is important since this means that all heavy neutral leptons above this mass will be produced only from kaon decays. As the value of m_N increases, the branching ratio of $K^{\pm} \to N\mu^{\pm}$ keeps increasing as well, surpassing the branching ratios of $K^{\pm} \to N\pi^0\mu^{\pm}$ at approximately 80 MeV and $K_L^0 \to N\pi^0\mu^{\pm}$ at

TABLE 2 HNL decay channels considered in this work. The minimum required value of m_N is shown for each channel.

Channel	Threshold [MeV]
$\nu\nu\nu$	10^{-9}
$\nu e^+ e^-$	1.02
$\nu e^\pm \mu^\mp$	106.17
$\nu\pi^0$	134.98
$e^\mp \pi^\pm$	140.08
$\nu\mu^+\mu^-$	211.32
$\mu^\mp \pi^\pm$	245.23

approximately 160 MeV. Finally, the branching ratio of $K^\pm \to N\mu^\pm$ reaches its maximum at approximately 260 MeV and then decreases until it is kinematically forbidden. The endpoint of each branching ratio corresponds to the maximum m_N given in Table 1.

The production of HNLs via semileptonic decays involves hadronic currents that cannot be calculated from first principles due to the non-perturbative nature of QCD at low energies. Therefore, the dynamics of these decays are modeled by form factors that represent the momentum distribution of the quarks inside the mesons and parametrize the momentum transfer between the hadronic current and the lepton pair [17]. For all the semileptonic decays shown in Table 1, we used the form factors presented in [16].

After their production, all the HNLs propagate and then decay on flight via mixing with active neutrinos. Table 2 shows all the decay channels for the HNLs considered in this work. We included all the kinematically allowed decays to final states involving pseudoscalar mesons and pure leptonic decays for $m_N < m_K$. A more complete table is found in [18].

The partial width of an HNL decay channel involving a final lepton l_α or light neutrino ν_α is directly proportional to the mixing parameter squared $|U_{\alpha 4}|^2$. Therefore, the total width and lifetime of the HNLs also depend on the relevant mixing parameters. The lifetime dependence on the values of $|U_{\alpha 4}|^2$ can have a huge impact on the position of the decay vertex of the HNL and, hence, on its possible signal in the detector. Setting small values for the $|U_{\alpha 4}|^2$ means that HNLs are being produced at a lower rate, but at the same time, these HNLs have a greater lifetime and therefore decay further away from the detector.

When we determine the individual partial widths of each channel, there is a factor of two that differentiates between the decays of Dirac and Majorana HNLs [18]. For instance, a Dirac HNL can decay to charged pions only via $N \to e^- \pi^+$, while a Majorana HNL can also decay through $N \to e^+ \pi^-$. This evidently has an effect on the rates of π^+/π^- production from HNL decays but does not affect the partial decay widths. This means that CC-mediated channels have the same partial widths for Dirac and Majorana neutrinos:

$$\begin{aligned} \Gamma(N_M \to l^- X^+) &= \Gamma(N_D \to l^- X^+), \\ \Gamma(N_M \to l^+ X^-) &= \Gamma(\bar{N}_D \to l^+ X^-). \end{aligned} \tag{1}$$

On the other hand, NC-mediated channels do distinguish between Dirac and Majorana HNLs. This is because the contractions of the NC operator add an additional contribution to differential decay widths of the Majorana HNLs [18, 19].

$$d\Gamma(N_M \to \nu X) = d\Gamma(N_D \to \nu X) + d\Gamma(\bar{N}_D \to \bar{\nu} X).$$

Therefore, a factor of two appears when comparing the partial widths of NC-mediated decays.

$$\Gamma(N_M \to \nu X) = 2\Gamma(N_D \to \nu X). \tag{2}$$

Equations 1 and 2 imply that the total widths (Γ_T) of Majorana and Dirac HNLs are related by

$$\Gamma_T(N_M) = 2\Gamma_T(N_D),$$

which translates into a difference between their lifetimes:

$$\tau(N_M) = \frac{1}{2}\tau(N_D).$$

For very low masses ($m_N \ll m_e$), the factor of two in Eq. 2 disappears [20], making the total widths and lifetimes of Dirac and Majorana HNLs indistinguishable. Part of the mass range that we will explore in this work falls in the region of very low masses.

At the end of this section, we will describe how the active neutrino flux is affected by the production of HNLs. For this purpose, we will show how the SM parent meson's branching ratios are modified when the production of HNL occurs. Let us start by defining the SM total decay rate of the pion ($\Gamma_\pi^{\rm SM}$):

$$\Gamma_\pi^{\rm SM} = \Gamma^{\rm SM}(\pi \to e\nu_e) + \Gamma^{\rm SM}(\pi \to \mu\nu_\mu),$$

and the decay rate with heavy neutral leptons ($\Gamma_\pi^{\rm BSM}$):

$$\begin{aligned} \Gamma_\pi^{\rm BSM} &= \Gamma^{\rm BSM}(\pi \to e\nu_e) + \Gamma^{\rm BSM}(\pi \to \mu\nu_\mu) + \Gamma(\pi \to NX) \\ &\approx \Gamma^{\rm SM}(\pi \to e\nu_e)\left(1 - \frac{|U_{e4}|^2}{2}\right) \\ &\quad + \Gamma^{\rm SM}(\pi \to \mu\nu_\mu)\left(1 - \frac{|U_{\mu 4}|^2}{2}\right) \\ &\quad + \Gamma(\pi \to NX). \end{aligned}$$

The branching ratio of ν_μ production from pion decays in the presence of HNLs can then be written as

$$\begin{aligned} {\rm BR}^{\rm BSM}(\pi \to \mu\nu_\mu) &= \frac{\Gamma^{\rm BSM}(\pi \to \mu\nu_\mu)}{\Gamma_\pi^{\rm BSM}} \\ &\approx \frac{\Gamma^{\rm SM}(\pi \to \mu\nu_\mu)\left(1 - \frac{|U_{\mu 4}|^2}{2}\right)}{\Gamma_\pi^{\rm SM}} \cdot \frac{\Gamma_\pi^{\rm SM}}{\Gamma_\pi^{\rm BSM}} \\ &\approx {\rm BR}^{\rm SM}(\pi \to \mu\nu_\mu) \cdot \frac{\Gamma_\pi^{\rm SM}}{\Gamma_\pi^{\rm BSM}}\left(1 - \frac{|U_{\mu 4}|^2}{2}\right). \end{aligned} \tag{3}$$

A similar relation can be found for the branching ratio of ν_e production from pion decays:

$$ {\rm BR}^{\rm BSM}(\pi \to e\nu_e) \approx {\rm BR}^{\rm SM}(\pi \to e\nu_e) \cdot \frac{\Gamma_\pi^{\rm SM}}{\Gamma_\pi^{\rm BSM}}\left(1 - \frac{|U_{e4}|^2}{2}\right), \tag{4}$$

where ${\rm BR}^{\rm SM}(\pi \to \mu(e)\nu_{\mu(e)})$ represents the branching ratio of $\nu_\mu(\nu_e)$ production from pion decays in the SM. We can see that the introduction of HNLs causes the production of either muon or electron neutrinos from pions to be suppressed by the factor:

$$\mathcal{K}_\pi^\alpha(m_N, |U_{\alpha 4}|^2) = \frac{\Gamma_\pi^{\rm SM}}{\Gamma_\pi^{\rm BSM}}\left(1 - \frac{|U_{\alpha 4}|^2}{2}\right), \tag{5}$$

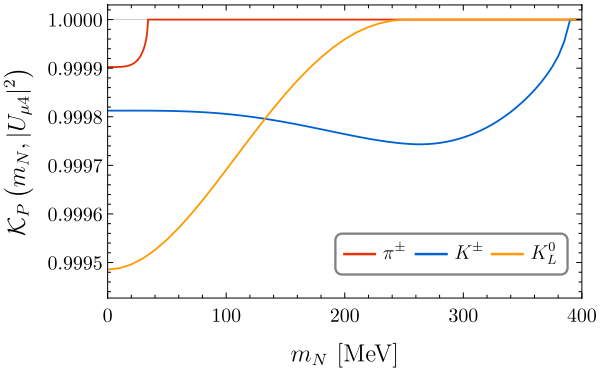

FIGURE 2
Suppression factor $\mathcal{K}^\mu(m_N, |U_{\mu 4}|^2 = 10^{-4})$ of muon neutrino production as a function of m_N.

with $\alpha = e, \mu$. Figure 2 illustrates the dependence on m_N of the factor $\mathcal{K}^\mu$ for several parents assuming $|U_{\mu 4}|^2 = 10^{-4}$. For each meson, the suppression factor acts only up to a maximum HNL mass due to kinematical constraints, which are the same constraints shown in Table 1; Figure 1. Although the effect is small, the high luminosity of DUNE makes it possible to use this effect to set limits on the heavy neutral lepton parameters.

Thus, each particle capable of producing active neutrinos can now produce HNLs, leading to a suppression of active neutrinos at DUNE. The latter happens for all neutrino flavors even when only one mixing $|U_{\alpha 4}|^2$ is turned on. In fact, we can see from Eqs 3, 4 that, if we set $|U_{\alpha 4}|^2 = 0$, the production of the active neutrinos ν_α is still suppressed by the factor $\Gamma_\pi^{\rm SM}/\Gamma_\pi^{\rm BSM}$. As we will show further ahead, the reduction in the active neutrino flux would imply the possibility that they do not reach the DUNEND, decreasing the number of expected CC events at this facility.

3 Experimental setup

In order to simulate how the presence of HNLs affects the number of ν CC events at DUNE, we based our experimental setup in the DUNE near detector, as described in [13].

We assume that the LBNF-DUNE beam collides protons with approximately 120 GeV of energy into a graphite target, producing 1.47×10^{21} POTs per year. At each collision, several mesons are produced, including mostly pions, kaons, and charmed mesons.

The muons and long-lived charged mesons ($\pi^\pm$ and $K^\pm$) produced are deflected by focusing magnetic horns located right after the target; as a consequence, their trajectories end up preferably oriented along the beam axis, as shown schematically in Figure 3. On the other hand, the trajectories of neutral mesons (D^0, K_L^0 and π^0), tau leptons, and short-lived charged heavy mesons ($D^\pm$ and $D_s^\pm$) are not affected by the focusing horns. Most particles decay in flight inside the decay pipe, a cylinder with a length of 230 m, and a diameter of 2 m; however, a small number of long-lived particles reach the end of the decay pipe and decay at rest at the decay pipe's surface.

The near detector liquid argon time projection chamber (LArTPC) is located at 574 m from the target. It is parallelepiped with a width and height (both transverse to the beam direction) of 7 m and 3 m, respectively, and a length of 5 m in the beam direction. The LArTPC is filled with a fiducial mass of 50 tons of liquid argon. There is also the multi-purpose detector (MPD), which is a magnetic spectrometer designed to study particles exiting the LArTPC and contains a one-ton high-pressure cylindrical gaseous argon time projection chamber. Since we are interested in the effects of HNLs on the ν CC events at the DUNE near detector, we will not take into account the MPD in our simulation setup because its impact on our results is negligible.

We also take into account the possibility of moving the detectors to several off-axis positions along the x-axis, a setup known as DUNE-PRISM [21].

4 Simulation route for HNLs

4.1 Parent production

For the simulation of the production of HNLs from light mesons, we used the data provided by the DUNE Beam Interface Working Group (BIWG) [22], which makes use of GEANT4 [23, 24] and FLUKA [25, 26]. These data include information about the decay positions and momenta of pions, kaons, and muons after they exit the focusing horns. The most abundant light parent in DUNE is the pion, followed by kaons and finally muons, as shown in Figure 4. In this work, we will consider that the neutrino CC event rates might have an overall normalization uncertainty of up to 20% due to

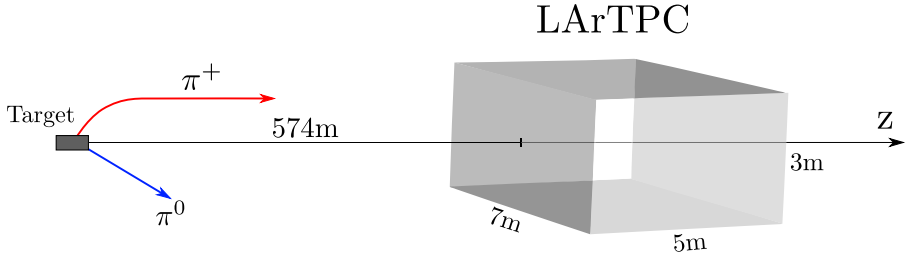

FIGURE 3
Experimental setup for the LArTPC in the neutrino mode (not to scale). Charged particles are deflected by the magnetic horns.

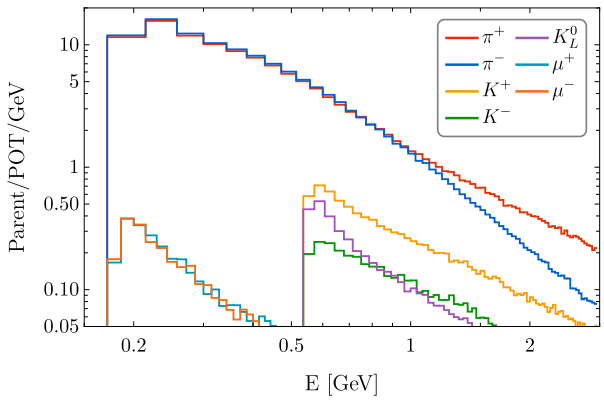

FIGURE 4
Spectra of light particles capable of producing HNLs in the DUNE beam. Different bin widths have been used for different particles.

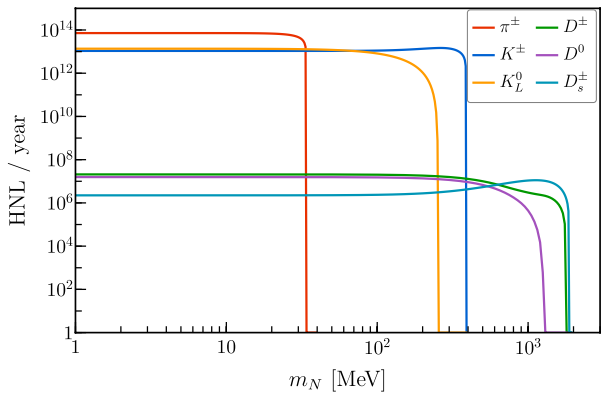

FIGURE 5
Heavy neutral leptons produced from mesons in 1 year in the neutrino mode for $|U_{\mu 4}|^2 = 10^{-4}$.

uncertainties in the modeling of the production of mesons and leptons at the DUNE target and neutrino cross sections. We encapsulate this uncertainty by a parameter σ_a that varies from 0.05 to 0.2. Setting $\sigma_a = 0.05$ is equivalent to assume a 5% overall normalization uncertainty in the DUNE neutrino CC event rates, whereas σ_a represents an uncertainty of 20%.

The production of HNLs from heavier particles such as D mesons and τ leptons is also possible, but it is expected to have a negligible effect on the active neutrino flux, which is totally dominated by the production from lighter mesons. In order to test the relevance of HNL production from these heavy particles, we used PYTHIA8 [27] to estimate the neutrino flux generated by $D^0, \bar{D}^0, D^\pm, D_s^\pm$ and $\tau^\pm$ at DUNE. We observed that these heavy parents do not contribute significantly to the DUNE neutrino flux, and hence, the production of HNLs coming from them will have a negligible effect on the number of CC events. Consequently, our analysis is restricted only to the production of HNLs from light mesons and muons.

4.2 Production of HNLs

The production and decay chain of an HNL will depend on its mass, the mass of its parent, the nature of its parent (lepton, scalar meson, or vector meson), the parent decay channel, the HNL nature (Dirac or Majorana), the HNL decay channel, and the value of the mixing parameter involved. In principle, we could turn on, simultaneously, the three mixing parameters $|U_{\alpha 4}|^2$, $\alpha = e, \mu$, and τ; however, in our analysis, we will consider only one non-zero mixing parameter at a time.

Given the HNL mass and nature, we gave PYTHIA8 the kinematic information on the parents and let it handle the kinematics of all the HNL production and decay chain up to final active neutrinos. As expected, the HNL production and decay channels are weighted with their corresponding branching ratios.

In Figure 5, we show the number of HNLs produced at DUNE from meson decays in 1 year and in the neutrino mode for $|U_{\mu 4}|^2 = 10^{-4}$. The production from pion decays dominates at low masses, followed by charged and neutral kaons. The spectrum endpoint for pions and kaons corresponds to the maximum allowed m_N displayed in Table 1 when they decay into muons. For completeness, we also present the production from charmed mesons, which, as expected, is comparatively smaller and completely overshadowed for masses below 387.81 MeV. Above this threshold, HNL production from pions and kaons is kinematically forbidden, and the contribution from charmed meson decays dominates. This contribution is several orders of magnitude smaller than the one from light mesons, as we already claimed.

4.3 Decay of HNLs—active neutrinos

We focus on the active neutrinos produced from the HNL decays. We are interested in differentiating the number of these neutrinos that fall within the detector's geometrical acceptance from those outside of it. With this aim, we parametrize the probability that an active neutrino hits the detector by two distances along the HNL propagation axis. These distances represent two different decay vertices of the HNL and are calculated considering the geometrical coverage of the detector and the kinematical information provided by PYTHIA8, which depends on its lifetime, production vertex, velocity, and the direction of the propagation of the active neutrino. The aforementioned probability is given by

$$w(d_1, d_2) = \exp\left(-\frac{d_1}{v\gamma\tau_0}\right) - \exp\left(-\frac{d_2}{v\gamma\tau_0}\right),$$

where v is the HNL's velocity, γ is the Lorentz factor, and τ_0 represents proper lifetime.

For illustrative purposes, we present, in Figure 6, the scheme of the explained above, for the case when the HNL moves along the beam axis. It is clear that our analysis is general and takes into account the tridimensional shape of the LArTPC and all the possible ways in which an active neutrino might enter the detector, including cases where the HNL is outside the detector coverage.

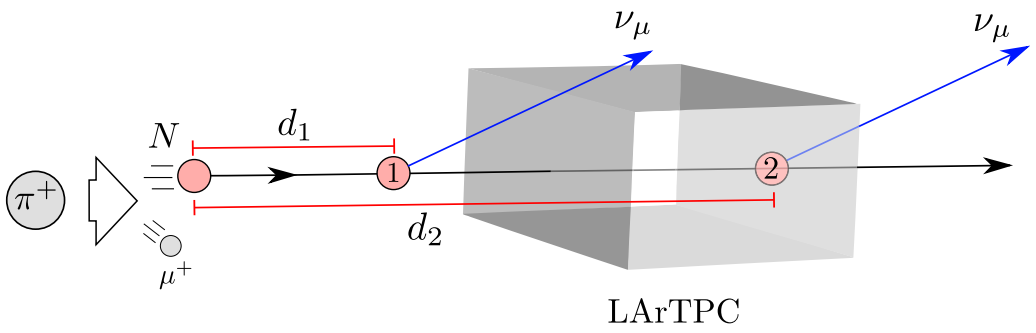

FIGURE 6
HNL N propagates and decays into an active neutrino ν_μ. If the HNL decays between positions 1 and 2, the active neutrino ν_μ hits the LArTPC.

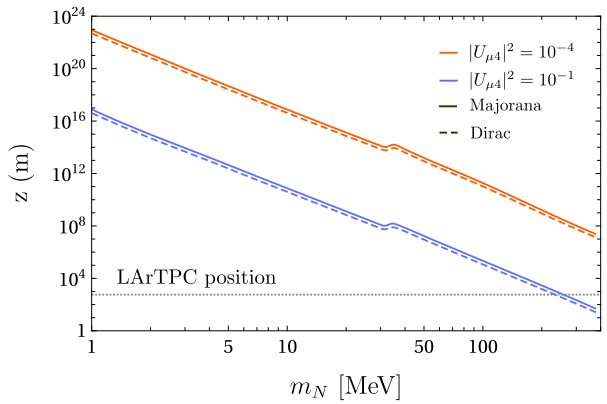

FIGURE 7
Average HNL's decay positions protected along the Z-axis for $|U_{\mu 4}|^2 = 10^{-4}$ and $|U_{\mu 4}|^2 = 10^{-1}$. The dotted line represents the position of LArTPC.

It is important to mention that when we deactivate the HNL production, we reproduce the (pure SM) active neutrino fluxes arriving at the LArTPC predicted by the DUNE collaboration [28].

Figure 7 displays the average HNLs' decay positions measured from the target and projected along the Z-axis for $|U_{\mu 4}|^2 = 10^{-4}$ and $|U_{\mu 4}|^2 = 10^{-1}$ and for Dirac and Majorana HNLs. The dotted line represents the position of the LArTPC, which is located at $z = 574$ m. Given that the lifetime of the HNL is inversely proportional to $|U_{\mu 4}|^2$, we can see that, as long as the mixing decreases, the average decay positions at Z increase. In the mass range, we studied, for $|U_{\mu 4}|^2 = 10^{-4}$, on average, all the HNL decays behind the LArTPC; hence, one active neutrino is lost in the DUNE flux at the LArTPC for each HNL produced. On the other hand, for $|U_{\mu 4}|^2 = 10^{-1}$, the average HNL decay position coincides with the LArTPC location at $m_N \approx 255$ MeV, which implies that, above this mass, the HNL decay mainly before the detector.

We also note that in both cases, there is a small increase in the average decay positions at approximately 30 MeV. This happens because the production of HNLs from pion decays becomes kinematically forbidden around this energy and decays from kaons starting to dominate. This makes the average HNL more energetic, and therefore, it can travel larger distances before decaying.

4.4 Oscillation effects in active neutrinos from meson decays

The existence of HNLs forces us to modify the neutrino oscillation probabilities. Therefore, the effects of neutrino oscillations have to be taken into account in our simulations. Particularly, the place where neutrino oscillations can affect our results is in the disappearance of active neutrinos produced in meson decays. The survival probability of these active neutrinos is given by

$$\begin{aligned} P_{\nu_\alpha \to \nu_\alpha} = &-4\left(1-|U_{\alpha 4}|^2\right)|U_{\alpha 4}|^2 \sin^2\left(\frac{1.27 m_N^2 L}{E}\right) e^{-\frac{\Gamma_4 L}{2}} \\ &+2\left(1-|U_{\alpha 4}|^2\right)|U_{\alpha 4}|^2 e^{-\frac{\Gamma_4 L}{2}} \\ &+\left(1-|U_{\alpha 4}|^2\right)^2 + |U_{\alpha 4}|^4 e^{-\Gamma_4 L}, \end{aligned} \tag{6}$$

where E represents the energy of the active neutrino, L is the distance that it travels before reaching the DUNEND, and Γ_4 is the decay rate of the HNL, and we have also considered that the mass of the active neutrino is negligible when compared to the HNL mass m_N. This survival probability will effectively decrease the number of active neutrinos that reach the DUNEND and the number of neutrino CC events at the near detector complex. For completeness, we incorporated Eq. 6 in our simulations as an extra weight for each active neutrino.

There is also the possibility of oscillation of HNLs into active neutrinos. However, since the HNL flux is very small when compared to the active neutrino flux, the effects of these oscillations in the neutrino CC event rates are negligible and were not considered in this work.

5 Results

5.1 Impact on CC events at DUNEND

As we can infer from what we have shown before, the DUNE neutrino flux fired at the DUNEND will be affected by the production of HNLs. Each HNL produced from the decay of its

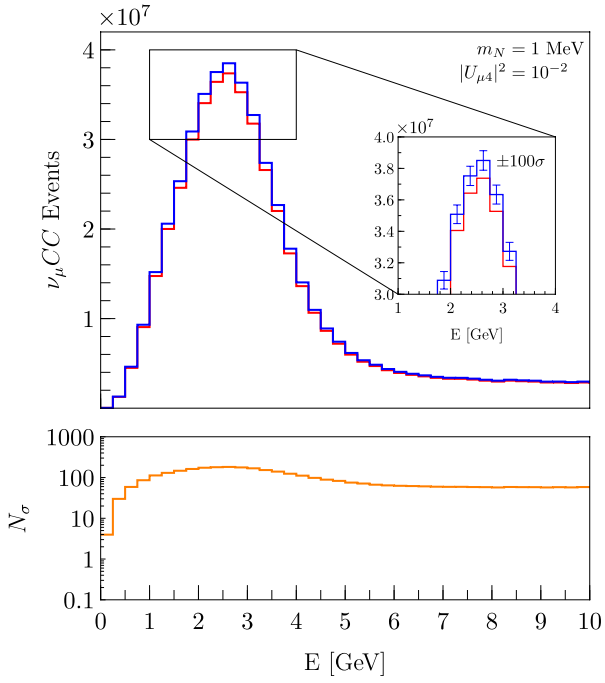

FIGURE 8
ν_μ CC event rates for m_N = 1 MeV assuming the maximum value allowed for $|U_{\mu 4}|^2$ at the 90% confidence level, on-axis position, 10 years of operation, and σ_a = 0. The error bars are amplified by 100.

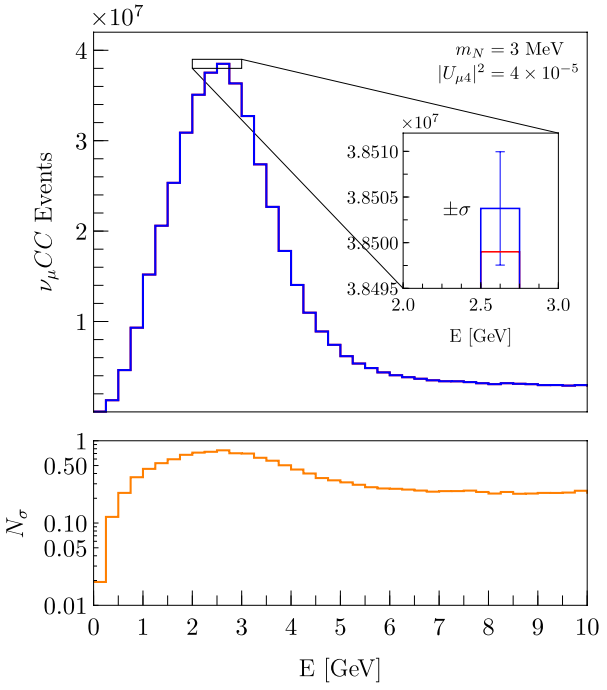

FIGURE 9
ν_μ CC event rates for m_N = 3 MeV assuming the maximum value allowed for $|U_{\mu 4}|^2$ at the 90% confidence level, on-axis position, 10 years of operation, and σ_a = 0.

parent meson (or muon) replaces one active neutrino in the SM DUNE neutrino flux. In principle, there is a possibility to recover this active neutrino since the HNL can decay into one or more active ones, which, depending on their direction, could or not impact the DUNEND. However, as demonstrated in Figure 7, it is unlikely that a relevant portion of these spurious active neutrinos would be created before or inside the LArTPC of the DUNEND for the mass range used in this work. This decrease in active neutrinos translates into a decrease in the CC event rates at the LArTPC. Our strategy is to use this deficit of CC events as an indirect signal of the existence (production) of HNLs at the DUNE neutrino flux. Hence, in that sense, we are conducting an indirect search for HNLs. This indirect method for searching HNLs is complementary to the direct searches [7], which look for HNL decays inside one of the DUNE's detectors. As we will show in the following sections, our method can work comparatively better than direct searches for masses below 10 MeV and is sensitive to masses below 1 MeV, a region primarily inaccessible through direct searches.

The deficit in the total CC event rates depends on the mass of the HNL, the value of $|U_{\alpha 4}|^2$, and the off-axis position of the detector. In order to have the first estimate of the maximum significance of this deficit allowed by current limits on the mixing parameters, we calculated the active neutrino flux in the presence of HNLs using the maximum values of $|U_{\alpha 4}|^2$ allowed by accelerator experiments at the 90% confidence level [29] and then convoluted these fluxes with GENIE 2.8.4 [30] CC inclusive cross sections.

In order to get an idea of the significance of the change in the neutrino CC event rates, we will ignore all systematic uncertainties in the neutrino flux prediction and work in the ideal case of no systematic uncertainties $\sigma_a = 0$. Figure 8 shows the ν_μ CC event rates at the LArTPC for $m_N = 1$ MeV and $|U_{\mu 4}|^2 = 10^{-2}$ assuming Majorana neutrinos, on-axis position, and 10 years of operation (five in the neutrino mode and five in the antineutrino mode) and $\sigma_a = 0$. The significance of the change in the number of the CC events in each bin is estimated by

$$N_\sigma = \frac{|N^{\mathrm{BSM}} - N^{\mathrm{SM}}|}{\sqrt{N^{\mathrm{SM}}}} = \frac{|\Delta N|}{\sigma},$$

where N^{SM} represents the expected number of CC events assuming only SM interactions and N^{BSM} the number of CC events when HNLs are produced. As we mentioned before, we are also ignoring all normalization uncertainties in the CC event rates so that $\sigma = \sqrt{N^{\mathrm{SM}}}$ is the uncertainty in each bin. Due to the high luminosity of the DUNE experiment, under this setup, the production of HNLs causes a decrease in the total number of CC event rates on the order of 10^6 events near 2.5 GeV. This implies a deviation from the SM prediction by approximately 100σ around this energy. This indicates that DUNE's sensitivity to $|U_{\mu 4}|^2$ might be beyond the current experimental limits for this particular HNL mass.

As the HNL mass increases, its production is suppressed, and consequently, its presence on the active neutrino flux is reduced. As an example of the latter, we displayed in Figure 9 the event rates for m_N = 3 MeV and the maximum value allowed for $|U_{\alpha 4}|^2$ by experiments at the 90% confidence level for this mass. In this case, there is a (small) deviation, from the SM prediction, lower than 1σ. This happens because of the tighter constraint on the mixing parameter.

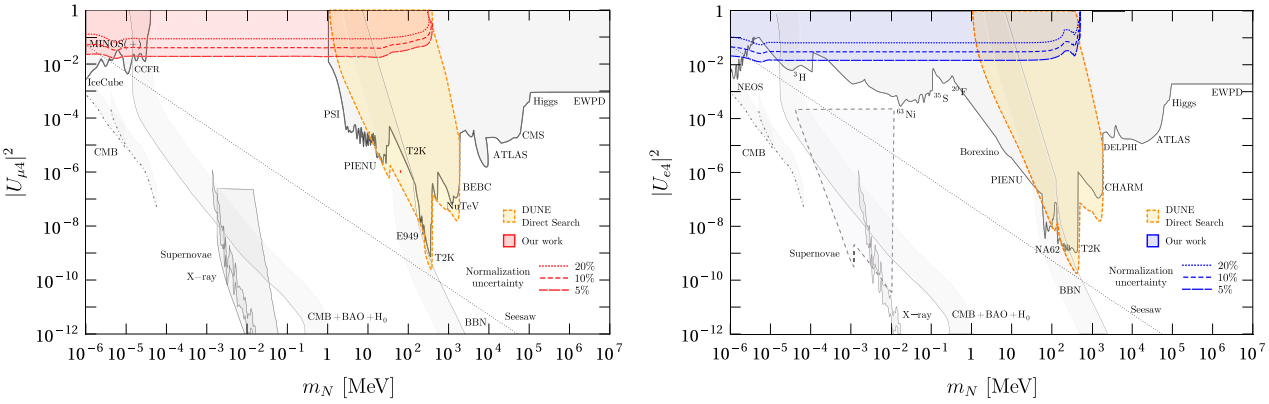

FIGURE 10
Estimated limits of DUNE to $|U_{\mu 4}|^2$ (left, red) and $|U_{e4}|^2$ (right, blue) at the 90% confidence level by CC event disappearance at the LArTPC of the DUNEND, for 10 years of operation (five in neutrino and five in antineutrino modes) and the on-axis position. The regions of experimental constraints (gray) were taken from [29, 32, 33]. The estimated sensitivity of DUNE obtained in [7] by direct searches of HNL decays is shown for comparison.

We have shown that in the ideal case of no systematic uncertainties $\sigma_a = 0$, DUNE will have good sensitivity for indirect hints of the existence of low mass HNLs, which are evidenced by a decrease in the neutrino CC event rates at the LArTPC. Of course, once systematic uncertainties are considered, the sensitivity and the limits are expected to decrease considerably.

5.2 Sensitivity

In order to estimate the future sensitivity of DUNE to HNLs due to the deficit of neutrino CC events, we have to consider that the predictions of our simulations carry systematic uncertainties related to the distributions of hadron production at the DUNE target, the neutrino CC cross section uncertainties, among others. We will incorporate these uncertainties in our calculations by assuming an overall normalization uncertainty in the spectra, which, in practice, means that the values of the event rates are not completely known and can fluctuate by a certain amount. This overall normalization uncertainty will be represented by the parameter σ_a that takes the values $\sigma_a = 0.05$, 0.1, and 0.2, which are equivalent to overall normalization uncertainties of 5%, 10%, and 20%, respectively. We are also considering shape uncertainties in each bin that are represented by the parameters σ_{ai}; for simplicity, we consider $\sigma_{ai} = \sigma_a$ for all bins. We estimate the sensitivity of DUNE to $(m_N, |U_{\alpha 4}|^2)$ through the following χ^2 [31]:

$$\chi^2 = \frac{a^2}{\sigma_a^2} + \sum_{\nu_e,\nu_\mu,\bar{\nu}_e,\bar{\nu}_\mu} \left[\sum_{i=1}^{\text{nbin}} \frac{a_i^2}{\sigma_{ai}^2} + \sum_{i=1}^{\text{nbin}} \frac{\left(N_i^{\text{SM}} - N_i^{\text{BSM}}(1 + a + a_i)\right)^2}{N_i^{\text{SM}}} \right],$$

where N_i^{BSM} represents the neutrino CC events in the ith bin when HNLs are produced and N_i^{SM} is the DUNE prediction of CC events in the ith bin, according to the standard model. The nuisance parameters a and a_i encompass the normalization uncertainties and allow for the values of N_i^{BSM} to fluctuate; these parameters are always profiled in the calculation of χ^2. We must note that the fact of combining all the neutrino flavors in our definition of χ^2 is fundamental for improving the sensitivity of our results. The tau neutrinos are not considered since their contributions to χ^2 are negligible.

The deficit of neutrino CC events at DUNE is an indirect signal of HNLs. Therefore, in the case that no significant deficit is found, the absence of this deficit can be used to set limits on the values of the parameters $(m_N, |U_{\alpha 4}|^2)$ with a particular confidence level. We calculated the value of χ^2 in the parameter space 10^{-6} MeV $< m_N < 10^7$ MeV and $10^{-12} < |U_{\alpha^4}|^2 < 1$ for $\alpha = e$, μ and $\sigma_a = 0.5$, 0.1, and 0.2 and then used these values to estimate the limits that DUNE might be able to set to the parameters $(m_N, |U_{\alpha 4}|^2)$ at the 90% confidence level.

Our results are presented in Figure 10. The left panel of this figure shows the estimated DUNE sensitivity to $|U_{\mu 4}|^2$ at the 90% confidence level on the LArTPC assuming Majorana neutrinos, 10 years of operation (five in neutrino and five in antineutrino modes), and on-axis position. In our analysis, the CC event rates from all neutrino flavors are considered (read the discussion at the end of Section 2). For masses close to 1 eV, the limits decrease because, for the typical energies and flight distances of active neutrinos at DUNEND, the probability of neutrino oscillations into HNLs tends to be zero as the value of m_N approaches 1 eV. Right above 1 eV, the limits start to oscillate since the survival probability of the active neutrinos is sensitive to m_N. For masses between 10 eV and 10 MeV, the limits are independent of m_N. The latter is because of three factors. The first one is the averaging out of the neutrino oscillations into HNLs for large values of m_N. The second one is that, for these very low masses, the total number of HNLs produced is practically independent of m_N (see Figure 5). The other factor is that the HNL lifetime for lower masses is enormous (see Figure 7), decaying all of them far away from the detector without the possibility of leaving a trace on it. As we already know, above $m = 33.91$ MeV, the production channel $\pi^+ \to \mu^+ N$ is kinematically forbidden, and there is a sudden loss in the sensitivity. As the mass increases, production from charged kaons starts to dominate and does so up to the end of the curve, which is at 387.81 MeV. For instance, for $\sigma_a = 0.05$ and $\sigma_a = 0.2$, the sensitivity of DUNE below 10 MeV is around $|U_{\mu 4}|^2 < 2 \times 10^{-2}$ and $|U_{\mu 4}|^2 < 8.5 \times 10^{-2}$, respectively. We point out that even in the conservative

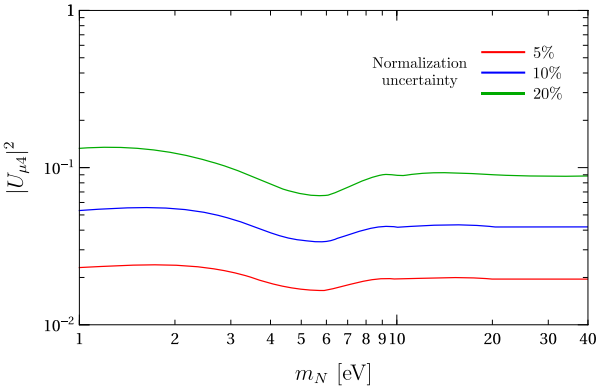

FIGURE 11
Zoom of the sensitivity to $|U_{\mu 4}|^2$ of Figure 10. The oscillation of the sensitivity near 1 eV is produced by the oscillation effects of Eq. 6.

case of $\sigma_a = 0.2$, our limits are competitive with direct searches below 1.3 MeV.

The right panel of Figure 10 shows the expected DUNE sensitivity when we turn on $|U_{e4}|^2$ being the other sensitivity zero. The rest of the characteristics are the same as for the left panel. In general, the sensitivity pattern is similar to the pattern observed for the left panel. The limits oscillate close to 1 eV, and for higher masses, they become mass-independent since most HNLs decay behind the LArTPC. Above 10 MeV, the pion decay channel $\pi^{\pm} \to e^{\pm} N$ starts to dominate because, in contrast to $\pi^{\pm} \to e^{\pm} \overset{(-)}{\nu}_e$, it is less suppressed by helicity due to the larger size of the HNL mass. This effect decreases the number of both ν_e and ν_μ CC events according to the suppression factor shown in Eq. 5, affecting the CC event rates of both electron and muon neutrinos. At approximately 139 MeV, the HNL production from pion decays becomes kinematically forbidden, which translates into a decrease in the sensitivity. Finally, the curve ends when the production from kaons is kinematically forbidden at 493.17 MeV. For $\sigma_a = 0.05$ and $\sigma_a = 0.2$, the sensitivity of DUNE below 10 MeV is around $|U_{e4}|^2 < 1.5 \times 10^{-2}$ and $|U_{e4}|^2 < 6.5 \times 10^{-2}$, respectively. Even in the conservative case of $\sigma_a = 0.2$, our limits are competitive with direct searches below 1.3 MeV and also provide a small increase in sensitivity by a factor of 1.5 at approximately 5 eV in comparison with experimental constraints.

Although we are making our calculations for 10 years of exposure, it is important to point out that our sensitivity for $|U|^2$ increases only slightly when compared with 1 year of exposure. If we had not included systematic uncertainties, the limits would roughly improve as $\frac{|U|^2}{\sqrt{T}}$, where T represents the exposure time; in this ideal scenario, after 10 years of operation, the limits would improve by a factor of around $1/\sqrt{10} \approx 0.32$. However, introducing uncertainties in our χ^2 prescription heavily penalizes the sensitivity of our approach: in this more realistic scenario, after 10 years of operation, the limits improve by only a factor of approximately 0.9 in comparison with 1 year of exposure. Therefore, in the context of our analysis, the first year of operation of DUNE is the most important.

Another important remark must be done about the effects of neutrino oscillations in this work. Neutrino oscillations involving HNLs are only relevant when $m_N \sim 1$ eV. Since our analysis starts approximately at 1 eV, the effects of neutrino oscillations will only be visible as a wiggle at the beginning of our sensitivity plots. For completeness, in Figure 11, we show a zoom of the left plot in Figure 10. We can see that close to 1 eV, the sensitivity oscillates as expected, but this effect is small and only restricted to the low tail of our sensitivity plot.

We must point out that our results are blind to the Dirac or Majorana nature of the HNL. The distinction between Dirac and Majorana HNLs is usually performed in direct searches by analyzing the distributions of charged mesons and leptons produced when the HNL decays inside the detector. We are not looking into the direct search mode since it has already been discussed in [7]. In addition to their decay products, Dirac and Majorana HNLs can also be differentiated by their lifetimes due to the factor of two present in Eq. 5. However, this effect is not relevant for us because, for the mass range we studied and small mixings, almost all the HNL decays occur behind the LArTPC, as shown in Figure 7. Furthermore, as we have discussed in Section 2, for very low m_N, the Dirac and Majorana neutrinos are indistinguishable. Thus, we can conclude that nearly all the active neutrinos produced from the HNL decays are lost independently of the nature of neutrinos. In this way, the critical magnitude in our analysis is the production rate of HNLs, which is independent of the nature of neutrinos, so the deficit of the CC event rates is independent too. Therefore, it would not be possible to distinguish between Dirac and Majorana neutrinos through the approach presented here.

5.3 Off-axis sensitivity

The DUNE experiment also considers the possibility of moving the DUNE near detectors horizontally, a setup known as DUNE-PRISM. We move the LArTPC by up to 30 m horizontally while maintaining the rest of the simulation parameters and study the impact in our estimated sensitivities. The results are shown in Figure 12, where all the lines represent the sensitivities at the 90% confidence level and the dashed curves represent the on-axis sensitivities. We see that the effect of moving the detector to an off-axis position does not affect considerably the limits, although the curves are less smooth due to the decrease in statistics. However, we see that the sensitivities increase at off-axis positions for masses close to 100 MeV.

5.4 Allowed regions for (m_N, $|U_{\alpha 4}|^2$)

We also explore the potential to constrain the (m_N, $|U_{\alpha 4}|^2$) parameter space region in the context of this indirect search. So, assuming that the disappearance CC events are originated by the presence of HNLs within the neutrino beam, we perform χ^2 analysis fixing our simulation in certain values of (m_N, $|U_{\alpha 4}|^2$). The 95% confidence regions for $m_N = 0.1$ MeV and $|U_{\mu 4}|^2 = 5 \times 10^{-2}$ are presented in Figure 13 for $\sigma_a = 0.05$ (red), $\sigma_a = 0.1$ (blue), and $\sigma_a = 0.2$ (green). For the case of 20% uncertainty, the analysis only gives upper limits to the values of $|U_{\mu 4}|^2$. For 5% and 10% uncertainties, the regions are bounded to the right but extend to the left up to $m_N =$ 1 eV, a mass degeneracy that reflects the fact that our approach is not

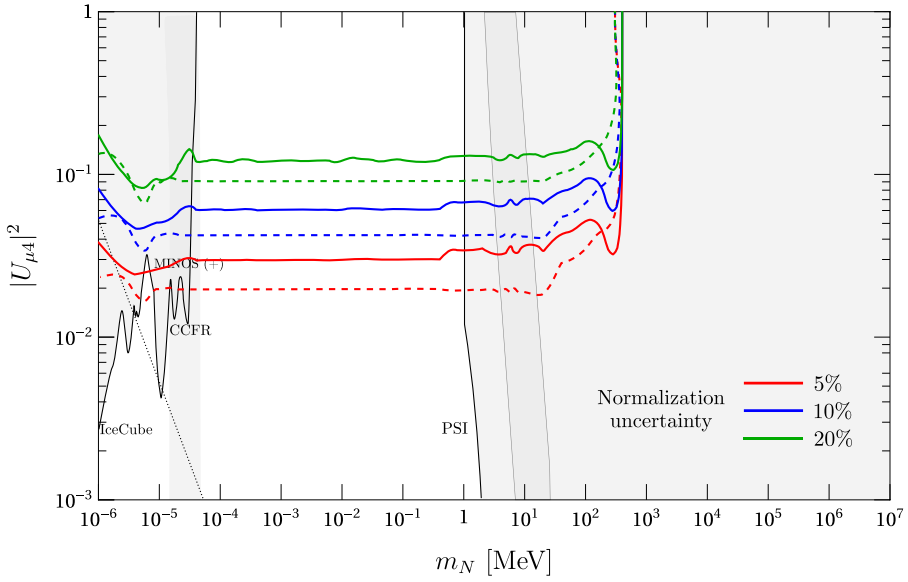

FIGURE 12
Comparison between on-axis (dashed) and 30 m off-axis (solid) estimated sensitivities of DUNE to $|U_{\mu 4}|^2$ at the 90% confidence level by neutrino CC event disappearance for 10 years of operation (five in neutrino and five in antineutrino modes). The regions of experimental constraints were taken from [29, 32, 33].

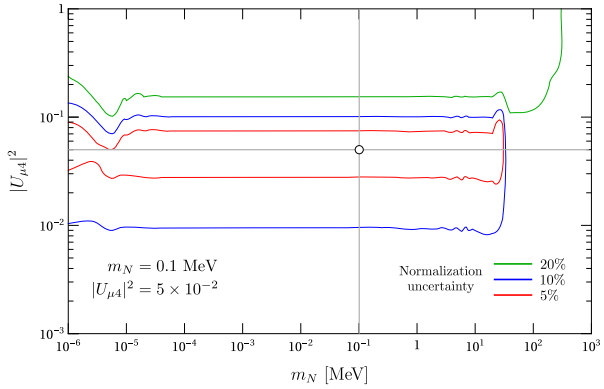

FIGURE 13
Regions having 95% confidence level for m_N = 0.1 MeV, $|U_{\mu 4}|^2 = 5 \times 10^{-2}$, 10 years of operation (five in neutrino and five in antineutrino modes), on-axis position, and several values of σ_a.

sensitive to m_N for low masses. For the case $\sigma_a = 0.05$ (red), the 95% confidence region is sufficiently small that it is possible to constraint $|U_{\mu 4}|^2$ within an uncertainty of 50%. However, when we include larger systematic uncertainties such as $\sigma_a = 0.1$ (blue), we found that we can only constrain the value of $|U_{\mu 4}|^2$ within an uncertainty of 100%.

6 Conclusion

The cornerstone of this work is the analysis of other ways in which the active neutrino flux at DUNE is affected by the production of HNLs besides neutrino oscillations. We found that, in the presence of HLNs, the production rates of active neutrinos decrease and their angular distributions widen, which translates into a decrease in the number of ν_μ and ν_e CC events in the LArTPC of the DUNEND. This neutrino disappearance represents an indirect signal of HNLs at DUNE that is not due to neutrino oscillations but rather to the kinematics of the meson and HNL decays. When combined with the effects of neutrino oscillations, it is possible to use this deficit in CC event rates to estimate limits of $|U_{e4}|^2$ and $|U_{\mu 4}|^2$. We found that these limits are very sensitive to the uncertainty of the neutrino flux prediction at the DUNEND. In order to get conservative estimates of these limits, we considered overall normalization uncertainties of up to 20%.

For 5 year per mode (neutrino/antineutrino), on-axis configuration, and a 5% overall normalization uncertainty, we obtain limits of $|U_{\mu 4}|^2 < 2 \times 10^{-2}$ and $|U_{e4}|^2 < 1.5 \times 10^{-2}$ below 1.5 MeV. We also included a more pessimistic scenario of a 20% systematic uncertainty and were still able to set bounds of $|U_{\mu 4}|^2 < 8.5 \times 10^{-2}$ and $|U_{e4}|^2 < 6.5 \times 10^{-2}$ below 1.4 MeV. These limits are better than the limits predicted by DUNE direct searches or even placed in mass regions inaccessible to them. These bounds are still competitive for the off-axis configuration. In addition, we explore the capacity of determining the allowed parameter space region (m_N, $|U_{\alpha 4}|^2$) for the specific parameter values $m_N = 0.1$ MeV and $|U_{\mu 4}|^2 = 5 \times 10^{-2}$ and found that although there is a large degeneracy in the value of m_N, it is possible to constrain $|U_{\mu 4}|^2$ with uncertainties in the order of 50 (100)% for a 5 (10)% overall normalization uncertainty in the CC event rates. Finally, it is worth noting that the disappearance of CC events as an HNL signature is complementary to the direct observation or HNL decays, showing an attractive potential to be used in neutrino ear detectors with high ν CC event rates.

Data availability statement

Publicly available datasets were analyzed in this study. These data can be found at: https://glaucus.crc.nd.edu/DUNEFluxes/.

Author contributions

SC: conceptualization, data curation, formal analysis, funding acquisition, investigation, methodology, project administration, resources, software, supervision, validation, visualization, writing–original draft, and writing–review and editing. AG: conceptualization, data curation, formal analysis, funding acquisition, investigation, methodology, project administration, resources, software, supervision, validation, visualization, writing–original draft, and writing–review and editing.

Funding

The authors declare that financial support was received for the research, authorship, and/or publication of this article. AG acknowledges funding by the Dirección de Gestión de la Investigación at PUCP, through grant nos DGI-2017-3-0019 and DGI 2019-3-0044. SC acknowledges CONCYTEC for the graduate fellowship under Grant No. 236-2015-FONDECYT.

Acknowledgments

The authors also want to thank Zarko Pavlovic for useful remarks regarding the interpretation of the BIWG data, Margot Delgado de la Flor for her help at the initial stages of this work, and R. E. Shrock, C. Argüelles, I. Shoemaker, A. de Roeck, O. Peres, and W. Rodejohann for their useful remarks on our first manuscript.

Conflict of interest

The authors declare that the research was conducted in the absence of any commercial or financial relationships that could be construed as a potential conflict of interest.

Publisher's note

References

1. Drewes M. The phenomenology of right handed neutrinos. *Int J Mod Phys E* (2013) 22:1330019. doi:10.1142/s0218301313300191

2. Atre A, Han T, Pascoli S, Zhang B. The search for heavy Majorana neutrinos. *JHEP* (2009) 05(030). doi:10.1088/1126-6708/2009/05/030

3. King SF Neutrino mass models. *Rept Prog Phys* (2004) 67:107–57. doi:10.1088/0034-4885/67/2/r01

4. Drewes M, Agostini M, Ky NA, Araki T, Archidiacono M, Bahr M, et al. A white paper on keV sterile neutrino dark matter. *JCAP* (2017) 2017:025. doi:10.1088/1475-7516/2017/01/025

5. Davidson S, Nardi E, Nir Y. Leptogenesis. *Phys Rept* (2008) 466:105–77. doi:10.1016/j.physrep.2008.06.002

6. Abazajian KN, Acero MA, Agarwalla SK, Albright CH, Antusch S, Balantekin AB, et al. Light sterile neutrinos: a white paper. *High Energ Phys - Phenomenology* (2012) 4. doi:10.48550/arXiv.1204.5379

7. Berryman JM, de Gouvea A, Fox PJ, Kayser BJ, Kelly KJ, Raaf JL. Searches for decays of new particles in the DUNE multi-purpose near detector. *JHEP* (2020) 02:174. doi:10.1007/jhep02(2020)174

8. Shrock RE. New tests for, and bounds on, neutrino masses and lepton mixing. *Phys Lett B* (1980) 96:159–64. doi:10.1016/0370-2693(80)90235-x

9. Shrock RE. General theory of weak processes involving neutrinos. I. Leptonic pseudoscalar-meson decays, with associated tests for, and bounds on, neutrino masses and lepton mixing. *Phys Rev D* (1981) 24:1232–74. doi:10.1103/physrevd.24.1232

10. Aguilar-Arevalo A, Aoki M, Blecher M, Britton D, vom Bruch D, Bryman D, et al. Search for heavy neutrinos in $\pi \rightarrow \mu\nu$ decay. *Phys Lett B* (2019) 798:134980. doi:10.1016/j.physletb.2019.134980

11. Artamonov. Search for heavy neutrinos in $K^+ \rightarrow \mu^+\nu_H$ decays. *Phys Rev D* (2015) 91:052001. doi:10.1103/PhysRevD.91.052001

12. Abi B, et al. Deep underground neutrino experiment (DUNE), far detector technical design report, volume I introduction to DUNE. *JINST* (2020) 15(08):T08008. doi:10.1088/1748-0221/15/08/T08008

13. Abi B, et al. Deep underground neutrino experiment (DUNE), far detector technical design report. *Vol. II DUNE Phys.* (2020) 2. doi:10.48550/arXiv.2002.03005

14. Giganti C, Lavignac S, Zito M. Neutrino oscillations: the rise of the PMNS paradigm. *Prog Part Nucl Phys* (2018) 98:1–54. doi:10.1016/j.ppnp.2017.10.001

15. Gronau M, Leung CN, Rosner JL Extending limits on neutral heavy leptons. *Phys Rev D* (1984) 29:2539–58. doi:10.1103/physrevd.29.2539

16. Bondarenko K, Boyarsky A, Gorbunov D, Ruchayskiy O. Phenomenology of GeV-scale heavy neutral leptons. *JHEP* (2018) 11:032. doi:10.1007/jhep11(2018)032

17. Richman JD, Burchat PR Leptonic and semileptonic decays of charm and bottom hadrons. *Rev Mod Phys* (1995) 67:893–976. doi:10.1103/revmodphys.67.893

18. Ballett P, Boschi T, Pascoli S. Heavy neutral leptons from low-scale seesaws at the DUNE near detector. *JHEP* (2020) 03:111. doi:10.1007/jhep03(2020)111

19. Abada A, Bečirević D, Sumensari O, Weiland C, Zukanovich Funchal R Sterile neutrinos facing kaon physics experiments. *Phys Rev D* (2017) 95(7):075023. doi:10.1103/physrevd.95.075023

20. Kayser B, Shrock RE Distinguishing between Dirac and Majorana neutrinos in neutral current reactions. *Phys Lett B* (1982) 112:137–42. doi:10.1016/0370-2693(82)90314-8

21. Adam AA, Kordosky M, On behalf of the Dune Collaboration . Deep underground neutrino experiment (DUNE) near detector conceptual design report. *Instruments* (2021) 5(4):31. doi:10.3390/instruments5040031

22. *DUNE Collaboration. Home* (2021). Available from: https://glaucus.crc.nd.edu/DUNEFluxes/.

23. Agostinelli S, Allison J, Amako K, Apostolakis J, Araujo H, Arce P, et al. GEANT4–a simulation toolkit. *Nucl Instrum Meth A* (2003) 506:250–303. doi:10.1016/s0168-9002(03)01368-8

24. Allison J, Amako K, Apostolakis J, Arce P, Asai M, Aso T, et al. Recent developments in Geant4. *Nucl Instrum Meth A* (2016) 835:186–225. doi:10.1016/j.nima.2016.06.125

25. Ferrari A, Paola R. Sala, Alberto fasso, and johannes ranft. FLUKA: a multi-particle transport code. *Program version 2005* (2005) 10. doi:10.5170/CERN-2005-010

26. Böhlen TT, Cerutti F, Chin MPW, Fassò A, Ferrari A, Ortega PG, et al. The FLUKA code: developments and challenges for high energy and medical

applications. *Nucl Data Sheets* (2014) 120:211–4. doi:10.1016/j.nds.2014.07.049

27. Sjöstrand T, Ask S, Christiansen JR, Corke R, Desai N, Ilten P, et al. An introduction to PYTHIA 8.2. *Comput Phys Commun* (2015) 191:159–77. doi:10.1016/j.cpc.2015.01.024

28. Abi B, Acciarri R, Acero MA, Adamov G, Adams D, Adinolfi M, et al. Experiment simulation configurations approximating DUNE TDR. *High Energ Phys - Exp* (2021) 3. doi:10.48550/arXiv.2103.04797

29. Bolton PD, Deppisch FF, Bhupal Dev PS Neutrinoless double beta decay versus other probes of heavy sterile neutrinos. *JHEP* (2020) 03:170. doi:10.1007/jhep03(2020)170

30. Andreopoulos C, Bell A, Bhattacharya D, Cavanna F, Dobson J, Dytman S, et al. The GENIE neutrino Monte Carlo generator. *Nucl Instrum Meth A* (2010) 614:87–104. doi:10.1016/j.nima.2009.12.009

31. Bischer I, Werner R. General neutrino interactions at the DUNE near detector. *Phys Rev D* (2019) 99(3):036006. doi:10.1103/physrevd.99.036006

32. Bryman DA, Shrock R Improved constraints on sterile neutrinos in the MeV to GeV mass range. *Phys Rev D* (2019) 100(5):053006. doi:10.1103/physrevd.100.053006

33. Argüelles CA, Foppiani N, Hostert M. Heavy neutral leptons below the kaon mass at hodoscopic neutrino detectors. *Phys Rev D* (2022) 105(9):095006. doi:10.1103/physrevd.105.095006

frontiers | Frontiers in Physics

TYPE Original Research
PUBLISHED 10 June 2024
DOI 10.3389/fphy.2024.1362209

OPEN ACCESS

EDITED BY
Aldo Ianni,
Gran Sasso National Laboratory (INFN), Italy

REVIEWED BY
Manish Sharma,
Pacific Northwest National Laboratory (DOE), United States
Hiroyasu Ejiri,
Osaka University, Japan

*CORRESPONDENCE
O. Gileva,
gilevaolga@ibs.re.kr
E. K. Lee,
freshblue@ibs.re.kr
D. S. Leonard,
dleonard_at_ibs.re.kr

RECEIVED 27 December 2023
ACCEPTED 18 March 2024
PUBLISHED 10 June 2024

CITATION
Agrawal A, Alenkov VV, Aryal P, Bae H, Beyer J, Bhandari B, Boiko RS, Boonin K, Buzanov O, Byeon CR, Chanthima N, Cheoun MK, Choe JS, Choi S, Choudhury S, Chung JS, Danevich FA, Djamal M, Drung D, Enss C, Fleischmann A, Gangapshev AM, Gastaldo L, Gavrilyuk YM, Gezhaev AM, Gileva O, Grigorieva VD, Gurentsov VI, Ha C, Ha DH, Ha EJ, Hwang DH, Jeon EJ, Jeon JA, Jo HS, Kaewkhao J, Kang CS, Kang WG, Kazalov VV, Kempf S, Khan A, Khan S, Kim DY, Kim GW, Kim HB, Kim HJ, Kim HJ, Kim HL, Kim HS, Kim MB, Kim SC, Kim SK, Kim SR, Kim WT, Kim YD, Kim YH, Kirdsiri K, Ko YJ, Kobychev VV, Kornoukhov V, Kuzminov VV, Kwon DH, Lee CH, Lee DY, Lee EK, Lee HJ, Lee HS, Lee J, Lee JY, Lee KB, Lee MH, Lee MK, Lee SW, Lee YC, Leonard DS, Lim HS, Mailyan B, Makarov EP, Nyanda P, Oh Y, Olsen SL, Panasenko SI, Park HK, Park HS, Park KS, Park SY, Polischuk OG, Prihtiadi H, Ra S, Ratkevich SS, Rooh G, Sari MB, Seo J, Seo KM, Sharma B, Shin KA, Shlegel VN, Siyeon K, So J, Sokur NV, Son JK, Song JW, Srisittipokakun N, Tretyak VI, Wirawan R, Woo KR, Yeon HJ, Yoon YS and Yue Q (2024), Radioassay of the materials for AMoRE-II experiment.
Front. Phys. 12:1362209.
doi: 10.3389/fphy.2024.1362209

Radioassay of the materials for AMoRE-II experiment

A. Agrawal, V. V. Alenkov, P. Aryal, H. Bae, J. Beyer, B. Bhandari, R. S. Boiko, K. Boonin, O. Buzanov, C. R. Byeon, N. Chanthima, M. K. Cheoun, J. S. Choe, S. Choi, S. Choudhury, J. S. Chung, F. A. Danevich, M. Djamal, D. Drung, C. Enss, A. Fleischmann, A. M. Gangapshev, L. Gastaldo, Y. M. Gavrilyuk, A. M. Gezhaev, O. Gileva *, V. D. Grigorieva, V. I. Gurentsov, C. Ha, D. H. Ha, E. J. Ha, D. H. Hwang, E. J. Jeon, J. A. Jeon, H. S. Jo, J. Kaewkhao, C. S. Kang, W. G. Kang, V. V. Kazalov, S. Kempf, A. Khan, S. Khan, D. Y. Kim, G. W. Kim, H. B. Kim, H. J. Kim, H. J. Kim, H. L. Kim, H. S. Kim, M. B. Kim, S. C. Kim, S. K. Kim, S. R. Kim, W. T. Kim, Y. D. Kim, Y. H. Kim, K. Kirdsiri, Y. J. Ko, V. V. Kobychev, V. Kornoukhov, V. V. Kuzminov, D. H. Kwon, C. H. Lee, D. Y. Lee, E. K. Lee *, H. J. Lee, H. S. Lee, J. Lee, J. Y. Lee, K. B. Lee, M. H. Lee, M. K. Lee, S. W. Lee, Y. C. Lee, D. S. Leonard *, H. S. Lim, B. Mailyan, E. P. Makarov, P. Nyanda, Y. Oh, S. L. Olsen, S. I. Panasenko, H. K. Park, H. S. Park, K. S. Park, S. Y. Park, O. G. Polischuk, H. Prihtiadi, S. Ra, S. S. Ratkevich, G. Rooh, M. B. Sari, J. Seo, K. M. Seo, B. Sharma, K. A. Shin, V. N. Shlegel, K. Siyeon, J. So, N. V. Sokur, J. K. Son, J. W. Song, N. Srisittipokakun, V. I. Tretyak, R. Wirawan, K. R. Woo, H. J. Yeon, Y. S. Yoon and Q. Yue

AMoRE Collaboration

The AMoRE-II experiment will search for the $0\nu\beta\beta$ decay of ^{100}Mo nuclei using molybdate crystal scintillators, operating at milli-Kelvin (mK) temperatures, with a total of 80 kg of ^{100}Mo. The background goal for the experiment is 10^{-4} counts/keV/kg/year in the region of interest around the $0\nu\beta\beta$ decay Q-value of 3,034 keV. To achieve this level, the rate of background signals arising from emissions produced by decays of radioactive impurities in the detector and shielding materials must be strictly controlled. To do this, concentrations of such impurities are measured and are controlled through materials selection and purification. In this paper, we describe the design and the construction materials used to build the AMoRE-II detector and shielding system, including

active and passive shielding, the cryostat, and the detector holders and instrumentation, and we report on measurements of radioactive impurities within candidate and selected materials.

KEYWORDS

double beta decay, radiopurity, radioassay, ICP-MS, HPGe

1 Introduction

Over the past few decades, results from experiments with solar, atmospheric, and reactor neutrinos have provided evidence about neutrino mixing angles, mass eigenvalues, and oscillations. However, major properties such as neutrino's absolute mass scale, hierarchy, and nature (Dirac or Majorana) still remain unknown.

An observation of the neutrinoless double beta ($0\nu\beta\beta$) decay is the only practical way to determine the nature of the neutrinos (Majorana or Dirac particle) [1] and to check the lepton number conservation [2, 3]. Since Wendell Furry [4] suggested searching for the $0\nu\beta\beta$ process almost 80 years ago, we do not yet have any direct evidence for the occurrence of this process. The AMoRE experiment aims to search for the $0\nu\beta\beta$ decay of ^{100}Mo nuclei using molybdate crystal scintillators operating at milli-Kelvin (mK) temperatures. The Q-value of ^{100}Mo double-beta decay has been reported to be 3,034.40 ± 0.17 keV [5]. The experiment aims to achieve zero-background measurements. In other words, the expected number of background events in the region of interest (ROI, 3,034 ± 7 keV) should be much less than one for the planned 5 year duration of the experiment. Our previous AMoRE-I [6] study using $^{48\text{depl}}Ca^{100}MoO_4$ crystals reported a background rate of about 0.03 counts/keV/kg/year (ckky) in the ROI [7, 8], normalized to crystal mass. The AMoRE-II experiment, which will have 85 kg of ^{100}Mo, targets a background rate of less than 10^{-4} ckky, which we note is the same as the CUPID target [9]. A measured full-width at half-maximum (FWHM) energy resolution of 7 keV has been achieved [10]. With an energy resolution of 10 keV and 5 years of data taking, the estimated half-life sensitivity, based on a 90% discovery potential, is 4×10^{26} years, corresponding to an effective neutrino mass in the range of 18–31 meV [8].

Background signals can arise from a number of sources, including two-neutrino double beta decay, cosmic-ray muons, environmental radon, and emissions from radioactive decays within the underground rock, the detector crystals, and all materials used in the detector assembly, support, shielding, etc. To achieve this background goal, we must measure the radioactive contaminants of all the materials to be used in the experiment and confirm that the contribution of each material is sufficiently low, satisfying the requirements of the AMoRE-II experiment. We must combine the radioactivity measurements with the Monte Carlo simulation for this confirmation. In this report, we will describe the works for the measurements of the material purity and radioactivities. The background estimation with the simulation will be reported in detail separately but does show that the targeted background rate should be achieved with the detector design and materials selection reported here.

2 Equipment and methods for radioassay

All the samples are measured with the equipment at above-ground or underground laboratories operated by the Center for Underground Physics (CUP). Above ground, we use an inductively coupled plasma mass spectrometer (ICP-MS). In the underground labs, we use three high-purity germanium (HPGe) detectors and one alpha counter. Here, we describe the equipment and related assay methods in detail. For all measurements, limits are reported if the signal is less than three times the statistical error, σ, and positive values are reported otherwise. For positive values, errors are reported with 1 σ statistical errors combined with any systematic error, typically a multiplicative calibration or efficiency error. For this reason, positive results can appear, as reported, to be less than 3 σ, but are still statistically inconsistent with zero at the 3 σ level. Limits at 90% C.L. are reported as the greater of zero or the central value plus 1.64 σ.

2.1 Direct counting

The concern for radioactive contaminants in detector materials is from detector signals (backgrounds for a double beta decay experiment) generated by radioactivity, including gamma rays and alphas, emitted from the radioactive decays. The most direct way to measure these is to detect such emissions with a sensitive detector. High-purity germanium detectors are the most standard choice for observing long-ranged gamma emissions, especially owing to their high efficiencies, good resolutions, and, as the name implies, high purity. In particular, HPGe detectors measure gamma emissions from decays in the ^{40}K, ^{238}U, and ^{232}Th decay chains. In this work, we generally report measured results as the activities of the long-lived isotopes that support gamma-emitting sub-chains. Particularly, ^{214}Pb and ^{214}Bi peak rates are used to derive the ^{226}Ra activities in the ^{238}U chain, and ^{208}Tl and ^{212}Pb are used to derive the ^{228}Th activity in the ^{232}Th chain. ^{228}Ac activities are equivalent to ^{228}Ra activities but are reported here as ^{228}Ac since it is the only gamma-emitting decay in that sub-chain. For all HPGe analyses, gamma detection efficiencies are determined using GEANT4-based Monte Carlo simulation of whole decay chains for decays distributed uniformly within the samples. For HPGe assay of high-density samples such as lead, copper, solder, tin, stainless steel, and neutron shielding materials, a systematic error was included for potential background reduction from shielding effects of the sample as previously presented in Ref. [11] and using a similar method to the one described in Ref. [12]. An example of the general procedure used is described in more detail in Section 3.4.

Alpha counters of various types can also be used to measure alpha emissions directly from the surface layers of materials.

2.1.1 Single coaxial HPGe detectors

For general-purpose screening, we maintain two 100% HPGe detectors in the Yangyang Underground Laboratory (Y2L). Both are single-element p-type coaxial detectors produced by CANBERRA Industries, each having separate shielding configurations. CANCOAX1 (CC1) is configured with 5 cm thick ancient lead as its innermost shielding layer surrounded consecutively by 10 cm-thick copper, again encased in, at minimum, 15 cm-thick general-purpose lead on all sides. Likewise, CANCOAX2 (CC2) is shielded, from inside to out, by a layer of 10 cm thick copper, followed by 5 cm of lead produced by the J. L. Goslar company, and a further 15 cm of generically sourced lead. To reduce Rn contamination by air while changing samples, an acrylic box was installed to enclose the shielding. Both detector chambers are flushed with nitrogen gas from liquid-nitrogen boil-off to purge Rn gas from the sample space. CC1 has a background rate of 8.2 mHz in the range of 50–4,000 keV. Without the acrylic box, the CC2 detector had a slightly higher overall background level of 10 mHz shortly after installation. After construction of the box and implementation of nitrogen flushing, the CC2 background rate dropped to 6.1 mHz. The sensitivities of the two detectors are still reasonably comparable, with background rates in the peaks of interest for ^{40}K decays and for the ^{232}Th and ^{238}U decay chains being at or below a few counts per day, even for the most prominent peaks. Both detectors have sensitivities to ^{228}Th and ^{226}Ra of about 1 mBq/kg for samples on the scale of about a kilogram with counting times of roughly 2 weeks. Similar conditions produce ^{40}K sensitivity of about 5 mBq/kg. To tune, or calibrate, the simulation efficiency, a mixed-isotope source with ten radioactive isotopes was prepared in a Marinelli beaker and measured on the detectors. Inactive Ge layer thicknesses were adjusted in the simulation geometry to match the measured and simulated efficiencies [13]. A systematic efficiency error of 7% is applied to all results from CC1 and CC2.

2.1.2 HPGe array detector

CUP operates an array of fourteen p-type coaxial HPGe detectors at Y2L. This detector system is referred to as the CAGe. The fourteen cylindrical elements are all arranged with their axes in vertical orientations. One cryostat holds seven detectors, with their coplanar ends facing upward towards an identical downward-facing set, with an adjustable gap between the two sets. This configuration allows for as much as 20 kg of sample material to be placed between the two sets of detectors, creating high detection efficiency for gamma emissions from contaminants in the samples. Further material can be placed around the detectors, with somewhat lower detection efficiency, allowing for several liters of total useful sample volume with much higher average detection efficiencies than that achievable from a single 100% relative-efficiency HPGe detector. Source-based efficiency calibration was reported in Ref. [14]. During operation, the detector array is flushed with boil-off nitrogen gas to purge background-generating radon gas from the detection volume. Some residual radon backgrounds can arise from the air inside the lead shielding doors but outside of the Vikuiti windows that enclose the sample volume. Radon backgrounds are, thus, further reduced (nearly eliminated) when radon-free air is supplied to the detector room. Details of the detector design, configuration, and performance are provided in Ref. [15].

This resource is used for physics searches and samples requiring the best detection sensitivities. Specifically, it has primarily been used to measure contaminant levels within the materials used for crystal fabrication. These measurements are the subject of other publications [16] and are thus outside of the scope of this article. We report here on other detector materials measured with the CAGe, specifically lead and copper. Measurements are reported with an included systematic efficiency error of generally about 10%.

2.1.3 α counter

Control over surface radioactivity contaminants in a material is an increasingly important topic in ultra-low radioactivity measurements. An UltraLo-1800 ionization chamber from XIA Co. has been installed at Y2L for detecting alpha particles. The size of the detector area is 1,800 cm^2 and 15 cm in height. A uniform electric field of about 70 V/cm is applied between the electrodes and the tray. The detector consists of two positively biased electrodes, called the anode and the guard, at the upper part of the chamber and a grounded sample tray at the bottom. The maximum thickness of a sample is about 8 mm, and the maximum size of the sample is about 47 cm × 47 cm. The detector is sensitive to emissivity values (ϵ) as low as 0.0001 count/cm^2/h [17]. This sensitivity is achievable at Y2L due to the low rate of cosmic-ray muon-induced background events in the deep underground lab. The detector is currently hosted in the COSINE dark-matter detector room where humidity and temperature are strictly controlled at 40% ± 3% and 25.4°C ± 0.1°C, respectively. With a dedicated Ar gas supply, a maximum length of a continuous month-long measurement is possible.

2.2 Upper-chain radioassay

The whole radioassay landscape is complicated. Two of the main background-producing decay chains occur through a sequence of many radioactive decays, starting with ^{238}U and ^{232}Th. Most background-producing radioactivity is from long-ranged gamma emissions, which are not easily shielded. These gammas are generally supported by long-lived isotopes in the decay chains, specifically ^{228}Ra and ^{228}Th in the ^{232}Th chain and by ^{226}Ra in the ^{238}U chain. However, some backgrounds are still generated by the upper-chain decays, particularly via alpha emissions from materials that face the detector material. For this reason it is still desirable to measure the ^{238}U and ^{232}Th concentrations directly to understand the complete background picture.

Furthermore, direct measurement of emissions from the gamma-emitting sub-chains is always challenging when selecting detector materials for a cutting-edge rare event experiment. By design, the background levels of interest should be barely detectable by the cutting-edge detector itself after it is built, even with years of data. As there are many construction materials to consider, counting times on assay detectors must generally be days or weeks, not years, and the detectors used for assay are often not as sensitive as the experiments themselves. This motivates alternative approaches.

In decay-chain-equilibrium, every isotope below ^{238}U and ^{232}Th decays at the same rate at which it is produced, which is the ^{238}U or ^{232}Th decay rate, respectively (otherwise, their concentrations would rise or fall until equilibrium is achieved). However, in that condition, the concentrations of the isotopes in the chain are proportional to their half-lives. Since the ^{238}U and ^{232}Th half-lives are billions of years, this would imply much higher concentrations and thus potentially easier detection relative to isotopes with shorter

half-lives lower in the chains. Chain equilibrium is established on the time scales of the long-lived isotopes that support the lower chains (1,600 years for ^{226}Ra) and is easily broken by geological or manufacturing processes. Still, using this relationship, concentrations or activities can be stated as equilibrium-equivalent concentrations of the other isotopes in the chain. If the equilibrium is assumed to be valid, measurements of the top-of-chain isotopes can result in much-enhanced sensitivity to the lower-chain concentrations. This assumption is questionable in many or most cases but has uses in some cases. The supporting isotopes of the lower ^{232}Th decay chain have half-lives of a few years, so equilibrium assumptions can be informative for some scenarios. In other cases, it is simply the best that can be done before building and testing the final detector. While the value of this approach is limited, it can be another motivation for measuring isotopes from the top of the decay chains.

While alpha emissions from the upper chain can be directly measured as with the lower chain, two approaches to measuring ^{238}U and ^{232}Th concentrations with significantly higher sensitivity are inductively coupled plasma mass spectroscopy (ICP-MS) and neutron activation analysis (NAA).

2.2.1 ICP-MS

ICP-MS involves dissolving materials and directly observing quantities of constituent isotopes via ion acceleration and detection. It provides high sensitivity to concentrations of ^{238}U and ^{232}Th using small amounts of digestible materials. Sample decomposition and ICP-MS analysis were performed at CUP in a class 1000 (ISO 6) cleanroom. Quantitative ^{238}U and ^{232}Th analyses were performed using an Agilent 7900 ICP-MS system. For the determination of Th and U, the machine's tuning and calibration were adjusted to maximum sensitivity to detect high-mass elements. The machine is equipped with a reaction cell and UHMI mode, but to avoid loss of sensitivity for ^{238}U and ^{232}Th, it was not used. For the ICP-MS analysis, samples must be reconstituted, and all analytes must be soluble. For the decomposition of the Vikuiti film sample, the Milestone PYRO microwave ashing system was employed. Copper samples were dissolved using an ODLAB heating block. Solid Phase Extraction (SPE) was performed with 2 mL of UTEVA®resin (50–100 μm) cartridges (Eichrom) for copper samples. The recovery yield of the extraction procedure was controlled by the addition of standard solutions with known Th and U concentrations.

2.2.2 NAA

Neutron activation analysis (NAA) uses incident neutrons to produce short-lived radioactive isotopes from more-stable isotopes of interest, thus allowing efficient detection with radiation detectors, HPGe detectors in particular. Like ICP-MS, it has high sensitivity to ^{238}U and ^{232}Th, and similarly requires relatively small sample sizes. It is particularly suitable for plastics which may be difficult to dissolve for ICP-MS. NAA is done at a research reactor facility, HANARO, in Daejeon city in Korea. The reactor has a maximum thermal power of 30 MW. The thermal neutron flux depends on the location of the irradiation hole. A dedicated hole, PTS #2, was used for this work. At full power, this location has a thermal neutron flux of about 3.5×10^{13} neutrons/cm^2/s. However, for the activations presented in this work, the reactor was operated at 15 MW, implying a flux of half of that value. We have measured samples of Teflon and PEEK using this facility.

3 Materials of the detector assembly

Figure 1 shows the schematic of a detector module. It consists of a crystal and a silicone wafer for light detection. The copper holder houses the crystals and the wafer with two MMC-SQUID sensors [18]. A module has many components that should have high radiopurity to satisfy the requirements of the AMoRE-II experiment. Here we describe radiopurity measurements of materials used within the detector assembly. Results are summarized in Tables 1, 2.

3.1 Molybdate crystals

The AMoRE-II experiment uses two types of scintillating crystals, $CaMoO_4$ and Li_2MoO_4. The internal contamination of the $CaMoO_4$ crystals is characterized by the AMoRE-Pilot and AMoRE-I detectors [19, 20]. Before growing the Li_2MoO_4 crystals, precursor materials (molybdenum trioxide and lithium carbonate powders) are tested to confirm the AMoRE-II purity requirements for precursors [16, 21]. The bulk contamination levels for ingots grown using preliminary purified and non-purified precursors are shown in Table 1. The internal contamination of all the enriched Li_2MoO_4 crystals grown from 2020 to 2023 by CUP and NIIC has been measured by ICP-MS to monitor the crystal production routine. For each crystal, about 1 g of sample is cut from the upper and bottom of the ingot after cutting the crystals and assayed with ICP-MS. For all recently tested 200 crystals, ^{238}U and ^{232}Th are found to be less than 10 pg/g.

3.2 Crystal surface treatment

After cutting the crystals from the original ingots, the crystal surfaces are lapped and polished. The SiO_2 abrasive powder is selected as the cleanest material for surface conditioning. The Admatechs SO-E (low-alpha beam grade) type powder is used. Powders with 8 μm and 1.5 μm particle sizes are used for lapping and final polishing of the crystal surface, respectively. Since lithium molybdate is highly hygroscopic, protection measures are required to save the crystal surface from moisture damage. The Lubriplate low-viscosity non-detergent mineral oil is selected as a lubricant to protect the crystal surfaces from moisture and smooth the polishing. The Ciegal 7355-000FE polyurethane polishing pads are used for buffing at the final polishing step.

3.3 Copper holder

We measured NOSV and OFE copper from Aurubis company in Germany and OFE copper from Mitsubishi company in Japan. Bulk contamination of the copper was studied and reported in Ref. [22]. For convenience, results are presented here in Table 2. Samples of about 1 cm^3 were cut from the initially received stock plates. The cubic samples were etched twice in strong nitric acid with sonication to remove the contaminated surface. Cleaned samples were reconstituted within strong nitric acid, and Th and U were extracted with a 2 mL UTEVA resin cartridge. The extraction efficiency was controlled by analyzing a sample spiked with a

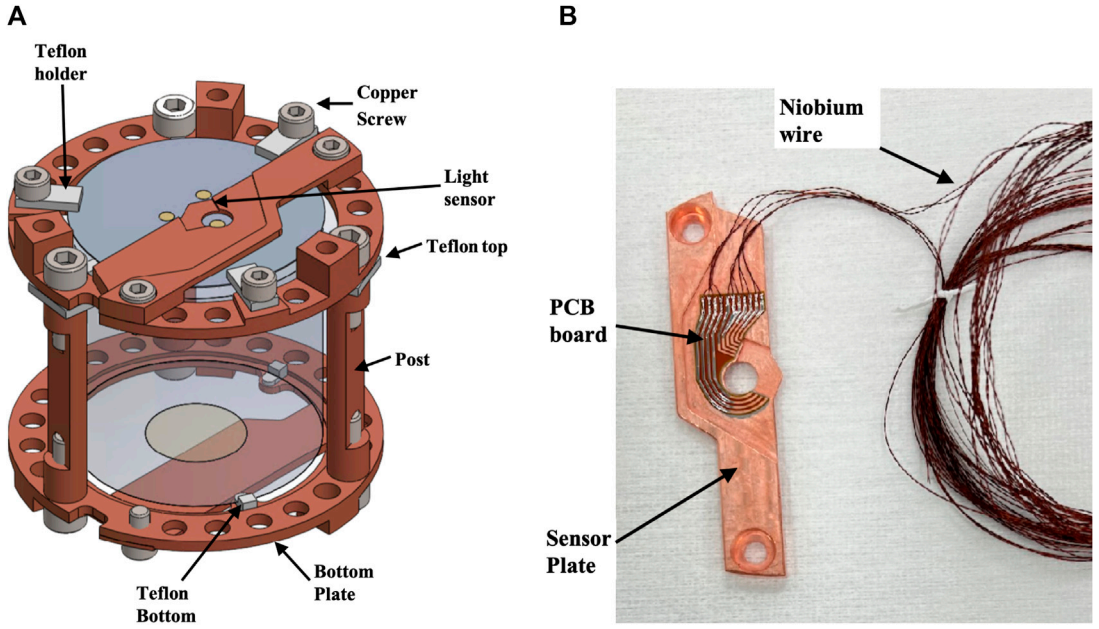

FIGURE 1
A schematic figure of a detector module **(A)** and a photo of a real detector sensor plate **(B)** of the AMoRE-II experiment. Crystals are used with diameters of both 5 and 6 cm, with module dimensions adjusted accordingly.

known amount of Th and U standard solution. Bulk contamination levels of ^{232}Th and ^{238}U in the NOSV-Cu stock plate purchased in 2014 were found to be unacceptable for AMoRE-II, while levels in the plates purchased later in 2018 and 2021 were found to be suitable use as crystal holder material. Holder units, except for the screws, were machined from the original copper plates of NOSV-Cu purchased in 2018 and 2021. The screws were machined from the 2018 OFE-Cu. Each holder unit was degreased with kerosene and ethanol, and then a surface layer of about 1 μm was removed by etching with sonication in 5% nitric acid solution. The etched surface of the copper units was passivized and rinsed with deionized water.

After the surface etching procedure, the sensor plates, posts, and screws were measured with ICP-MS. Metal from the bodies of the pieces was digested in nitric acid and moved to the extraction procedure. Analysis of the sensor plates with simple flat surfaces showed efficient Th and U removal with this cleaning procedure. Each post has two screw threads, which, due to the machining process, may have more deeply-embedded contamination. The screws, like the posts, could not be etched deeper than 1 μm without compromising their functional integrity. The screws, which were made of OFE-Cu, showed about 10 pg/g of ^{232}Th and 2 pg/g of ^{238}U, while the bulk concentration of the stock OFE-Cu was about 1 pg/g for both.

3.4 HPGe constraints on radioactivities in copper

While ICP-MS proved suitable levels for ^{232}Th and ^{238}U, proving sufficiently low levels of ^{226}Ra and ^{228}Th is a different challenge. To this end, we prepared a large sample of the 2014 NOSV copper reported in Ref. [22] to be counted on the CAGe array detector. The total sample mass was 145 kg, prepared as eleven plates, each 2 cm thick, with one 30 cm × 30 cm plate placed horizontally between the array halves, and the others (19.6 cm × 35 cm and 19.6 cm × 38 cm) placed on edge around the four sides of the detector elements. Before installation, the plates were all cleaned by scrubbing with Alconox, by a weak nitric, etch, and finally by rinsing in DI water. A supporter was designed to fill the space around the bottom array cryostat, thus supporting the outer copper plates at a height level with the bases of the cans housing the lower array detector elements. The supporter was machined from low-activity cast acrylic and made in four parts for assembly around the detector. Figure 2 shows the arrangement of the copper in the CAGe detector chamber with the acrylic supporter. The sample was counted for about 83 days with Rn-free air supplied to the room. Background data was taken in a similar condition for about 32 days with the supporter in place but with the sample removed.

For large samples, on any of the HPGe detectors, we often simulate potential background shielding of the sample [11, 12] and use the difference between the full background and the potentially shielded background as a systematic error. To be specific, backgrounds originating from sources near to or within the detector will not be shielded by the sample, while backgrounds originating from sources blocked by the sample could be significantly shielded. Since we do not know the distribution of background sources, this represents a systematic error. The simulation allows optional selection of a sample, as well as one of any pre-defined volumes for generating background decays, both as run-time configurations to the program. A batch submission script runs simulation jobs for events in the sample, in the background generation volume with the sample in place, and in the background generation volume without the sample, for any selected isotopes. A

TABLE 1 HPGe assay results for internal materials.

Item	Material	Supplier	^{226}Ra (mBq/kg)	^{228}Ac (mBq/kg)	^{228}Th (mBq/kg)	^{40}K (mBq/kg)	Detector
Crystal	Natural CMO (1902)[a]	CUP	56 (4)	< 5.5	< 5.3	< 39	CC1
	Enriched CMO (SE#3)[b]	CUP	< 2.0	< 3.2	< 1.6	< 3.2	CC2
	Natural LMO (1602)[a]	CUP	< 3.3	< 2.6	< 1.5	29 (9)	CC1
	Natural LMO (1801)[b]	CUP	< 1.2	< 3.2	< 1.3	< 14	CC1
	Enriched LMO (1901)[c]	CUP	< 1.5	< 5.7	< 3.4	< 14	CC2
	Enriched LMO (2005)[b]	CUP	< 3.5	< 4.1	< 3.6	< 14	CC2
Crystal surface	SiO_2 8 μm	Admatechs	3.5 (6)	< 3.1	1.4 (4)	108 (10)	CC1
	SiO_2 1.5 μm	Admatechs	< 1.7	< 2.3	< 0.90	< 16	CC2
	Diamond, 1 μm	Saint-Gobain	8.2 (12)	64 (5)	54 (3)	34 (7)	CC2
	SiC, 1 μm	Saint-Gobain	193 (10)	95(6)	101 (6)	100 (12)	CC2
	SiC, 3 μm	Saint-Gobain	176 (10)	350 (20)	365 (20)	220 (23)	CC2
	Mineral oil	LUBRIPLATE	< 0.81	< 1.8	< 0.69	< 7.9	CC1
	Polishing pad	Ciegal	< 8.5	< 13	14 (3)	290 (50)	CC1
	Polishing pad	Chem. pol.	840 (45)	55 (10)	71 (7)	480 (60)	CC1
	Gold (4N)	TAEWON	< 5.9	< 6.0	< 11	< 33	CC1
Cu holder	NOSV Cu[d]	Aurubis (2014)	< 0.087	< 0.068	< 0.075	< 1.8	CAGe
	NOSV Cu	Aurubis (2016)	< 0.67	< 0.80	< 0.65	< 3.5	CC1
	Cu post	Aurubis (2021)	< 0.49	< 1.4	< 1.0	< 6.0	CC2
	M3 Brass screws	SANCO	< 0.15	< 0.57	< 0.37	< 2.8	CC2
Reflector	Vikuiti film	3M	0.59 (18)	< 0.93	< 0.64	9.4 (24)	CC1
Sensor assembly	Superconducting wire	Supercon Inc.	< 4.2	< 6.2	< 4.1	< 170	CC1
	Polyimide PCB, HGLS-D211EM	Hanwha L&C	< 1.1	< 1.3	< 1.1	< 12	CC1
	Pb/Sn solder (2021)	KNU	< 0.88	< 1.2	< 2.2	< 12	CC2
	Pb/Sn solder (2023)	KNU	< 0.56	< 1.1	< 0.83	< 4.1	CC1
	Tin (5N)	Alfa Aesar	1.38 (16)	0.75 (17)	< 0.47	5.1 (8)	CC1
	Tin (6N)	Alfa Aesar	< 0.32	0.83 (24)	< 0.81	< 5.2	CC1
	Stycast 2850	Emerson & Cuming	440 (45)	600 (50)	600 (50)	400 (120)	CC1
	Stycast 1266 resin	Loctite	< 1.1	< 4.2	< 1.2	< 9.9	CC1
	Stycast 1266 hardener	Loctite	< 11	< 12	< 3.1	< 36	CC1
	Solder paste (UP78)	ALPHA	< 2.7	< 3.2	< 1.6	< 29	CC1
	Solder paste	G.F. Thompson Co.	19.4 (12)	7.9 (13)	5.7 (6)	650 (40)	CC2
	Si light detector wafer	IEMT	< 4.1	< 3.2	< 2.0	< 23	CC1
Heater	Araldite AW 106 CI	Huntsman	1.7 (4)	< 1.7	< 1.0	11 (4)	CC2
	Hardener, HV 953 U CI	Huntsman	2.8 (6)	< 2.2	< 1.2	< 8.9	CC2
	Si heat detector wafer	Microchemicals	< 2.0	< 3.0	< 2.0	< 18	CC1

[a]Raw materials were not purified.
[b]Raw materials were purified.
[c]Only $^{100}MoO_3$ was purified.
[d]See Section 3.4 for other reported activities.

TABLE 2 Concentrations of ^{238}U and ^{232}Th in the internal materials, determined by ICP-MS analysis, or by NAA where indicated.

Item	Material	Supplier	^{238}U (pg/g)	^{232}Th (pg/g)
Reflector	Vikuiti film [22]	3M	< 3.6	< 4.5
Holder	NOSV copper bulk [22]	Aurubis (2014)	1.6 (7)	5.1 (12)
	NOSV-Cu bulk [22]	Aurubis (2016)	0.29 (14)	0.34 (12)
	NOSV-Cu bulk [22]	Aurubis (2021)	0.33 (12)	0.26 (11)
	NOSV-Cu sensor plate[a]	Aurubis (2021)	0.45 (12)	0.33 (12)
	NOSV-Cu post	Aurubis (2021)	0.79 (30)	3.1 (13)
	NOSV-Cu holder (top & bottom)	Aurubis (2021)	0.32 (14)	0.53 (21)
	PTFE, Eriflon plates	Maagtechnic	< 100[b]	< 200[b]
Screw	OFE-Cu bulk [22]	Aurubis (2018)	1.01 (15)	0.98 (10)
	OFE-Cu bulk [22]	Aurubis (2021)	0.83 (11)	0.98 (14)
	OFE-Cu screw machined	Aurubis	1.8 (5)	10.7 (12)
	Brass screw machined	Sanco	0.49 (12)	1.43 (13)
PCB board	Polyimide-based, HGLS-D211EM	Hanwha L&C	890 (90)	< 1.2
Soldering	Tin 6N	Alfa Aesar	< 50	< 50
	Tin 5N	Alfa Aesar	< 50	< 50

[a]etched, before mounting the sensors.
[b]Measured by NAA.

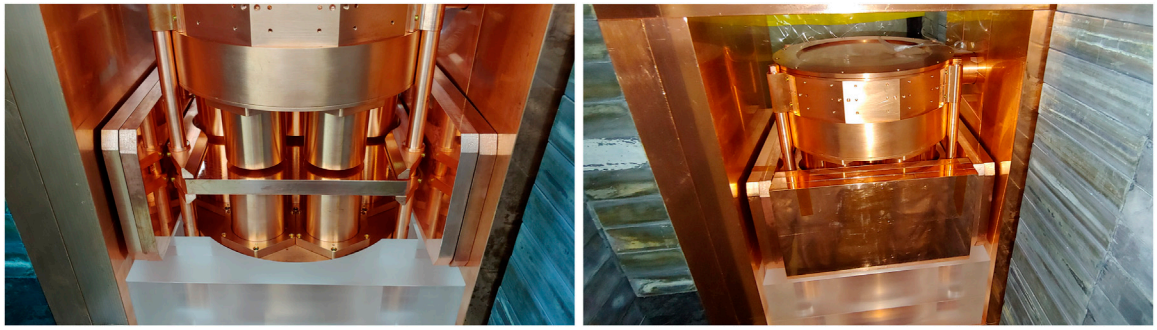

FIGURE 2
NOSV 2014 copper sample plates, 145.5 kg in total, installed in the CAGe detector chamber. In the left image, the acrylic base supporter supports four sample plates, two on each side of the detector. A central plate rests on the sample supporter blades, which support it horizontally between the upper and lower halves of the detector array. The right image shows the final three vertical plates installed on the near side, with three more out of view on the far side.

batch analysis determines detection efficiency for decays in the sample and compares background decay spectra with and without the sample to quantify the background-shielding effect of the sample. For the CAGe, we simulate background decays from the vicinity of two opposing copper shielding walls, specifically between the door shielding and the thin Vikuiti window sheets that seal the two detector openings. These volumes represent a realistic location for radon decays, and also represent a region where backgrounds are expected to be maximally shielded by the sample. In the case of the 2014 NOSV measurement, because of the unusually high density and thickness of the sample, the backgrounds from this simulation were attenuated to 20% of their un-shielded rates, or less, depending on the gamma energy. Since we do not know the true source of the backgrounds, or if they are shielded at all, we perform the analysis with full background subtraction, and again with subtraction of the attenuated background rates, treating the difference as a systematic error. For any decay sub-chain, if either scenario is consistent with zero, a 90% limit is derived from the higher result. In this case, because the potential background shielding is nearly absolute, the procedure is nearly equivalent to deriving upper limits from the sample data alone.

Peak rates from ^{228}Th, ^{228}Ac, and ^{40}K were conclusively positive but consistent with measured background levels. The ^{226}Ra rates in the sample data were slightly below the background level. Results from the analysis are shown in Table 1. However, we note that the striking similarity between the sample and background rates, particularly in the

^{40}K and ^{232}Th chains, leaves the likely possibility that the background sources are primarily internal to the detector and not shielded by the sample, such that full background subtraction would be appropriate. In particular, it was previously reported that o-rings in the detector construction contain high levels of ^{40}K [15]. A traditional background subtraction analysis, assuming no background shielding, implies stronger limits in the range of 19–26 μBq/kg for ^{228}Th, ^{228}Ac, and ^{226}Ra, and <200 μBq/kg for ^{40}K, as limited by counting statistics, close to limits for earlier production batches of NOSV copper previously reported in Refs. [23, 24]. The ^{226}Ra limits without background subtraction meet the requirements for AMoRE-II, while the ^{228}Th results are also limits, but are close to our goals only if full background subtraction is assumed.

As copper is a material of particularly general interest for low-background experiments, in addition to the tabulated results, we report limits of <44 μBq/kg for ^{235}U, <690 μBq/kg for ^{231}Pa, <32 μBq/kg for ^{227}Ac, and <330 μBq/kg for ^{234}Th. To handle interferences, particularly for ^{231}Pa and ^{223}Ra, analysis was performed using an updated version of GDFIT [25], with a coupled fit of activities to the entire spectrum, where peak rates were modelled by the fitted activities and by efficiencies, branching rations, and intensities, with constrained background contributions to each peak. In the ^{235}U chain, since the measurement was performed many months after production of the material, ^{227}Ac was assumed to be in decay equilibrium with ^{223}Ra and its daughters.

This measurement was prepared before ICP-MS measurements determined that the ^{238}U and ^{232}Th concentrations in the 2014 NOSV batch were not suitable for AMoRE. As reported in Ref. [22], the ^{232}Th levels measured in the 2021 NOSV copper used for AMoRE-II were about 17 times lower than the levels in the 2014 copper measured on the CAGe. The combination of low ^{226}Ra, ^{228}Ra, and ^{228}Th levels in the 2014 copper, and greatly reduced ^{232}Th levels in the 2021 copper give reason for optimism that the ^{228}Ra and ^{228}Th activities in the 2021 copper may be significantly below the obtained limits.

In addition to the CAGe measurement of the 2014 NOSV copper, samples of the 2016 and 2021 NOSV coppers were assayed with the CC1 and CC2 100% HPGe detector. The results for all activities in the ^{238}U, ^{232}Th, and ^{40}K chains were limits for both, although with much worse sensitivities.

3.5 PTFE

The detector crystals are cooled to low temperature via heat conduction through the copper holders to the thermal bath. However, the thermal conductivity between the crystals and the thermal bath should be low since the athermal phonons should be collected efficiently by the phonon collector. Therefore, the crystals are mechanically connected to the copper holders by small pieces of insulating PTFE. Specifically, the parts are machined from a product sold by the Maagtechnic company, listed as "ERIFLON Plastic plate PTFE pure virgin white," and sold in various thicknesses.

ICP-MS measurement of PTFE and other fluorocarbon plastics is challenging because digestion requires particularly hazardous chemicals. However, as these have been found to be very clean materials, a number of high-sensitivity measurements have been performed [26–31]. Maagtechnic PTFE was selected largely because measurements have already been performed for other rare-event experiments and reported in Refs. [27, 29]. Both references report only limits for a range of naturally occurring radioactivies, with Ref. [29] reporting less than about 63 μBq/kg or better for all of ^{226}Ra, ^{228}Ra, and ^{228}Th from direct HPGe assay and reporting corroborating limits inferred from ICP-MS measurements. At CUP, we prepared samples of the material (purchased as plates from the Eriflon product line) for measurement using neutron activation analysis (NAA). Samples were prepared as discs of 10 mm diameter by 5 mm height, machined from 15 mm stock, and cleaned along with irradiation vials via a procedure using ultrasonic cleaning and nitric acid etching. A total sample mass of 3.4 g was analyzed with NAA by the Korea Atomic Energy Research Institute using 4 h of sample irradiation at the HANARO reactor operated at a power of 15 MW. The resulting limits were <200 pg/g and <100 pg/g for ^{232}Th and ^{238}U, respectively, as tabulated in Table 2. This was the first attempt to use NAA at HANARO for sample analysis. Several factors can be optimized in the procedure, including reactor power, sample mass, counting time, and counting delay.

3.6 Vikuiti

One of the most serious backgrounds to the $0\nu\beta\beta$ signal is from alpha decays from contaminants on or near the surfaces of the crystals. Because of energy loss in non-sensitive material, the resulting signals can be at any energy from zero to the alpha emission energy. To avoid this continuum of alpha signals, the scintillation from detector events is measured by photon sensors above the crystals. We positioned a Vikuiti reflective film around the sides of the crystals to improve photon transport. About 80 cm^2 is required for the 5 cm diameter crystals, and over 110 cm^2 is needed for the 6 cm diameter crystals. Since this film directly faces the detectors, it is critical that it has low levels of radioactive contaminants. Both a roll-type and sheet-type film were tested at CUP with a procedural detection limit of about 1 pg/g for ^{232}Th and ^{238}U [22].

The sample decomposition was performed without any preliminary cleaning, as in the real experiment. After a protection cover was peeled off, the Vikuiti film was cut into small pieces of about 0.5 g. Then the samples were ashed step-wise in quartz crucibles using microwave heat. The resulting ash was quantitatively dissolved in nitric acid, and thorium and uranium were directly measured with ICP-MS without any column separation. The roll-type Vikuiti film was found to have two times lower Th concentration and four times lower U concentration than the sheet-type film, and was selected for the detector assembly. Vikuitti is no longer manufactured, but we have enough supplies for AMoRE-II.

3.7 Sensor assembly

Energy depositions in the crystals are read by sensors composed of metallic magnetic calorimeters (MMCs) and superconducting

quantum interference devices (SQUIDs). The sensors for each detector module are mounted on a copper sensor plate, with connections wire bonded to a printed circuit board (PCB) which is attached to the same plate, as shown in Figure 1. This arrangement serves to prevent strain on the connection to the sensors. Superconducting niobium wires from Supercon Inc. connect from this PCB to a connection board at the mixing chamber, above the lead shielding. This connection is about 2 m long. From there, bundled NOMEX ribbon cables make the connection to a junction box at room temperature. Ceramic or plastic PCBs have high radioactivity. The selected PCB board (sometimes called a flex cable) is model HGLS-D211EM made by Hanwha L&C, having copper foil (35 μm thick) glued with adhesive (10 μm thick) to both sides of a polyimide film (25 μm thick). One side is etched to make the circuit. The other side of the PCB board is attached to the copper plate by lead-tin solder. The PCBs were measured by ICP-MS and also by HPGe counting. The sample for HPGe counting had a mass of 1.16 kg and was measured with the detector for 20 days. This gave upper limits of 1.08 mBq/kg for ^{214}Bi and 1.07 mBq/kg for ^{228}Th. The ICP-MS results were 893 ± 90 pg/g and <1.2 pg/g for U and Th, respectively.

The MMC and SQUID were attached to the copper sensor plate by Loctite brand Stycast glue. Both Stycast 2850 and Stycast 1266 were assayed with HPGe. We used Stycast 1266 for AMoRE-II as Stycast 2850 had high radioactivity. Stycast 1266 has two parts: resin and hardener. Both were measured individually, and the measurements gave upper limits, as shown in Table 1.

We use lead-tin solder to attach the PCB to the copper sensor plate and to attach the niobium wires to the PCB. The total mass of solder connecting this board to wires and the plate is nominally about 70 mg per board, and two boards are used (one for heat and one for light) for each detector module. Since the radiopurity of the lead solder is critical, we made this material in one of our chemical labs. The ratio of lead to tin is 6:4. We have measured different grades of tin material from the Alfa Aesar company. We started by measuring their 99.85% purity grade tin powder. The ^{210}Pb activity was observed to be about 500 Bq/kg, which was unacceptable for use in AMoRE-II. Zone-refining purification was implemented to reduce contamination of the lead. With 35 sequential zone melting cycles, the contamination level was still several hundred Bq/kg, so we then tested the tin bead samples with 5N and 6N purity grades from the same company. Upper limits of 2.1 Bq/kg for ^{210}Pb were found for both products using HPGe, and a 50 pg/g upper limit was found for both ^{238}U and ^{232}Th using ICP-MS. The 5N and 6N products were used for the solder production without any preliminary treatment. To be melted with the tin, lead pieces were cut from bulk plates of ancient lead [32] and were then cleaned with sonication using 10% nitric acid, rinsed with deionized water, and dried.

3.8 Heater

The low-background AMoRE physics run data is dominated by the $2\nu\beta\beta$ spectra and has few events in full-energy gamma peaks. For calibration, we need to have a steady source of events with well-defined energy and shape. For this purpose, we inject a thermal signal by flowing a small current with a resistance. The heater is made of a silicon wafer and is attached to the crystal surface by Araldite glue.

4 Materials of the cryostat

The cryostat is under vacuum, and cooling is provided by pulsed tube refrigeration and a dilution refrigeration unit. The dilution refrigerator and the cryostat are made by the Leiden company in the Netherlands. The overview of the cryostat is shown in Figure 3. The system contains six consecutively-colder vacuum-separated cylindrical containers, with the outermost vacuum can (OVC) at room temperature. The cylinders with attached bottom plates are referred to as "cans", and a connected series of lids, or cooling plates, closes the top of each respective layer.

The lowest cooling plate houses the mixing chamber and is connected to the upper copper plate of the detector assembly by soft copper braids. The detector assembly consists of inner lead shielding, superconducting magnetic field shielding, and the towers of crystal detectors. The mass of the detector assembly is about 3.1 tonnes. The inner lead shielding is 26 cm thick, with 25 cm of low radioactivity lead, and 1 cm of ancient lead. The upper (outer) 25 cm of lead shielding is composed of five layers of 5 cm thick lead bricks, and the lower (inner) 1 cm of lead shielding is made in a disk shape.

Since we have 26 cm of lead shielding just over the detector assembly, the constraints on the radioactivity of the materials in the cryostat system are not strong. The G11 supporting rods connecting the cooling plates are some of the highest sources of radioactivity in the cryostat and account for a background contribution of 5×10^{-7} ckky in the ROI. Other materials over the mixing chamber, including the supporting Kevlar strings, will not contribute significant backgrounds.

4.1 OVC

The outer vacuum chamber is made of 304-grade stainless steel. It is divided into two cylinders coupled with stainless screws M8. Therefore, it has three flanges in total. The flanges are made of stainless steel plate, bent and welded to make a hoop. The welding of flange ends to form the hoops is done with flux core welding rods (K-308LT from KISWEL Korea Welding company) with radioactivities found to be high, 48.4 ± 2.4 Bq/kg for ^{226}Ra and 20.6 ± 1.0 Bq/kg for ^{228}Th. The flux inside the welding rods may contribute strongly to the radioactivity of the rods, but the flux is not fully incorporated into the weld. It is thus necessary to evaluate the radioactivity contamination of the welded part after welding. We made a welding part similar to the flange structure by welding stainless steel with flux core welding with a similar weld geometry and applying a similar amount of weld material. We measured the resulting 1.77 kg sample part with the HPGe detector, and found activities of 16.4 ± 1.6 mBq/kg for ^{226}Ra and 12.9 ± 1.5 mBq/kg for ^{228}Th. The hoop-shaped flanges are welded to the cylinders with TIG welding using AWS AS.9 ER308L rod from Hyundai welding company. The cylinders themselves are also formed with a TIG-welded seam. Each part of the OVC is cleaned by electropolishing.

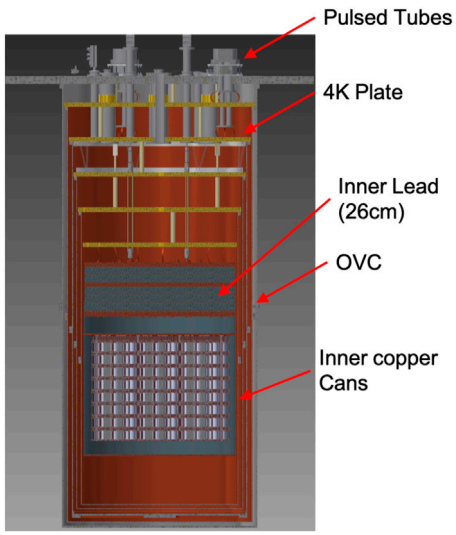

FIGURE 3
A schematic figure of the cryostat of the AMoRE-II experiment.

4.2 IVC and inner cans

There are four copper plates and cans from outside to inside the plates at temperatures of 50 K and 4 K, the dilution refrigerator still, and the 50 mK stage. The inner vacuum can (IVC) is connected to the 4 K plate. The copper cans are made by bending the OFE copper plates of various thicknesses supplied by the Aurubis company. The size and thickness of the cans are listed in Table 3. The radioactivity is measured and is shown in Table 4. All cans are divided into two cylinders coupled with stainless screws M8 of 16 mm diameter. The surfaces were cleaned with 5% nitric acid before assembling. The welding is done by e-beam welding.

4.3 Inner lead shielding

The inner lead is 26 cm thick, and the total mass of the shielding is about two tonnes. The outer 25 cm thick lead consists of lead bricks supplied by JL Goslar Gmbh in Germany. The lead bricks are in the size of 5 cm × 10 cm × 20 cm. The radioactivities of these bricks were measured with the CAGe [33]. The bricks were first sliced with a water jet cutting machine into 5 mm thick plates. The plates were cleaned with 10% nitric acids for 20 min. Then, six plates were located between the top and bottom arrays of the CAGe. This setup has a sensitivity to ^{226}Ra of around 0.1 mBq/kg. The Goslar bricks samples were found to have ^{226}Ra activity of 0.55 ± 0.17 mBq/kg and ^{228}Th activity of 0.58 ± 0.17 mBq/kg. The ^{210}Pb content was 30 ± 1 Bq/kg. The ancient lead, forming the 1 cm inner layer and supplied by the Lemer Pax company, had ^{210}Pb activity of only 100 ± 10 mBq/kg. As this layer sits inside the Goslar lead, it shields the detector from the higher ^{210}Pb activity of the Goslar bricks. To increase the thermal conductivity between the mixing chamber plate and the detector assembly structure via the lead shielding, the lead bricks are divided into two sections and pressed by M20 (12 each) and M10 (9 each) copper rod-screws, with copper sheets between the lead blocks.

4.4 Superconducting lead shielding

To remove the noise produced by the alternating and static magnetic fields in the detector environment, we installed the lead superconducting magnetic shield surrounding the detector towers. The lead sheet is made with ancient lead ingot imported from the Lemer Pax company in France. The ingot was melted to make a block about 1 cm thick and rolled with a drum to make plates with a thickness of about a millimeter. A cylindrical copper structure is made with a copper frame of 3 mm thickness and assembled with brass screws. The rolled lead sheets are welded to the structure with ultra-low radioactive lead-tin solder. The manufacturing process contaminated the surface of the lead sheets. A sample of 10 cm × 10 cm lead sheet is measured with the alpha counter, and the surface alpha emission rate was 2.53 ± 0.15 × 10^{-2}/cm^2/hour after 20 min in 10% nitric acid. Further cleaning with 40 min in 10% nitric acid reduced the rate to 1.25 ± 0.07 × 10^{-2}/cm^2/hour. The whole structure, including the lead sheets, is submerged in 10% nitric acid to remove surface contamination during the manufacturing processes. The superconducting shielding structure will be attached to the copper plate at the bottom of the inner lead shielding.

5 Materials for shielding

The shielding structure is shown in Figure 4. The primary passive gamma shielding is provided on four sides and the bottom by a 25 cm thick lead wall surrounding the cryostat. The corresponding top shielding is provided by the 26 cm of lead at the top of the detector assembly, within the cryostat, as described in Section 4. The wall is surrounded by 1 cm thick borated-rubber [34] sheets that capture thermal neutrons and reduce the background produced by neutron reactions, particularly on copper and lead. This layer is then covered by 70 cm thick polyethylene for fast neutron attenuation, with the muon veto detectors forming the outermost layers. The sides and bottom of the structure are covered by plastic scintillator muon detectors (PSMDs). Each PSMD module is made with two plates of extruded plastic scintillator read by wavelength-shifting fibers attached to each and separated by a gap of 2 cm. The fibers are read by two SiPM sensors for each plate. This entire structure, including the lead, polyethylene, and scintillator detectors, is divided into two halves that sit on a motor-driven system, allowing them to separate for access to the cryostat. The top of the cryostat is covered by a water Cherenkov muon detector (WCMD) with 48 PMTs, including a mix of eight-inch (R5912) and ten-inch (R7081) PMTs. The lead shielding efficiently blocks gamma emissions from contaminants in construction materials, so radioactive contaminants in the mentioned materials outside of the lead contribute negligibly to the detector backgrounds. Below, we describe the shielding components from the lead wall inward.

5.1 Outer lead shielding

The outer lead shielding consists of 25 cm thick walls that surround the cryostat on five sides, with a total mass of about

TABLE 3 The cans of the cryostat and dilution refrigerator.

Temperature	Can size, OD × H × T (mm)	Mass (kg)	Material
300K (OVC)	1,300 × 2,671 × 5	508	STS
50K	1,240 × 2,501 × 4	436	Cu
4K (IVC)	1,180 × 2,244 × 8	700	Cu
Still	1,120 × 1,986 × 3	238	Cu
50 mK	1,060 × 1,765 × 3	204	Cu

TABLE 4 HPGe assay results for cryostat materials.

Item	Material	Supplier	^{226}Ra (mBq/kg)	^{228}Ac (mBq/kg)	^{228}Th (mBq/kg)	^{40}K (mBq/kg)	Detector
Structural materials	OFE Cu	Aurubis (2021)	< 0.64	< 2.1	< 1.5	< 5.4	CC2
	Pb brick	JL Goslar	0.55 (17)	1.21 (28)	0.58 (17)	< 1.2	CAGe
	G11	Leiden	2,700 (200)	930 (110)	906 (66)	9,400 (800)	CC2
	Ultra-low Pb	Lemer Pax	< 3.6	< 2.6	< 2.2	< 16.1	CC1
Fasteners	STS screws M8	Unknown	8.6 (10)	24 (3)	23.1 (17)	18 (6)	CC2
	STS 304 plate	POSCO	1.00 (16)	1.7 (4)	2.36 (22)	7.5 (14)	CC1
Welding materials	Pb/Sn solder (2021)	KNU	< 0.88	< 1.2	< 2.2	< 11	CC2
	TIG Welding rod, ER308L	Hyundai Welding	< 1.1	5.1 (12)	4.2 (8)	< 29	CC1
	Flux core, K-308LT	KISWEL	48,400 (2,400)	15,900 (800)	20,600 (1,000)	129,700 (6,600)	CC1
	STS welded sample	CUP	16.4 (16)	9.6 (18)	12.9 (15)	104 (12)	CC1

N/a stands for not analyzed.

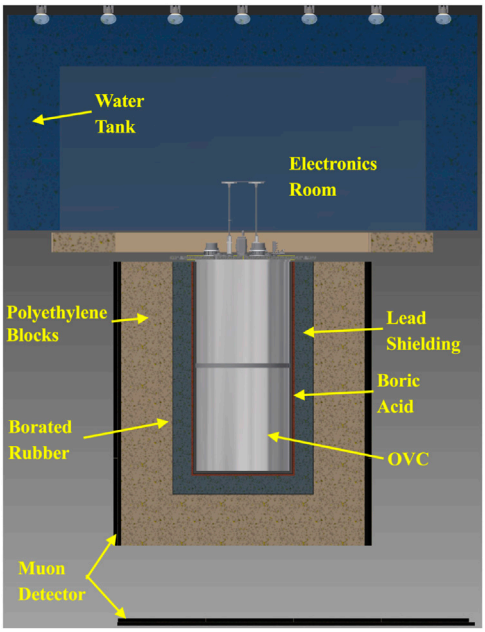

FIGURE 4
A schematic figure of the shielding structure of the AMoRE-II experiment.

60 tons. The outer 20 cm thick lead is made of normal lead supplied by a Korean company. It consists of lead bricks with dimensions of 5 cm × 10 cm × 20 cm.

As described in Section 4.3, we have assayed two batches of lead bricks with the CAGe detector at Y2L. The average radioactivities of these bricks used for the outer 20 cm of shielding are 0.38 ± 0.16 mBq/kg for ^{226}Ra and <0.25 mBq/kg for ^{228}Th. The inner 5 cm of shielding was filled with Boliden lead that was dismantled from the shielding of the KIMS experiment at Y2L. The average radioactivities measured with the CAGe detector are 0.48 ± 0.12 mBq/kg for ^{226}Ra and 0.45 ± 0.11 mBq/kg for ^{228}Th. This is similar to the activities of the JL Goslar lead as reported in Section 4.3. More details on lead measurements will be reported [33]. Since the 0.5 mBq/kg contamination level of ^{226}Ra is about two times higher than the AMoRE-II requirement of an individual item, we will exchange this inner 5 cm of lead with lower background lead before we run the full-scale phase of the AMoRE-II experiment.

We considered placing a few centimeters thickness of additional copper inside the lead shielding to reduce the gamma rays from Bremsstrahlung produced by the decay of ^{210}Pb in the lead shield. However, the simulation shows that even with the neutron shielding layers described here, the background could increase due to thermal neutron capture in the copper plates.

TABLE 5 HPGe assay results for shielding materials.

Item	Material	Supplier	^{226}Ra (mBq/kg)	^{228}Ac (mBq/kg)	^{228}Th (mBq/kg)	^{40}K (mBq/kg)	Detector
Air balloon	Urethane 0.3 mm	Seokyeong Industry	< 2.2	< 2.5	< 0.86	< 8.9	CC1
	Urethane 0.5 mm	Seokyeong Industry	< 1.2	< 1.9	< 1.4	< 9.7	CC2
Neutron shielding	Boric acid (99.5%)	Fisher Scientific	1.2 (4)	< 2.3	< 0.69	< 9.5	CC2
	Boric Acid (99.5%)	Samchun	10.8 (10)	< 2.8	< 1.8	< 6.5	CC1
	Boric acid (99.99%)	Alpha Aesar	< 0.46	< 1.5	< 0.50	98 (8)	CC1
	Boric acid (99.5%)	Samchun	12.0 (9)	< 1.5	< 0.81	< 9.0	CC2
	Boric acid (99.5%)	Samchun	10.2 (7)	< 1.3	< 0.64	< 11	CC2
	Boric acid (99.5%)	KANTO	< 1.4	< 1.3	< 0.95	< 11	CC2
	Boric Acid (99.5%)	Samchun	< 2.0	< 1.3	< 1.1	< 7.2	CC2
	Silicon	HRS Co.	< 0.57	< 1.4	2.1 (3)	< 4.9	CC1
Outer Lead Shielding	Pb brick	Boliden	0.48 (12)	0.36 (8)	0.45 (11)	1.05 (34)	CAGe
	Pb brick	Haekgwang	0.38(16)	n/a	< 0.25	< 1.5	CAGe
	Ingot Pb	Korea Zinc	0.32 (13)	n/a	0.40 (15)	< 1.3	CAGe
	Pb brick	JL Goslar	0.55 (17)	1.21 (28)	0.58 (17)	< 1.2	CAGe
Boric-acid rubber plate	Borated rubber I	CUP	< 1.9	2.3 (6)	1.2 (3)	< 6.2	CC1
	Borated rubber II	CUP	15.0 (15)	< 1.6	3.2 (8)	< 8.8	CC1

N/a stands for not analyzed.

5.2 Boric acid

Boron is a very effective material for absorbing thermal neutrons. The thermal neutrons are hazardous to the $0\nu\beta\beta$ experiment by way of generating high energy gammas from neutron capture reactions in the shielding materials. The effective cross-section of thermal neutrons in copper, iron, and lead are 3.78, 2.75, and 0.17 barn. We may put a few centimeter-thick additional copper layer inside the lead shielding to reduce the ^{210}Pb Bremsstrahlung gamma rays, but the simulation shows it could increase the background due to the thermal neutron capture in the copper plates. Therefore, we try to minimize the copper or iron inside the lead shielding. To minimize the thermal neutron contribution, we placed acrylic boxes containing ultra-pure boric acid powder. The boxes are 500 mm × 500 mm × 10 mm in size, with a wall thickness of 1 mm, so the boric acid is 8 mm thick. These boxes are attached to the lead shielding structure. Since the boric acid is inside the lead shielding, there are limits on its allowable radioactivity levels. We have measured the radioactivity levels of various grades of commercially available boric acid, as shown in Table 5. The radiopurity of boric acid of 99.99% purity supplied by Alpha Aesar company was assayed by HPGe counting with resulting activities of <0.46 mBq/kg for ^{226}Ra and <0.5 mBq/kg for ^{228}Th, though it has 97.9 ± 8.0 mBq/kg for ^{40}K. Another satisfactory boric acid powder, the one which will be used for AMoRE-II, is the 99.5% purity grade supplied by KANTO company with <1.4 mBq/kg for ^{226}Ra and <0.95 mBq/kg for ^{228}Th as shown in Table 5.

5.3 Air balloon

Since the lead shielding structure has a square cross-sectional footprint, and the cryostat cans are circular, there is a sizable volume of air inside the lead shielding (and inside the boric acid layer). We will surround the shielding structure with a vinyl curtain and flush the interior by injecting a constant flow of Rn-free air with an estimated maximum Rn level in the air of about 5 Bq/m^3. At the same time, we will insert urethane balloons filled with nitrogen gas to fill the four corners. This further reduces the Rn level within the balloons and reduces the remaining flushing volume in the tent for more efficient removal of outside air from the tent. Two balloons made of urethane film will be installed inside the lead shielding for each half of the shielding structure. After 10 days of installing the balloons, the activity of ^{214}Bi inside the balloons should be less than 1 mBq in total if no radon penetrates the Urethane film. Two different film samples were assayed with an HPGe detector and found to have less than 1–2 mBq/kg for ^{226}Ra and less than 1 mBq/kg for ^{228}Th, implying a total activity level of less than 50 mBq for this film for all balloons combined.

The volume between the OVC and outer lead shielding is mainly filled by the nitrogen balloon, but some air remains outside of the balloon. The average radon level for the whole volume, including the air balloon, must be below 0.3 Bq/m^3. The air in the balloons is expected to have negligible levels of radon activity. Therefore, the requirement for the remaining air is relaxed by a ratio of the total volume to the volume not filled by balloons.

5.4 Calibration source

To calibrate the energy and detector response, we will irradiate the detector with gammas emitted from a ^{232}Th source. In particular, the 2614 keV gamma is useful since its energy is near the $0\nu\beta\beta$ Q-value, and since it penetrates the shielding better than low-energy gammas. The source will be attached outside of the OVC cans. The source material is ThO_2 powder with 602 Bq/kg of ^{228}Th activity. The powder is mixed with silicone oil, injected inside a Urethane tube of 8 mm diameter, and cured at room temperature for about 24 h to be a flexible solid tube. The source tube is about 8.5 m long, looping the OVC two times, and can be moved within a tube with a larger diameter of 20 mm. A system of two driving motors located in the electronics room over the cryostat will position the source at different locations for calibration. Since the outer tube is fixed outside the OVC, the radioactivity of the tube will be assayed by the HPGe detector before installation to the OVC.

6 Conclusion

We have studied the radioactivity of the materials used in the AMoRE-II experiment, where the presented design has already been iterated to reflect the results. We used equipment for ICP-MS, alpha counting, HPGe detection, and NAA to estimate the radioactivity. For HPGe measurements, we have tried to lower the upper limits of the samples by increasing the sample mass and, in some cases, by using the high-efficiency CAGe array detector system. The actual background level from all the components studied in this paper is estimated with Monte Carlo simulations that will be reported separately. These studies show that the experiment would benefit from an upgrade to improve the radiopurity of the inner 5 cm of the 25 cm thick primary passive shielding lead, used to shield gammas from the surrounding environment. We are considering plans to replace this with a lower-activity selection of lead. All the other materials were confirmed to satisfy the requirements for the AMoRE-II experiment to reach a background level of less than 1×10^{-4} ckky.

Data availability statement

The original contributions presented in the study are included in the article/supplementary material, further inquiries can be directed to the corresponding authors.

Author contributions

AA: Writing–review and editing. VA: Writing–review and editing. PA: Writing–review and editing. HB: Writing–review and editing. JB: Writing–review and editing. BB: Writing–review and editing. RB: Writing–review and editing. KB: Writing–review and editing. OB: Writing–review and editing. CB: Writing–review and editing. NC: Writing–review and editing. MC: Writing–review and editing. JCo: Writing–review and editing, Formal Analysis. SChi: Writing–review and editing. SChu: Writing–review and editing. JCu: Writing–review and editing. FD: Writing–review and editing. MD: Writing–review andediting. DD: Writing–review and editing. CE: Writing–review and editing. AF: Writing–review and editing. AGa: Writing–review and editing. LG: Writing–review and editing. YG: Writing–review and editing. AGe: Writing–review and editing. OG: Formal Analysis, Validation, Writing–original draft, Writing–review and editing. VDG: Writing–review and editing. VIG: Writing–review and editing. CH: Writing–review and editing, Software. DHa: Writing–review and editing. EH: Writing–review and editing. DHw: Writing–review and editing. EJ: Software, Writing–review and editing. JJ: Writing–review and editing. HJ: Writing–review and editing. JK: Writing–review and editing. CK: Resources, Visualization, Writing–review and editing. WGK: Writing–review and editing. VKa: Writing–review and editing. SKe: Writing–review and editing. AK: Writing–review and editing. SKh: Writing–review and editing. DYK: Writing–review and editing. GK: Writing–review and editing. HBK: Writing–review and editing. HJK: Writing–review and editing. HJK: Writing–review and editing, Conceptualization, Project administration. HLK: Writing–review and editing. HSK: Writing–review and editing. MK: Writing–review and editing. SCK: Writing–review and editing. SKK: Writing–review and editing. SRK: Writing–review and editing. WTK: Writing–review and editing. YDK: Conceptualization, Project administration, Writing–review and editing. YHK: Writing–review and editing, Conceptualization, Project administration. KK: Writing–review and editing. YJK: Writing–review and editing. VKy: Writing–review and editing. VKn: Writing–review and editing. VKm: Writing–review and editing. DHK: Writing–review and editing. CL: Writing–review and editing. DYL: Writing–review and editing. EL: Formal Analysis, Validation, Writing–original draft, Writing–review and editing. HJL: Writing–review and editing, Resources, Visualization. HLe: Writing–review and editing. JL: Writing–review and editing, Project administration. JYL: Writing–review and editing. KL: Writing–review and editing. MHL: Writing–review and editing. MKL: Writing–review and editing. SL: Writing–review and editing. YL: Writing–review and editing. DSL: Writing–review and editing, Formal Analysis, Validation, Writing–original draft. HLi: Writing–review and editing. BM: Writing–review and editing. EM: Writing–review and editing. PN: Writing–review and editing. YO: Writing–review and editing. SO: Writing–review and editing. SIP: Writing–review and editing. HKP: Writing–review and editing. HSP: Writing–review and editing. KP: Writing–review and editing. SYP: Writing–review and editing, Formal Analysis. OP: Writing–review and editing. HP: Writing–review and editing. SR: Writing–review and editing. SSR: Writing–review and editing. GR: Writing–review and editing. MS: Writing–review and editing. JSe: Writing–review editing, Formal Analysis. KSe: Writing–review and editing. BS: Writing–review and editing. KSh: Writing–review and editing. VS: Writing–review and editing. KSi: Writing–review and editing. JSo: Writing–review and editing. NVS: Writing–review and

editing. JKS: Writing–review and editing. JWS: Writing–review and editing. NS: Writing–review and editing. VT: Writing–review and editing. RW: Writing–review and editing. KW: Writing–review and editing. HY: Writing–review and editing. YY: Writing–review and editing. QY: Writing–review and editing.

Affiliations of the group members of AMoRE Collaboration

Abdul Wali Khan University Mardan, Mardan, Pakistan; Ajou University, Suweon, Republic of Korea; Baksan Neutrino Observatory, Institute for Nuclear Research (RAS), Moscow, Russia; Bandung Institute of Technology, Bandung, Indonesia; Center for Underground Physics, Institute for Basic Science, Daejeon, Republic of Korea; Chung-Ang University, Seoul, Republic of Korea; Department of Physics and Astronomy, Kirchhoff-Institute for Physics, Heidelberg University, Heidelberg, Germany; Florida Institute of Technology, Melbourne, FL, United States; Fomos Material, Moscow, Russia; Indian Institute of Science (IISc), Bangalore, India; Institute for Nuclear Research (RAS), Moscow, Russia; Institute for Nuclear Research, National Academy of Sciences of Ukraine (NAS Ukraine), Kyiv, Ukraine; Kohat University of Science and Technology, Kohat, Pakistan; Korea Research Institute of Standards and Science, Daejeon, Republic of Korea; Korea University, Sejong, Republic of Korea; Kyungpook National University, Daegu, Republic of Korea; Nakhon Pathom Rajabhat University, Nakhon Pathom, Thailand; National Research Nuclear University MEPhI, Moscow, Russia; Nikolaev Institute of Inorganic Chemistry (RAS), Novosibirsk, Russia; Padang State University, Padang, Indonesia; Physical-Technical Federal Institute, Braunschweig, Germany; Sejong University, Seoul, Republic of Korea; Seoul National University, Seoul, Republic of Korea; Seoul National University Hospital, Seoul, Republic of Korea; Shiv Nadar University, Greater Noida, India; Soongsil University, Seoul, Republic of Korea; State University of Malang, Malang, Indonesia; The University of Tokyo, Bunkyo, Japan; Tsinghua University, Beijing, China; University of Mataram, Mataram, Indonesia; University of Science and Technology, Daejeon, Republic of Korea; V. N. Karazin Kharkiv National University, Kharkiv, Ukraine.

Funding

The authors declare that financial support was received for the research, authorship, and/or publication of this article. This research was funded by the Institute for Basic Science (Korea) under project codes IBS-R016-D1 and IBS-R016-A2. It is also supported by the Ministry of Science and Higher Education of the Russian Federation (N121031700314-5), the MEPhI Program Priority 2030, the National Research Foundation of Korea (NRF-2021R1I1A3041453, NRF-2021R1A2C1013761 NRF-2018K1A3A1A13087769), and the National Research Facilities and Equipment Center (NFEC) of Korea (No. 2019R1A6C1010027).

Acknowledgments

The authors acknowledge Dr. Boyoung Han at KAERI for helping with the NAA measurements of the plastic samples. These acknowledgments are not to be interpreted as an endorsement of any statement made by any of our institutes, funding agencies, governments, or their representatives.

Conflict of interest

Author VA and OB were employed by the company Fomos Material.

The remaining authors declare that the research was conducted in the absence of any commercial or financial relationships that could be construed as a potential conflict of interest.

Publisher's note

References

1. Jones BJP. *Theoretical advanced study institute in elementary particle physics: the obscure universe: neutrinos and other dark matters* (2021).

2. Giunti C, Kim CW. *Fundamentals of neutrino physics and astrophysics*, 710. Oxford, UK: Univ. Pr. (2007). p. 2007.

3. Mohapatra RN, Antusch S, Babu KS, Barenboim G, Chen MC, de Gouvêa A, et al. Theory of neutrinos: a white paper. *Rept Prog Phys* (2007) 70:1757–867. doi:10.1088/0034-4885/70/11/R02

4. Furry WH. On transition probabilities in double beta-disintegration. *Phys Rev* (1939) 56:1184–93. doi:10.1103/PhysRev.56.1184

5. Rahaman S, Elomaa VV, Eronen T, Hakala J, Jokinen A, Julin J, et al. Q values of the 76Ge and ^{100}Mo double-beta decays. *Phys Lett B* (2008) 662:111–6. doi:10.1016/j.physletb.2008.02.047

6. Kim HB, Ha DH, Jeon EJ, Jeon JA, Jo HS, Kang CS, et al. Status and performance of the AMoRE-I experiment on neutrinoless double beta decay. *Phys* (2022) 209(5-6): 962–70. doi:10.1007/s10909-022-02880-z

7. Kim HB, AMoRE Collaboration. Result of AMoRE-I Experiment [Conference presentation]. *TAUP* 2023 (2024). Available from: https://indico.cern.ch/event/1199289/contributions/5445986/

8. Oh Y. AMoRE-II preparation status. *PoS TAUP2023* (2024) 214. doi:10.22323/1.441.0214

9. Pavan M. CUPID: CUORE upgrade with particle IDentification. *J Phys Conf Ser* (2020) 1468(1):012210. doi:10.1088/1742-6596/1468/1/012210

10. Kim WT, Kim S, Sharma B, Gileva O, Grigorieva V, Jeon J, et al. Optimization of cryogenic calorimetric detection with lithium molybdate crystals for AMoRE-II experiments. *JINST* (2022) 17(07):P07034. doi:10.1088/1748-0221/17/07/P07034

11. Lee EK, et al. *HPGe measurements of detector material samples and background screening study at Yangyang laboratory*. Fall Meeting: Korean Physical Society (2019).

12. Thiesse M, Scovell P, Thompson L Background shielding by dense samples in low-level gamma spectrometry. *Appl Radiat Isot* (2022) 188:110384. doi:10.1016/j.apradiso.2022.110384

13. Lee EK, Hahn KI, Jeon E, Kang W, Kazalov V, Kim G, et al. Measurements of detector material samples with two HPGe detectors at the YangYang Underground Lab. *PoS ICHEP2018* (2019) 809. doi:10.22323/1.340.0809

14. Park SY, Hahn K, Kang W, Kazalov V, Kim G, Kim Y, et al. Detection efficiency calibration for an array of fourteen HPGe detectors. *Appl Radiat Isot* (2023) 193:110654. doi:10.1016/j.apradiso.2023.110654

15. Leonard DS, Hahn KI, Kang WG, Kazalov V, Kim GW, Kim YD, et al. Development of an array of fourteen HPGe detectors having 70% relative efficiency each. *Nucl Instrum Meth* (2021) A989:164954. doi:10.1016/j.nima.2020.164954

16. Yeon H, Choe J, Gileva O, Hahn KI, Kang WG, Kim GW, et al. Preparation of low-radioactive high-purity enriched $^{100}MoO_3$ powder for AMoRE-II experiment. *Front Phys* (2023) 11:1142136. doi:10.3389/fphy.2023.1142136

17. Ha C, Adhikari G, Adhikari P, Jeon E, Kang W, Kim B, et al. Initial performance of the high sensitivity alpha particle detector at the Yangyang underground laboratory. *Nucl Instr Methods Phys Res Section A: Acc Spectrometers, Detectors Associated Equipment* (2019) 913:15–9. doi:10.1016/j.nima.2018.09.129

18. Alenkov V, Bae HW, Beyer J, et al. First results from the AMoRE-Pilot neutrinoless double beta decay experiment. *Eur Phys J* (2019) C79(9):791. doi:10.1140/epjc/s10052-019-7279-1

19. Lee JY, Alenkov V, Ali L, Beyer J, Bibi R, Boiko RS, et al. A study of radioactive contamination of crystals for the AMoRE experiment. *IEEE Trans Nucl Sci* (2016) 63(2):543–7. doi:10.1109/TNS.2016.2530828

20. Lee JY, Aryal P, Karki S, Kim HJ, Kim SK, Kim YD, et al. A study of $^{48depl}Ca^{100}MoO_4$ scintillation crystals for the AMoRE-I experiment. *IEEE Trans Nucl Sci* (2018) 65:2041–5. doi:10.1109/TNS.2018.2818332

21. Gileva O, Aryal P, Choe JS, Yena K, Kim Y, et al.Purification of lithium carbonate from radioactive contaminants using a MnO_2-based inorganic sorbent. *Inorganics* (2023) 11:11100410. doi:10.3390/inorganics11100410

22. Gileva O, Choe J, Kim Y, Lee MH, Leonard DS, Shin K, et al. Thorium and uranium trace ICP-MS analysis for AMoRE project. *Appl Radiat Isot* (2023) 194:110673. doi:10.1016/j.apradiso.2023.110673

23. Laubenstein M, Hult M, Gasparro J, Arnold D, Neumaier S, Heusser G, et al. Low Underground measurements of radioactivity, *Appl Radiat Isot* 61(2), 167–72. (2004). doi:10.1016/j.apradiso.2004.03.039

24. Laubenstein M, Geusser G. Cosmogenic radionuclides in metals as indicator for sea level exposure history. *Appl Rad Isot* (2009) 67:750–4. doi:10.1016/j.apradiso.2009.01.029

25. Leonard DS, Auty D, Didberidze T, Gornea R, Grinberg P, MacLellan R, et al. Nuclear instruments and methods in physics research section A: accelerators, spectrometers, detectors and associated equipment , 871, 169–79. (2017). DOI doi:10.1016/j.nima.2017.04.049

26. Leonard DS, et al. Systematic study of trace radioactive impurities in candidate construction materials for EXO-200. *Nucl Instrum Meth* (2008) 591:490–509. doi:10.1016/j.nima.2008.03.001

27. Aprile E, Arisaka K, Arneodo F, Askin A, Baudis L, Behrens A, et al. Material screening and selection for XENON100. *Astroparticle Phys* (2011) 35(2):43–9. doi:10.1016/j.astropartphys.2011.06.001

28. Abgrall N, et al. arXiv:1601.03779 [physics.ins-ex] (2016)

29. Aprile E, Aalbers J, Agostini F, Alfonsi M, Amaro FD, Anthony M, et al. Material radioassay and selection for the XENON1T dark matter experiment. *J C* (2017) 77(12):890. doi:10.1140/epjc/s10052-017-5329-0

30. Sisti M. (2019).*Workshop in low radiation techniques*. nuetron activation analysis

31. Augier C, et al. arxiv:2305.01402 [hep-ex] (2023)

32. Danevich FA, et al. (2009).*Nucl Instrum Meth* A603. 328.

33. Agrawal A, et al. To be submitted to arXiv. Consideration of screen effect in radioassay of high effective atomic number material for AMoRE-II double-beta decay experiment

34. Ha DH, Kim G, Kim H, Kim J, Kim Y, Lee E, et al. Development of thermal neutron shield with low radioactivity. *J Instrumentation* (2022) 17(10):P10041. doi:10.1088/1748-0221/17/10/P10041

frontiers | Frontiers in Physics

TYPE Review
PUBLISHED 14 August 2024
DOI 10.3389/fphy.2024.1433347

OPEN ACCESS

EDITED BY
Luca Pattavina,
Gran Sasso National Laboratory (INFN), Italy

REVIEWED BY
Ettore Segreto,
State University of Campinas, Brazil
Olga Gileva,
Institute for Basic Science (IBS), Republic of Korea

*CORRESPONDENCE
L. Consiglio,
lucia.consiglio@lngs.infn.it

RECEIVED 15 May 2024
ACCEPTED 08 July 2024
PUBLISHED 14 August 2024

CITATION
Consiglio L, Flammini A, Ianni A, Marasciulli A, Panella G, Pietrofaccia L, Sablone D and Tartaglia R (2024), NUOVA OFFICINA ASSERGI: a novel infrastructure for the production of cryogenic and radiopure Si-based photodetectors.
Front. Phys. 12:1433347.
doi: 10.3389/fphy.2024.1433347

NUOVA OFFICINA ASSERGI: a novel infrastructure for the production of cryogenic and radiopure Si-based photodetectors

L. Consiglio[1]*, A. Flammini[2], A. Ianni[1], A. Marasciulli[1], G. Panella[1], L. Pietrofaccia[1], D. Sablone[1] and R. Tartaglia[1]

[1]INFN LNGS, Assergi (AQ), Italy, [2]INFN Bologna, Bologna, Italy

The NUOVA OFFICINA ASSERGI (NOA) is a new facility for the production and integration of large-area silicon photodetectors operating at cryogenic temperatures. Silicon photomultipliers are proving to be a promising technology for next-generation experiments searching for rare events in underground laboratories. New photosensor technology with high performance at cryogenic temperature has been developed by Fondazione Bruno Kessler (FBK) and integrated at Laboratori Nazionali del Gran Sasso (LNGS) into large-area optical units, thus opening the frontiers toward the realization of scalable liquid argon experiments probing dark matter. The massive production of such detectors is now feasible in NOA, a clean room of 421 m^2 designed to operate in a radon-free mode. NOA, commissioned and operational at LNGS, hosts the most advanced packaging machines and electronic test facilities for the integration of silicon devices in a dust-controlled environment. The infrastructure layout is split into two experimental areas: one for the production of electronic devices and cryogenic temperature tests and the other for operating with large detector installations. The NOA facility can be operated with a radon abatement system, making it a unique facility for packaging and testing SiPM-based photosensors and for assembling detector components in a radon-free environment. Therefore, NOA supports the deployment of underground experiments at LNGS and the development of new technologies for the search of rare events, such as dark matter and neutrinoless double-beta decay.

KEYWORDS

clean room, silicon photomultipliers, packaging, photodetectors, cryogenics, radiopurity

1 Introduction

In the last few decades, silicon photomultiplier (SiPM) detectors [1] have obtained overwhelming success and worldwide recognition in the detection of low photon fluxes due to their key features, such as low operating voltages, insensitivity to magnetic fields, robustness and reliability, high performance at cryogenic temperatures, and scalability in creating large arrays. Such characteristics make them attractive for a variety of scientific applications, such as large-scale time projection chambers (TPCs) based on noble liquids searching for rare events in extremely low background conditions. The collection of scintillation light is crucial to detecting neutrino or dark matter interactions in cryogenic environments. One of the issues

FIGURE 1
Left: NOA CR3 test area. Right: NOA CR2.

with large cryogenic detectors for low background applications is the amount of radioactive contaminants in electronic components, connections, and cabling. Typically, SiPMs cover active areas of several tens of square millimeters. This means that for a large surface experiment, a huge number of devices and readout channels are in the close proximity to the detector electronics. To overcome this issue, one possibility is to group SiPMs into arrays to achieve a larger surface that could be read as a single-channel device. Since 2014, FBK (https://www.fbk.eu/it/), in synergy with LNGS, has been working on the development of SiPM arrays [2] of cryogenic photosensors [3, 4] with large aggregated output [5] and has operated successfully with high performance at cryogenic temperatures. This represents a big technological challenge, as in the case of the DarkSide-20k dark matter experiment [6], which aims to build thousands of SiPM-based optical units for an overall sensitive surface exceeding 20 m^2. The massive production of SiPMs has been successfully transferred to LFOUNDRY (www.lfoundry.com), while the photosensor packaging and integration will be operated inside the NOA clean room [7]. In this paper, we will review the main features of the NOA facility, the description of the packaging machines and tools, the technological solutions available, and future perspectives.

2 NOA infrastructure

Born within the framework of the DarkSide-20k experiment, the NOA infrastructure is an ISO-6 clean room according to the ISO 14644-1 standard classification[1], with an overall surface of 421 m^2. It is divided into two main areas: the first, named CR3 (Figure 1, left), is devoted to the packaging, testing, and assembly of cryogenic large-area SiPM-based devices; the second, named CR2 (Figure 1, right), is designed for handling and mounting of big detectors. The infrastructure also includes two dedicated small rooms, namely, the dressing room (CR1-IS) and the pass-box (CR2-IS), while a third area (HVAC), approximately 42 m^2, is completely dedicated to the air ventilation system. All the environments are sketched, as shown in Figure 2.

NOA CR3, with a surface area of 353 m^2 and a height of approximately 3 m, hosts 25 workbenches, is provided with different utilities (gas nitrogen, vacuum, compressed air, electricity, LAN, and telephone line), and is equipped with antistatic mats in order to prevent electronic component damage due to electrostatic discharges. A liquid nitrogen charging station has also been set up for the filling of small dewars for device characterization at cryogenic temperatures. Two chemical hoods have been installed, each equipped with compressed air, gas nitrogen, and vacuum; one of them is also provided with a deionized water sink. Furthermore, two water sinks equipped with both industrial and deionized water are available inside the CR3 and a 5 °C chilled water line. All the distribution pipes of the mentioned utilities, together with the electrical lines, are located above the counter ceiling of the clean room in the space dedicated to the air plenum. Utility columns are placed in correspondence with the workbenches and the production machines to provide rapid connections. CR2 covers a surface area of 68 m^2 with the purpose of integrating large experimental setups[2]; for this reason, the room height is 5.8 m and the floor has been designed to withstand a

1 Referred to the maximum particle concentration suspended in one m^3 of air, an ISO 6 clean room allows a maximum of 1×10^6 (one million) particles of 0.1 micron size.

2 The DarkSide-20k TPC optical planes will be assembled in CR2 before installation in the apparatus in the LNGS underground cavern.

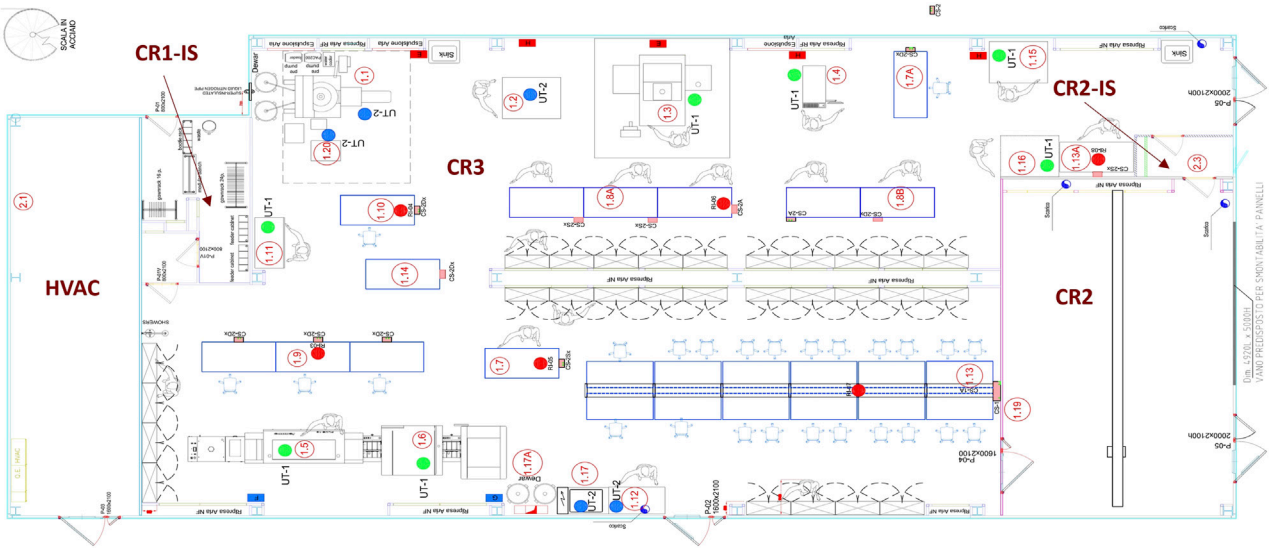

FIGURE 2
NOA clean room layout.

nominal load of 2000 kg/m^2 although it has been successfully tested with a 3,000 kg/mm^2 load. In CR2, a 2-ton manual crane is also available. A dedicated air lock allows entry to CR2, while CR3 is off. The air lock can be also used as a "pass-box" for the transfer of materials inside/outside the clean room since it is provided with a dedicated window properly interlocked with the access doors. Electrical plugs, both from normal and UPS supply, are placed along the clean room walls together with LAN net plugs. The NOA infrastructure has been built with selected materials to reduce radon gas emanation and diffusion; moreover, the air ventilation system has been designed to be compatible with a radon abatement system to supply air to the clean room with a low radon concentration. The combination of these features would make NOA a radon-free environment for packaging photodetectors and electronic devices, with an expected gas concentration reduced by at least of a factor 100. A radon-free environment is crucial for rare event experiments to avoid the plate-out of ^{210}Pb, which is a proxy of ^{222}Rn. Values less than 1 Bq/m^3 should be achieved to reduce this contamination in detector components assembled inside the clean room [8]. Existing radon-free clean rooms have achieved levels between 10 and 500 mBq/mm^3.

3 Production machines

The CR3 area has been equipped with sophisticated machines dedicated to the cryogenic characterization, handling, packaging, and test of large-area Si-based devices:

- FormFactor PAC200 (https://www.formfactor.com/product/probe-systems/wafer-multi-chip-cryogenic-systems/pac200/), a semi-automated probe station for wafers and substrates in a high vacuum environment, for testing devices at cryogenic temperatures down to 77 K;
- Advanced Dicing Technology 7122 (www.adt-dicing.cn/home/product/info?id=450), an automatic wafer dicer for dicing Si wafer or other thin substrates with high accuracy;
- AMICRA NOVA PLUS Flip Chip Bonder (https://amicra.semi.asmpt.com/en/products/die-flip-chip-bonder/nova-plus-die-bonder-und-flip-chip-bonder/), a modular machine with a precision die attach method for micro-assembly applications;
- HESSE BJ855 (https://www.hesse-mechatronics.com/en/products/fine-wire-bonder/bj855/), a high-speed fully automatic wire bonder;
- Ultron semiconductor assembly systems (https://www.ultronsystems.com/USI-Products.html);
- Two microscopes with different magnifications for device visual inspection to assess possible damages or defects.

A part of CR3 has been devoted to the testing and characterization of the assembled devices and the related electronics: small dewars with sealed flanges, equipped with input/output and vacuum tight feedthroughs and provided with a mechanical structure to hold the devices, are available together with the related instrumentation in order to perform test measurements and data acquisition and analysis both at room temperature and in liquid nitrogen.

3.1 Cryogenic probe system

FormFactor PAC200 (Figure 3) represents a robust platform for performing electrical tests of integrated circuits at the wafer level, performing automatic testing of wafers and substrates up to 200 mm in a cryogenic environment down to 77 K. The probe plate is designed to mount a high-pin count probe card that can be thermally anchored to a cryogenic shield to reduce the heat load through the probe needles. The probe card contacts are very soft and short in length and can be numerous, depending on the specific requests. A high-resolution video microscope is mounted on a

FIGURE 3
Left: cryogenic probe station. Right: dicer.

microscope movement with a travel range of 50 mm × 50 mm in the XY direction and 130 mm in the *Z* direction. PAC200 is equipped with a stable, vibration-isolating frame. The chuck and the motorized chuck stage, with 200 mm × 200 mm X–Y travel, theta, and *Z*-axis, are located inside the high-vacuum chamber. A radiation shield covers the movable chuck of the station to establish conditions of 80 K and below. Two separate cooling circuits for the shield and chuck are provided with precise temperature control that ensures stability at 0.1 K. The machine exhibits excellent measurement accuracy and repeatability.

3.2 Dicer

ADT7122 (Figure 3) is a semi-automatic dicer system with an 8" diameter (or 200 mm × 200 mm square area) dicing area. It is an advanced, fully programmable saw for dicing thin materials into smaller pieces with 1-micron accuracy. Typical applications are Si wafer dicing, but it can also be used for other thin materials and substrates such as sapphire, glass, thin film devices, silicon, and many others with the proper choice of blade type.

3.3 Flip chip bonder

ASMPT AMICRA Nova Plus (Figure 4) is an advanced dual-head die bonding system capable of achieving placement accuracy down to few microns while bonding at temperatures exceeding 350°C and applying high bonding forces. This type of die bonding can be classified as thermo-compression bonding, and in some cases, these capabilities are required for different applications like the through-silicon vias (TSVs). Some tools of the machine have been developed for custom applications requiring the placement and bonding of large-size silicon dies (11.7 mm × 7.9 mm) on a PCB substrate using soft solder paste. A wafer magazine has been provided for die loading, while substrate loading can be done manually. The modular concept of the machine allows for enough flexibility to be upgraded to perform different processes like 3D/2.5D interconnections, TSVs, chip on chip, chip on wafer, chip on substrates, and optoelectronics.

3.4 Wire bonder

Bondjet BJ855 (Figure 4) is a fully automatic ultrasonic fine wedge–wedge fine wire bonder. BJ855 fulfills all wire bonding challenges on one platform. The machine is flexible and can be used with different types of bond heads (included in the machine equipment) to create bonds based on different process technologies:

- Bondhead BK06: designed for thin wire processes according to the wedge–wedge process
- Bondhead DA06: deep access with a compact design, available for bonding inside difficult-to-access devices or tight packages, providing a cavity access of 14.5 mm with a 1-inch wedge tool length. The pivot-free transducer suspension guarantees a constant vertical wedge alignment.
- Bondhead BW01: developed for gold wire processes for the ball–wedge bonding method.

Bonding wires can be positioned precisely on the large, 305 mm × 410-mm, working area. Multilevel bonding is made possible with the 32-mm *Z*-axis lift. Several bond stations can be placed within the working area to enable a high throughput. A permanent real-time monitoring process is in operation during the bond process, monitoring wire deformation, transducer current, frequency, and impedance within a programmable tolerance range. The system can be used in fully automatic and manual operations.

FIGURE 4
Left: flip chip bonder. Right: wire bonder.

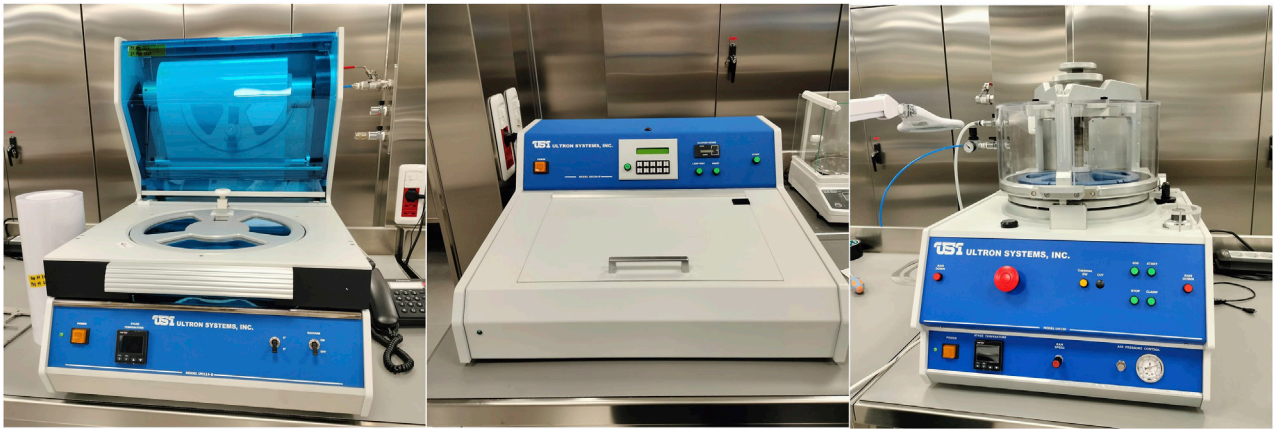

FIGURE 5
Manual packaging tools. From left to right: tape release, UV curing, and wafer expander.

To evaluate the strength and reliability of wire bonds, a high-quality and compact pull-tester unit (LAB-Tester LT-101), equipped with most up-to-date software and available for thin and heavy wire applications, is available inside NOA.

Two microscopes with different objective magnifications are also available for optical inspection and quality control of the devices.

3.5 Semiconductor assembly systems

NOA CR3 has also been equipped with a set of semiconductor assembly systems (Figure 5) for frame film mounting, ultraviolet (UV) curing, and die expansion to handle silicon wafers.

- Ultron Model UH114 accommodates up to 8-inch (200 mm) wafers/film frames to hold the wafer during the dicing/sawing operations, where uniform adhesive plastic film lamination is crucial. The unit features a retractable film-cutting system with adjustable cutting pressure to accommodate various tape base materials and different thicknesses. Roller pressure is adjusted from the topside of the unit for different process requirements and to accommodate various wafer thicknesses;
- Ultron Model UH104 UV tape exposure accommodates up to an 8-inch grip ring or film frame-mounted wafer. It provides uniformity of UV exposure and fast UV curing times using an ozone-free UV lamp array with a cool, low-temperature UV-A 365-nm curing process. Adhesion reduction is necessary to

allow the die-bonding process to pick up every single die, and it is performed before the die-expansion process;
- Ultron UH-132 Motor Drive Die Matrix Expander offers digital speed control for great precision in wafer expansion by producing both linear and uniform expansion throughout the entire drive stroke. This operation improves die handling after dicing in the subsequent die-attaching process.

4 Future perspectives

The NOA clean room at LNGS is a new INFN infrastructure definitively commissioned in February 2023 and designed for the production, testing, and integration of large arrays of SiPMs in a dust-controlled environment with low radon emanation. The current main user of the clean room is the DarkSide-20k collaboration, whose goal is to produce more than 500 SiPM-based photodetection units (PDUs), each sized 20 × 20 cm for an overall surface of 21 m^2 of silicon. Some of the machines have been partially designed, following the DarkSide-20k demands, but they are flexible enough to be upgraded with more commercial tools. The cryogenic probe station can be configured with different probe-card technologies available on the market. The flip chip bonder is one of the most advanced die bonding systems for semiconductor packaging with high placement accuracy, and the bond tools and other custom parts can easily be replaced with new ones with a different design, according to the customer's requirements. The HESSE Wire Bonder is the latest generation of fully automated fine wire bonders. An interesting perspective under evaluation through a feasibility study is the implementation of a radon abatement plant. This upgrade would make the infrastructure unique for the packaging, testing, and assembly of photodetectors in a Rn-free environment. A memorandum of understanding of the infrastructure has been elaborated, collecting the access rules, operating procedures, technical aspects, and plant design of the clean room, with a detailed description of the packaging machines and the cost for running and maintenance. For at least 1 year, NOA will mainly host the DarkSide-20k activities; nevertheless, it is already receiving requests from other research groups interested in the clean room usage and related equipment, demonstrating its intrinsic potential to become a technological hub for the packaging and testing of photodetectors and electronic devices in a controlled atmosphere environment.

Author contributions

LC: writing–original draft. AF: writing–review and editing. AI: writing–review and editing. AM: software and writing–review and editing. LP: writing–review and editing. GP: writing–review and editing. DS: writing–review and editing. RT: writing–review and editing.

Funding

The author(s) declare that financial support was received for the research, authorship, and/or publication of this article. The authors acknowledge support from the financial funds of "Piano Operativo Nazionale 2014–2020" (PON) and "Programma di Sviluppo RESTART, Delibera CIPE 49/16," as well as the scientific agreement between LNGS, Regione Abruzzo, and Comune dell'Aquila.

Conflict of interest

The authors declare that the research was conducted in the absence of any commercial or financial relationships that could be construed as a potential conflict of interest.

The author(s) declared that they were an editorial board member of Frontiers, at the time of submission. This had no impact on the peer review process and the final decision.

Publisher's note

References

1. Acerbi F, Gundacker S. Understanding and simulating SiPMs. *Nucl Instr Methods Phys Res Section A* (2019) 926:16–35. doi:10.1016/j.nima.2018.11.118

2. D'Incecco M, Galbiati C, Giovanetti GK, Korga G, Li X, Mandarano A, et al. Development of a novel single-channel, 24 cm2, SiPM-based, cryogenic photodetector. *IEEE Trans Nucl Sci* (2017) 65(1):591–6. doi:10.1109/tns.2017.2774779

3. Piemonte C, Ragazzoni V, Zorzi N. NUV-sensitive silicon photomultiplier technologies developed at Fondazione Bruno Kessler. *Sensors* (2019) 19(308):1–24. doi:10.3390/s19020308

4. Consiglio L. The cryogenic electronics for DarkSide-20k SiPM. *J Instrumentation* (2020) 15:1–5. doi:10.1088/1748-0221/15/05/C05063

5. Razeto A, Consiglio L. Very large SiPM arrays with aggregated output. *J Instrumentation* (2022) 17(P05038):1–11. doi:10.1088/1748-0221/17/05/P05038

6. DarkSide CollaborationAalseth CE, Acerbi F, Agnes P, Albuquerque IFM, Alexander T, Alici A, et al. DarkSide-20k: a 20 tonne two-phase LAr TPC for direct dark matter detection at LNGS. *The Eur Phys J Plus* (2018) 133(3):131. doi:10.1140/epjp/i2018-11973-4

7. Consiglio L. The nuova officina assergi:future perspectives beyond DarkSide-20k. *PoS TAUP2023* (2024) 310:1–6. doi:10.22323/1.441.0310

8. Di Marcello V, Ianni A, Panella G. Numerical analysis of radon behavior in radon-suppressed clean room environments. *JINST* (2022) 17:P06033. doi:10.1088/1748-0221/17/06/p06033

frontiers | Frontiers in Physics

TYPE Brief Research Report
PUBLISHED 05 December 2024
DOI 10.3389/fphy.2024.1387069

OPEN ACCESS

EDITED BY
Jeter Hall,
SNOLAB, Canada

REVIEWED BY
Olga Gileva,
Institute for Basic Science (IBS), Republic of Korea
Michel Sorel,
Spanish National Research Council (CSIC), Spain

*CORRESPONDENCE
M. Caravati,
mauro.caravati@gssi.it

RECEIVED 16 February 2024
ACCEPTED 09 April 2024
PUBLISHED 05 December 2024

CITATION
Agnes P, Back HO, Bonivento W, Boulay MG, Canci N, Caravati M, Cebrian S, Cocco V, Diaz Mairena D, Franco D, Gabriele F, Gahan D, Galbiati C, Garcia Abia P, Gendotti A, Hessel T, Horikawa S, Lopez Manzano R, Luzzi L, Martinez M, Pesudo V, Razeti M, Renshaw AL, Romero L, Rubbia A, Santorelli R, Simeone M, Stefanizzi R, Steri A and Sulis S (2024), The underground argon project: procurement and purification of argon for dark matter searches and beyond.
Front. Phys. 12:1387069.
doi: 10.3389/fphy.2024.1387069

The underground argon project: procurement and purification of argon for dark matter searches and beyond

P. Agnes[1,2], H. O. Back[3], W. Bonivento[4], M. G. Boulay[5], N. Canci[6], M. Caravati[1,2]*, S. Cebrian[7], V. Cocco[4], D. Diaz Mairena[8], D. Franco[9], F. Gabriele[4], D. Gahan[4,10], C. Galbiati[1,2,11], P. Garcia Abia[8], A. Gendotti[12], T. Hessel[9], S. Horikawa[2,13], R. Lopez Manzano[8], L. Luzzi[8], M. Martinez[7], V. Pesudo[8], M. Razeti[4], A. L. Renshaw[14], L. Romero[8], A. Rubbia[12], R. Santorelli[8], M. Simeone[6,15], R. Stefanizzi[4,10], A. Steri[4,10] and S. Sulis[4,16] on behalf of the Global Argon Dark Matter Collaboration (GADMC)

[1]Gran Sasso Science Institute, L'Aquila, Italy, [2]INFN Laboratori Nazionali del Gran Sasso, Assergi (AQ), Italy, [3]Savannah River National Laboratory, Jackson, SC, United States, [4]INFN Cagliari, Cagliari, Italy, [5]Department of Physics, Carleton University, Ottawa, ON, Canada, [6]INFN Napoli, Napoli, Italy, [7]Centro de Astropartículas y Física de Altas Energías (CAPA), Universidad de Zaragoza, Zaragoza, Spain, [8]Centro de Investigaciones Energeticas, Medioambiéntales y Tecnologicas (CIEMAT), Madrid, Spain, [9]APC, Université de Paris Cité, CNRS, Astroparticule et Cosmologie, Paris, France, [10]Physics Department, Università degli Studi di Cagliari, Cagliari, Italy, [11]Physics Department, Princeton University, Princeton, NJ, United States, [12]Institute for Particle Physics, ETH Zürich, Zürich, Switzerland, [13]Department of Industrial Engineering, Information Engineering, and Economics, Università degli Studi dell'Aquila, L'Aquila, Italy, [14]Department of Physics, University of Houston, Houston, TX, United States, [15]Chemical, Materials, and Industrial Production Engineering Department, Università degli Studi "Federico II" di Napoli, Napoli, Italy, [16]Department of Electrical and Electronic Engineering, Università degli Studi di Cagliari, Cagliari, Italy

The existence of dark matter in the universe is inferred from abundant astrophysical and cosmological observations. The Global Argon Dark Matter Collaboration (GADMC) aims to perform the searches for dark matter in the form of weakly interacting massive particles (WIMPs), whose collisions with argon nuclei would produce nuclear recoils with tens of keV energy. Argon has been considered an excellent medium for the direct detection of WIMPs as argon-based scintillation detectors can make use of pulse shape discrimination (PSD) to separate WIMP-induced nuclear recoil signals from electron recoil backgrounds with extremely high efficiency. However, argon-based direct dark matter searches must confront the presence of intrinsic ^{39}Ar as the predominant source of electron recoil backgrounds (it is a beta-emitter with an endpoint energy of 565 keV and half-life of 269 years). Even with PSD, the ^{39}Ar activity in atmospheric argon (AAr), mainly produced and maintained by cosmic ray-induced nuclear reactions, limits the ultimate size of argon-based detectors and restricts their ability to probe very-low-energy events. The discovery of argon from deep underground wells with significantly less ^{39}Ar than that in AAr was an important step in the development of direct dark matter detection experiments using argon as the active target. Thanks to pioneering research and successful R&D, in 2012, the first 160 kg batch of underground argon (UAr) was extracted from a CO_2 well in Cortez, Colorado. The DarkSide-50 experiment at the Gran

Sasso National Laboratory (LNGS) in Italy, the first liquid argon detector ever operated with a UAr target, demonstrated a ~ 1,400 suppression of the ^{39}Ar activity with respect to the atmospheric argon. An even larger suppression is expected for ^{42}Ar (another intrinsic beta-emitter with the ^{42}K daughter isotope, also a beta-emitter) as its production is expected mainly in the upper atmosphere. Following the results of DarkSide-50, the GADMC initiated the UAr project for extraction from underground and cryogenic purification of 100 t of argon to be used as a target in the next-generation experiment DarkSide-20k. This paper contains a description of the Urania Plant in Cortez, Colorado, where UAr is extracted; the Aria Plant in Sardinia, Italy, an industrial-scale plant comprising a 350-m state-of-the-art cryogenic isotopic distillation column, designed for further purification of the extracted argon and further reduction of the isotopic abundance of ^{39}Ar; and DArT, a facility for UAr radiopurity qualification at the Canfranc Underground Laboratory (LSC), Spain. Moreover, the high radiopurity of UAr leads to other possible applications, for instance, for those neutrinoless double-beta decay experiments using argon as shielding material or, more generally, for all those activities on argon-based detectors in high-energy physics or nuclear physics, which will be briefly discussed.

KEYWORDS

underground argon, ^{39}Ar, ^{42}Ar, dark matter instrumentation, 0νββ-decay instrumentation, low-radioactivity technique, low-background counting

1 Introduction

Liquefied noble gases have been employed in rare event searches since more than 3 decades, due to their good scintillation and ionization yields, chemical stability, and good intrinsic radiopurity. Argon offers excellent particle identification capability thanks to pulse shape discrimination (PSD), which makes it an ideal candidate for searching for rare nuclear recoil processes, such as dark matter orcoherent neutrino–nucleus interactions [1].

Several experiments are currently underway [2,3] or will employ a liquid argon target in the future [4–6]. The relative abundance of argon in the Earth atmosphere (0.94%) makes the extraction of this gas from air convenient. Although argon derived from the atmosphere is predominated by ^{40}Ar, it contains the cosmogenically produced long-lived radioactive isotopes ^{39}Ar and ^{42}Ar. These radioactive contaminants are of little concern for searches at the GeV scale but may represent a limiting background for experiments aiming at discovering low-energy processes such as those expected from the weakly interacting massive particle (WIMP)–nuclei interaction. These experiments are typically operated in the dual-phase configuration, in which the liquid bulk is immersed in a uniform electric drift field (200 ÷ 500 V/cm) to extract ionization electrons from the interaction sites. These electrons are collected in the gaseous phase at the anode and provide, in combination with prompt scintillation, 3D vertex reconstruction and extremely low thresholds [7,8]. The reconstruction of one full event becomes possible at the cost of long acquisition time, corresponding to the maximum drift time along the drift direction (the drift velocity is ~ 1 mmμs at a 200 V/cm drift field [9]).

Argon extracted from the atmosphere contains approximately 1 part in 10^{15} of ^{39}Ar, giving a specific activity of approximately 1 Bq/kg [10,11], whereas the β-decay of ^{42}Ar (as its daughter ^{42}K in secular equilibrium) gives approximately four orders of magnitude less specific activity than ^{39}Ar [12]. Both the direct background and pileup from ^{39}Ar decays set limits on the sensitivity and maximum practical size of liquid argon dark matter searches in the case of single-phase experiments because of the background rate and also in the case of dual-phase experiments because of pileup. A source of argon with a reduced ^{39}Ar content is necessary to allow sensitive argon-based dark matter searches at the ton scale and beyond. Moreover ^{42}Ar and, in particular, its progeny ^{42}K is a dominant background in neutrinoless double-beta decay experiments using argon as shielding, such as GERDA [13] and Large Enriched Germanium Experiment for Neutrinoless Double-Beta Decay (LEGEND) [14].

Because of the long half-life of ^{39}Ar (half-life 269 ± 9 years, [2]), established methods to reduce the amount of ^{39}Ar in atmospheric argon (AAr) are centrifugation and differential thermal diffusion together with isotope separation, some rather costly and time-consuming processes. Alternatively, considering that much of the ^{40}Ar in the atmosphere is produced by electron capture decays of long-lived ^{40}K within the Earth and much of the ^{40}Ar remains underground, it is expected that argon from underground sources would have less ^{39}Ar radioactivity since cosmic rays, producing ^{39}Ar in the upper atmosphere principally via the ^{40}Ar(n,2n)^{39}Ar reaction, are effectively attenuated by rocks. Nevertheless, α-decays in the decay chains of long-lived natural uranium and thorium can lead to *in situ* production of ^{39}Ar, meaning that not all underground argon samples from different underground gas wells show reduced ^{39}Ar-specific activity compared to AAr [15]. As the concentration of uranium and thorium in the mantle is typically of the order of a thousand times lower than that in the crust, it was also suggested that the concentration of ^{39}Ar in argon gas from the Earth's mantle should have to be lower [16]. That possibility pushed the DarkSide collaboration to perform pioneering research and R&D, leading to the discovery of less ^{39}Ar radioactivity argon in the National Helium Reserve in Amarillo, Texas, in 2007; in that case, the ^{39}Ar concentration was measured with a factor of at least 20 below that of AAr [17]. Afterward, argon with low ^{39}Ar radioactivity was found in gas samples from the Reliant Dry Ice

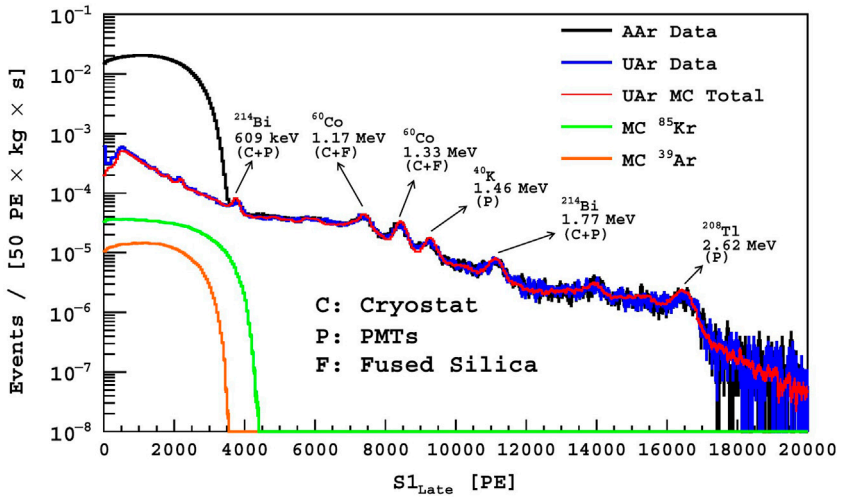

FIGURE 1
Figure obtained from [19]: spectra for the UAr (blue) and AAr (black) targets, normalized to exposure. Also shown are the Monte Carlo (MC) fit to the UAr data (red) and individual components of ^{85}Kr (green) and ^{39}Ar (orange) extracted from the fit. The presence of ^{85}Kr on the UAr spectrum was unexpected.

Plant in Bueyeros, New Mexico, and from a CO_2 well in Cortez, southwestern Colorado (CO), for which preliminary measurements studies showed a promising upper limit of ^{39}Ar concentration of less than 0.65% of the ^{39}Ar concentration in AAr [18]. This was an important step in the development of the next-generation direct dark matter detection experiments using underground argon (UAr) as the active target.

The first use of low-radioactivity argon in a dark matter search is pioneered by the DarkSide-50 experiment; after an initial use of AAr as target material, the DarkSide-50 detector was filled with UAr from the Cortez CO_2 gas field source in April 2015. DarkSide-50 ultimately showed that the ^{39}Ar activity in the Cortez UAr is reduced by a factor of $(1.4 \pm 0.2) \times 10^3$ relative to AAr; that is, an ^{39}Ar activity of 0.73 mBq/kg was measured [19]. Figure 1 shows the comparison of the DarkSide-50 data collected with AAr and UAr. The energy spectra extend to above 2.6 MeV. Below approximately 570 keV, the AAr spectrum is dominated by ^{39}Ar, clearly suppressed in the UAr dataset. A spectral analysis using Monte Carlo-generated spectra to describe the background components was performed, in order to measure the ^{39}Ar activity. This analysis revealed the presence of ^{85}Kr in the UAr spectrum, which was unexpected; this was interpreted as the result of a possible air leak during that UAr batch extraction, leading to the possibility to obtain even higher depletion factors in next UAr batches.

It is worth reporting that due to the fact that the dominant production channel of ^{42}Ar is ultimately through interactions of alpha particles on ^{40}Ar via ^{40}Ar(α,2p)^{42}Ar with an energy threshold of approximately 14 MeV (not available from radioisotopic decays rather in the upper atmosphere where primary cosmic rays are "harder"), it is expected that the underground production of ^{42}Ar is strongly suppressed [20,21].

The Global Argon Dark Matter Collaboration (GADMC) aims at performing the most sensitive WIMP dark matter search of the next decade with the DarkSide-20k experiment, using the low-radioactivity UAr as the target from the Cortez CO_2 gas field [4]. A 5-ton active (20-ton fiducial) UAr mass will be hosted in a double-phase time projection chamber (TPC) of dimension 3.5 m wide and 3.5 m high. The TPC will be installed in a steel vessel, in turn operated in a DUNE-like cryostat, currently under construction in Hall C at Laboratori Nazionali del Gran Sasso (LNGS). The UAr filling the vessel, outside the TPC, will be instrumented and used as active veto to suppress the radiogenic neutron background. A total amount of approximately 100 t of UAr will be required in order to operate the full system.

The supply chain begins with the Urania Plant in CO, which can produce UAr at a purity of 99.99% from a CO_2 stream sourced from a deep well that reaches the Earth's mantle at a rate of approximately 330 kg/day. After this initial purification stage, the argon will be transported to Carbosulcis S.L.R. in Sardinia, Italy, where the Aria Plant, based on a 350-m cryogenic distillation column, will further suppress impurities. After processing UAr in the Aria Plant, it will be transported from Aria to LNGS, Abruzzo, Italy. A fraction of the production will be shipped to the Canfranc Underground Laboratory (LSC), Spain, where it will be qualified at the DArT through the ArDM experiment [22].

The remainder of the article is organized as follows: Sections 2, 3, and 4 describe the aforementioned steps. Since the importance of this supply chain and associated techniques extends well beyond DarkSide-20k, Section 5 addresses some possible additional applications.

2 The Urania Plant

The Urania Plant is the gas processing plant built by the Italian company Polaris S.r.l. under the supervision of the GADMC to extract 120 tons of UAr for the DarkSide-20k experiment. It will be installed in Cortez, CO, in a new facility operated by the GADMC and currently under construction. The Urania facility will be located in proximity to a private commercial plant for the extraction of CO_2 from underground. Urania will process the CO_2-rich stream extracted from deep underground to separate UAr, which is present at a concentration of 400 ppm ca. In addition to CO_2

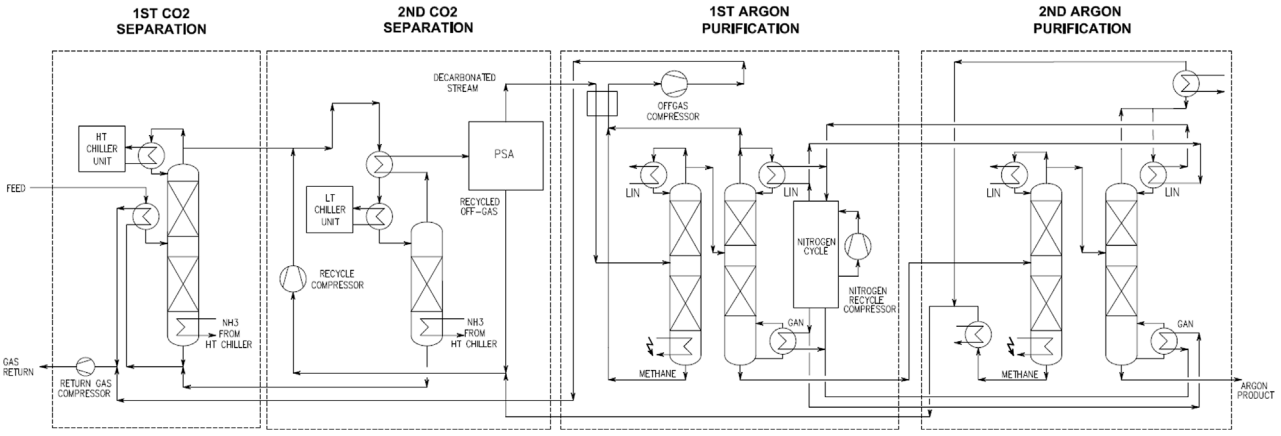

FIGURE 2
Block flow diagram of the Urania Plant.

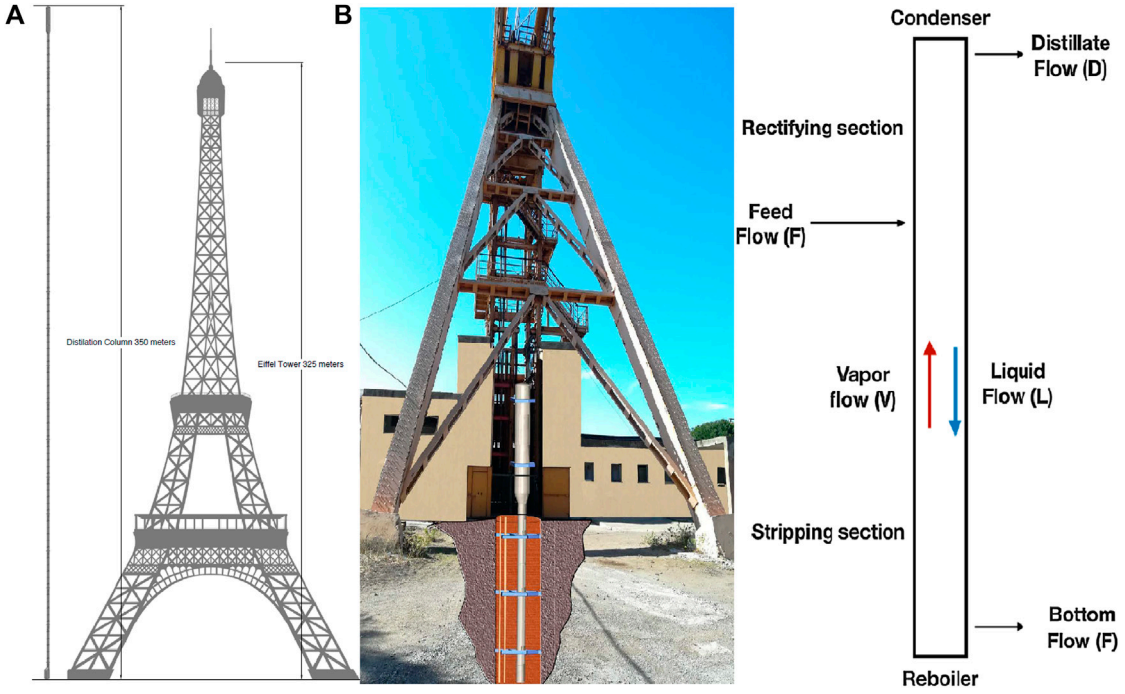

FIGURE 3
(A) Drawing to scale with the Aria 350-m-high column and the Eiffel Tower. **(B)** Picture showing some parts (drawn to scale) of the above-ground vertical mine shaft with the higher part of the column emerging from the mine shaft (from http://www.carbosulcis.eu/). **(C)** Basic operation principles of a continuous distillation column (from obtained [23]).

and Ar, the plant input also contains small amounts of nitrogen and methane. The UAr separation process is based on cryogenic distillation and adsorption, as schematized in the block flow diagram in Figure 2. For more details, please refer to [4].

A first group of distillation columns operating at high pressure removes bulk CO_2, and full removal of CO_2 is achieved in the pressure swing adsorption (PSA) unit operating in loop with one of the distillation columns upstream. The stream leaving the PSA unit is essentially made of nitrogen, methane, and UAr and enters a second group of distillation columns operating at lower pressure, at much lower temperature and located inside a coldbox. The second group of distillation columns separates nitrogen, methane, and UAr and delivers liquid UAr at a nominal rate of 330 kg/day and with a purity better than 99.99% based on the simulation done using Aspen HYSYS® software. With the exception of UAr, all other components are merged and refed to the main plant in full.

The installation of the Urania Plant should begin in mid-2024 in order to enter full operation in 2025. The extraction of UAr needed for DarkSide-20k should be completed by mid-2026. To account for processing losses during the UAr purification phase in Aria, during

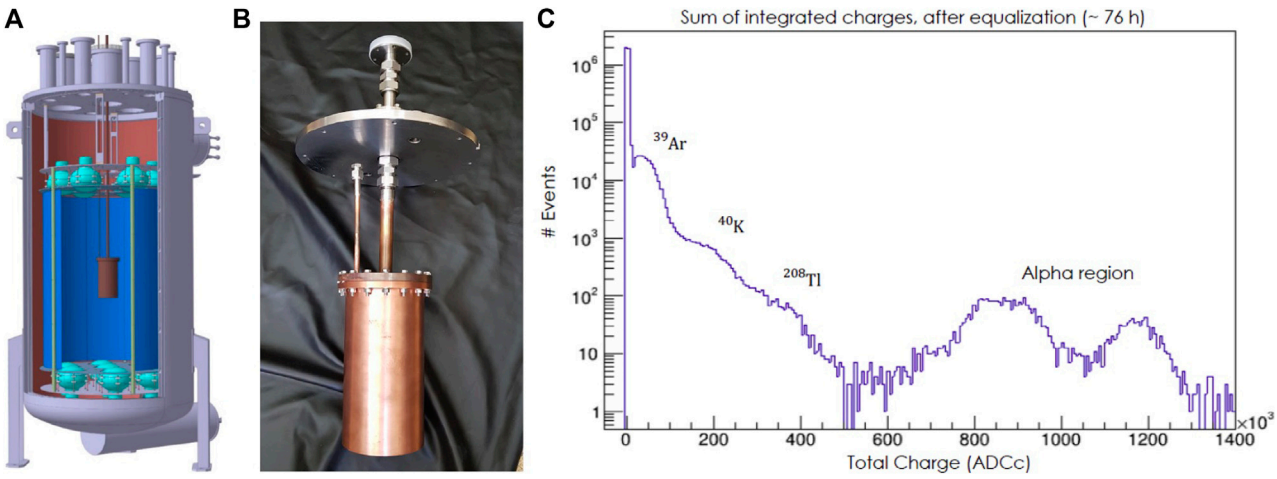

FIGURE 4
(A) Rendering of the DArT in the ArDM experiment. **(B)** Picture of the DArT chamber before its installation inside the ArDM detector. **(C)** Energy spectrum of data collected during a test run underground at LSC.

the filling of the transportation vessels and during shipping, Urania target production quantity for the DarkSide-20k experiment is 120 t.

3 The Aria Plant

The crude UAr from the Urania Plant is shipped to Sardinia, Italy, where it is purified through cryogenic distillation in the so-called Aria Plant. Aria is an industrial-scale plant comprising a 350-m-high cryogenic distillation column, the highest distillation column in the world, and is currently being installed in an underground vertical mine shaft, excavated in 1940, with dimensions 5 m diameter and 350 m deep, at Carbosulcis S.p.A., Nuraxi-Figus (SU), Italy (Figure 3).

Aria was designed to be capable of argon isotopic separation. Cryogenic isotopic distillation with rectifying columns is a well-established technique. However, this is the first time that such a plant is being proposed and constructed for argon isotopic distillation.

Isotopic separation by cryogenic distillation exploits the relative volatility of different isotopes, which for ideal mixtures is given by the ratio of the isotope's vapor pressures at a given temperature. Although the relative volatility of isotopes is close to unity, it allows for the separation of isotopes by continuous distillation using a large number of distillation stages, where the liquid and vapor phases undergo a countercurrent exchange at thermodynamic equilibrium. Aria has been designed to further reduce the concentration of ^{39}Ar by cryogenic distillation in UAr by a factor of 10 per pass and at a rate of approximately 7 kg/day. More information on this, together with a full description of the Aria Plant and the column structure and expected performances, has been provided in [23].

Although the Aria Plant is still in the installation phase, a smaller version of the Aria column, 28 m high, using only the reboiler, the condenser, and one central module, together with all the auxiliary equipment of the full column, installed in a tall surface building has been tested over the last 3 years providing positive results. The first important achievement of this project was an isotopic nitrogen distillation run of the prototype plant [23]. Subsequent to this first achievement, an isotopic separation of argon with the same prototype of the cryogenic distillation plant was achieved. In this case, the column demonstrated the ability to isotopically separate the two stable isotopes, ^{36}Ar and ^{38}Ar, other than ^{40}Ar in AAr, which in AAr, have the non-negligible isotopic abundance of 0.334% and 0.063%, respectively [24], and was considered a milestone for the UAr project. The successful outcome of those runs paved the way to the continuation of the project and the construction of the full plant.

For the DarkSide-20k experiment, the Aria Plant will not be used to reduce ^{39}Ar but rather to chemically purify crude UAr from Urania (with purity already better than 99.99%) to produce detector-grade UAr, i.e., to further reduce nitrogen concentration to 1 ppm, given that from simulations, we can assume that all other impurities are removed by Urania. For this chemical purification, Aria will produce approximately 1,000 kg/day of purified UAr.

Beyond argon isotopic enrichment, the Aria Plant has also commercial applications in the production of isotopes for nuclear energy and medicine.

4 The DArT in the ArDM experiment

The goal of the DArT in the ArDM experiment at LSC is to measure the ^{39}Ar content in batches of UAr delivered by Urania and Aria [22]. DArT in ArDM will be sensitive to very high depletion factors of ^{39}Ar, which is of the order of 1,000, reaching 10% statistical uncertainty in 1 week of data-taking. It will use a single-phase detector, with a total capacity of approximately 1 L (the DArT chamber) filled with samples of UAr. The DArT chamber is a hollow cylinder made of acrylic (PMMA), and it is hosted inside a radiopure copper vessel. The internal surfaces are coated with tetraphenyl butadiene (TPB) wavelength-shifter and the outer surfaces with an enhancer specular reflector. On the top and bottom caps, two ~ 1-cm^2 silicon photomultipliers are placed to collect wavelength-shifted scintillation light from the bulk of the liquid. The amount of collected photoelectrons (PEs) is proportional to the energy

deposited in the liquid bulk. A spectral analysis is performed in order to extract the residual ^{39}Ar contamination from the collected data.

Assuming the ^{39}Ar activity in the UAr as measured by DarkSide-50 (0.73 mBq/kg), the expected number of signal events is approximately 600 per week. Minimizing radiogenic backgrounds is therefore critical for identifying ^{39}Ar signals. In DArT, the internal background generated by the detector's components is effectively reduced through the measurement of radioactive contamination within the materials and the identification of the radiopure samples used to construct the detector's components. To mitigate the background produced by gamma rays originating from the surrounding rock, the DArT vessel will be installed inside the active volume of ArDM shielding [25]. A detailed background model of the experiment based on Monte Carlo simulations reveals that the combination of the ArDM passive shielding (50 cm of HDPE + 6 cm of lead shield) and active veto (40 cm of AAr instrumented with 13 × 8″ photomultipliers) is sufficient to achieve an overall background of a few hundreds of untagged events per week in the DArT region of interest. Figures 4A,B show a rendering of the DArT in the ArDM experiment and a picture of the DArT chamber.

In order to study the detector's performance and gain a preliminary understanding of the internal background, the DArT detector has been operating underground in a test setup for several months, concurrently with the refurbishment of the ArDM setup. The operating conditions in this temporary setup were optimized for cooling and maintaining DArT at 85 K, achieved using liquid nitrogen (LN_2). Hardware and software parameters for the data acquisition system were optimized; noise was minimized through the use of filters, external insulation on cables and connections, common grounding, and setting trigger threshold conditions for robust continuous operation. The setup was installed within a purpose-built lead castle that was flushed with Rn-free air. A preliminary plot of the data analysis taken underground in the test setup is reported in Figure 4B. It shows the alpha peaks arising from the ^{222}Rn contamination in LAr (eventually identifiable by PSD), along with two bumps consistent with the gamma emissions, resulting from ^{40}K and ^{208}Tl contaminations present in the detector materials. The low-energy spectrum aligns with the ^{39}Ar beta-spectrum. A run with UAr from the DarkSide-50 experiment aimed to evaluate ^{39}Ar activity and is expected to begin in 2024 to validate the designed setup.

5 Beyond the WIMP search

In addition to WIMP dark matter detection, leading experimental searches across particle physics will benefit from the availability of low-radioactivity UAr.

The ^{39}Ar decays represent the dominant intrinsic background source in argon-based experiments searching for coherent elastic neutrino–nucleus scattering. A $\mathcal{O}(10-1000)$ reduction of this contamination could extend their live-time and improve the statistical significance of the measurement [5].

The LEGEND-1000 experiment will search for $0\nu\beta\beta$-decay of ^{76}Ge in cryogenic Ge detector strings distributed among four 250-kg modules. The modules are immersed in liquid argon serving simultaneously as a radiation shield, coolant, and scintillation detector. Beta decays from ^{42}K (beta-emitter daughter of ^{42}Ar) are a potential intrinsic background in the LEGEND-1000 LAr shield, as reported using the GERDA experiment [13]. The ^{42}Ar depletion of UAr makes it an ideal candidate to suppress this class of backgrounds in the argon that surrounds the germanium crystals, with a consequent improvement in the experiment sensitivity.

A reduction of ^{42}K and ^{39}Ar in DUNE-like detectors would also enable the measurement of low-energy neutrinos [6]. ^{42}K and ^{39}Ar are currently one of the largest expected backgrounds at low energy, impacting the energy resolution for $\lesssim$ 10 MeV events and representing a challenge from the trigger strategy and event classification. Although the procurement of multi-kiloton target of UAr is currently an open challenge, its availability would enlarge the physics reach of a DUNE-like detector to improve, among the others, the sensitivity to supernova bursts.

Furthermore, a dedicated ton-scale detector optimized for the collection of ~ keV ionization signals from low-mass dark matter candidates could benefit from lower-energy thresholds [26].

The potential needs for UAr, motivated by disparate scientific goals as those described above, span from tens of kilograms (i.e., for the COHERENT experiments) and tens of tons (i.e., for LEGEND-1000) to tens of kilotons (i.e., for a DUNE-like modules), across several orders of magnitude in the reduction of long-lived argon radioisotope concentration.

6 Conclusion

The ability to extract argon from deep underground was demonstrated for the first time using the DarkSide-50 experiment, which measured an ^{39}Ar depletion factor of $(1.4 \pm 0.2) \times 10^3$ compared to the argon found in the atmosphere. The discovery of UAr with reduced ^{39}Ar content represents a major breakthrough for the argon-based technology and broadens the physics reach of argon detectors in high energy and nuclear physics.

The GADMC aims at performing the most sensitive search for WIMP dark matter in the next decade using the DarkSide-20k detector at LNGS. One of the requirements to meet this ambitious goal is the extraction of 120 t of low-radioactivity argon from deep underground. The supply chain for extraction, purification, and quality check of the target for DarkSide-20k includes the Urania (Cortez, CO), Aria (Sardinia, Italy), and DArT in ArDM (LSC, Spain) facilities, currently being constructed or commissioned.

The scaling up of these facilities is under consideration to meet the increased demand for low-radioactivity argon beyond the DarkSide-20k WIMP search and toward Argo, the next-generation UAr multi-hundred-ton dark matter detector, aiming to reach sensitivity beyond the neutrino floor with a 3,000 t-yr exposure run [27].

Data availability statement

The original contributions presented in the study are included in the article/Supplementary Material; further inquiries can be directed to the corresponding author.

Author contributions

PA: writing–original draft. HB: writing–original draft, writing–review and editing. WB: writing–review and editing. MB: writing–review and editing. NC: writing–review and editing. MC:

writing–original draft. SC: writing–review and editing. VC: writing–review and editing. DM: writing–review and editing. DF: writing–review and editing. FG: writing–original draft, writing–review and editing. DG: writing–review and editing. CG: writing–review and editing. PG: writing–review and editing. AG: writing–review and editing. TH: writing–review and editing. SH: writing–review and editing. RL: writing–review and editing. LL: writing–review and editing. MM: writing–review and editing. VP: writing–review and editing. MR: writing–original draft, writing–review and editing. ALR: writing–review and editing. LR: writing–review and editing. ARu: writing–review and editing. RSa: writing–review and editing. MS: writing–review and editing. RSt: writing–review and editing. AS: writing–review and editing. SS: writing–review and editing.

Funding

The author(s) declare that financial support was received for the research, authorship, and/or publication of this article. This research is part supported by the Spanish Ministry of Science and Innovation (MICINN) through the grant PID2022-138357NB-C22.

Conflict of interest

The authors declare that the research was conducted in the absence of any commercial or financial relationships that could be construed as a potential conflict of interest.

Publisher's note

All claims expressed in this article are solely those of the authors and do not necessarily represent those of their affiliated organizations, or those of the publisher, the editors, and the reviewers. Any product that may be evaluated in this article, or claim that may be made by its manufacturer, is not guaranteed or endorsed by the publisher.

References

1. Adhikari P, Ajaj R, Araujo GR, Batygov M, Beltran B, Bina CE, et al. The liquid-argon scintillation pulseshape in deap-3600. *The Eur Phys J C* (2020) 80:303. doi:10.1140/epjc/s10052-020-7789-x

2. Adhikari P, Ajaj R, Alpízar-Venegas M, Amaudruz P-A, Anstey J, Araujo GR, et al. Precision measurement of the specific activity of ^{39}Ar in atmospheric argon with the deap-3600 detector. *Eur Phys J C* (2023) 83:642. doi:10.1140/epjc/s10052-023-11678-6

3. Abratenko P, Andrade Aldana D, Anthony J, Arellano L, Asaadi J, Ashkenazi A, et al. First constraints on light sterile neutrino oscillations from combined appearance and disappearance searches with the microboone detector. *Phys Rev Lett* (2023) 130:011801. doi:10.1103/PhysRevLett.130.011801

4. Aalseth CE, Acerbi F, Agnes P, Albuquerque IFM, Alexander T, Alici A, et al. Darkside-20k: a 20 tonne two-phase lar tpc for direct dark matter detection at lngs. *The Eur Phys J Plus* (2018) 133:131. doi:10.1140/epjp/i2018-11973-4

5. Akimov D, Albert JB, An P, Awe C, Barbeau PS, Becker B, et al. First measurement of coherent elastic neutrino-nucleus scattering on argon. *Phys Rev Lett* (2021) 126:012002. doi:10.1103/PhysRevLett.126.012002

6. Abi B, Acciarri R, Acero M, Adamov G, Adams D, Adinolfi M, et al. Volume i. introduction to dune. *J Instrumentation* (2020) 15:T08008. doi:10.1088/1748-0221/15/08/T08008

7. Agnes P, Albuquerque IFM, Alexander T, Alton AK, Araujo GR, Asner DM, et al. Low-mass dark matter search with the darkside-50 experiment. *Phys Rev Lett* (2018) 121:081307. doi:10.1103/PhysRevLett.121.081307

8. Agnes P, Albuquerque IFM, Alexander T, Alton AK, Ave M, Back HO, et al. Search for low mass dark matter in darkside-50: the bayesian network approach. *Eur Phys J C* (2023) 83:322. doi:10.1140/epjc/s10052-023-11410-4

9. Agnes P, Albuquerque IFM, Alexander T, Alton AK, Araujo GR, Ave M, et al. Darkside-50 532-day dark matter search with low-radioactivity argon. *Phys Rev D* (2018) 98:102006. doi:10.1103/PhysRevD.98.102006

10. Loosli H. A dating method with39ar. *Earth Planet Sci Lett* (1983) 63:51–62. doi:10.1016/0012-821X(83)90021-3

11. Benetti P, Calaprice F, Calligarich E, Cambiaghi M, Carbonara F, Cavanna F, et al. Measurement of the specific activity of 39ar in natural argon. *Nucl Instr Methods Phys Res Section A: Acc Spectrometers, Detectors Associated Equipment* (2007) 574:83–8. doi:10.1016/j.nima.2007.01.106

12. Ajaj R, Araujo GR, Batygov M, Beltran B, Bina CE, Boulay MG, et al. Electromagnetic backgrounds and potassium-42 activity in the deap-3600 dark matter detector. *Phys Rev D* (2019) 100:072009. doi:10.1103/PhysRevD.100.072009

13. Lubashevskiy A, Agostini M, Budjáš D, Gangapshev A, Gusev K, Heisel M, et al. Mitigation of ^{42}Ar/^{42}K background for the gerda phase ii experiment. *Eur Phys J C* (2018) 78:15. doi:10.1140/epjc/s10052-017-5499-9

14. Abgrall N, Abt I, Agostini M, Alexander A, Andreoiu C, Araujo GR, et al. LEGEND-1000 preconceptual design report. *arXiv* (2021). e-prints, arXiv:2107.11462. doi:10.48550/arXiv.2107.11462

15. Loosli H, Lehmann B, Balderer W. Argon-39, argon-37 and krypton-85 isotopes in stripa groundwaters. *Geochimica et Cosmochimica Acta* (1989) 53:1825–9. doi:10.1016/0016-7037(89)90303-7

16. Šrámek O, Stevens L, McDonough WF, Mukhopadhyay S, Peterson R. Subterranean production of neutrons, 39ar and 21ne: rates and uncertainties. *Geochimica et Cosmochimica Acta* (2017) 196:370–87. doi:10.1016/j.gca.2016.09.040

17. Galbiati C, Acosta-Kane D, Acciarri R, Amaize O, Antonello M, Baibussinov B, et al. *Discovery of underground argon with a low level of radioactive* ^{39}Ar *and possible applications to WIMP dark matter detectors. J Phys Conf Ser* (2008) 120:042015. doi:10.1088/1742-6596/120/4/042015

18. Back HO, Calaprice F, Condon C, de Haas E, Ford R, Galbiati C, et al. *First large scale production of low radioactivity argon from underground sources* (2012).

19. Agnes P, Agostino L, Albuquerque IFM, Alexander T, Alton AK, Arisaka K, et al. Results from the first use of low radioactivity argon in a dark matter search. *Phys Rev D* (2016) 93:081101. doi:10.1103/PhysRevD.93.081101

20. Zhang C, Mei D-M. Evaluation of cosmogenic production of ^{39}Ar and ^{42}Ar for rare-event physics using underground argon. *Astroparticle Phys* (2022) 142:102733. doi:10.1016/j.astropartphys.2022.102733

21. Poudel SS, Loer B, Saldanha R, Hackett BR, Back HO. *Subsurface cosmogenic and radiogenic production of* ^{42}*Ar* (2023). doi:10.48550/arXiv.2309.16169

22. Aalseth C, Abdelhakim S, Acerbi F, Agnes P, Ajaj R, Albuquerque I, et al. Design and construction of a new detector to measure ultra-low radioactive-isotope contamination of argon. *J Instrumentation* (2020) 15:P02024. doi:10.1088/1748-0221/15/02/P02024

23. Agnes P, Albergo S, Albuquerque IFM, Alexander T, Alici A, Alton AK, et al. Separating ^{39}Ar ^{40}Ar by cryogenic distillation with aria for dark-matter searches. *Eur Phys J C* (2021) 81:359. doi:10.1140/epjc/s10052-021-09121-9

24. Agnes P, Ahmad I, Albergo S, Albuquerque IFM, Alexander T, et al. Measurement of isotopic separation of argon with the prototype of the cryogenic distillation plant aria for dark matter searches. *Eur Phys J C* (2023) 83:453. doi:10.1140/epjc/s10052-023-11430-0

25. Calvo J, Cantini C, Crivelli P, Daniel M, Luise SD, Gendotti A, et al. Commissioning of the ardm experiment at the canfranc underground laboratory: first steps towards a tonne-scale liquid argon time projection chamber for dark matter searches. *J Cosmology Astroparticle Phys* (2017) 2017:003. doi:10.1088/1475-7516/2017/03/003

26. Agnes P, Ahmad I, Albergo S, Albuquerque IFM, Alexander T, Alton AK, et al. Sensitivity projections for a dual-phase argon tpc optimized for light dark matter searches through the ionization channel. *Phys Rev D* (2023) 107:112006. doi:10.1103/PhysRevD.107.112006

27. Agnes P, Albergo S, Albuquerque I, Alexander T, Alici A, Alton A, et al. Sensitivity of future liquid argon dark matter search experiments to core-collapse supernova neutrinos. *J Cosmology Astroparticle Phys* (2021) 2021:043. doi:10.1088/1475-7516/2021/03/043

Frontiers in Physics

Investigates complex questions in physics to understand the nature of the physical world

Addresses the biggest questions in physics, from macro to micro, and from theoretical to experimental and applied physics.

Discover the latest Research Topics

See more →

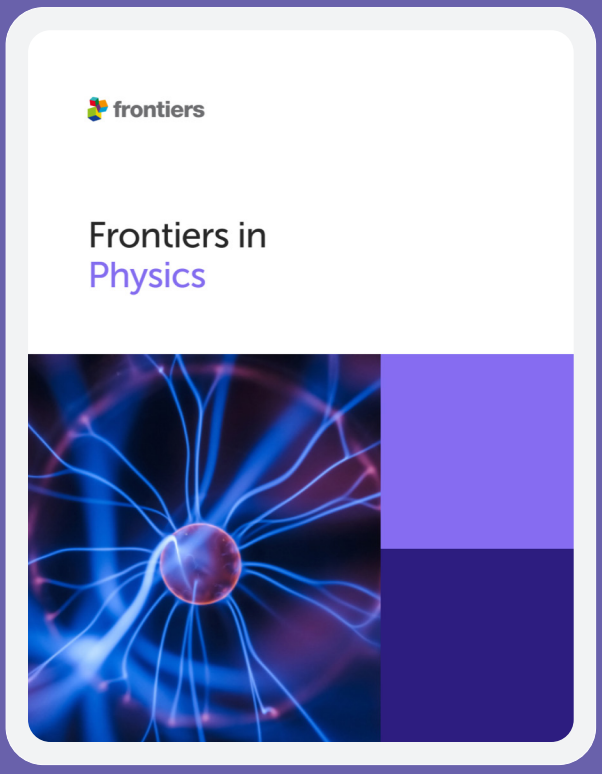

Frontiers

Avenue du Tribunal-Fédéral 34
1005 Lausanne, Switzerland
frontiersin.org

Contact us

+41 (0)21 510 17 00
frontiersin.org/about/contact